# The Properties of Grain Boundaries in $YBa_2Cu_3O_{7-\delta}$

James H. T. Ransley
Darwin College,
Department of Materials Science
and IRC in Superconductivity
University of Cambridge
United Kingdom

Dissertation submitted as part of the requirement
for the degree of Doctor of Philosophy
University of Cambridge

January 2004

# Declaration

This dissertation is my own work and contains nothing which is the outcome of work done in collaboration with others, except as specified in the text and Acknowledgements. No part of this dissertation has been submitted for a degree or diploma or other qualification at this or any other university. This dissertation does not exceed 60,000 words in length. 

James Ransley
Cambridge
January 2004

# Contents

# List of Figures

# List of Tables

# Summary

Grain boundaries form the basis of an important Josephson junction technology in the cuprates and also limit the superconducting critical currents attainable in practical, polycrystalline materials. An improved understanding of these defects is therefore important for applications. The status of the current understanding of cuprate grain boundaries is summarised and experimental investigations are presented, focusing on the less well understood high angle boundaries.

Measurements of the capacitance of grain boundaries in the overdoped superconductor $Y_{1-x}Ca_xBa_2Cu_3O_{7-\delta}$, were performed as a function of the calcium content, using the Josephson coupling across the boundaries. Particular care was taken to eliminate the effects of heating and stray capacitance due to the substrate. The effect of thermal noise was also assessed. These measurements provide important information about the area and the width of the grain boundaries, that highlights their inhomogeneous nature.

A new technique was applied to measure the normal state properties of $YBa_2Cu_3O_{7-\delta}$ grain boundaries above the critical temperature. Since the resistance of the adjacent material at high temperatures is comparable to, or greater than that of the grain boundary, a compensating Wheatstone bridge structure was used. The errors involved in this technique are carefully assessed and quantified. The normal state resistance of a number of different grain boundary orientations was measured from room temperature to the critical temperature. Detailed characterisation of the grain boundaries, including measurements of the critical current and the current voltage characteristics at low temperatures, was performed. The results obtained are used to assess the validity of the various theories for the grain boundary electrical structure. A tunneling model that accounts for the band structure of the material is developed and applied to potential barriers consistent with a band bending model. This theory is shown to provide a convincing account of the experimental results presented in this thesis.

# Acknowledgements

First I want to thank my supervisor Prof. Jan Evetts, who, by his patient support, guidance and encouragement, made the work in this thesis possible. His confidence and good humour have sustained me throughout the experimental work and through the preparation of this thesis. Dr Edward Tarte also provided informal supervisory support, particularly throughout the work in Chapter 6 and during the year I spent growing thin films. I am grateful for his never-failing cheerfulness, even through what I know must have been some difficult times for him. I must also extend my heartfelt thanks to Sibe Mennema, who collaborated with me during the measurements described in Chapters 5 and 6. His commitment to the work and his friendship made the task of passing on accumulated experimental knowledge much more enjoyable, and I really missed working with him when the time came for him to work independently. Dr Mark Blamire provided valuable suggestions for improving both the experimental work on the normal state resistance and the tunneling model. Dr Karl Sandeman's good humour and patience despite many difficulties were very encouraging during the modelling part of the work. I was very privileged to work with him. I haven't forgotten the bottle of whisky I promised you Karl!

Thanks are also extended to Dr Philip McBrien, who invested considerable time at the beginning of this work, teaching me how to process and measure devices. Dr Micheal Hogg provided invaluable assistance with learning atomic force microscopy and Dr Gary Gibson taught me the basics of depositing thin films by pulsed laser ablation. My thanks are also extended to Dr John Durrell, who spent time teaching me how to use the group's angular critical current rig, for a series of experiments that were never completed. I'll always remember his good humoured advice and his delight in discussing all things political. Dr Gavin Burnell deserves particular thanks: it's hard to think of any part of the lab that he hasn't been involved in automating, or building, and he has therefore contributed to this work in too many ways to mention individually. Dr Doug Astill provided valuable technical support during the year I spent growing thin films at the IRC in Superconductivity,

for which I am extremely grateful. In the same year I was very blessed with the companionship and advice of David Ansell — who also taught me how to solder properly! Dr Robert Schultz, Dr Jeong-Il Kye and Dr Byungdu Oh are all acknowledged for providing thin films used in this investigation. Sibe Mennema, Dr Henny Zandbergen and Mr Sorin Lazar are thanked for their contributions to the Transmission Electron Microscopy work. Thanks also go to Dr John Lister for providing me with an instant solution to an integral I couldn't do on one occasion! I'd like to thank Paul and Ken in the Materials workshop for their patience with all the little (and not so little) jobs that they patiently worked at. The same goes for Sam, Eric and Ian in the IRC workshop, who have all built parts of apparatus that I have used in this investigation.

I owe a good deal to various scientists who have provided valuable comments on the work in this thesis. Dr John Cooper and Dr John Loram were particularly patient in discussing the details of the normal state properties of cuprates with me, for which I am very grateful. Dr Christian Jooss was also very kind in sharing experimental results with me prior to publication and in discussing the details of the band bending model in considerable depth. Dr Christof Schnieder was also kind enough to share some preliminary data with me and to discuss the use of the bridge technique. I am grateful for discussions with the following people: Dr Alex Guerevich, Dr Juergen Halbritter, Dr Hans Hilgenkamp, Prof. David Larbalestier, Prof. Peter Littlewood and Prof. Jochen Mannhart . I would like to thank the group of Prof. Jochen Mannhart (and in particular Dr Robert Schultz) for being so hospitable during a visit to learn about their pulsed laser deposition facility.

I would also like to express my appreciation to the Interdisciplinary Research Centre in Superconductivity and the Department of Materials Science and Metallurgy for the award of a research council grant, financial support in my final year and the provision of experimental facilities.

Needless to say I am very grateful for the support of many other people, including: Dr Mark Blamire, Dr Nadia Stelmashenko, Dr Zoe Barber (I'll always remember the band of three visitors at the end of my first term when I was unwell), Dr Robert Hadfield, Chris Bell, Dr Rumen Tomov (I'm going home now Rumen!), Dr Bartek Glowacki, Dr Vassilka Tsaneva and Dr Karen Yates. Special thanks go to Dr Chiranjib Mitra, who has been a valued companion in prayer about work and life, as well as a great friend. I've enjoyed working with everyone in the Device Materials group and particularly thank my contemporary PhD students for the fun we've had together. Thanks also go to Alicia, the IRC secretary, and to the IRC cleaners: John, Ron and Graham - who all spurred me on during the difficult days of writing!

I'm very grateful for the friendship and support provided by my many

friends. Special thanks also go to James, Dave and Sheetala, who have always been there for me during my time in Cambridge.

My family deserve enormous gratitude. They have always been ready to go the extra mile for me, and have taught me by example the meaning of love. Their support has always kept me going and inspired me. I wouldn't be here without them. Chau - you are now included in the family and your patience with me in these last months has made me so glad that you will soon be my wife.

Finally there is One who deserves the most thanks and all the praise. As I write the last few words of this thesis I am reminded of 1 Corinthians 4:7, "For who makes you different from anyone else? What do you have that you did not receive? And if you did receive it, why do you boast as though you did not?". Without You, my God, I would never even have started a PhD, let alone finished this thesis. I commit it to You. In the words of David, which I now echo: "I love you, O Lord, my strength. The Lord is my rock, my fortress and my deliverer; my God is my rock in whom I take refuge. He is my shield and the horn of my salvation, my stronghold. I call to the Lord, who is worthy of praise, and am saved from my enemies." (Psalm 18:1-3)

# Chapter 1

# Introduction

The discovery of high temperature superconductivity in 1986 [1] led to much excitement about widespread practical applications of superconducting materials. Shortly after the discovery of these materials it was realised that the critical currents attainable in polycrystalline material were severely reduced by grain boundaries [1, 2, 3, 4, 5]. Since polycrystalline samples are necessary for the production of long length superconducting wires or tapes, essential for bulk applications, grain boundaries in superconducting materials have become a subject of intensive study. Grain boundaries are also important for many high $T_c$ devices — for use in electronic applications. High angle grain boundaries are Josephson coupled [6, 7] and have been used as the basis of several junction technologies in the cuprates.

This chapter begins with a brief introduction to grain boundaries and the nomenclature used to describe them. A brief review of superconductivity and the Josephson effect follows. The important role of grain boundaries in both bulk and electronic applications of high $T_c$ superconductivity is then highlighted. The remainder of this thesis is focused on investigating these technologically important defects.

## 1.1 An Introduction to Grain Boundaries

The main features of grain boundary phenomenology are highlighted by the nomenclature used to describe them. Three distinct classes of grain boundary can be defined on the basis of the alignment of the crystallographic axis either side of the boundary plane: [001] tilt, [100] tilt and [100] twist. These three orientations are defined in Fig. 1.1. The term 'tilt' refers to a rotation about an axis in the plane of the boundary whilst 'twist' refers to a rotation about an axis perpendicular to the boundary. In general a grain boundary may

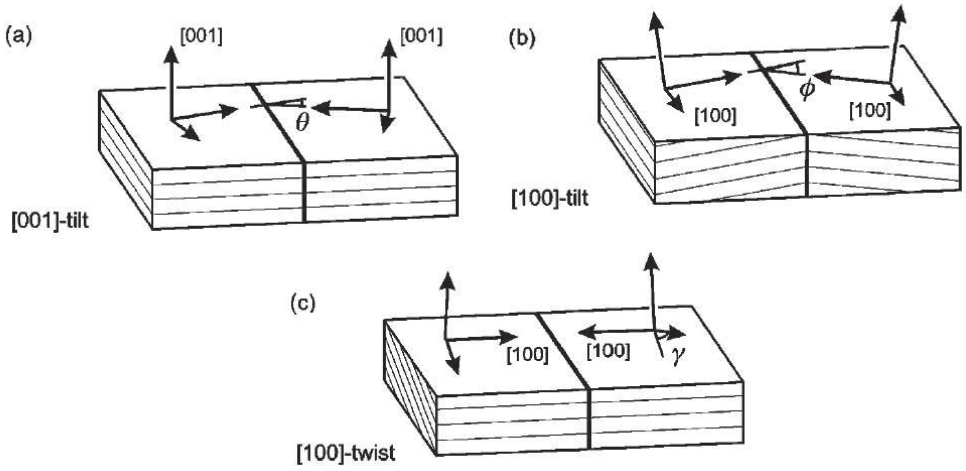


Figure 1.1: Schematic illustrating the definitions of a) [001]-tilt, b) [100]-tilt and c) [100] twist boundaries (adapted from [2]).

have components of all three of these misorientation types — boundaries with more than one component are termed 'mixed'.

The 'misorientation angles' ($\theta$, $\phi$ and $\gamma$) are also defined in Fig. 1.1. For the case of tilt boundaries additional 'inclination angles', $\alpha_1$ and $\alpha_2$, can be defined on each side of the grain boundary. The inclination angle is defined as the angle between the grain boundary plane and the axis that is rotated out of that plane as the misorientation angle is increased from zero (see Fig. 1.2 for a schematic representation). For a 'symmetric' tilt boundary $\alpha_1 = \alpha_2$. The term 'asymmetric' is commonly used to denote boundaries in which $\alpha_1 = 0$ and $\alpha_2$ is the total misorientation angle - this nomenclature is adopted in this study.

The structure of the grain boundary is strongly dependent on the magnitude of the misorientation angle. Grain boundaries of a given type can be divided into distinct 'low angle' and 'high angle' classes. In 'low angle' boundaries the misorientation is accommodated by arrays of dislocations separated by well lattice matched regions. Depending on the orientation of the boundary several sets of dislocations may be required to accommodate the misorientation. The distance between dislocations is determined by the misorientation angle of the boundary. For example for an ideal [001]-tilt boundary the misorientation, $\theta$, is accommodated by an array of edge dislocations with Burgers vectors, $\mathbf{b}$ in the [100] or [010] directions separated by a distance $D$ given by the Read-Shockley (or Frank's) formula:

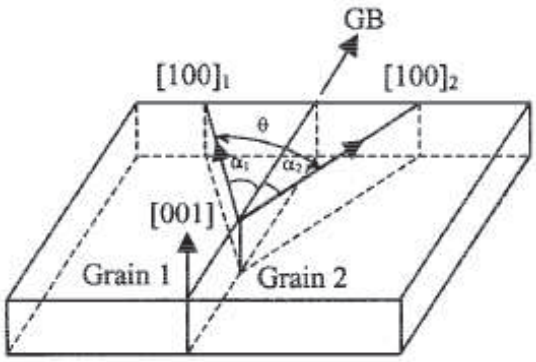


Figure 1.2: Schematic illustrating the definition of the inclination angles in an [001] tilt boundary (adapted from [8]).

$$D = \frac{|\mathbf{b}|}{2\sin(\theta/2)} \tag{1.1}$$

As the misorientation angle is increased, the spacing between the dislocations is reduced until a continuous disordered region appears at the boundary. When this occurs, the boundary is termed a 'high angle' boundary. The gradual merging of the grain boundary dislocation structure is well illustrated in the high resolution transmission electron microscopy images of Wen *et al.* [9], shown in Fig. 1.3. The change in the atomic structure at the boundary is evident from z-contrast images of the boundary, due to Browning *et al.* — which have sufficient resolution that the columns of atoms can be clearly seen. Figure 1.4 shows two images, for high and low angle grain boundaries in $YBa_2Cu_3O_{7-\delta}$. A clear difference in the atomic structure at the boundary can be seen. Babcock and Vargas [10] identified that for [001] tilt boundaries in $YBa_2Cu_3O_{7-\delta}$ the dislocations merge into a continuous structure at an angle of approximately 20°.

Browning *et al.* have identified that high angle boundaries are comprised of a number of structural units. The same structural units make up the dislocation cores of low angle boundaries. Fundamental work on high angle boundaries can therefore lead to an improved understanding of the electrical structure of low angle grain boundary dislocation cores, as discussed below.

This study focuses on [001] tilt, high angle grain boundaries. As discussed in the next section these grain boundaries are particularly important for applications. Although this thesis focuses on high angle boundaries, the insights gained may prove useful in furthering the understanding of low angle boundary dislocation cores.

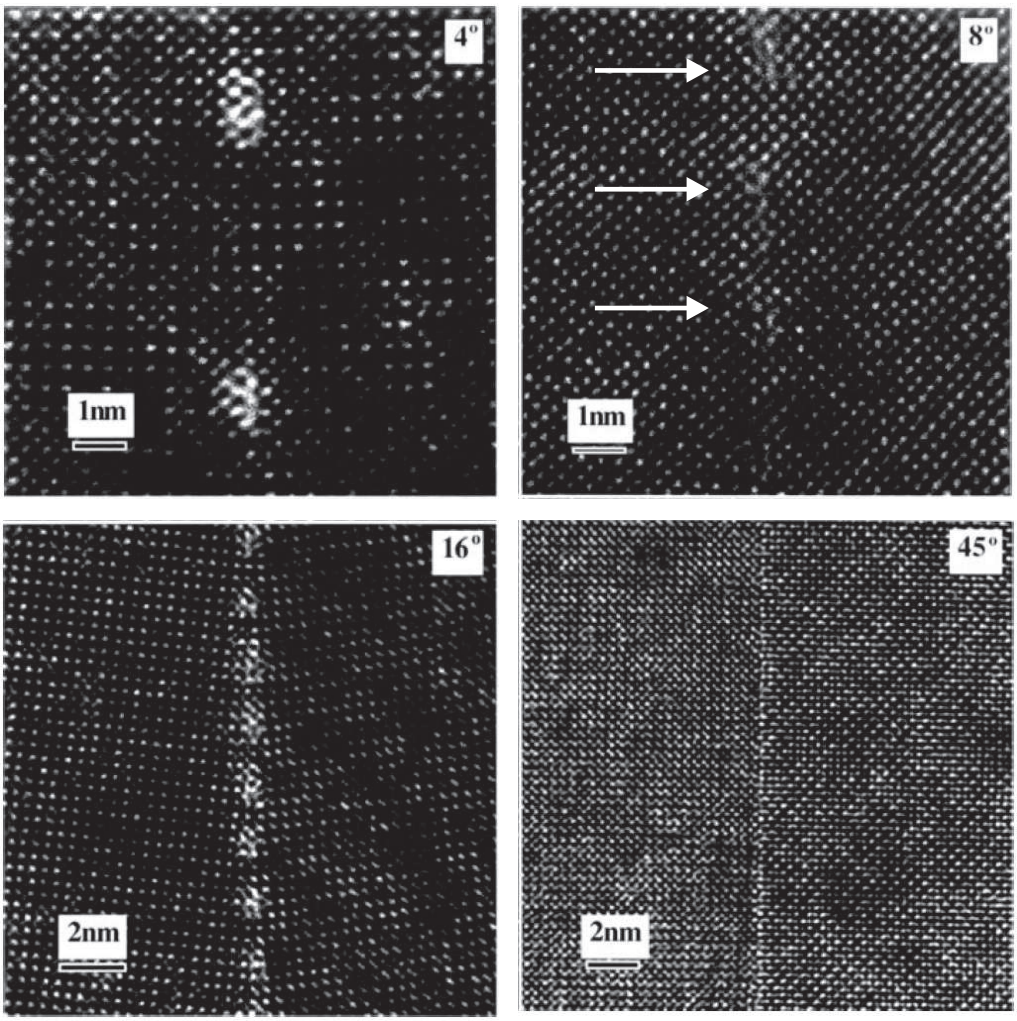


Figure 1.3: High resolution electron microscopy images of $YBa_2Cu_3O_{7-\delta}$ [001] tilt grain boundaries of increasing misorientation angles. The white arrows mark the locations of the dislocations where these are difficult to see. In the case of the 45° boundary the dislocation structures have merged and a continuous barrier is formed at the interface. These grain boundaries have been prepared by liquid phase epitaxy growth on MgO substrates [9].

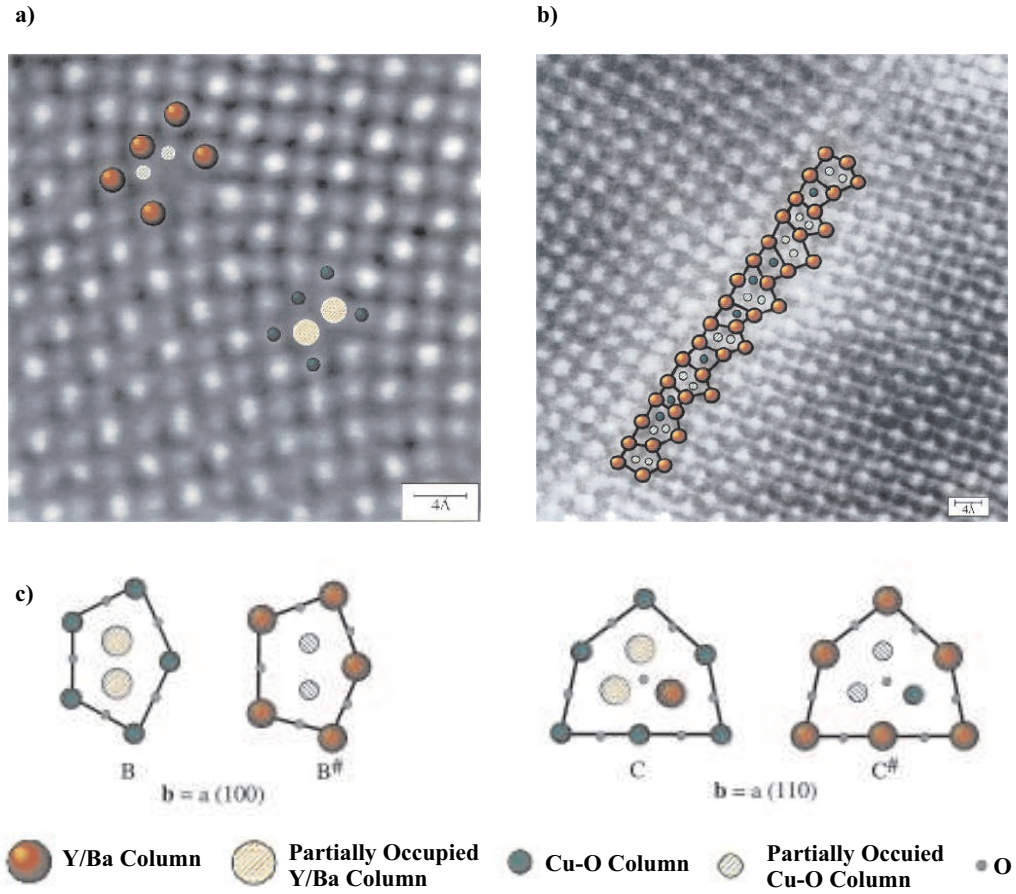


Figure 1.4: Z contrast images of a) a low angle [001] tilt boundary and b) a 30° [001] tilt high angle boundary. The inferred locations of the atomic columns are marked. c) The structural units that are the constituents of both the dislocation cores and the high angle grain boundaries. Adapted from [11].

## 1.2 An Introduction to Superconductivity and the Josephson Effect

In this section a brief overview of the important properties of superconductors is given. The basic principles of superconductivity are reviewed and then the Josephson effect is described in more detail, because of its importance for the understanding of high angle grain boundaries in high-$T_c$ materials.

### 1.2.1 An Overview of the Basic Theory of Superconductivity and its Development

Superconductivity was discovered by the Dutch physicist Heike Kamerlingh Omnes in 1911, two years after he invented a process to liquefy helium [12]. He found that just below 4.2 K the electrical resistance of mercury disappeared and that a loop of material was capable of carrying a persistent current. He also noticed that at any given temperature this effect could be suppressed by the application of a sufficiently strong magnetic field. The temperature at which the resistance disappeared was termed the critical temperature, $T_c$, whilst the critical field required to return the superconductor to a resistive state was termed the thermodynamic critical field, $B_c$. In 1933 Meissner discovered that superconductors exhibit perfect diamagnetism [13], that is they exclude magnetic field from their interior. The Meissner effect distinguishes superconductors from perfect electrical conductors and is one of the most fundamental properties of superconductivity.

In 1935 the first theoretical framework to provide a detailed understanding of superconductivity was developed. The London theory was based on the observation of perfect diamagnetism and the earlier suggestion (by Gorter and Casimir [14]) that the magnetic properties of superconductors could be understood by a two fluid model. Within the two fluid model there is an electron charge density $\rho_s = n_s e$ associated with electrons in the superfluid condensate and a charge density $\rho_n$ of electrons excited out of the condensate and subject to the usual scattering processes. The London brothers introduced two equations, which, in conjunction with Maxwell's equations, described the properties of the superconductor in a phenomenological manner [15]:

$$\frac{d\mathbf{J_s}}{dt} = \frac{n_s e^2}{m}\mathbf{E} \tag{1.2}$$

$$\nabla \times \mathbf{J_s} = -\frac{\mu_0 n_s e^2}{m}\mathbf{B} \tag{1.3}$$

where $\mathbf{J_s}$ is the supercurrent density, $\mathbf{B}$ is the magnetic field density in the superconductor and $m$ is the mass of the electron.

The first London equation implies an accelerating current in a DC electric field and so predicts zero resistance. Taking the curl of the Maxwell equation $\nabla \times \mathbf{B} = \mu_0(\mathbf{J_s} + \mathbf{J_n})$ and substituting in the second London equation (as well as assuming $J_n = 0$, as is usually the case) we obtain: $\nabla^2\mathbf{B} = \mu_0 n_s e^2 \mathbf{B}/m$. This result has the form of a screening equation and therefore defines a characteristic decay length for the magnetic field $\lambda_L = \sqrt{(m/(\mu_0 n_s e^2))}$. Within the London penetration depth surface currents flow to screen the magnetic field from the interior of the superconductor. The penetration depth is temperature dependent since it depends on $n_s$. A good empirical approximation for its temperature dependence is $\lambda_L(T) = \lambda_L(0)/(1-(T/T_c)^4)^{1/2}$.

The experiments of Pippard in the late 1940's revealed that the penetration depth $\lambda$ was markedly greater than $\lambda_L$ in materials with short electronic mean free paths. In order to explain this behaviour he proposed a form of the second London equation in which the supercurrent is sensitive to non-local electromagnetic fields in a region determined by the electromagnetic coherence length, $\xi_{em}$ [16]. If $l$ is the electron mean free path, $\xi_{em}^{-1} = \xi_0^{-1} + l^{-1}$, where $\xi_0$ is the coherence distance in the pure metal.

At about the same time as Pippard's work on the coherence length Ginzburg and Landau developed a theory of superconductivity by applying Landau's theory of phase transitions to the superconducting state. Landau had previously introduced the concept of an 'order parameter' to quantify the ordering process that occurs during a phase transition. He had shown that the free energy could be expressed in terms of this order parameter. In the case of superconductors Ginzburg and Landau proposed a complex order parameter $\psi(\mathbf{r}) = |\psi(\mathbf{r})| \exp[i\theta(\mathbf{r})]$. The order parameter is related to the density $n_s^*$ of the superconducting condensate by the equation $n_s^* = |\psi(\mathbf{r})|^2$. By expanding the free energy in powers of $\psi(\mathbf{r})$, neglecting high order terms and minimising the resulting expression with respect to $\psi^*(\mathbf{r})$, Ginzburg and Landau derived a non-linear Schrödinger-like equation to determine $\psi(\mathbf{r})$ (the first Ginzburg Landau equation). In addition they showed that the current density $\mathbf{J}_s$ was related to this wavefunction by the equation:

$$\mathbf{J}_s = \frac{e^*|\psi(\mathbf{r})|^2}{m^*}(\hbar\nabla\theta - e^*\mathbf{A}) \tag{1.4}$$

where $\mathbf{A}$ is the magnetic vector potential and $e^*$ and $m^*$ are the charge and the mass per condensate unit respectively (this is the second Ginzburg Landau equation). The curl of this equation reduces to the form of the second London equation, so the London penetration depth $\lambda_L$ and the Meissner effect are derived naturally from the Ginzburg-Landau theory. Note that, since we now know the condensate consists of pairs of electrons, $e^* = 2e$, $m^* = 2m$ and $n_s^* = n_s/2$. Note also that, because the theory is derived by neglecting high order terms in the expansion of the free energy, it can only be applied at temperatures close to the critical temperature, where the assumption that $n_s^*$ is small is valid. However equation 1.4 can be shown to follow from the existence of a macroscopic wavefunction and is therefore much more generally valid.

An important consequence of the existence of an order parameter is the phenomenon of 'fluxoid quantisation'. Consider a toroidal region of superconductor threaded by a magnetic field. Since the line integral of $\nabla\theta$ around a closed loop, $L$, must be an integral number of $2\pi$ if $\psi$ is to be single valued, the following equations can be derived from the second Ginzburg Landau equation:

$$\oint_L \frac{m}{e^2 n_s}\mathbf{J}_s + \mathbf{A}.\,\mathrm{d}l = \frac{\hbar}{2e}\oint_L \nabla\theta.\,\mathrm{d}l = \frac{nh}{2e}. \tag{1.5}$$

The left hand side of this equation is referred to as the fluxoid. Under most circumstances $L$ can be chosen so that it lies well away from the edges of the sample, where the persistent screening supercurrents flow within a distance of approximately $\lambda_L$ of the surface. The supercurrent term $\mathbf{J_s}$ is zero in such regions. By Stokes' theorem, the integral around the closed loop of $\mathbf{A}$ is equivalent to the surface integral of $\mathbf{B} = \nabla \times \mathbf{A}$ over a bounding surface of the loop — i.e. it is equivalent to the magnetic flux threaded through the loop. The flux through the loop is therefore quantised in units of $\Phi_0 = h/2e$.

Solutions to the Ginzburg-Landau equations have a characteristic length scale — the Ginzburg-Landau coherence length ($\xi_{GL}$) over which the order parameter varies. The ratio of the coherence length to the penetration depth $\kappa = \lambda_L/\xi_{GL}$ determines whether the superconductor is classified as type I ($\kappa < 1/\sqrt{2}$) or type II ($\kappa > 1/\sqrt{2}$). These two classes of superconductor are distinguished by the sign of the surface energy of the boundary between the superconducting and normal regions of the material. To understand this effect consider the variation of both the order parameter and the magnetic field at a boundary between a superconductor and a normal metal (an S-N

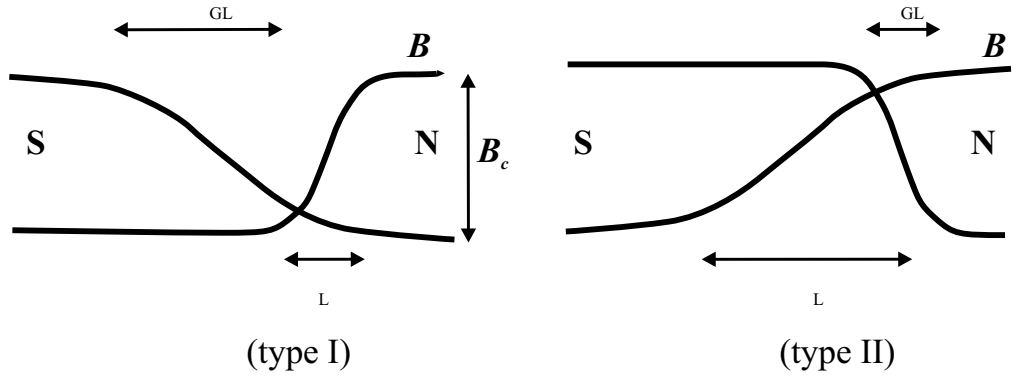


Figure 1.5: Schematic diagram showing the variation of the magnetic field $B$ and the magnitude of the order parameter $|\psi|$ at a boundary between a superconductor (S) and a normal metal (N) in a type I and a type II superconductor.

boundary), as shown in Fig. 1.5. In a type I superconductor it is clear that there is a region of thickness $\approx (\xi_{GL} - \lambda_L)$ from which the magnetic field is held out, contributing a positive diamagnetic energy while not enjoying the full condensation energy due to the depression of $|\psi|$. The surface energy of such materials is therefore positive. The argument is reversed for a type II superconductor, leading to a negative surface energy. As a result of the tendency to minimise the surface energy, a long rod of type I superconductor (aligned parallel to the applied magnetic field) exhibits a perfect Meissner effect up to the thermodynamic critical field $B_c$, at which point the energy of the field excluded from the superconductor is equal to the energy of the condensate. In contrast, a similar rod of type II superconductor only displays a perfect Meissner effect up to a smaller field $B_{c1}$, at which point it becomes favourable for the condensate to split into alternating superconducting and normal regions, to maximise the surface area. The so called 'mixed state' occurs in a field range between $B_{c1} < B < B_{c2}$. The magnetic energy associated with the mixed state is less than that associated with the Meissner state, so $B_{c2} > B_c$.

The mixed state of type II superconductors was first described by Abrikosov in 1957 [17]. In recognition of their work on superconductivity both he and Ginzburg were awarded Nobel prize in Physics in 2003. Abrikosov derived a solution to the Ginzburg-Landau equations that he interpreted as a periodic array of quantised vortex lines. The order parameter $\psi(\mathbf{r})$ goes to zero along the axis of the vortex where the magnetic field is maximal (see Fig. 1.6). Circulating supercurrent around the vortices gives rise to a single quantum of flux in each vortex. By splitting the field inside

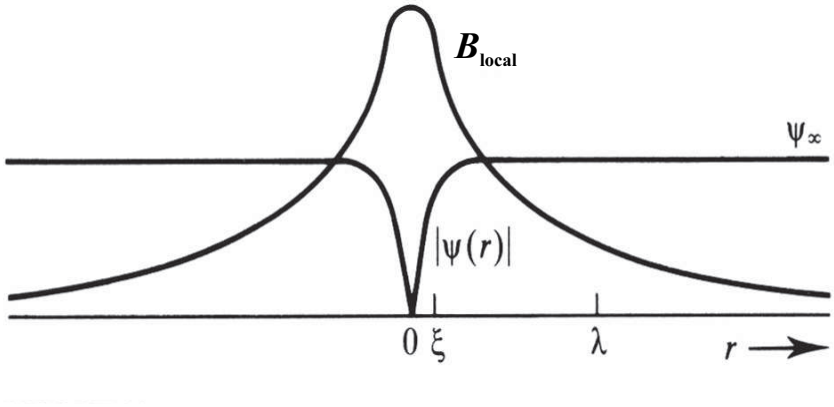


Figure 1.6: Diagram showing the structure of an isolated flux line in a material with $\kappa = 8$. The variation of the local magnetic field $B_{\text{local}}$ and the order parameter $\psi(r)$ is shown. Adapted from [18].

the superconductor into its smallest possible units the surface area of the N-S surfaces is maximised. The flux-line lattice determines many of the practical properties of superconductors. When current density, $\mathbf{J_c}$, flows through a superconductor the flux line lattice experiences a force per unit volume, $\mathbf{F_p} = \mathbf{J_c} \times \mathbf{B}$. This force tends to move the flux lines in a direction perpendicular to both the applied magnetic field and the current, producing an electric field $\mathbf{E} = \mathbf{B} \times \mathbf{v_f}$. In practice the flux lines are pinned by defects in the material, so the force on them is opposed by some pinning force, which gives the material a finite critical current above $B_{c1}$. It is the pinning of vortices that usually limits the critical current in practical materials. The irreversibility field, $B_{irr}$, is the magnetic field strength at which the onset of dissipation occurs ($B_{irr} < B_{c2}$) and is also determined by the collective pinning of the vortices.

The next major advance in the understanding of superconductivity was the development of a microscopic theory of superconductivity by Bardeen, Cooper and Schrieffer [19], for which they were awarded the 1972 Nobel prize. Within the 'BCS theory' electrons near the Fermi energy are coupled by a small attractive force due to electron-electron interactions via phonons. Cooper had already shown that at zero temperature electron pairs in states with opposite $\mathbf{k}$ vectors and spins are unstable to the formation of bound states when there is an attractive force between them, no matter how small the force is [20]. Within the BCS weak coupling theory electrons within an energy $\hbar\omega_D$ of the Fermi surface are coupled in this way as a result of the

electron phonon interaction and form a condensate of pairs that has many Bose-like properties ($\omega_D$ is the Debye frequency) . In order for there to be an electron phonon interaction it must be possible for the electrons to scatter, which at zero temperature requires some available states at the Fermi energy. The Fermi level is therefore smeared out, with the gain in the kinetic energy of the electrons being offset by their increased potential energy due to the attractive interaction. The smearing of the Fermi surface occurs on an energy scale of $\hbar\omega_D$, with only those electrons within this range of the Fermi energy involved in the pairing process. Because of the attraction between the pairs a finite energy, $2\Delta$, is required to break them and there is therefore a gap of $\Delta$ in the excitation spectrum of the superconductor. The excitations (also known as quasiparticles) must also occur in pairs.

In 1958 Gor'kov developed a non-local form of BCS theory [21]. The theory introduced a complex, gap field $\Delta(\mathbf{r})$, such that $|\Delta(\mathbf{r})|$ is equal to the local value of the gap $\Delta$. Gor'kov was able to show that the BCS theory reduces to the Ginzburg-Landau theory in the limit when $\Delta(\mathbf{r})$ does not vary too rapidly with position. The Ginzburg-Landau order parameter $\psi(r)$ is essentially proportional to the gap field $\Delta(\mathbf{r})$. The important phenomenological and microscopic theories were therefore reconciled.

In 1973, another Nobel prize was awarded for work on superconductivity, in this case to Giaever for his initial experiments on superconducting tunneling [22] and to Josephson for his pioneering contributions to the theory of tunneling between superconductors [23]. The next section is devoted to the theory of weak links between superconductors, of which the tunnel junctions are one type. Such Josephson junctions form the basis of many of the most important applications of superconductivity.

### 1.2.2 The Josephson Effect

The Josephson effect is a direct consequence of the macroscopic quantum nature of the superconducting state. A wide variety of different structures exhibit the Josephson effect, but in general these structures can be classified into three groups: junctions with insulating barriers (SIS junctions), junctions with normal metal barriers (SNS junctions) and regions of weakened superconductivity due a constriction in the superconductor (ScS junctions). In each case the wavefunctions of the superconducting electrodes are weakly coupled in the junction region. Josephson treated the specific case of SIS tunnel junctions, but the theory he derived is applicable in all three cases (in some cases with minor modifications). Both ScS and SIS junctions play important roles in determining the transport through grain boundaries in $YBa_2Cu_3O_{7-\delta}$ in different misorientation ranges.

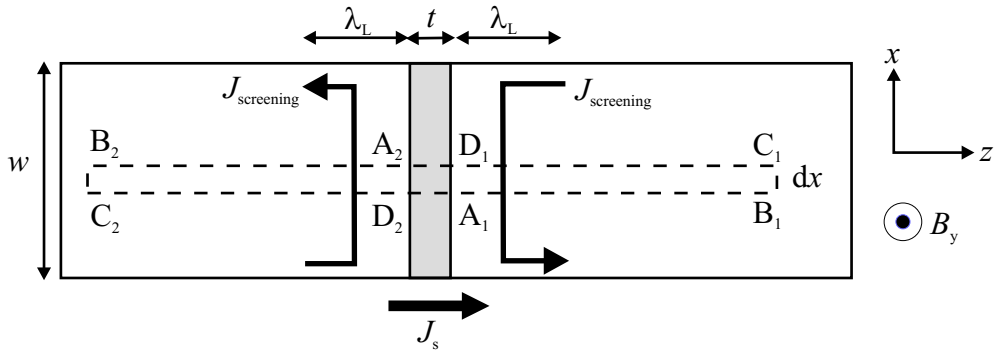


Figure 1.7: Contours of integration used to derive the magnetic field dependence of the gauge invariant phase difference at different points across the junction. The screening currents are also shown.

The DC Josephson equation relates the current density through the junction $J_s$ to the gauge invariant phase difference, $\phi$, across it:

$$J_s = J_0 \sin(\phi) \tag{1.6}$$

where $J_0$ is the critical current density of the junction, which is the maximum supercurrent density that the junction can sustain. In zero applied field $\phi$ is simply the phase difference itself ($\theta_2 - \theta_1$, measured in the direction opposite to the current flow), but because the phase difference is not gauge invariant in the presence of a magnetic field an additional term is required:

$$\phi = \theta_2 - \theta_1 - \frac{2\pi}{\Phi_0} \int_2^1 \mathbf{A} \cdot \mathrm{d}\mathbf{l} \tag{1.7}$$

where $\Phi_0$ is the flux quantum and $\mathbf{A}$ is the magnetic vector potential. Note that equation 1.6 is the simplest appropriate form of the current phase relation and deviations from such a form can occur (for example in certain conditions ScS junctions have a non-sinusoidal current phase relation [24]).

The dependence of the phase on the vector potential means that the supercurrent through the junction is dependent on the magnetic field. The gauge invariant phase difference at a point $x$ along the junction, as shown in Fig. 1.7, can be related to the local magnetic field density in the following manner. From equation 1.7 the difference between the gauge invariant phase at $x$ and at a point $x$+d$x$ is given by:

$$\phi(x+\mathrm{d}x)-\phi(x) = (\theta_{A_2}-\theta_{D_1})-(\theta_{D_2}-\theta_{A_1})-\frac{2\pi}{\Phi_0}\left(\int_{A_2}^{D_1}\mathbf{A}\cdot\,\mathrm{d}\mathbf{l}-\int_{D_2}^{A_1}\mathbf{A}\cdot\,\mathrm{d}\mathbf{l}\right) \tag{1.8}$$

where the points $A_1$, $B_1$ etc. are defined in Fig. 1.7. Using the second Ginzburg Landau equation (equation 1.4), the phase at $D_1$ can be related to that at $A_1$ by integrating $\nabla\theta$ along a horseshoe shaped path that runs out of the region in which screening currents flow (the path $A_1B_1C_1D_1$). The path of the loop is chosen to run perpendicular to the direction of the screening currents which flow in the electrodes within a distance of the order of the London penetration depth of the weakly linked region. It is closed well within the superconductor where no currents flow. The phase difference is therefore dependent only on the magnetic vector potential and the current term does not contribute to the integral. We therefore have:

$$\theta_{D_1}-\theta_{A_1} = \frac{2\pi}{\Phi_0}\int_{A_1B_1C_1D_1}\mathbf{A}\cdot\,\mathrm{d}\mathbf{l} \tag{1.9}$$

The same argument can be used to relate the phase difference between points $A_2$ and $D_1$ to an integral around the contour $A_2B_2C_2D_2$. Thus all the phase terms in equation 1.8 can be replaced by contour integrals and the result is that the phase difference $\phi(x+\mathrm{d}x)-\phi(x)$ is related to the integral of $\mathbf{A}$ around the closed contour $A_1B_1C_1D_1A_2B_2C_2D_2A_1$. The integral of the magnetic vector potential $\mathbf{A}$ around a closed loop is simply the flux, $\Phi$, enclosed by the loop, which in this case is $B(2\lambda_L+t)dx$ (where $B$ is the magnetic field density). $\phi$ is therefore related to $B$ via the equation:

$$\frac{\mathrm{d}\phi}{\mathrm{d}x} = \frac{2\pi B(2\lambda_L+t)}{\Phi_0} \tag{1.10}$$

If we assume the magnetic field is independent of $x$ we can derive the field dependence of the critical current, $I_c$, of the junction, by integrating this expression, substituting into equation 1.6 and integrating again. For a junction with a uniform critical current density $J_0$ the result obtained is:

$$I_c = I_0\left|\frac{\sin(\frac{\pi\Phi}{\Phi_0})}{\frac{\pi\Phi}{\Phi_0}}\right| \tag{1.11}$$

where $I_0 = J_0A$ ($A$ is the junction area). This is the classic 'Fraunhofer' pattern that is so called as a result of the analogy with Fraunhofer diffraction from a single slit, which produces the same interference pattern. It is illustrated in Fig. 1.8.

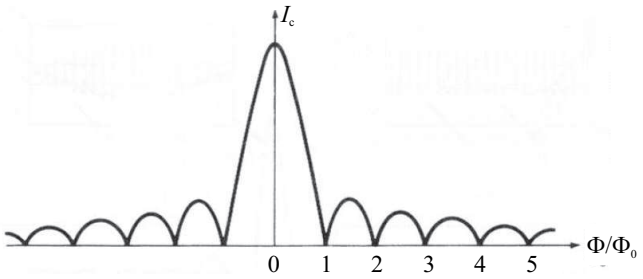


Figure 1.8: The ideal critical current versus applied flux curve (Fraunhofer pattern) for a short, uniform Josephson junction. Adapted from [18].

In the general case the magnetic field is not independent of the position in the junction, as a result of screening currents which flow within the junction. For the simple case depicted in Fig. 1.7 the Maxwell equation $\mathrm{d}B_y/\mathrm{d}x = \mu_0 J_z$ can be substituted into the differential of equation 1.10 to yield:

$$\frac{\mathrm{d}^2\phi}{\mathrm{d}x^2} = \frac{2\pi\mu_0(2\lambda_L + t)J_z}{\Phi_0} = \frac{2\pi\mu_0(2\lambda_L + t)J_0 \sin\phi}{\Phi_0} = \frac{\sin\phi}{\lambda_J^2} \tag{1.12}$$

where we have defined the Josephson penetration depth $\lambda_J = [\Phi_0/(2\pi\mu_0 J_0]^{1/2}$. When the junction's largest lateral dimension is less than $\lambda_J$ the right hand side of this equation is effectively zero and the field can be treated as uniform. Long junction effects occur when the Junction has one or more dimensions significantly greater than $\lambda_J$. The form of the Fraunhofer pattern is altered and typically sharper features are observed. Depending on the geometry of the junction the curve may also become asymmetric.

The DC Josephson relation determines the properties of junctions biased below the critical current. When a junction is biased in a finite voltage state the AC Josephson relation also applies. The AC Josephson relation relates the rate of change of phase across the junction to the voltage, $V$, dropped across it:

$$\hbar\frac{\partial\phi}{\partial t} = 2eV. \tag{1.13}$$

For a constant voltage bias the AC Josephson relation predicts that the phase increases linearly with time: $\phi = 2eVt/\hbar + \phi_0$. Substitution of this phase into the DC Josephson relation (equation 1.6) leads to a supercurrent that oscillates at a frequency $V/\Phi_0$ — the Josephson frequency ($\omega_J/2\pi$). If a combination of a DC and AC voltage is applied (for example by means of a

microwave source) then the phase itself oscillates at the angular frequency of the source $\omega_{rf}$. When the angular frequency of the Josephson oscillations is an integer multiple of $\omega_{rf}$ ($\omega_J = n\omega_{rf}$) the time averaged Josephson current is non-zero and a Shapiro spike is observed [25]. Equivalently the spikes occur at voltages given by $V_n = n\hbar\omega_{rf}/2e$. The appearance of these spikes in the current-voltage characteristic is known as the inverse AC Josephson effect. The effect is now utilised in the international standard of the volt [26].

In practice a voltage bias is hard to achieve because of the low impedance of the junction. Under most circumstances the junction is therefore biased by a constant DC current. Under a DC bias, typical high $T_c$ junctions are well described by the resistively and capacitively shunted junction (RCSJ) model. Within this model the Josephson current, quasiparticle current and the displacement current are treated as parallel contributions to the total current through the device. The quasiparticle current is modelled as an ohmic resistance, an approximation which is reasonable for high $T_c$ junctions when the current bias is such that the voltage across the junction is of order 10 mV or less. Adding the current components in parallel gives the following expression for the total current through the device:

$$I = I_0 \sin\phi + \frac{V}{R_n} + C\frac{\mathrm{d}V}{\mathrm{d}t}. \tag{1.14}$$

where $R_n$ is the normal state resistance of the junction and $C$ is its capacitance. Using equation 1.13 to express each component in terms of the phase gives:

$$I = I_0 \sin\phi + \frac{\hbar}{2eR_n}\frac{\mathrm{d}\phi}{\mathrm{d}t} + \frac{\hbar C}{2e}\frac{\mathrm{d}^2\phi}{\mathrm{d}t^2}. \tag{1.15}$$

We can re-arrange this equation into the form:

$$-\frac{\mathrm{d}}{\mathrm{d}\phi}\left(-I\phi - I_0\cos\phi\right) - \frac{\hbar}{2eR_n}\frac{\mathrm{d}\phi}{\mathrm{d}t} = \frac{\hbar C}{2e}\frac{\mathrm{d}^2\phi}{\mathrm{d}t^2}. \tag{1.16}$$

This equation is similar to the equation of motion of a particle sliding down a tilted washboard potential in a viscous fluid. If we interpret $\phi$ as the distance of the particle along the x-axis, the first term on the left hand side is minus the gradient of the potential (i.e. the force), which takes the form of a uniform slope modulated by a cosine (i.e. a tilted washboard). The second term is a viscous damping force, proportional to the velocity, which acts in the direction opposite to the particle's motion. The term on the right hand side is the acceleration of the particle, with the quantity $\hbar C/2e$ being proportional to the inertia of the particle. The slope of the washboard

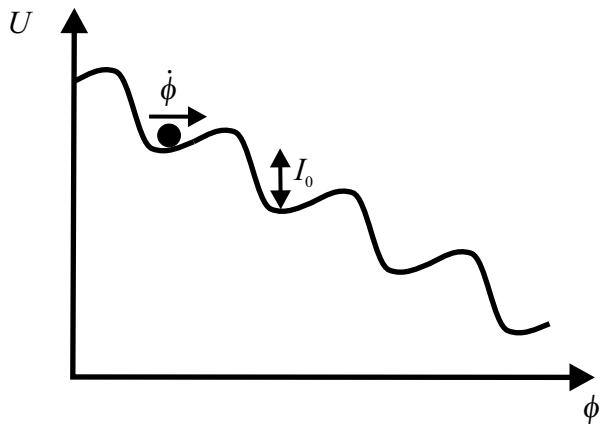


Figure 1.9: The tilted washboard analogue for the RCSJ model. The phase difference across the junction is analogous to the position of the particle along the $x$-direction. The particle is moving in a viscous fluid (the viscosity being dependent on the normal state resistance) and its inertia is determined by the value of the capacitance. The slope of the washboard is determined by the applied current whilst the size of the crenulations is related to the critical current.

is determined by the applied current, whilst the size of the crenulations is determined by the critical current. This scenario is illustrated in Fig. 1.9.

In the limit of zero capacitance a balance is maintained between the force down the slope and the viscous damping term. For small tilts ($I < I_c$) the particle comes to rest in the washboard hollows. For larger tilts ($I > I_c$) the particle slides continuously but unsteadily down the washboard producing a finite but varying voltage. With a finite capacitance the particle remains at rest as the current is increased from zero to $I_c$ and begins to move when the current reaches $I_c$. However, as the current is decreased below the critical current in the voltage state the particle is not immediately brought to rest as its finite inertia carries over the part of the washboard where it receives a force in the opposite direction to its motion. A finite voltage is therefore obtained at currents below the critical current on the return portion of the current voltage characteristic and the current voltage characteristic becomes hysteretic. When the junction is in the voltage state (independent of the capacitance), the voltage oscillates at the Josephson frequency $V/\Phi_0$. For currents just above the critical current the voltage time characteristic consists of a series of narrow pulses, whilst at higher applied currents it reduces to a sinusoidal form. In each case the integral over a single voltage pulse with respect to time is a single flux quantum.

For non-zero capacitance equation 1.15 must be solved numerically. Mc-

Cumber has published the results obtained from a numerical analysis [27]. In the case of zero capacitance an analytical solution exists. The time averaged voltage in this instance is given by: $V = I_0 R_n \sqrt{(I/I_0 - 1)^2}$.

The RCSJ model and its mechanical analogue are useful tools for analysing the current voltage characteristics of Josephson junctions. It is important for the capacitance measurements described in Chapter 4 of this thesis. In the next section the importance of grain boundaries for high temperature superconductor technology is highlighted. Josephson effects form the basis of a number of the applications of the technology.

## 1.3 Grain Boundaries and Applications of High $T_c$ Superconductors

Applications of high $T_c$ materials can be divided into two categories, electronic and large scale. Electronic applications typically rely on the unique high frequency properties of Josephson junction devices or on the low microwave surface resistance of superconductors. Large scale applications require long lengths of conductor and often involve operation in magnetic fields of several Tesla. Grain boundaries are important for both types of application: grain boundary Josephson junctions are employed in many electronic applications of high $T_c$ superconductors and grain boundaries limit the performance of the second generation of long length high $T_c$ conductors.

### 1.3.1 Grain Boundary Josephson Junctions for Electronic Applications

Much of the effort to produce a viable high $T_c$ junction technology has been focused on the superconductor $YBa_2Cu_3O_{7-\delta}$, primarily because it's physical properties and growth mechanisms are well understood and because high quality thin films can be grown in situ by several deposition techniques on various substrates. A number of the junction technologies developed are dependent on the weak link properties of grain boundaries. The bicrystal [4], step edge [28] and biepitaxial [29, 30] junction technologies are all based on the formation of artificial grain boundaries in thin films usually, though not exclusively of $YBa_2Cu_3O_{7-\delta}$. These different types of junction are illustrated in Fig. 1.10.

The most flexible type of junction is the bicrystal junction. These are fabricated by sintering two orientated singe crystals of $SrTiO_3$ together and then cutting the resulting bicrystal into thin substrates. This fabrication

process allows any grain boundary orientation to be produced, but is unsuitable for some applications since the location of the junctions is fixed by the bicrystal line. For most applications, [001] tilt boundaries are employed. The work in this thesis is focused on such [001] tilt bicrystal boundaries, since they offer a flexible means of studying individual boundaries in a controlled manner and have the most relevant geometry for applications.

Step edge junctions make use of the fact that $YBa_2Cu_3O_{7-\delta}$ grows in a different orientation on milled ramps in $LaAlO_3$ (and on various other substrates). Since the milled steps can be located anywhere on the boundary, the technique is suitable for scale up, however the junction to junction reproducibility is relatively poor. Figure 1.11 shows how the step in the substrate produces two 90°, asymmetric tilt boundaries. Step edge junctions have now been largely superseded by interface engineered, ramp type junctions [31, 32]. Instead of a step in the substrate a $YBa_2Cu_3O_{7-\delta}$-insulator bilayer is milled into a ramp which is subsequently treated to damage the $YBa_2Cu_3O_{7-\delta}$ near the surface (for example by a high energy ion mill or by plasma etching). Finally an additional $YBa_2Cu_3O_{7-\delta}$ layer is deposited over the ramp, or alternatively, a thin metallic or insulating layer is deposited followed by a $YBa_2Cu_3O_{7-\delta}$ counter-electrode. While these more complex structures are not simply grain boundaries, an improved understanding of grain boundaries will contribute to the understanding of the physics of these more complex interfaces.

The various biepitaxial techniques exploit differences in the epitaxial relationships of various buffer layers to rotate the crystallographic axes of the $YBa_2Cu_3O_{7-\delta}$ in selected regions of the film. The technique was originally proposed by the Conductus group [29], but has recently been used by the group in Naples to produce both tilt and twist grain boundaries on a single device [30]. The Naples geometry can exploit the d-wave order parameter symmetry of the cuprates to produce $\pi$ loops, in principle allowing the fabrication of novel, scalable devices with possible applications in quantum computing [33].

The most wide-spread application of these junction technologies is the fabrication of high $T_c$ SQUIDs (Superconducting Quantum Interference Devices). Since large numbers of junctions are not required for SQUIDs, the bicrystal technology, which is still the most reliable and straightforward means of fabricating high $T_c$ junctions, is the most widely employed. An extensive review of the applications of SQUIDs employing high $T_c$ junctions has been performed elsewhere [34]. SQUIDs function as extremely sensitive magnetic field sensors. Although high $T_c$ SQUIDs are typically slightly less sensitive then their low $T_c$ counterparts, there is often a significant advantage gained in the signal to noise ratio as the SQUID can be placed

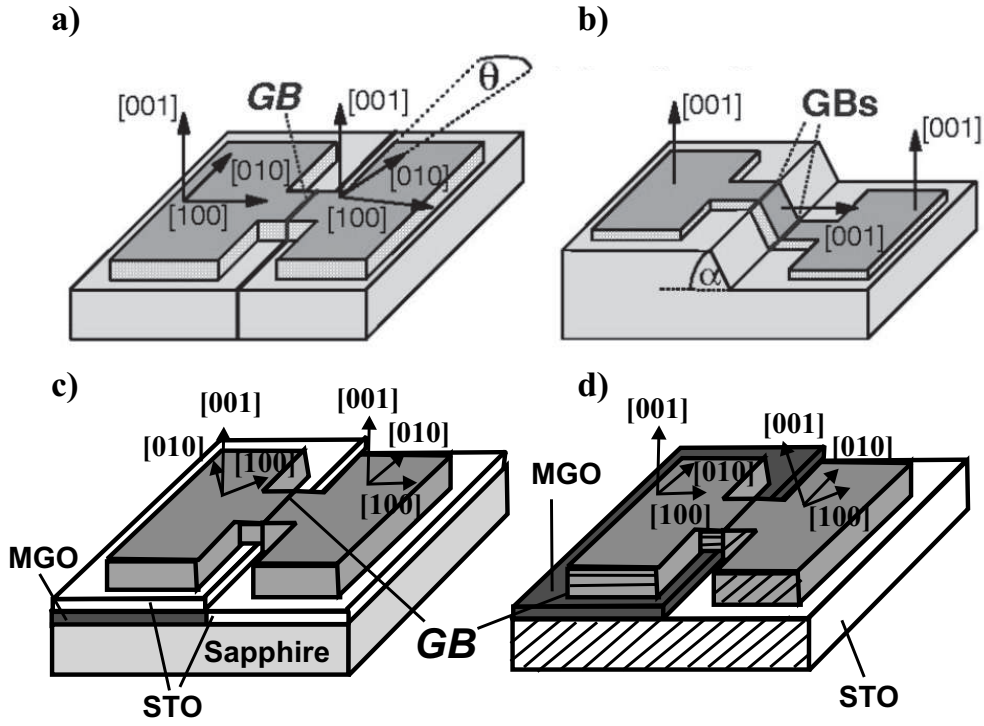


Figure 1.10: Schematics showing the geometries of the various types of Cuprate Josephson junction technologies that use grain boundaries. a) Bicrystal grain boundary. An artificial grain boundary is fabricated in the substrate and a thin film is grown epitaxially on it. b) Step edge junction. A step is milled in the substrate (typically $LaAlO_3$ or $SrTiO_3$) and a film is deposited over the step. Grain boundaries form since the film grows in a different orientation on the step. c) Biepitaxial junction as developed by Char [29]. A layer of MgO is used to rotate the orientation of a $SrTiO_3/YBa_2Cu_3O_{7-\delta}$ bilayer grown on a sapphire substrate. d) Biepitaxial junctions as developed by Di Chiara *et al.* [30]. In this case a (110) orientated $SrTiO_3$ substrate is employed and an MgO layer rotates the $YBa_2Cu_3O_{7-\delta}$ orientation. Both tilt and twist boundaries can be obtained by this technique by patterning the microbridge either as shown in the figure (for a tilt boundary) or perpendicular to the orientation shown (for a twist boundary). Panels a) and b) are adapted from reference [34].

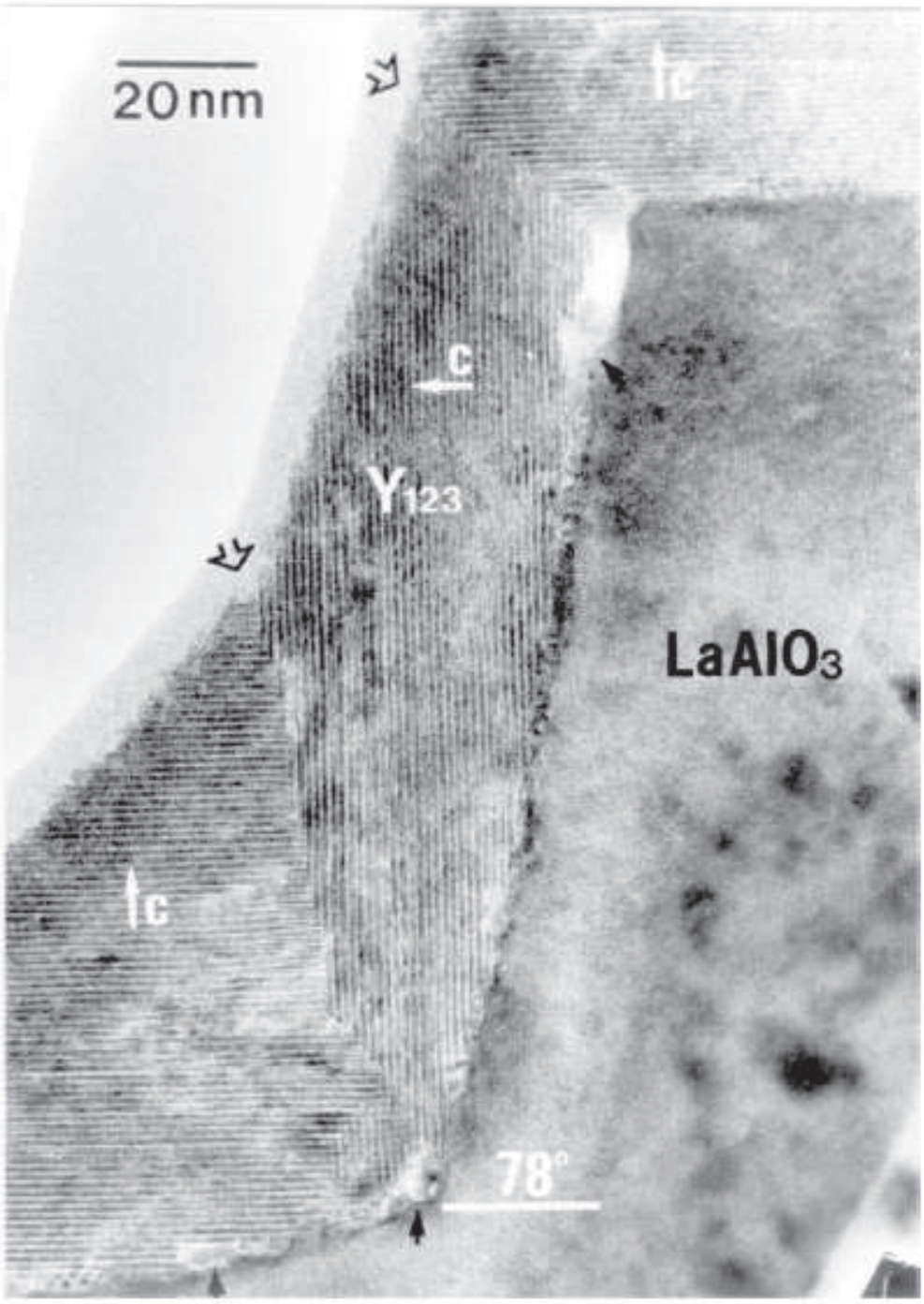


Figure 1.11: Transmission electron micrograph of a cross section through a step edge boundary. Two 90° grain boundaries that form at the edges of the step can be clearly seen and are marked by the open arrows. Part of the step-edge $YBa_2Cu_3O_{7-\delta}$ film was removed during the TEM specimen preparation.

closer to room temperature specimens due to relaxed cooling constraints. Of particular current interest are applications in magnetoencephalography (measurements of magnetic signals from the human heart), non-destructive evaluation, scanning SQUID microscopy and geophysics. Other potential applications involving high $T_c$ junctions include radiation detectors and mixers. Since the Josephson junction technologies in the Cuprates are still much less reproducible than those in low temperature superconductors, high $T_c$ digital circuits are a distant prospect. The need for improved understanding of materials issues is critical for the development of electronics applications.

### 1.3.2 Grain Boundaries in Coated Conductors

Large scale applications of high $T_c$ superconductors require long lengths of continuous superconducting material. Conductors must necessarily be polycrystalline and therefore contain grain boundaries. Since the current carrying capacity of even low angle boundaries is less than that of the bulk, grain boundaries play a critical role in conductor technologies.

The development of high $T_c$ conductors has focused on two materials: $(Bi,Pb)_2Sr_2Ca_2Cu_3O_{10+\delta}$ (Bi-2223) and $YBa_2Cu_3O_{7-\delta}$ (YBCO-123). Bi-2223 conductors (often termed first generation conductors) are currently in commercial production with the major market being current leads to low $T_c$ magnets. The rolling deformation used to produce the tape leads to a filamentary structure with a marked, uniaxial, c-axis texture, as shown in Fig. 1.12a. $(Bi,Pb)_2Sr_2Ca_2Cu_3O_{10+\delta}$ is strongly anisotropic and it is the anisotropy in the current transfer, rather than the grain boundary network, that limits the critical current in significant applied fields at the 77 K operating temperature [35] (the crossover from grain boundary limited transport to bulk limited transport has been found to occur at fields of a few 10's of mT at 77 K by irradiation experiments [36]). It is this anisotropy that restricts the use of Bi-2223 conductors to low fields, since the irreversibility field, $B_{irr}$, at which the conductor has zero critical current, is also anisotropic. The use of the conductor is limited by the strongly suppressed ab-plane $B_{irr}$ at 77 K (approximately 0.2 T) and by its high cost [37]. For this reason a second generation of conductors is being developed based on the less anisotropic material $YBa_2Cu_3O_{7-\delta}$ (YBCO-123), which has an ab-plane $B_{irr}$ of approximately 7 T at 77 K. Up to fields of several Tesla at 77 K, the current carrying capacity of these $YBa_2Cu_3O_{7-\delta}$ conductors is limited by the reduced critical current of [001] tilt boundaries that occur between adjacent grains [38]. Much of the technology focuses on improving the grain to grain alignment of the material, either by epitaxial growth on textured, buffered metallic tapes or by producing a textured buffer layer on top of an untextured metallic tape

by special deposition techniques. The two most widely applied techniques, which typify each of these routes, are the rolling assisted biaxially textured substrate (RABiTS$^{TM}$) process and the ion beam assisted deposition (IBAD) process. These two processes, which currently produce the highest critical current conductors, are described in brief below.

Within the RABiTS$^{TM}$ process Ni or Ni alloy substrates are rolled and annealed to produce a textured metal substrate. Various buffer layers are deposited to maintain the texture of the substrate (in fact the texture can be slightly improved by these buffer layers) and to provide a diffusion barrier to the Ni. The $YBa_2Cu_3O_{7-\delta}$ is then deposited onto the final buffer layer and a silver cap-layer is added to provide environmental protection, a resistive shunt in case of quenches and good electrical contact to the conductor. A typical architecture would be: Ni (50-100 $\mu$m) - $Y_2O_3$ (10 nm) - Y-$ZrO_2$ (300 nm) - $CeO_2$ (10 nm) - $YBa_2Cu_3O_{7-\delta}$ (0.3-2 $\mu$m) - Ag (3 $\mu$m). Recent results from the RABiTS$^{TM}$ process are given in reference [41].

More flexibility on the substrate choice is available with the IBAD technique: typically Inconel or Hastelloy substrates are employed but some groups use other materials, such as stainless steel [42]. The substrate is coated with an IBAD layer which is usually a 0.5-1$\mu$m thick Y-$ZrO_2$ film textured by bombardment with an inclined beam of Ar-ions (a much thinner IBAD layer ($\sim$10 nm) of MgO may be used, but the texture produced is not as good as Y-$ZrO_2$). This layer must necessarily be deposited in vacuum, which is both costly and time consuming — this is the major drawback of the IBAD process. The $YBa_2Cu_3O_{7-\delta}$ can be deposited directly onto the IBAD layer, or for some processes, an additional thin buffer layer of Ce-$O_2$ is deposited. Finally the cap layer is added - which is typically Ag or Au. Recent IBAD results are given in reference [43].

The IBAD and RABiTS$^{TM}$ conductors represent the current state of the art in coated conductor technology. The detailed processing of these complex conductors is beyond the scope of this thesis and the reader is referred to the literature for more detailed reviews [37]. The current carrying capacity of all of the second generation of coated conductors is limited by the grain boundary networks in these conductors. This is illustrated in the magneto-optical image of a RABiTS$^{TM}$ conductor shown in Fig. 1.13. The bright, field penetrated regions of the conductor coincide with the resistive regions at currents above the critical current. It is clear that the grain boundary network limits the self field critical current through the conductor. The problem of current percolation through grain boundary networks is complex and of considerable technological importance [44]. The percolation is quite different in IBAD and RABiTS$^{TM}$ conductors due to significant differences in grain size (typically 0.5 microns for IBAD and 50 $\mu$m for RABiTS$^{TM}$). This work focuses on

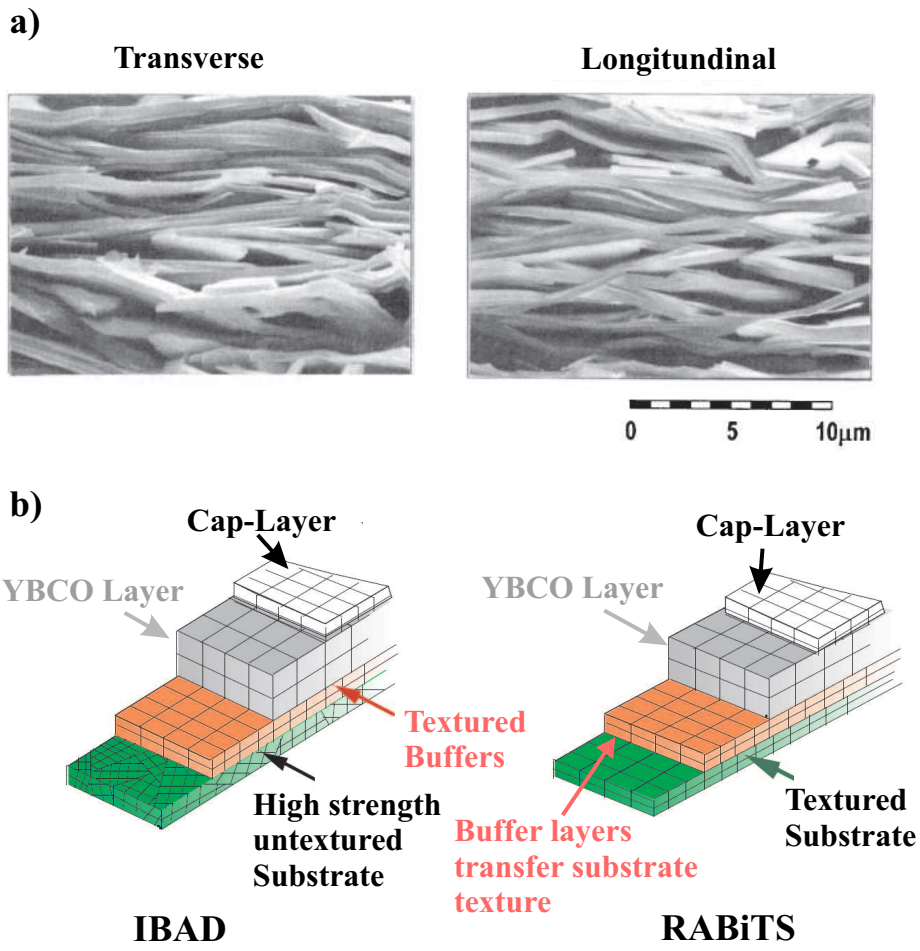


Figure 1.12: First and second generation high $T_c$ conductors. a) Scanning electron microscope images of the longitudinal and transverse fracture surfaces of a $(Bi,Pb)_2Sr_2Ca_2Cu_3O_{10+\delta}$ filament from a first generation conductor. Adapted from [39]. b) Second generation coated conductor architecture for the RABiTS$^{TM}$ and the IBAD processes. Adapted from [40].

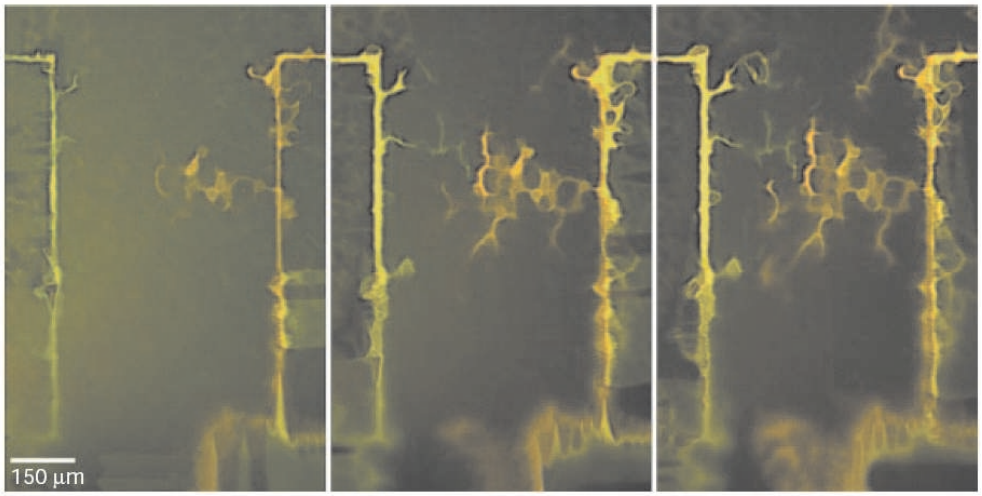


Figure 1.13: Magneto-optical images at 77 K of a RABiTS conductor in self-field with different applied currents. The bright regions show the penetration of magnetic field into the conductor, which clearly occurs along the grain boundary network. Even at currents well below the critical current magnetic flux penetrates into the superconductor. Adapted from [37].

studying the fundamentals of transport through individual grain boundaries, which are the basic building block of these complex networks. The grain to grain alignment is sufficiently good in coated conductors that high angle [001] tilt boundaries, of the type studied in this work, are extremely rare (or non-existent) in coated conductors. Despite this the electronic structure of high angle boundaries is almost certainly similar to that found in the dislocation cores of low angle [001] tilt boundaries, which are structurally similar to the high angle boundaries studied here. Already improvements in the critical currents of high angle boundaries by calcium doping [45] have been transferred to low angle boundaries [46] and to coated conductors [47]. An improved understanding of grain boundaries in these complex materials may open the way to further engineering of grain boundary properties.

# Bibliography


[1] J. G. Bednorz and K. A. Müller, Zeitschrift für Physik B **54**, 189 (1986).

[2] H. Hilgenkamp and J. Mannhart, Reviews of Modern Physics **74**, 485 (2002).

[3] P. Chaudhari et al., Physical Review Letters **60**, 1653 (1988).

[4] D. Dimos, P. Chaudhari, J. Mannhart, and F. K. Legoues, Physical Review Letters **61**, 219 (1988).

[5] D. Dimos, P. Chaudhari, and J. Mannhart, Physical Review B **41**, 4038 (1990).

[6] B. Häuser, B. G. Klopman, G. J. Gerritsma, J. Gao, and H. Rogalla, Applied Physics Letters **54**, 1368 (1989).

[7] Y. Y. Divin, J. Mygind, and N. F. Peterson, Applied Physics Letters **61**, 3053 (1992).

[8] Q. Jin and S.-W. Chan, Journal of Materials Research **17**, 323 (2002).

[9] J. G. Wen, T. Takagi, and N. Koshizuka, Superconductor Science and Technology **13**, 820 (2000).

[10] S. E. Babcock and J. L. Vargas, Annual Review of Materials Science **25**, 193 (1995).

[11] N. D. Browning, J. P. Burban, C. Prouteau, G. Duscher, and S. J. Pennycook, Micron **30**, 425 (1999).

[12] H. K. Onnes, Communications of the physics laboratory of the University of Leiden **124c** (1911), and subsequent work at the Leiden laboratory.

[13] W. Meissner and R. Ochsenfeld, Naturwissenschaften **21**, 787 (1933).

[14] C. J. Gorter and H. B. G. Casimir, Zeitschrift für Physik **35**, 963 (1934).

[15] F. London and H. London, Physica **2**, 341 (1935).

[16] A. B. Pippard, Proceedings of the Royal Society of London A **216**, 547 (1953).

[17] A. A. Abrikosov, Soviet Physics JETP **5**, 1174 (1957).

[18] M. Tinkham, *Introduction to Superconductivity*, McGraw-Hill, New York, second edition, 1996.

[19] J. Bardeen and L. N. C. adn J. R. Schrieffer, Physical Review **108**, 1175 (1957).

[20] L. N. Cooper, Physical Review **104**, 1189 (1956).

[21] L. P. Gor'kov, Soviet Physics JETP **7**, 505 (1958).

[22] I. Giaever, Physical Review Letters **5**, 147 (1960).

[23] B. D. Josephson, Physics Letters **1**, 251 (1962).

[24] K. K. Likharev, Reviews of Modern Physics **51**, 101 (1979).

[25] S. Shapiro, Physical Review Letters **21**, 80 (1963).

[26] M. T. Leinsen, R. Y. Chiao, M. J. Feldman, and B. A. Tucker, Applied Physics Letters **31**, 776 (1977).

[27] D. E. McCumber, Journal of Applied Physics **39**, 3113 (1968).

[28] K. P. Daly, W. D. Dozier, J. F. Burch, S. B. Coons, and R. Hu, Applied Physics Letters **58**, 543 (1991).

[29] K. Char, M. S. Colclough, N. Newman, and G. Zaharchuk, Physical Review Letters **59**, 733 (1991).

[30] A. D. Chiara et al., IEEE Transactions on Applied Superconductivity **7**, 3327 (1997).

[31] J.-K. Heinsohn et al., Journal of Applied Physics **89**, 3852 (2001).

[32] B. H. Moeckly and K. Char, Applied Physics Letters **71**, 2526 (1997).

[33] F. Tafuri et al., Physical Review B **62**, 14431 (2000).

[34] D. Koelle, R. Kleiner, F. Ludwig, E. Dantsker, and J. Clarke, Reviews of Modern Physics **71**, 631 (1999).

[35] B. Zeimetz, R. P. Baranowski, and J. E. Evetts, Journal of Applied Physics **88**, 5283 (2000).

[36] S. Tönies et al., Applied Physics Letters **78**, 3851 (2001).

[37] D. Larbalestier, A. Guerevich, D. M. Feldmann, and A. Polyanskii, Nature **414**, 368 (2001).

[38] D. T. Verebelyi et al., Applied Physics Letters **76**, 1755 (2000).

[39] B. Hensel, G. Grasso, and R. Flükiger, Physical Review B **51**, 15456 (1995).

[40] U. B. Balachandran, Status of the coated conductor resaerch in Japan, http://www.eere.energy.gov/superconductivity/pdfs/1-balu-anl.pdf.

[41] M. W. Rupich et al., IEEE Transactions on Applied Superconductivity **13**, 2458 (2003).

[42] A. Usoskin et al., IEEE Transactions on Applied Superconductivity **13**, 2452 (2003).

[43] Y. Iijima, K. Kakimoto, and T. Saitoh, **13**, 2466 (2003).

[44] B. Zeimetz, B. A. Glowacki, and J. E. Evetts, The European Physical Journal B **29**, 359 (2002).

[45] A. Schmehl et al., Europhysics Letters **47**, 110 (1999).

[46] G. A. Daniels, A. Guerevich, and D. C. Larbalestier, Applied Physics Letters **77**, 3251 (2000).

[47] A. Weber et al., Applied Physics Letters **82**, 772 (2003).

# Chapter 2

# $YBa_2Cu_3O_{7-\delta}$ and Grain Boundaries in $YBa_2Cu_3O_{7-\delta}$

In this chapter the properties of $YBa_2Cu_3O_{7-\delta}$ that are relevant to high angle grain boundary transport are reviewed. The properties of grain boundaries in this material are then discussed, with particular emphasis on the observations important for understanding the nature of these defects. In view of the huge amount of literature in the field this review is not intended to be exhaustive, and the reader is referred to the extensive review recently published in the literature [1]. Instead the important work in the field is highlighted, with an emphasis on experiments that probe the nature of the boundaries themselves.

## 2.1 Properties of $YBa_2Cu_3O_{7-\delta}$

The superconductor $YBa_2Cu_3O_{7-\delta}$ was identified [2, 3] shortly after the discovery of the discovery of high $T_c$ superconductivity by Bednorz and Müller [4]. Its discovery was met with significant excitement since it was the first superconductor to have a critical temperature above liquid nitrogen temperatures. The importance of $YBa_2Cu_3O_{7-\delta}$ for both bulk and electronic applications of high $T_c$ superconductivity was discussed in the previous chapter. In this section we review the basic properties of this superconductor that are relevant for the remainder of this thesis.

### 2.1.1 Physical Structure

The detailed structure of $YBa_2Cu_3O_{7-\delta}$ with a range of $\delta$ has been characterised in considerable detail by neutron powder diffraction [5]. The key structural results obtained are summarised in Fig. 2.1. The superconducting

phase is orthorhombic, with the tetragonal symmetry being broken by the formation of the C-$O_x$ chains shown at the base and top of the unit cell in Fig. 2.1a. The structure is related to the cubic perovskite structure with the copper oxide planes and chains being separated by blocking layers that contain the barium or yttrium cations. Doping experiments in which the blocking layer cations are replaced by other elements with different valencies helped to elucidate the role of the oxygen content in determining the physical properties of the cuprates [6]. In $YBa_2Cu_3O_{7-\delta}$ oxygen doping creates vacancies in the Cu-$O_x$ chains and this changes the effective Cu valency of the $CuO_2$ planes, altering the carrier density and hence the electrical properties. The chains can be thought of as providing a charge reservoir for hole doping the $CuO_2$ planes. It is certainly the case that in other cuprates without Cu-$O_x$ chains, the oxygen content in the blocking layers, which are essentially ionic with no free carriers, acts as a simple charge reservoir. The situation in $YBa_2Cu_3O_{7-\delta}$ is more complex than this simple picture, since the chains themselves contain free carriers and contribute to the normal conductivity, and to the supercurrent [7].

In practice untreated single crystals and thin films of the superconducting, tetragonal phase of $YBa_2Cu_3O_{7-\delta}$ are microtwinned with a domain size in the range of 30-100 nm. The twin boundaries form in the {110} type planes. Twining in thin film samples is well illustrated by a recent experiment in which suspended bridges are detwinned by thermal anneals [8] (for single crystals thermal anneals must be performed by applying a uniaxial stress to the crystal but in the film this is already present due the mis-match with the substrate). Figure 2.2 shows polarised light optical micrographs of twinned and untwinned microbridges. The characteristic 'tweed' pattern of twinning observed in panel a) will be present in all $YBa_2Cu_3O_{7-\delta}$ films grown on $SrTiO_3$. This means that in practice any transport measurements average the properties of the material in the a and b directions and anisotropy between these two directions cannot be observed.

### 2.1.2 The p-T Phase Diagram

A detailed survey of the physics of $YBa_2Cu_3O_{7-\delta}$ is beyond the scope of this thesis. Here some of the important features of the physics that are relevant to grain boundaries are reviewed from a purely phenomenological viewpoint. As discussed in the previous section the superconductivity and many of the other transport properties of $YBa_2Cu_3O_{7-\delta}$ and in cuprates in general are primarily associated with the $CuO_2$ planes. It is convenient to draw a phase diagram for the properties of the planes at various temperatures as a function of the number of holes $p$ per $CuO_2$ plane. The so called $p-T$ phase diagram

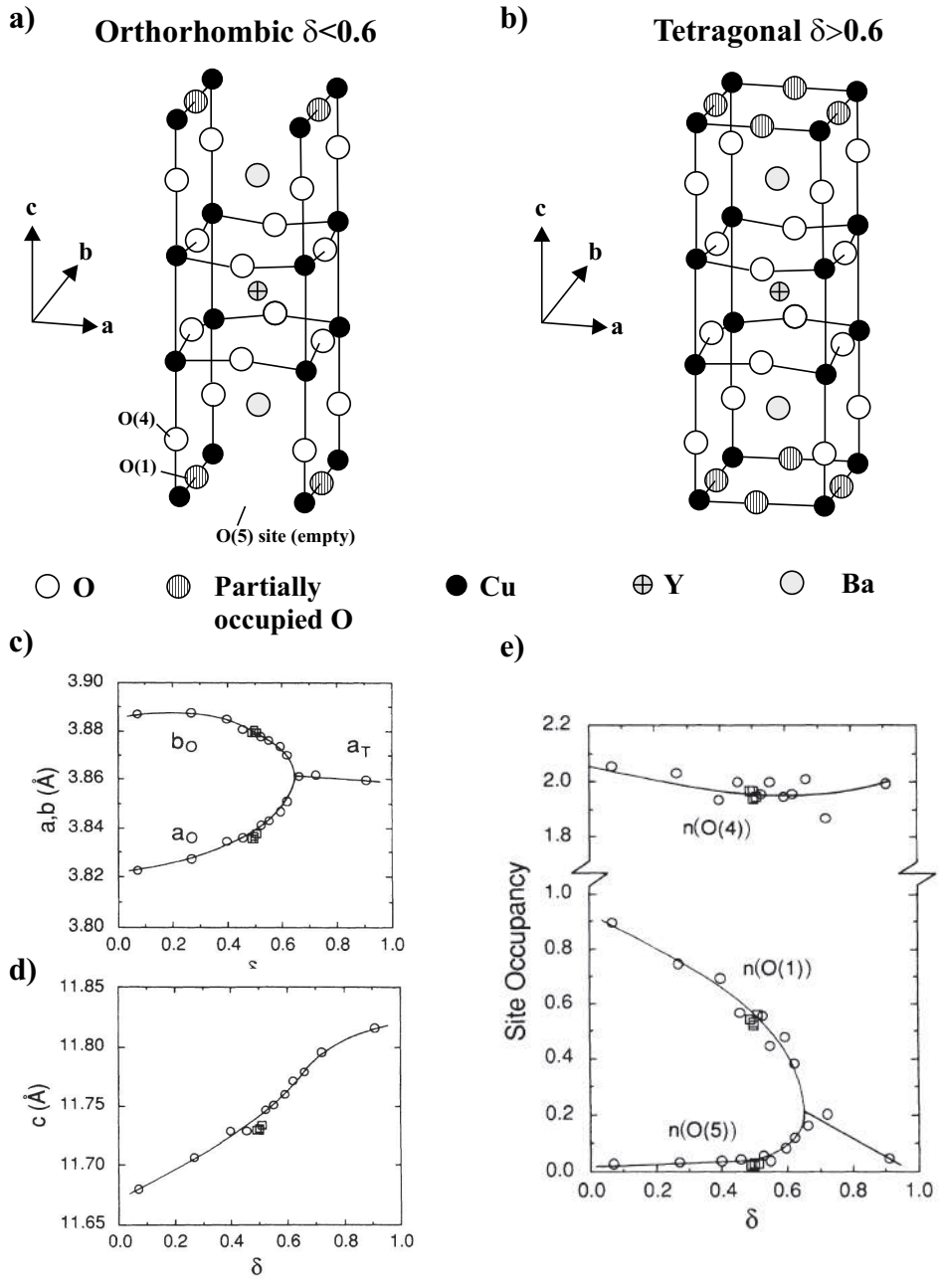


Figure 2.1: Summary of the structure of $YBa_2Cu_3O_{7-\delta}$ as a function of oxygenation $\delta$, as detrmined by neutron powder diffraction. a) Orthorhomic and b) tetragonal unit cells. c) and d) show the unit cell parameters as a function of oxygenation. The occupancy of various sites as a function of oxygenation is shown in e). Adapted from [5].

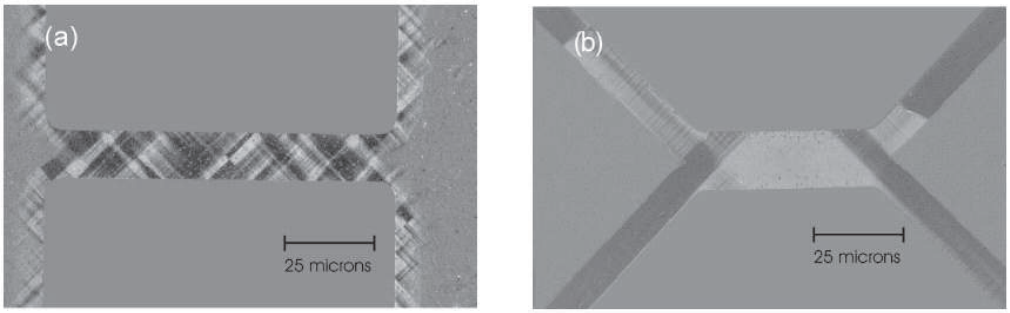


Figure 2.2: Polarised light optical micrographs of a) twinned and b) untwinned $YBa_2Cu_3O_{7-\delta}$ microbridges. From [8].

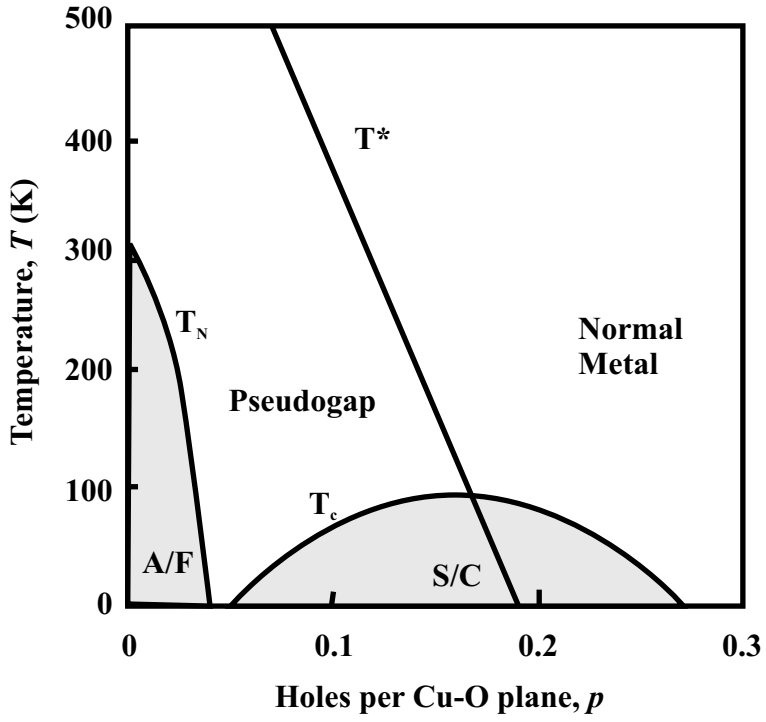


Figure 2.3: Phenomenological phase diagram of the high $T_c$ cuprates. The properties of cuprates are shown as a function of the charge per $CuO_2$ plane and the temperature. Three characteristic temperatures separate distinctive regions of the phase diagram, the Néel temperature, $T_N$, below which the material is an antiferromagnetic insulator (marked A/F), the critical temperature, $T_c$, below which superconductivity occurs (marked S/C) and the pseudogap characteristic temperature $T^*$. $T^*$ is an energy scale for the anisotropic gap that occurs in the density of states at the Fermi energy in the under-doped region of the phase diagram (i.e. for doping below that which maximises $T_c$). Adapted from [9].

is reasonably universal for hole doped cuprates and and data from a number of different materials and measurements is found to produce a consistent picture [9].

Figure 2.3 shows a schematic of the $p-T$ phase diagram as proposed by Tallon and Loram [9]. In the center of the phase diagram is a 'dome' shaped region of superconductivity with a maximum in $T_c$ just below $p = 0.2$. A more detailed discussion of the superconducting state is carried out in the next section. The $T_c$ maximum defines the location of 'optimal doping', below which the material is described as being 'under-doped' and above which it is referred to as 'over-doped'. Slightly under-doped samples have properties dominated by a pseudogap (that is a reduction in the density of states at the Fermi-energy), which is a present only in certain regions of the Fermi-surface. The pseudogap is found to be maximum along the $< 100 >$ directions and minimum along $< 110 >$ type directions [10] (as discussed in the next section this is the same symmetry as the order parameter in the superconducting state). The highly underdoped region is one of the few parts of the phase diagram that is theoretically understood. In this region the material is an antiferromagnetic insulator, which is somewhat surprising from the point of view of band theory as by simply counting charges the material is expected to be metallic with a half filled band. The antiferromagnetic state is caused by strong electron-electron interactions which lead to an additional Coulomb energy, $U$, for double occupancy of each electron state. The so called Hubbard $U$, causes the band to split in two and produces a Mott insulator. On the over-doped side of the phase diagram more conventional Fermi liquid behaviour is restored and a coherent, 3 dimensional Fermi surface is visible in both angle resolved photoemission spectroscopy measurements (ARPES) [11] and recently in polar angular magnetoresistance oscillations (AMRO) [12]. The Fermi surface here is found to agree well with band structure calculations that use conventional techniques. For the particular case of $YBa_2Cu_3O_{7-\delta}$, with $\delta = 0$ the material is only slightly overdoped, so to obtain large overdoping substitution of the yttrium cation must be performed (for example by calcium). In the optimally and overdoped regimes the Fermi surface is well described by band structure calculations [11].

One possible phenomenological understanding of the $p-T$ phase diagram is that the pseudogap is caused by increases in the electron-electron correlations. When the on site repulsion is much less than the bandwidth then instead of two Hubbard bands a smearing out of the Fermi-surface occurs to avoid double occupancy, leading to the pseudogap. As the number of holes per Cu-O plane is reduced the onsite repulsion increases in magnitude, as does the pseudogap. Such an interpretation must be treated tentatively but it nonetheless helps to understand how on the underdoped side the mate-

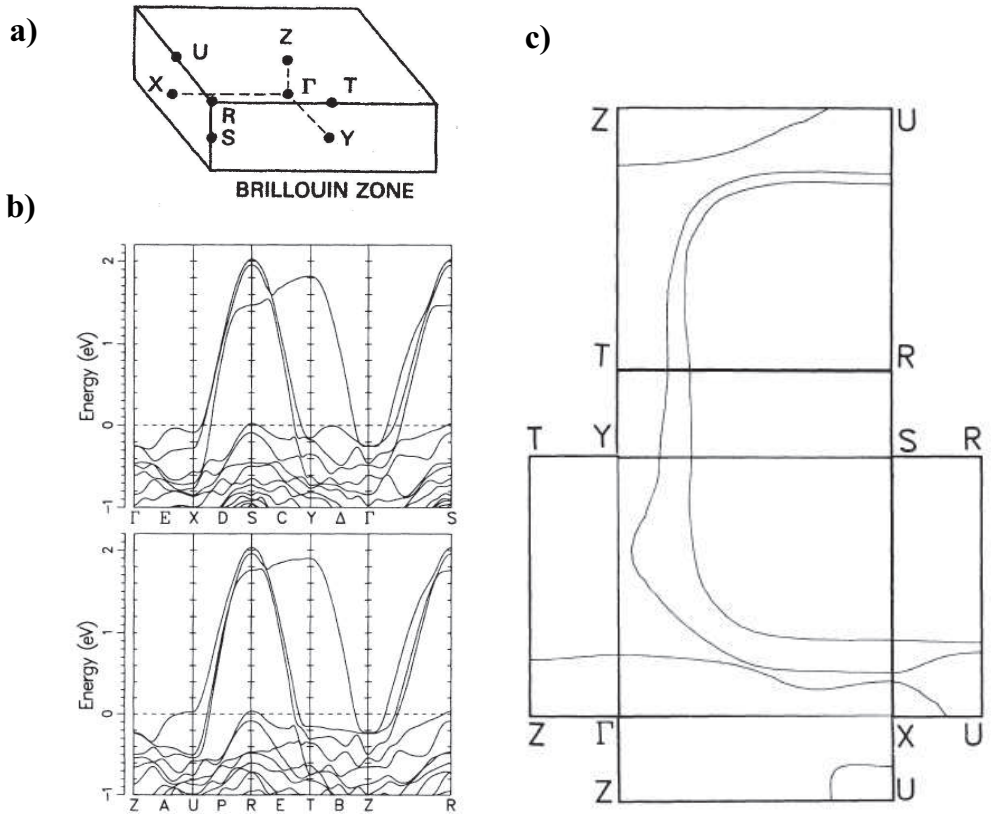


Figure 2.4: Calculated band structure and Fermi surface of $YBa_2Cu_3O_{7-\delta}$, from local density functional theory. a) The orthorhombic unit cell. b) Bands in the range -1 eV to +2 eV relative to the Fermi energy. c) Fermi surface cross sections in all of the symmetry planes. Adapted from [13].

rial can be treated as an insulator, whilst on the overdoped side it can be considered to be a metal with a less than half full band.

Band structure calculations for $YBa_2Cu_3O_7$ are shown in Fig. 2.4. The Fermi surface consists of two nested, tubular hole surfaces due to the two $CuO_2$ planes centered on the $(\pi/a,\ \pi/b)$ axis, and a planar surface that originates from the chains (towards the $(\pi/a,\ 0)$ point the chain surface folds over at the top of the Brillouin zone to form a saddle like structure). The Fermi surface geometry is very different from the spherical geometry appropriate for many metals and is essentially two dimensional.

### 2.1.3 Superconductivity in $YBa_2Cu_3O_{7-\delta}$

As yet the mechanism for superconductivity in the cuprates is not established. However a large amount of experimental work has been carried out and a great deal is known about the nature of superconductivity in these materials. Here we briefly mention some of the ways in which $YBa_2Cu_3O_{7-\delta}$ differs from low temperature superconductors with a particular focus on the properties relevant to grain boundaries. The basic theory and history of superconductivity was reviewed in the previous chapter.

$YBa_2Cu_3O_{7-\delta}$ is a strongly type II superconductor. Although the pairing mechanism is clearly different from that of low temperature superconductors many aspects of transport are familiar. The fluxoid quantum in $YBa_2Cu_3O_{7-\delta}$ is $h/2e$ [14] (where $h$ is Plank's constant and $e$ is the electronic charge) which suggests that the superfluid consists of pairs of holes or electrons as in conventional BCS superconductivity. Flux lines are present in the material, and though the localised nature of the superconductivity leads to some unusual behaviour, many of the transport properties can be understood within the context of the anisotropic Ginzburg Landau theory. The anisotropy in the penetration depth, $\lambda$, and the coherence length, $\xi$, is caused by the association of superconductivity with the C-O layers. The c-axis penetration depth is approximately 5-7 times larger than the ab plane penetration depth ($\lambda_{ab} \approx 135$ nm [15]), likewise the c-axis coherence length is the same factor larger than the ab plane value ($\xi_{ab} \approx 1.6$ nm [15]). Anisotropic Ginzburg Landau theory assumes a homogenous material and for some high $T_c$ superconductors the superconducting planes are sufficiently decoupled that the vortices also decouple between Cu-O planes, forming flux pancakes. While the anisotropy in $YBa_2Cu_3O_{7-\delta}$ is unlikely to be sufficient for such a flux line structure, flux pancakes are widely believed to underlie many of the transport properties of $Bi_2Sr_2CaCu_2O_8$, where $\lambda_c/\lambda_{ab} \approx 150$. The material anisotropy also leads to enhanced pinning for field parallel to the ab plane and produces an anisotropic irreversibility field. The collective properties of vortices in $YBa_2Cu_3O_{7-\delta}$ and other high temperature superconductors (often termed 'vortex matter') is a subject of considerable interest and complexity [16]. In addition it is the pinning and channelling of vortices by dislocation arrays that determines the transport properties of low angle grain boundaries in many temperature and field regimes (see [17] and references therein and [18]).

It is now clear that in $YBa_2Cu_3O_{7-\delta}$ and other related compounds the pair wavefunction has $d_{x^2-y^2}$ symmetry [19], which means that the superconducting gap is zero in some directions of the crystal. The gap nodes occur in the same directions as the nodes of the pseudogap in the normal state. The

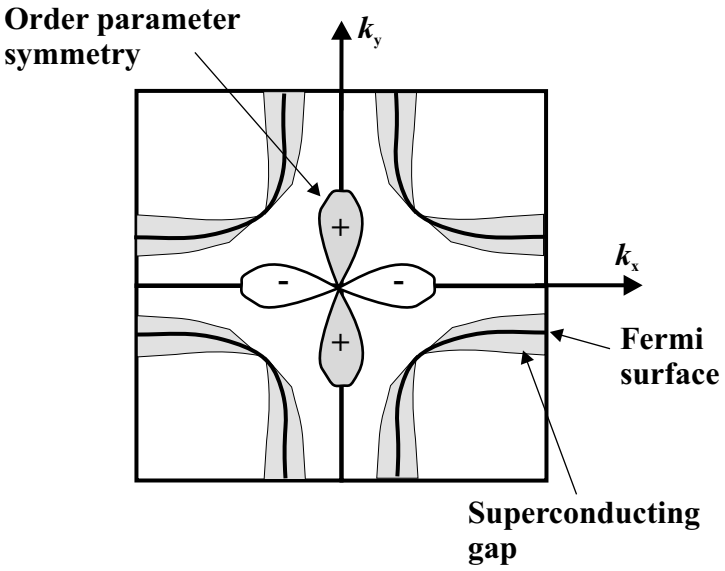


Figure 2.5: Order parameter symmetry of $YBa_2Cu_3O_{7-\delta}$. The figure shows a plane of the Brillouin zone with a schematic Fermi surface. The order parameter symmetry is shown in the center of the figure and the variation of the superconducting gap is drawn schematically around the Fermi surface.

main features of the order parameter symmetry are shown diagrammatically in Fig. 2.5. The order parameter symmetry has a number of important implications for the properties of grain boundaries as the complex, facetted structure of these defects can lead to frustration effects and the generation of '$\pi$ shift' Josephson junctions. This will be discussed in greater detail below.

In this section the properties of the superconductor $YBa_2Cu_3O_{7-\delta}$ have been briefly reviewed, with a strong emphasis on the relevant physics for grain boundaries. The important role of the $CuO_2$ planes was emphasised and the phenomenology of these planes was discussed in terms of the different properties obtained at different doping levels. The non-spherical Fermi surface geometry in the overdoped regime was emphasised — in this thesis the important implications of this geometry from the point of view of tunneling calculations are highlighted. The properties of the superconducting condensate were also discussed and the anisotropic nature of the material as well as the $d_{x^2-y^2}$ order parameter symmetry were highlighted as being relevant to grain boundary transport. In the next section the techniques used to prepare artificial grain boundaries, as well as their influence on the grain boundary microstructure are discussed in detail.

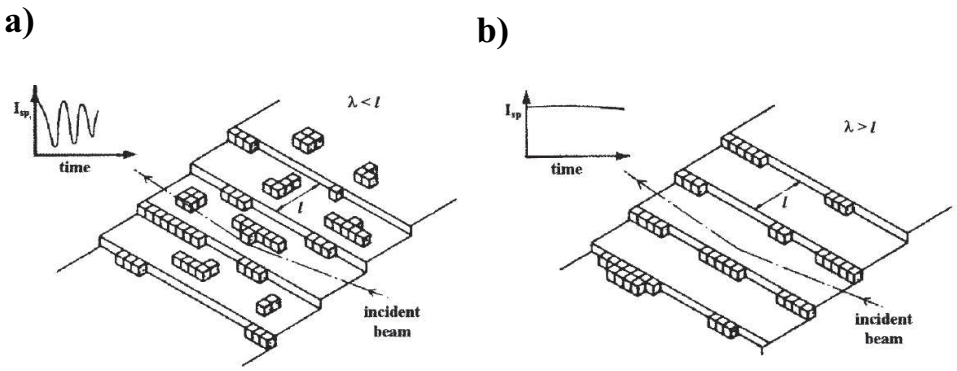


Figure 2.6: Schematic of the nucleation of high $T_c$ films under different growth conditions. a) Surface migration length $\lambda$ is much smaller than substrate terraces $l$, leading to growth by 2D islands or 3D spirals. b) $\lambda > l$ produces growth by migration to the substrate steps. The transition from island to step flow growth can be observed by the loss of the reflection high energy electron diffraction (RHEED) oscillations as shown in the figure. Adapted from [21].

## 2.2 Growth and structure of grain boundaries in $YBa_2Cu_3O_{7-\delta}$

The properties of grain boundaries are strongly affected by the detailed microstructure of these complex defects. The microstructure is in turn determined by the growth conditions. The growth conditions depend strongly on the technique used to produce the grain boundaries and also on the details of the deposition procedure. It is therefore clear that some of the structural features observed in grain boundaries may not be universal. Most of the work performed to date has been carried out on artificial grain boundaries, prepared by the epitaxial growth of thin films on bicrystalline substrates [20]. Usually $SrTiO_3$ bicrystals are employed, and pulsed laser deposition is used to grow the films, as in this study. The microstructure of films grown by other techniques on different substrates can vary significantly. This is an important issue and may effect the applicability of results from bicrystal grain boundaries to coated conductor systems. Here the results obtained on $SrTiO_3$ bicrystals with pulsed laser deposition are considered, although results obtained by other techniques are highlighted at the end of this section.

Critical in producing the microstructure of a thin film is the nucleation and growth mode of the film on the substrate. Three types of microstructure are typically observed in $YBa_2Cu_3O_{7-\delta}$ thin films, characteristic of different growth modes [22, 21]. These growth modes are step flow growth, 2D island

growth and 3D spiral growth (note that the growth in each of these modes should be considered to be a form of layer by layer, or Frank-Van der Merwe, growth [22]). Step flow growth occurs when the surface migration length, $\lambda$, of the incoming atoms is significantly greater than the length of the terraces formed by the step edges on the substrate, $l$. When $\lambda > l$ growth occurs due to the attachment of atoms to the edges of the terraces in the substrate. For $YBa_2Cu_3O_{7-\delta}$ the step flow growth mode is observed only on vicinal substrates (with a surface deliberately cut at an angle to the c-axis) and is therefore not observed in films used to produce [001] tilt grain boundaries. For $\lambda < l$ nucleation of growth islands occurs and growth occurs by the addition of atoms to those islands, either producing 2D growth islands or growth spirals. Spirals are favoured either for smaller values of $\lambda$ or for higher growth rates (and hence supersaturation of atoms on the surface) [22]. The value of $\lambda$ is determined by the diffusivity of atoms on the surface of the substrate, $D$, (determined by the substrate temperature and properties) and the residence time , $\tau$, that the atoms remain on the substrate for (determined by the deposition technique and for vacuum techniques the background pressure): $\lambda = D\tau$. Figure 2.7 shows $YBa_2Cu_3O_{7-\delta}$ films displaying each of these three growth modes. For pulsed laser deposition the typical growth mode is the 2D island mode, which leads to a granular structure for the thin films defined by the merging of the different growth islands. It is also possible to induce spiral growth in the films under certain deposition conditions [22].

The island growth mechanism of the films leads to a meandering microstructure [24] on the micron length scale for [001] tilt boundaries. A typical meandering grain boundary is shown in Fig. 2.8a, which shows a low magnification transmission electron microscopy image of the boundary, with the view direction along the c-axis. The meanders are caused by the overgrowth of individual growth islands onto the opposite side of the substrate. The 3 dimensional topography of the overgrowth has been a subject of some debate, with some authors claiming that the overgrowth occurs at the film-substrate interface, leading to non-epitaxial growth [25] and others that the grain boundary wanders away from the bicrystal line as the film grows thicker [26, 27]. In fact, as the cross sectional TEM images in Figs. 2.8b and c show, both types of behaviour can be observed, depending on the growth conditions of the films. The overall meander structure is strongly dependent on the growth conditions of the film and can be modified by altering the deposition conditions [24, 28]. It is clear that the detailed microstructure of these grain boundaries is extremely complex and highly dependent on the details of the film deposition.

On smaller length scales the grain boundaries are composed of nanoscale facets, which form in order to minimise the grain boundary energy. A TEM

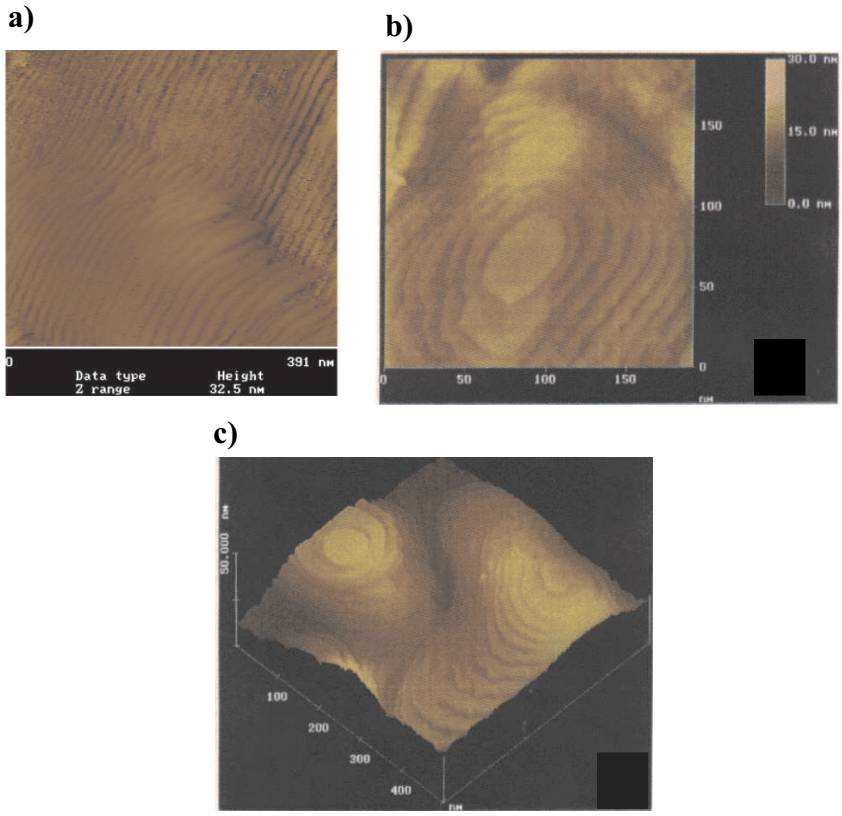


Figure 2.7: Atomic force microscopy images of different growth structures in $YBa_2Cu_3O_{7-\delta}$ thin films. a) Step flow growth structures for a pulsed laser deposition (PLD) film on a vicinal $SrTiO_3$ substrate. From [23] b) 2D island growth structure of a PLD film on a c-axis orientated $SrTiO_3$ substrate. From [21]. c) 3D growth spirals (right) and 2D islands (left) shown together on a sputtered film grown on a c-axis orientated $SrTiO_3$ substrate. From [21].

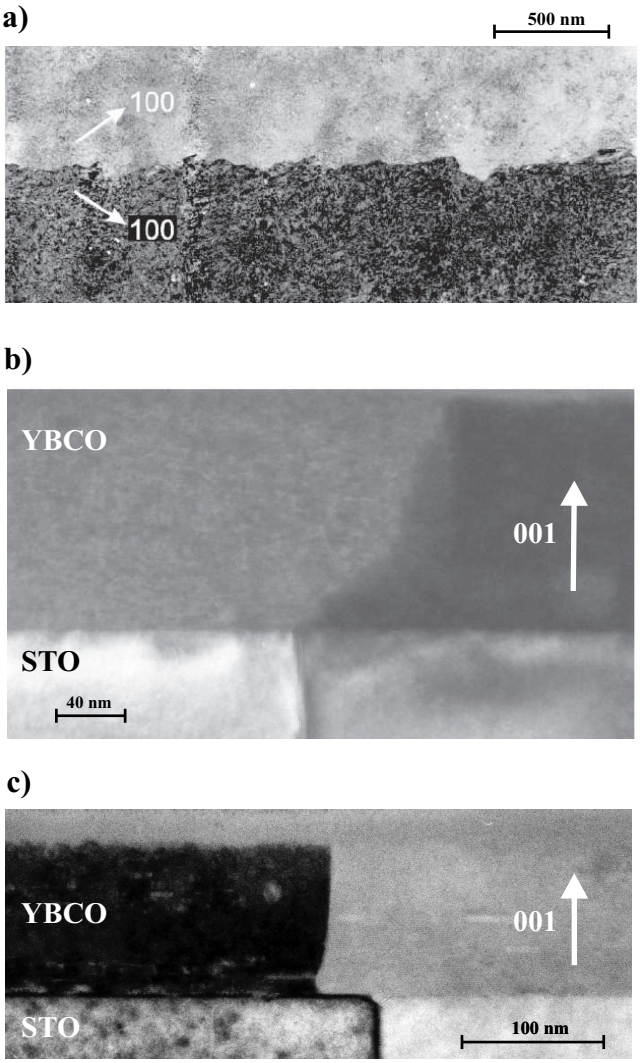


Figure 2.8: a) Low magnification TEM image showing the meandering grain boundary microstructure. The viewing direction is slightly tilted away from the [001] zone axis to improve the contrast between the two sides. From [27]. b) TEM image through a cross section of a 5° [001] tilt grain boundary, grown by off axis laser ablation. From [17]. c) TEM image through a cross section of a 24° [001] tilt grain boundary (from chapter 6 of this thesis).

image of a facetted grain boundary is shown in Fig. 2.9. Jin *et al.* have performed extensive studies on the nature of facetting in various grain boundaries in different geometries [29, 30], for sputter deposited films. They conclude that for [001] tilt boundaries there are three factors that control the formation of facets. Firstly the boundary plane is defined in miller indices $(hk0)$ in both crystals where $h, k \leq 5$. Secondly the sum of the inclination angles of [100] axes ($\alpha_1$ and $\alpha_1$) of the two crystals with respect to the grain boundary plane is equal to, or extremely close to the misorientation angle ($\theta$): $\alpha_1 + \alpha_2 - \theta \leq 2^\circ$. Note that finite values of $\alpha_1 + \alpha_2 - \theta$ are possible if a disinclination (that is a wedge shaped crystal defect that is added or removed to the local lattice) is present at both ends of the facet. The third factor determining the allowable facets is that the angle between the designed grain boundary plane and the facet plane should not be greater than 30°. These rules, which are essentially empirical, are based upon observations from a wide range of grain boundary geometries. It is the individual facets which form the basic building blocks of $YBa_2Cu_3O_{7-\delta}$ grain boundaries and the boundary behaviour can be considered in terms of large numbers of individual facets wired in parallel. The inhomogeneous nature of the grain boundaries, down to the smallest length scales, makes it hard to make definitive conclusions about the transport through them, since any measurement necessarily involves a complex averaging process.

The structure of $YBa_2Cu_3O_{7-\delta}$ grain boundaries has also been characterised on an atomic length scale, by means of z-contrast TEM imaging [31]. On these small length scales the distinction between low and high angle boundaries becomes evident, and the boundary is seen to consist of either an array of dislocations (a low angle boundary) or a continuously disordered layer (a high angle boundary), as discussed in the previous chapter. For convenience, Fig. 1.4, which illustrates the differences in atomic structure between high and low angle boundaries is reproduced here as Fig. 2.10. Both the low angle boundary dislocation cores and the high angle boundary disordered layer were found to consist of the same structural units. It is estimated that the cross over from low to high angle behaviour occurs at grain boundary misorientation angles of approximately 20° [32]. These images confirm that there are no second phases or segregated impurities present at the grain boundary.

The complex structure of $YBa_2Cu_3O_{7-\delta}$ grain boundaries represents a significant challenge to researchers trying to understand their fundamental properties. Recently, however, it has been shown that for thin films grown by liquid phase epitaxy (LPE), large single facet grain boundaries can be fabricated for certain misorientation angles [33]. The single facets are obtained since the growth spirals favoured for LPE growth form with much

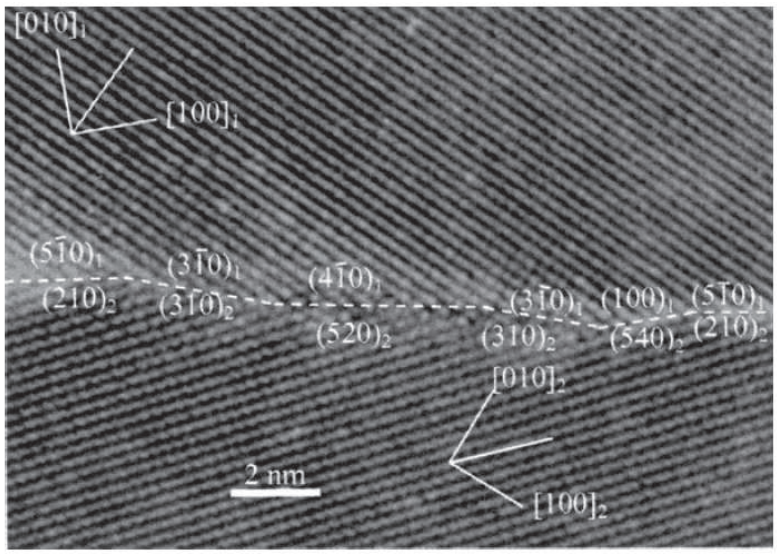


Figure 2.9: HRTEM image of an $\alpha_1$ =11°, $\alpha_2$ =26° [001] tilt boundary (total misorientation 37°) showing the facetted structure.The crystallographic planes of the individual facets are marked either side of the boundary. From [29].

larger dimensions than the islands typically observed in pulsed laser deposition. By repeating some of the work performed on PLD grown bicrystals with these single facet boundaries it should be possible to eliminate many of the experimental uncertainties associated with the complex microstructure and inhomogeneities.

The use of vicinal bicrystal substrates (such as a symmetric [100] tilt bicrystals) induces a step flow growth mechanism on the electrodes and therefore leads to grain boundaries that do not meander. Recent studies indicate a more homogenous microstructure for such grain boundaries, although the nature and extent of the grain boundary facetting has not been characterised in detail [34, 35]. The use of vicinal substrates may be an alternative route to obtaining single facet boundaries with deposition techniques other than LPE.

## 2.3 Phenomenology of Low and High Angle Grain Boundaries

This thesis focuses on the transport properties of high angle grain boundaries, so this will be the focus of this review. The properties of low angle grain

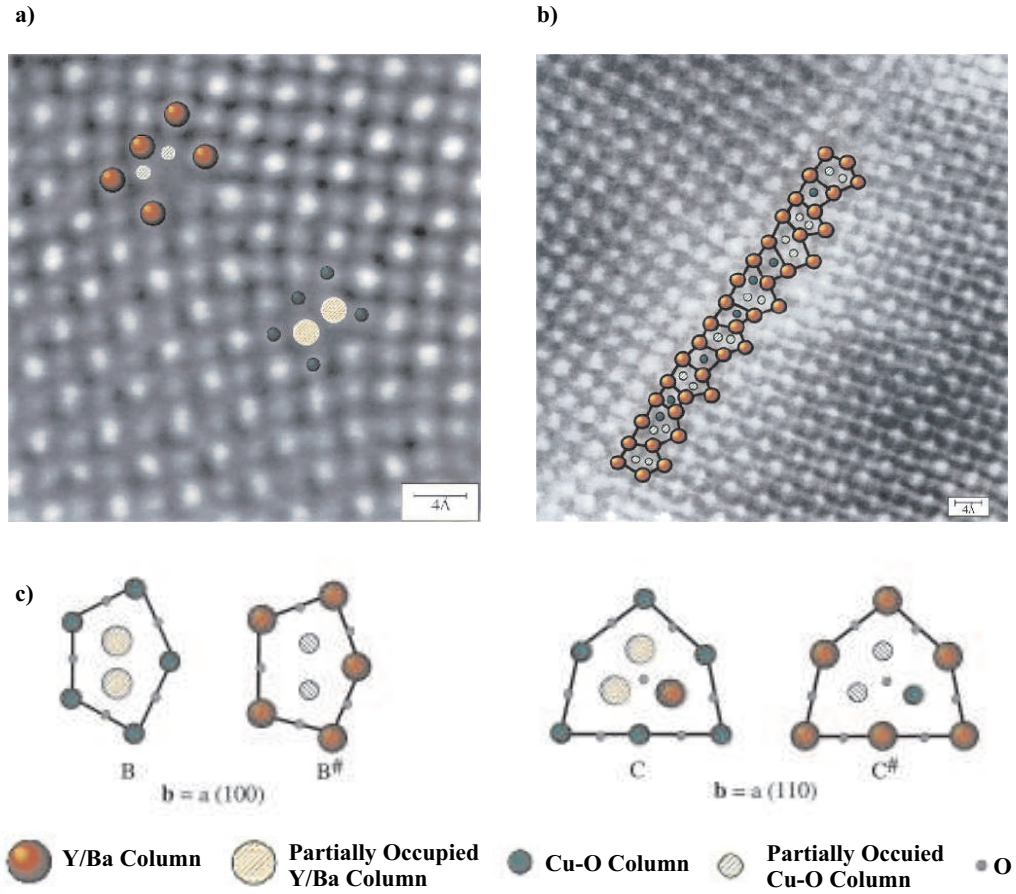


Figure 2.10: Z contrast images of a) a low angle [001] tilt boundary and b) a 30° [001] tilt boundary. The inferred locations of the atomic columns are marked. c) The structural units that are the constituents of both the dislocation cores and the high angle grain boundaries. Adapted from [31].

boundaries have been discussed in depth elsewhere [17, 18] and so will not be covered in detail here. The transport properties of low angle boundaries are determined by the reduced cross sectional area of the conductor due to the dislocations at the boundary (the dislocations themselves are insulating), as well as the pinning, channelling or cutting of vortices in the grain boundaries. As a result of the interaction of the flux lattice with the dislocations the transport properties are strongly dependent on the angle of the applied magnetic field to both the grain boundary plane and the Cu-O planes. In a high angle boundary the dislocation array is replaced by a continuous layer of disordered material at the boundary. Transport is dominated by the Josephson coupling across the boundary (a brief overview of the basic theory of the Josephson effect is given in the previous chapter) although the nature of the barrier is still disputed [1].

In section 1.1 the distinction between high and low angle grain boundaries is made on the basis of the structure of the boundary region. Low angle boundaries were defined in terms of an array of dislocations, whilst high angle boundaries have a continuous disordered layer present at the boundary. Based on this definition of low and high angle boundaries (which is conventional in other materials) it is estimated that the crossover between the two behaviors occurs at a misorientation angle of approximately 20° [32]. However in the literature the low/high angle distinction is often made on the basis of the phenomenology discussed above — i.e. low angle boundaries show flux flow type behaviour whilst high angle boundaries are Josephson coupled. Because Josephson coupling can occur across narrow superconducting constrictions [36], these two definitions produce different crossover misorientation angles. Furthermore a single grain boundary can show high and low angle behaviour in different temperature regimes. To understand this effect consider a single (low angle by the structural definition) grain boundary as an array of superconducting microbridges, separated by the dislocation cores. Within the isotropic Ginzburg Landau theory the occurrence of Josephson coupling in a microbridge is determined by the ratio of the Ginzburg Landau coherence length $\xi_{GL}$ to the effective length over which the non-linear effects of the weak link extend, $L_{eff}$ [37]. Note that $L_{eff}$ is typically determined by the larger of the dimensions of the microbridge, so that if the length $L$ is much less than the width $w$ then $L_{eff} \approx w$. Josephson coupling is predicted to occur for values of $L_{eff} < 3.5\,\xi_{GL}$ for the isotropic case, although this value is likely to be different for the anisotropic high $T_c$ superconductors ($L_{eff} < a\,\xi_{GL}^{ab}$, for some constant a). Since $\xi_{GL}$ is a function of temperature it is possible to observe a crossover from strong to weak coupled behaviour for certain samples in which the dislocation spacing (or channel length) is of the order of $\xi_{GL}$. Such a crossover has been observed by Redwing *et al.* in a 10°

symmetric [001] tilt boundary at 75 K [38]. The authors interpret their results in terms of long narrow channels ($L_{eff} \approx l$), whilst in fact the behaviour is more likely determined by the dislocation spacing ($L_{eff} \approx w$), which, according to Equation 1.1 is approximately 2 nm at this misorientation angle. As a result of the observation of this crossover the high angle/low angle distinction based on the Josephson effect is often taken as 10°, although in fact it is likely that such crossover behaviour is observable in a range of grain boundary angles (those for which $w < a\,\xi_{GL}^{ab}(T = 0)$). To avoid confusion between the two ways of defining the low/high angle boundaries in this work grain boundaries which are Josephson coupled but nonetheless have distinct, separate dislocations will be termed 'intermediate angle' boundaries. Note that Redwing *et al.* observe no Josephson coupled temperature range for 7° symmetric [001] tilt boundaries and no strong coupled temperature range for 15° symmetric [001] tilt boundaries. This sets some limits on the angular range of the intermediate angle boundaries.

The situation is complicated by the fact that both the stress field and possibly the charge on the grain boundary can extend the insulating region of the dislocation cores beyond their physical size [39, 40], so it is possible that there is a continuous electrical barrier at the interface when distinct dislocations are sufficiently closely spaced. Fortunately this study focuses on [001] tilt boundaries with a misorientation greater than 20°, where there is a continuous structural barrier at the interface. These boundaries can therefore be straightforwardly classified as high angle boundaries.

## 2.4 An Experimental Survey of Important High Angle Grain Boundary Properties

In this section a number of the experimental results that shed light on the transport mechanism through high angle boundaries are highlighted. Key results that provide clues as to the transport mechanism are discussed — for a comprehensive survey of the transport properties, see the recent review by Hilgenkamp and Mannhart [1].

### 2.4.1 Current-voltage characteristics

Until this study the current-voltage characteristics of high angle grain boundaries were believed to be similar to those predicted by the resistively and capacitively shunted junction (RSCJ) model, except in the case of some deoxygenated boundaries. Indeed at low voltages the RSCJ model is obeyed. The observation of Shapiro steps upon microwave irradiation confirms that

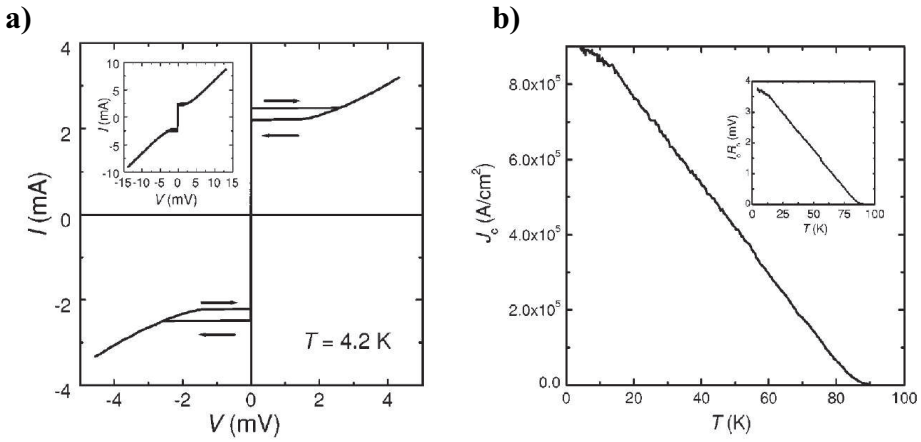


Figure 2.11: a) Current voltage characteristic of a 24° [001] tilt $YBa_2Cu_3O_{7-\delta}$ grain boundary. The thickness of the track across the boundary is 2.3$\mu$m, and the film is 120 nm thick. The measurement is taken at 4.2 K. b) Temperature dependence of the critical current and the $I_cR_n$ product for this junction. Data obtained by C. W. Schneider, adapted from [1].

the boundaries are Josephson coupled, and the amplitude of the steps is typically well described by the RSJ model for boundaries with low capacitance [41] (note that subharmonic Shapiro steps, due to long junction effects, can also be observed). A typical current-voltage characteristic for a 24° symmetric [001] tilt boundary is shown in Fig. 2.11a. Over the measurable voltage range (which is limited by the critical current of the track) the normal resistance is constant. The current voltage characteristic is hysteretic, which can be caused by either heating of the boundary or a capacitive shunt (see chapter 4).

The measurements on a slightly deoxygenated 36° symmetric [001] tilt boundary and a fully oxygenated asymmetric 45° [001] tilt boundary presented in chapter 6, confirm that non-linear behaviour can be observed on larger voltage scales of approximately 100 mV. The results obtained from asymmetric 45° [001] tilt grain boundaries are shown in Fig. 2.12, together with results from symmetric 24° [001] tilt boundaries for comparison. Non-linear current-voltage characteristics have been observed in deoxygenated 24° symmetric [001] tilt boundaries [42] and have now been confirmed in an additional asymmetric 45° [001] tilt grain boundary [43]. The form of these current voltage characteristics is discussed in detail in chapters 6 and 7.

A number of authors have measured the temperature dependence of the current voltage characteristic below the critical temperature. For junctions

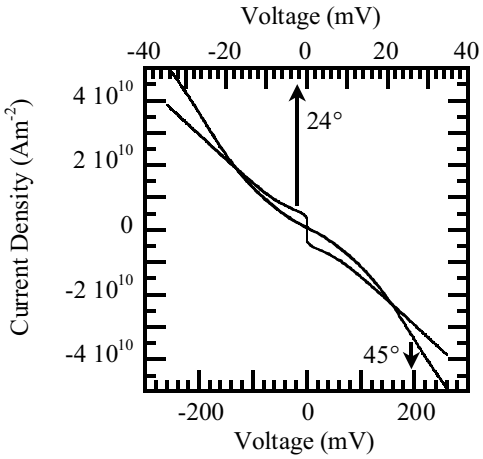


Figure 2.12: Current density voltage curves at 10 K for 24° symmetric and 45° asymmetric [001] tilt grain boundaries. The data were obtained from a Wheatstone bridge and have consequently been normalized so that the results are representative of a single grain boundary.

with an RSCJ like form as shown in Fig. 2.11a the temperature dependent properties can be characterised by the critical current and the normal resistance. Fig. 2.11b shows that the critical current changes almost linearly with temperature over a wide range. A review concludes that similar temperature dependencies are observed for grain boundary junctions fabricated in a number of different ways [44]. The normal state properties of the grain boundaries (in the case of the junction in Fig. 2.11 - the normal resistance) are temperature independent up to the critical temperature [45].

### 2.4.2 Magnetic Field Dependence of the Critical Current

The magnetic field dependence of the critical current gives important information about the spatial homogeneity of the Josephson current. As discussed in the previous chapter, in a planar vertical low $T_c$ junction the field dependence is strongly effected by whether the dimensions of the junction are significantly longer or shorter than the Josephson penetration depth, $\lambda_J = \Phi_0/(2\pi\mu_0 J_c(2\lambda + t))$ (where, $\Phi_0$ is the flux quantum $\mu_0$ is the permeability of free space, $J_c$ is the critical current density, $\lambda$ is the London penetration depth and $t$ is the thickness of the Junction in the direction of the current flow — $t \ll \lambda$ in this case). For junction lengths of the order

of, or greater than, the penetration depth, self field effects are important and the junction is in the long junction limit. For a 24° symmetric [001] tilt boundary with a critical current of order $10^9$ $Am^2$ such a calculation yields a value of $\lambda_J$ of order 1 $\mu m$ at 4.2 K. The situation is complicated in the high $T_c$ grain boundary geometry by 'flux focusing' effects due to the adjacent electrodes [46, 47]. Such effects alter the effective value of $\lambda_J$ since the field penetrates further into the electrodes than the London penetration depth. They also make it difficult to assess the field in the junction region, which is increased significantly above the applied field. From an experimental point of view long junction type critical current-field dependencies can be observed in 24° symmetric boundaries with widths of order $10\mu m$ at 4.2 K.

Figure 2.13 shows typical critical current–field dependencies for a number of junctions of different misorientation angles. The 24° boundary has sharp features characteristic of long junction effects. These effects are reduced as the misorientation angle is increased, the critical current falls and the Josephson penetration depth increases. Even when the Josephson penetration depth is larger than the size of the junction the curves usually deviate significantly from the classic single slit Fraunhofer patterns characteristic of low $T_c$ small junctions, indicative of inhomogeneity in the current distribution. Various authors have attempted to retrieve the current distribution by phase retrieval algorithms [48, 49], and they report inhomogeneous current distributions for all the solutions they find. It seems likely that the unusual field dependency of the critical current is caused by the inhomogeneous, facetted and meandering microstructure. For some grain boundary angles (particularly 45° asymmetric boundaries) the interaction of the facetted microstructure with the $d_{x^2-y^2}$ order parameter symmetry may also lead to the formation of $\pi$ junctions at the grain boundary, leading to highly anmolous, symmetric curves with maxima at finite fields. Non integer flux quanta, characteristic of $\pi$ junction effects, have been observed at 45° asymmetric grain boundaries [50]. The observation of regular Fraunhofer patterns at some 45° asymmetric [001] tilt, single facet, liquid phase epitaxy (LPE) grown bicrystals confirms the important role of the microstructure in producing such irregular Fraunhofer patterns [51]. Interestingly, not all the LPE bicrystals showed such regular Fraunhofer patterns. Some displayed them only on certain cool downs, with symmetric, irregular patterns with minima at zero field observed on subsequent cool downs [52] (this may be indicative of unusual effects due to trapped flux in junctions of this geometry).

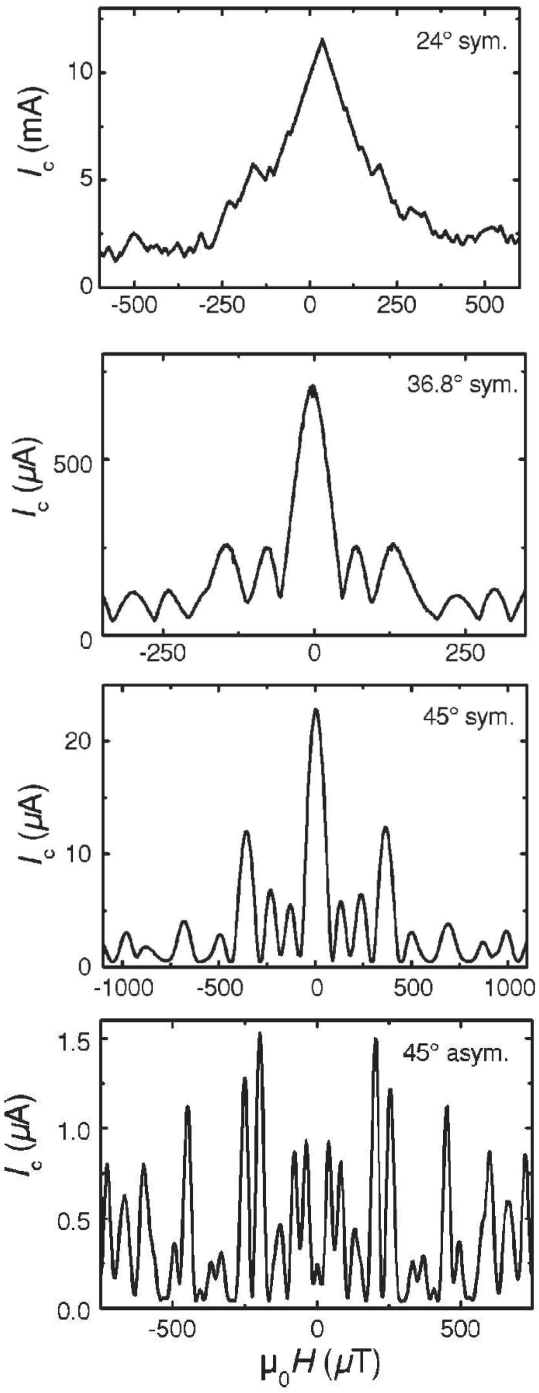


Figure 2.13: Critical current vs. magnetic field for [001] tilt boundaries of various misorientations at 4.2 K. The magnetic field is orientated parallel to the c-axis of both grains and its value has not been corrected for demagnetisation effects. The films were all 120 nm thick except the 45° asymmetric boundary, which was 40 nm thick. Junction widths were between 3 and 6 $\mu m$. Data obtained by C. W. Schneider, adapted from [1].

### 2.4.3 Orientation Dependence of Grain Boundary Properties

Many authors have collated critical current data for grain boundaries of various misorientations from different studies. There is usually a large amount of scatter in the data from a given misorientation angle, reflecting the strong dependence of the properties of the boundaries on the growth conditions. Rather than presenting collated data with a large amount of scatter, data from a single study is shown here. Hilgenkamp and Mannhart's data [53], showing the angular dependence of the critical current and the normal state resistance, are shown in Fig. 2.14. In this study all the films were grown in the same laboratory so the scatter is less than that typically observed. Detailed coverage of the literature is given in [1] — the data in Fig. 2.14 is representative of that of the whole literature.

Between 15° and 45° the critical current drops by a factor of 1000 and the normal resistance increases by a factor of 20. This leads to a decrease in the $I_cR_n$ product from close to 2 mV to 0.1 mV. The exponential decrease in the critical current density is evident in these plots and an exponential decrease in the resistance area product is also suggested, with a possible plateau at 45° (although there is considerable scatter here). There is little difference between the behaviour of the symmetric and asymmetric boundaries (note that for this study asymmetric boundaries are defined so that the inclination angle on one side of the boundary, $\alpha_1$, is fixed at $\alpha_1 = 45°$). It is important to note that this result does not imply that the critical current and the normal resistance are dependent only on the total misorientation. In a study by Ivanov *et al.* the critical current was found to vary by a factor of 1000 as the inclination angle was changed with fixed misorientation angle [54]. The results obtained from this study are shown in Fig. 2.15. Ivanov *et al.* use a direct tunneling model incorporating the order parameter symmetry and the anisotropy in the Fermi surface, similar to that developed in Chapter 7, to explain the decrease in the critical current. Their model, which is able to predict the $I_cR_n$ product, explains why this is typically much less than the superconducting gap.

Since both the critical current and the normal state resistance of the boundaries depend strongly on the detailed orientation of the the grains either side of the boundary, the facetted and meandering microstructure described in the previous section is likely to lead to highly inhomogeneous transport across the boundary. Such effects are further exaggerated in the critical current distribution across the junction due to the $d_{x^2-y^2}$ order parameter symmetry of $YBa_2Cu_3O_{7-\delta}$, as discussed in the previous subsection.

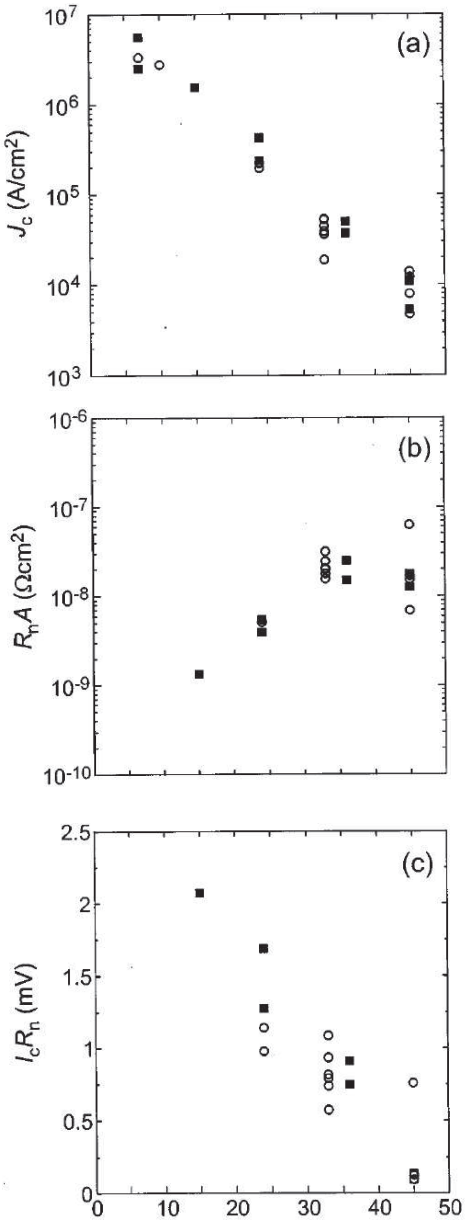


Figure 2.14: Misorientation dependence of a) the critical current density, b) the normal state resistance area product and c) the $I_cR_n$ product for symmetric (open circles) and asymmetric (filled squares) [001] tilt boundaries. The asymmetric grain boundaries were arranged with the [110] direction parallel to the boundary plane normal (i.e. with one of the inclination angles $\alpha_1$ fixed at $\alpha_1 = 45°$). All the data were obtained at 4.2 K. Note that for the 45° boundaries the maximum in the critical current does not necessarily occur at zero applied field, $H_a$, so in the case of these boundaries the maximum critical current in the range $0 \leq H_a \leq 20$ G were taken.

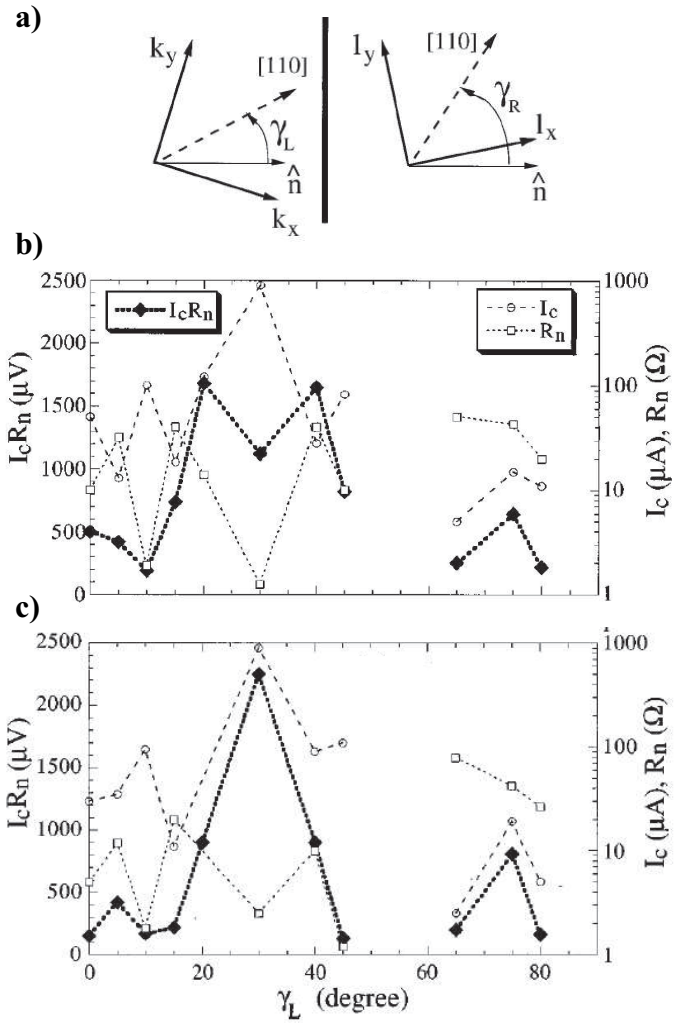


Figure 2.15: a) Schematic view of the bicrystal Josephson junction: $\gamma_{L,R}$ are the angles between the boundary normal vector and the [110] directions on opposite sides of the grain boundary ($\gamma_L = 45° - \alpha_1$, $\gamma_R = 45° - \alpha_2$ for the inclination angles $\alpha_1$ and $\alpha_2$ used in this work). b) $I_c$ (open circles) $R_n$ (open squares), and their product $I_cR_n$ (solid diamonds) vs. fan angle $\gamma_L$ ($\gamma_R = \gamma_L - 32°$) for b) a 3.5 $\mu$m wide microbridge and c) a 7 $\mu$m wide microbridge. The total misorientation is kept fixed at 32°. Adapted from [54].

### 2.4.4 Grain Boundary Capacitance and Fiske Resonances

The capacitance of $YBa_2Cu_3O_{7-\delta}$ grain boundaries was first measured by Winkler *et al.*, who observed convincing Fiske resonances in a 36° asymmetric boundary [55]. The Fiske resonances enabled them to determine the junction capacitance independently from the hysteresis in the current voltage characteristic and thus convincingly determine its value. This early experiment has since been repeated by a number of groups, who all report similar values of the grain boundary capacitance [56, 57, 58, 59, 60, 61, 62, 63].

The observation of Fiske resonances in the junction not only enables the grain boundary capacitance to be determined but also demonstrates that the grain boundary itself is insulating. A Fiske resonance is essentially a cavity mode resonance of the insulating part of the junction. It occurs when the frequency of the Josephson oscillations ($V/\Phi_0$, where $V$ is the voltage across the junction and $\Phi_0$ is the flux quantum) matches a cavity resonance of the insulating junction cavity. The voltage ($V_n$) at which an $n$th order Fiske resonance occurs is given by the following equation:

$$V_n = \frac{n\Phi_0}{2l\sqrt{L'C'}}, \tag{2.1}$$

where $l$ is the width of the junction and $L'$ and $C'$ are the inductance and capacitance, per unit length of the junction. $1/\sqrt{L'C'}$ is the velocity of the waves in the junction cavity. An $n$th order Fiske resonance corresponds to a cavity resonance in which $n/2$ wavelengths fit into the junction cavity, and so has a frequency $n/2l\sqrt{L'C'}$. The resonances are strongest when the critical current is suppressed to a minimum by the magnetic field. The data of Winkler *et al.* is summarised in Fig. 2.16. The field dependencies of the resonances are in striking agreement with the theoretically predicted forms.

From equation 2.1 $1/\sqrt{L'C'}$ can be extracted from a series of resonances by plotting $n/2l$ versus $V_n$. The capacitance can then be calculated if the inductance per unit length of the junction, given by $L' = \mu_0(t + 2\lambda_{eff})/h)$ (where $\mu_0$ is the Permeability of Free space, $h$ is the film thickness, $\lambda_{eff}$ is the effective London penetration depth and $t$ is the thickness of the junction — $t \ll \lambda_{eff}$) is known. The effective penetration depth $\lambda_{eff}$ is equal to the London penetration depth $\lambda_L$ in the thick film limit ($\lambda_L \gg h$) and is given by $\lambda_{eff} = \lambda_L^2/h$ in the thin film limit ($\lambda_L \ll h$). In practice $\lambda_L$ is of the same order as the film thickness, so both expressions yield similar results and different authors have assumed both limits [55, 61].

It is desirable to have both Fiske resonance and hysteresis estimates of the grain boundary capacitance. Generally these two techniques yield similar

values, confirming the validity of the technique and demonstrating that the hysteresis in the current voltage characteristic is caused by the capacitance. Typical values for the capacitance of well oxygenated [001] tilt symmetric 24° grain boundaries are in the range 0.1-0.2 $Fm^{-2}$ [63].

Fiske resonances could not be supported in a metallic layer so there must be an insulating layer that is continuous from one end of the junction to the other (although it is still possible that there are pinholes in this layer). The work of Winkler *et al.* therefore ruled out all SNS type models for $YBa_2Cu_3O_{7-\delta}$ grain boundaries.

### 2.4.5 Relationships between Ic, Rn and C

The IBM group were the first to speculate that the critical current – normal resistance ($I_cR_n$) product of the grain boundaries appeared to scale with the junction critical current density, $J_c$ [45]. Since then the scaling of the junction critical voltage with the resistance has been a controversial topic, with a wide range of results reported. Some authors assert that the $I_cR_n$ product scales with the critical current as $I_cR_n \propto J_c^{0.5}$, for all grain boundaries. Other authors claim that the scaling law is not always observed [53]. The reason for the controversy becomes clear when the data is carefully examined. Fig. 2.17a shows the type of plot that is often presented in the literature as an argument for $I_cR_n \propto J_c^{0.5}$ behaviour [64]. Data from a huge variety of junction types and with a great range of critical currents are presented in the same plot. Fig. 2.17b shows data from all the 24° symmetric [001] tilt grain boundaries measured by P. F. McBrien during his PhD, fabricated in Cambridge and at Strathclyde [65]. For this data the scaling is clearly not apparent and it appears that for this fixed grain boundary angle $I_cR_n$ is approximately constant over the measurable range (to within the scatter in the data).

This controversy has been resolved by the experiments of the Cornell group. Sydow *et al.* took a series of similar symmetric 24° [001] tilt grain boundaries and altered their oxygen content by a series of anneals and by electromigration (the application of a large DC current to the microbridge across the boundary — which alters the local oxygen content of the sample in its vicinity) [66]. With both techniques the $I_cR_n$ product shows $I_cR_n \propto J_c^{0.5}$ at low critical currents and $I_cR_n \approx$ constant at currents above approximately $10^4$ $Acm^{-2}$ (note that the current above which $I_cR_n \approx$ constant seems to be sample dependent). The data of Sydow *et al.* is shown in Fig. 2.17c and d.

To draw any conclusions from these scaling laws it is necessary to to determine the cause of the variations in the critical current and the normal resistance. Proponents of the resonant tunneling model argue that it

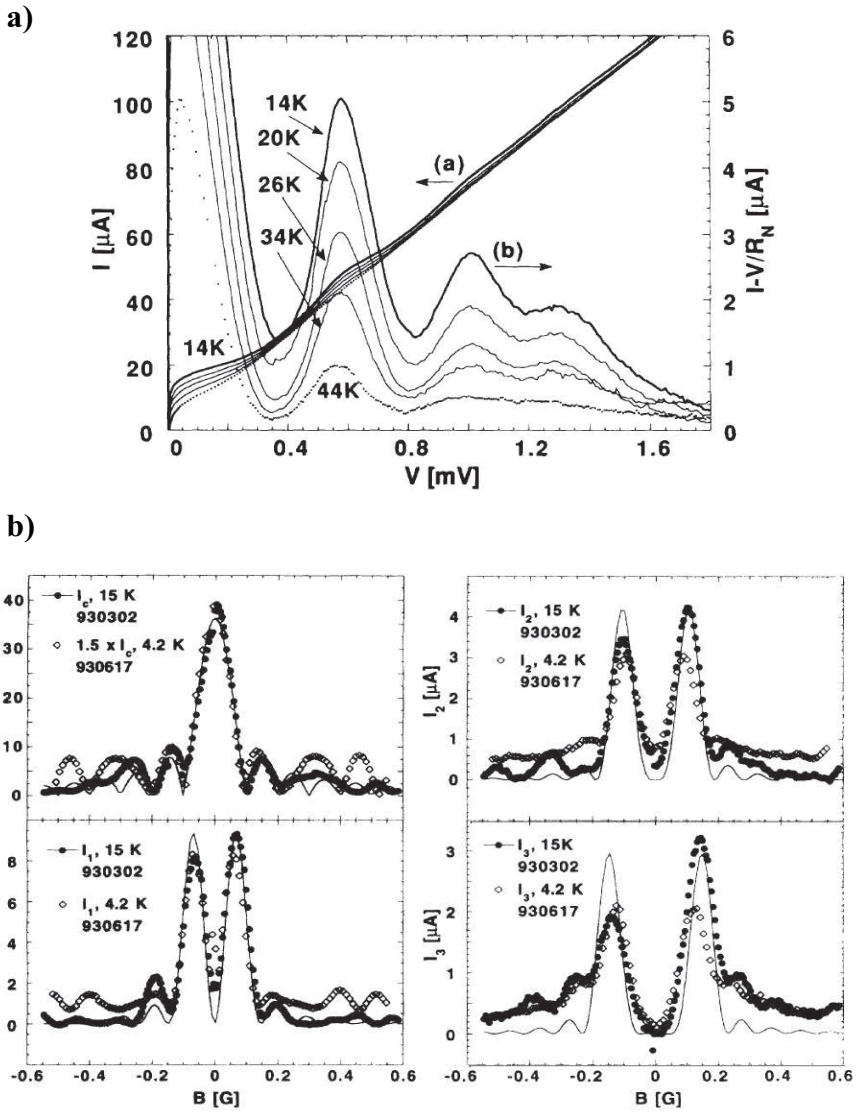


Figure 2.16: Results demonstrating the observation of Fiske resonances in a 30° asymmetric ($\alpha_1 = 0$, $\alpha_2 = 30°$) grain boundary. a) Resonances spaced at regular voltages are clearly observable in the current voltage characteristics at different temperatures. b) The amplitude of the first, second and third Fiske resonances ($I_1$, $I_2$ and $I_3$ respectively) display maxima at the minima in the junction critical current ($I_0$) as the applied field is changed (different symbols denote different measurement times and the solid curves are the theoretically predicted curves). Adapted from [55].

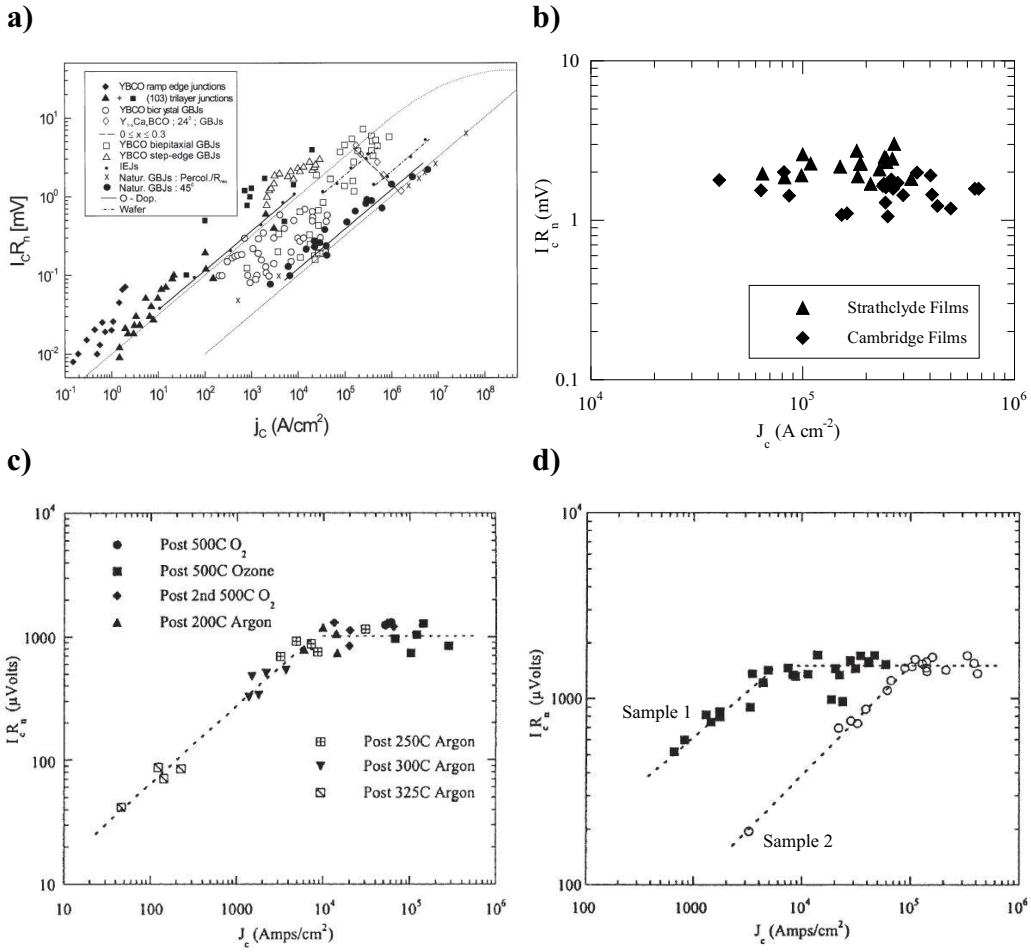


Figure 2.17: Scaling of the critical voltage ($I_cR_n$) with the critical current density $J_c$. a) Data collation due to Halbritter [64], supposedly demonstrating the universal $I_cR_n \propto J_c^{0.5}$ behaviour. b) Data from symmetric 24° [001] tilt grain boundaries grown in Cambridge and Strathclyde and measured by P. F. McBrien [65]. The $I_cR_n$ product is a constant for these boundaries over an order of magnitude in $J_c$ within the scatter of the data. c) and d) Data from a series of grain boundaries that have been oxygen treated by anneals in ozone, oxygen and argon and b) by electromigration. Both types of treatment are expected to alter the oxygen content of the films (the former globally and the latter locally at the grain boundary). Only at lower critical currents is the $I_cR_n \propto J_c^{0.5}$ scaling observed. At higher currents $I_cR_n \approx$ constant.

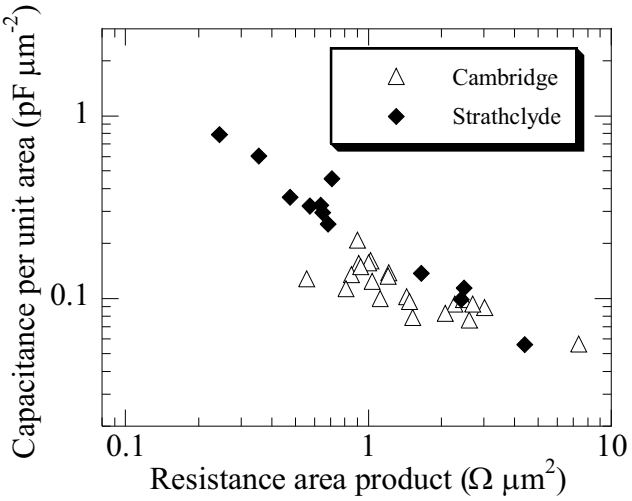


Figure 2.18: Scaling of the junction capacitance with the normal resistance for symmetric 24° [001] tilt grain boundaries grown in Cambridge and Strathclyde. This data was measured by P. F. McBrien [65], and corresponds to that shown in Fig. 2.17b.

is the barrier thickness that is changing [67, 64]. Within a resonant tunneling framework the Cooper pairs tunnel directly across the barrier whilst quasiparticles tunnel via intermediate states. For a barrier of thickness $2d$ the tunnel current for the superconducting component is therefore proportional to $e^{-2Kd}$ whilst that for the quasiparticles is proportional to $e^{-Kd}$, for some constant, $K$. This (very simplified) picture, predicts that $I_c \propto 1/R_n^2$, or equivalently $I_c R_n \propto I_c^{1/2}$. Such a picture may apply in the case of poorly oxygenated grain boundaries. $I_c \propto 1/R_n$ behaviour observed in well oxygenated samples seems to be more indicative of direct tunneling. For a series of fully oxygenated samples (such as that shown in Fig. 2.17b) such changes may be associated with variations in the grain boundary active area. If certain facet orientations carry the bulk of the current through the boundary then changes in the facet structure could lead to changes in the effective area. However this does not explain how deoxygenating a single sample produces the same scaling laws.

Measurements of the grain boundary capacitance appear to confirm an effective area model for fully oxygenated samples. Fig. 2.18 shows the variation of the capacitance (measured as described in the previous subsection) with the grain boundary resistance for the same set of samples shown in Fig. 2.17b. The capacitance gives information about the grain boundary barrier

width independently of its height and so provides further useful insights into the variations occurring in the electrical barrier. The capacitance, $C$, is found to vary approximately as $C \propto 1/R_n$, which seems to be more consistent with variations in effective area.

In recent work on 32° and 40° asymmetric mesoscopic junctions Tzalenchuk *et al.* report that the scaling law $I_cR_n \propto I_c^{1/2}$ is obeyed [68]. They also note that the junction critical current no longer scales with width below a critical junction length, which may indicate that these submicron junctions are particularly prone to deoxygenation effects. The capacitance of the grain boundaries scales as $1/R_n$. These results do not seem compatible with either a resonant tunneling model or with changes in effective area, and appear to indicate that the situation is more complex than either picture can account for.

Unfortunately no capacitance data exists for a single grain boundary that has been oxygen depleted in a controlled manner, so the mechanisms underlying the $I_cR_n \propto I_c^{1/2}$ and the $I_cR_n \approx$constant behaviour remain unclear.

### 2.4.6 Noise Properties

Studies of the noise produced by grain boundary junctions give further insights into the transport mechanism. A number of groups have investigated the noise properties of grain boundary junctions of various types. Here a brief summary of the results that are relevant to the grain boundary transport mechanism is given. A detailed overview is given by Hao *et al.* [69].

In experiments to measure the grain boundary noise the quantity measured is usually the spectral density of the voltage fluctuations at a fixed bias current, $S_V(f)$. $S_V(f)$ is defined in the following way:

$$S_v(f) = \int_0^\infty \left( < V(\tau)V(0) > - < V >^2 \right) \cos(2\pi f\tau)\, \mathrm{d}\tau, \qquad (2.2)$$

where $< V(\tau)V(0) >$ is the autocorrelation of the voltage at time $\tau$ with that at the start of the measurement, $< V >$ is the DC voltage and $f$ is the frequency of the measurement. $S_V(f)$ is the fourier transform of the autocorrelation function of the voltage fluctuations and is therefore proportional to the energy density of the fluctuations per unit frequency interval (according to the Wiener-Kinchin theorem). It has units of $V^2Hz^{-1}$.

Of particular interest for understanding the transport mechanism through grain boundaries is the excess noise observed in grain boundary junctions. This is the noise that occurs above the thermal (white) noise that is present in all Josephson junctions [70]. The frequency dependence of the excess noise observed in $YBa_2Cu_3O_{7-\delta}$ bicrystal junctions has been observed to be

proportional to $1/f$. Such $1/f$ noise can be caused by charge trapping in the barrier, or by thermally activated flux motion at the grain boundary or in the nearby film, but is most likely attributable to charge trapping, for reasons discussed below. Because the trapping of charge alters the potential of the grain boundary barrier, $1/f$ noise contains important information about the properties of the grain boundary barrier.

Kawasaki *et al.* [71] demonstrated that at low bias currents this $1/f$ excess noise was dominated by fluctuations in the critical current and that at high bias currents it is dominated by resistance fluctuations. Fig. 2.19a shows the dependence of the measured noise of a $YBa_2Cu_3O_{7-\delta}$ grain boundary as a function of the bias current, together with calculated components from different sources — which confirms this observation. The critical current and normal resistance fluctuations can be extracted by measuring currents, $I$, close to the critical current, $I_c$ and at currents much greater than the critical current. The critical current fluctuations are therefore given by $|\delta I_c/I_c| = S_V^{1/2}/I_c R_d$ at $I \approx I_c$ and the normal resistance fluctuations are given by $|\delta R_n/R_n| = S_V^{1/2}/IR_n$ at $I \gg I_c$ ($R_d$ is the dynamic resistance). The $1/f$ frequency dependence of both of these noise sources is apparent from the data shown in Fig. 2.19c and d.

From the point of view of grain boundary mechanisms two results are particularly important. The first is the question of whether the critical current and normal resistance fluctuations are correlated. If so this would demonstrate that their origin is charge trapping at the boundary, which increases the critical current and decreases the resistance simultaneously by increasing the local barrier potential. Whilst increases in the critical current are expected to occur at the same time as decreases in the normal resistance (anti-correlation) the measured voltage fluctuations are expected to occur in the same direction because an increase in the critical current results in a decrease in the measured voltage (see Fig. 2.19b). Thus if the measured resistance and current fluctuations are directly correlated a charge trapping mechanism seems likely. Marx *et al.* have indeed observed such a positive correlation between critical current and resistance fluctuations in 24° symmetric [001] tilt $YBa_2Cu_3O_{7-\delta}$ grain boundaries [72]. However, in an earlier experiment, Hammond *et al.* observed no correlation between the two quantities in an asymmetric 45° [001] tilt bi-epitaxial junction (Conductus type) [73]. Hilgenkamp and Mannhart have noted that a likely explanation for this is d-wave pairing effects, which lead to a redistribution of the supercurrent along the facetted boundary for large misorientation angles (and particularly for asymmetric 45° boundaries) [1]. The normal current and supercurrent distribution is therefore different in higher angle boundaries, leading to un-

correlated behaviour. Because the correlation is observed in the absence of these d-wave effects, the work of Marx *et al.* demonstrates that the $1/f$ noise is indeed due to charge trapping in the grain boundary. Subsequent work on submicron junctions has confirmed this conclusion [74].

Since the critical current and resistance fluctuations originate from small changes in the barrier potential at the grain boundary the ratio of $|\delta I_c/I_c|$ to $|\delta R_n/R_n|$ is of particular interest. If $R_n$ is related to $I_c$ by an equation of the form $R_n = KI_c^{q-1}$ (implying $I_cR_n \propto I_c^q$) then it must also be true that $R_n(1+\delta R_n/R_n) = KI_c^{q-1}(1+\delta I_c/I_c)^{q-1}$. Using a binomial expansion the following result is therefore implied: $|\delta I_c/I_c|/|\delta R_n/R_n| = 1/(q-1)$. Most previous measurements of excess noise in grain boundary junctions report $|\delta I_c/I_c|/|\delta R_n/R_n| \approx 2$ [67, 69, 71] which implies $q \approx 0.5$ in agreement with the result obtained from the scaling of the critical voltage at low critical currents discussed in the previous section. A major problem in assessing the literature is that in most noise studies the authors do not publish the critical current density of the boundaries being measured. This makes it hard to compare the noise data with the scaling laws discussed in the previous subsection — since this scaling appears to occur in lower critical current grain boundaries. It would be interesting to study the noise properties of high critical current grain boundaries as oxygen is removed - to see whether the observations of Sydow *et al.* [66] are confirmed in the noise data. A further point to note is that the noise data implies that the addition of a small amount of charge to the grain boundary causes similar changes to the grain boundary barrier as those that occur in the scaling laws, which appear to be associated with the local oxygen content of the boundary. This suggests a link between the charge on the boundary and the doping in the boundary region.

### 2.4.7 The Influence of Calcium Doping

Calcium doping, both globally and locally, has been shown by a number of independent groups to significantly increase the critical current of both low and high angle boundaries [75, 76, 77, 78, 79]. The $Ca^{2+}$ ions substitute for $Y^{3+}$ in the blocking layers between the Cu-O planes, leading to the creation of additional holes in the Cu-O planes to maintain the charge balance. This allows the overdoped region of the phase diagram in Fig. 2.3 to be accessed when the material is well oxygenated [80]. In addition it is possible that the calcium may diffuse preferentially to the grain boundaries and alter charge that is present on it.

Schmehl *et al.* were the first to demonstrate that calcium doping of the films increases the critical current density of the grain boundaries [75]. They

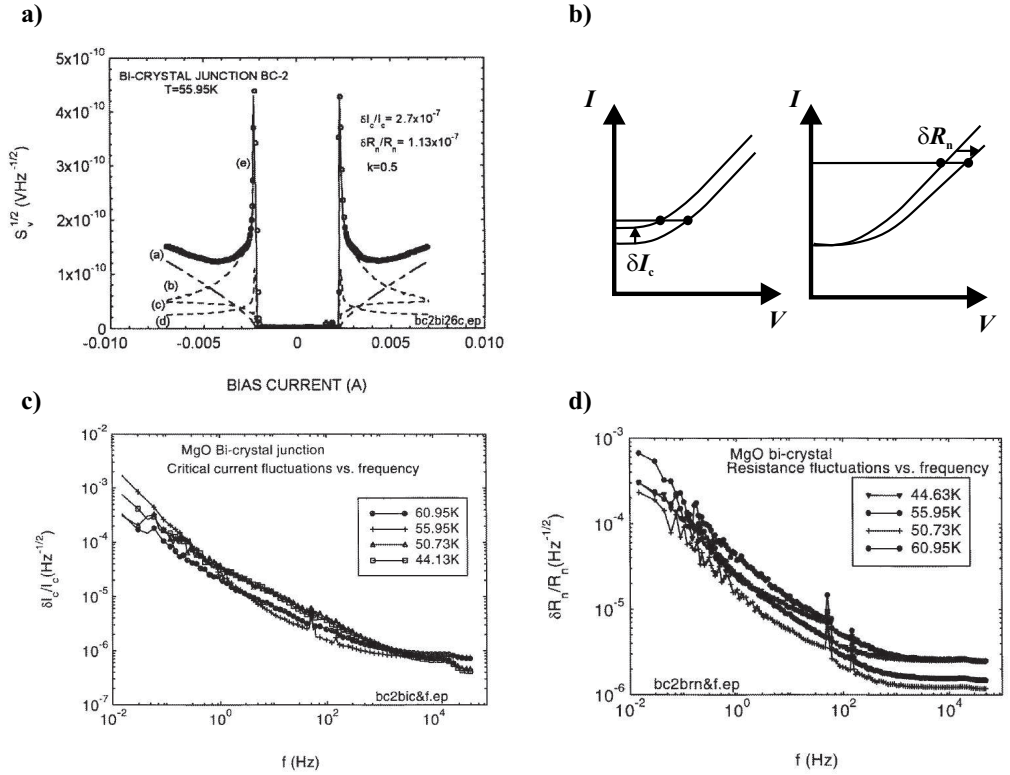


Figure 2.19: A summary of the important noise properties of grain boundaries. a) Spectral density of noise measured at 60 kHz as a function of bias current, for a $YBa_2Cu_3O_{7-\delta}$ grain boundary grown on a 24° symmetric [001] tilt $SrTiO_3$ bicrystal. The total noise (e) can be broken down into several components — resistance fluctuations (a), critical current fluctuations (b) a correlation term (c) and thermal noise (d). At low bias critical current fluctuations dominate the observed spectral density, whilst at high bias the resistance fluctuations dominate. b) Diagram illustrating how fluctuations in the critical current, $\delta I$, result in voltage fluctuations, $\delta V$, of opposite sign to fluctuations of the normal resistance, $\delta R$. The correlation between the two types of fluctuation demonstrates whether the supercurrent and the normal current flow in the same channels. Frequency dependence of c) the critical current and d) the normal resistance fluctuations measured on a 24° symmetric [001] tilt MgO bicrystal. Adapted from [69].

observed over an order of magnitude enhancement in the critical current density of 24° symmetric [001] tilt boundaries when the films were homogenously doped. A corresponding decrease in the normal resistance area product was also observed. Their results are shown in Fig. 2.20. Enhancements in the critical current density of low angle grain boundaries were subsequently observed by several groups [78, 79]. The work in Chapter 4 of this study also confirms the result on high angle grain boundaries.

The interpretation of these results remains difficult. Schmehl *et al.* interpret their results in terms of a band bending model, with the principle change occurring being an increase in the local carrier density (leading to a decrease in the extent of the band bending — see the next section for a discussion of the band bending model). It is known from experiments on thin films that Calcium substitution leads to over-doping [80], but there are a number of additional ways in which the Calcium could alter the grain boundary properties. For example Calcium could segregate preferentially to the grain boundary and alter the charge on it. Recent TEM evidence shows that the basic structural units comprising the grain boundary are unchanged by the addition of Calcium [81], but also highlights that the substitution of Calcium for Yttrium may be greater within the structural units. Alternatively, if all grain boundaries are oxygen depleted then the Calcium doping could lessen the effect of this, since a reduction in the oxygen content of overdoped films initially results in an increase in the critical temperature. In Chapter 4 a careful examination of the capacitance of Calcium doped films is performed. The results obtained from this study indicate that the situation may be more complex than a simple reduction in the width of the band bending.

In this section the transport properties of high angle grain boundaries have been reviewed, with an emphasis on experiments that shed light on the nature of the boundary. A number of important points come out of these experimental results:

- From the Fiske resonance data it is clear that the boundaries are largely insulating (although they may contain pinholes).

- The orientation dependence of the junction properties is strongly suggestive of tunneling behaviour.

- With the exception of LPE junctions of certain misorientation angles the Fraunhofer patterns of the junctions indicate that the current transport is extremely inhomogeneous. The scaling of the capacitance with the normal resistance in well oxygenated grain boundaries is character-

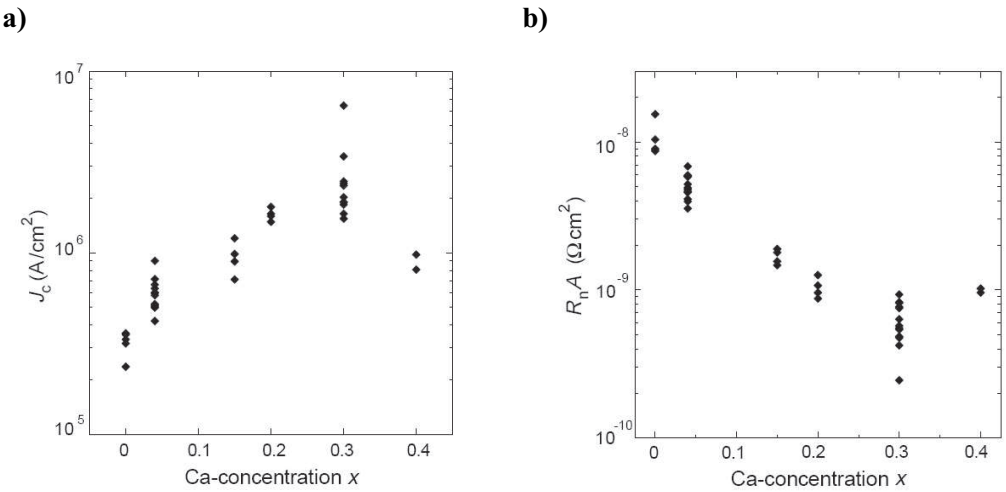


Figure 2.20: The effect of Calcium doping on the grain boundary properties. a) the increase of the critical current and b) the decrease of the normal state resistance as the calcium concentration $x$ is increased in the $Y_{1-x}Ca_xBa_2Cu_3O_{7-\delta}$ films. Adapted from [75].

istic of variations in the effective area of the boundary and therefore also indicates inhomogeneous transport properties.

- The role of oxygen in the grain boundary is critical. Deoxygenated grain boundaries obey the scaling law $I_cR_n \approx J_c^{1/2}$. Such a law is consistent with a resonant tunneling model of transport through the boundary. Similar scaling of the critical voltage is implied by the noise data, although the range of critical currents over which this observation is valid is uncertain. Higher critical current boundaries show different scaling, with $I_cR_n \approx$ constant.

- Calcium doping clearly leads to increases in the grain boundary critical current and decreases in its resistance. This may indicate that the charge on the boundary and the carrier density of the film play important roles in the transport through it. The addition of Calcium may make the boundary less sensitive to changes in oxygenation, since removal of oxygen from an over-doped region will initially increase its critical temperature.

In addition to these general points it is clear that a large number of issues need clarification. The observations on sub-micron junctions in which the scaling of capacitance with resistance seem indicative of changes in effective area but which nonetheless show $I_cR_n \approx J_c^{1/2}$ behaviour [68] seem to indicate

that a simple resonant tunneling interpretation of the scaling laws is not appropriate for these junctions. Another issue is that, as a result of sample to sample variations, it is very difficult to compare different studies in the literature, especially when important grain boundary parameters, such as the critical current and normal resistance, are not always quoted. This is a major problem with the noise data, for example. In order to make further progress in the field, it is necessary to establish either a technology that produces junctions with reproducible properties (the single facet LPE bicrystals seem to be a promising avenue of research [33]) or to perform many different types of experiment on a single sample. The controlled alteration of the properties of a single boundary, for example by oxygen annealing, offers a way to explore the spread in grain boundary properties that is much better defined than the growth of large numbers of samples.

In the next section the physics of grain boundary transport is discussed, in the light of these experimental results.

## 2.5 Grain Boundary Mechanisms

In this section the different mechanisms that are proposed to be responsible for the observed grain boundary transport properties are reviewed. First, mechanisms associated with the $d_{x^2-y^2}$-wave order parameter are discussed, as it is now established that $YBa_2Cu_3O_{7-\delta}$ has such an order parameter and that it plays an important (though probably not dominating) role in grain boundary transport. Secondly, the electrical structure of the boundary is discussed and, as a result of an absence of convincing microstructural data, this section is necessarily more tentative. A number of authors propose models with varying degrees of complexity and these models often produce conflicting predictions. The assertion in a recent review that the models are not mutually exclusive [1], cannot be generally applied, as there are clear cut differences between the mechanisms proposed. However it is certainly true that the influence of several effects can occur concurrently — for example it is now clear that $d_{x^2-y^2}$ order parameter effects will certainly occur in addition to one of the other proposed mechanisms (or possibly some mechanism that has not been thought of).

### 2.5.1 The $d_{x^2-y^2}$-Wave Order Parameter

Predominant $d_{x^2-y^2}$ order parameter symmetry is now well established for $YBa_2Cu_3O_{7-\delta}$ [19]. This has a number of implications for studies on grain boundary transport, some of which are illustrated in Fig. 2.21.

Even in the absence of a grain boundary tunnel barrier Fig. 2.21a shows that the order parameter itself must be depressed as a function of position in a direction perpendicular to the boundary in order that it remains single valued at the plane of the boundary. Such a depression occurs over a distance of approximately one coherence length [82]. This order parameter depression gives rise to quasiparticle states bound by Andreev reflections at the grain boundary plane. Depending on the trajectory of quasiparticles incident on the grain boundary they may also experience a sign change of the pair potential when they are reflected at the boundary, or transmitted through it. This effect can give rise to bound quasiparticle states at mid-gap energy, which can be observed as zero-bias anomalies in tunneling spectroscopy. Such zero bias anomalies have been observed in $YBa_2Cu_3O_{7-\delta}$ grain boundary junctions [42, 83], and are expected to cause further reductions in the critical current [84].

In addition to these frustration effects the tunneling process itself is dependent on the orientation of the adjacent grains, as a result of the $d_{x^2-y^2}$ symmetry (see Fig. 2.21b). The orientation dependence of the tunnel current has been calculated for the case of a highly directional tunneling process [85]. For an unfacetted 24° symmetric [001] tilt boundary this mechanism results in a 17% suppression of the critical current from tunneling across the same barrier with a 0° misorientation [86], much less than that observed (see Fig. 2.14). It is therefore significant, but not the primary mechanism that depresses the junction critical current.

The facetting of the grain boundary, can, in specific configurations, produce frustrated geometries in which some facets become $\pi$ junctions. One such configuration is illustrated in Fig. 2.21c. At zero applied field the current flow across the $\pi$ junctions occurs in the opposite direction to that through the normal junctions and this can result in a significant reduction of the critical current [86]. Hilgenkamp predicts such an effect can lead to approximately an order of magnitude depression in the critical current of a typical facetted 36° symmetric [001] tilt boundary (compared to an identical, unfacetted boundary with a misorientation of 0°) — this should be compared with the three order of magnitude decrease in the critical current observed [1, 53]. It is therefore clear that this effect does not dominate the transport through the boundary. Furthermore unfacetted 45° asymmetric [001] tilt boundaries grown by LPE have been shown to have critical currents only slightly greater than facetted grain boundaries [33, 53]. Some other mechanism must therefore produce the majority of the current depression at the grain boundary.

The effects of the $d_{x^2-y^2}$ pairing are therefore significant, but another mechanism must be responsible for much of the suppression of the grain

boundary critical currents. Since it is known that the grain boundary is insulating the obvious mechanism is tunneling of some form, although several different possibilities have been highlighted. In the next section the detailed nature of the barrier itself is discussed, with particular reference to the mechanisms of current transfer.

### 2.5.2 The Nature of the Grain Boundary Barrier

It is known that the grain boundary is largely insulating but its precise nature is still disputed. The type of barrier present is a critical question in terms of the development of a tunneling model. There are essentially two schools of thought as to the type of insulator present at the grain boundary. The first proposes that in the region of the grain boundary the compound reverts to the insulating parent phase that occurs when the Cu-O planes are not doped by holes (see Fig. 2.3). The mechanism for this can be either local oxygen depletion [87] or disruption of the charge transfer mechanism due to disorder or strain [64]. This mechanism yields an insulator with a high density of localised states. The appropriate insulating gap is approximately 2 eV. The tunnel barrier would therefore have a height of order 1 eV and be interrupted by a number of localised states, through which quasiparticles (but not pairs) may tunnel resonantly. Such models are usually referred to as 'resonant tunneling' models. Hopping transport through intermediate states has been described theoretically by Glazman and Matveev, for the equivalent system of a thin amorphous film [88]. They predicted the form of the low temperature conductance voltage curve and the temperature dependence of the normal state resistivity in the form of power series with variable coefficients. The Glazman-Matveev theory has been successfully applied to describe the properties of $YBa_2Cu_3O_{7-\delta}$ ramp-edge junctions with various barrier materials (e. g. $SrRuO_3$ [89] and $PrBa_2Cu_3O_{7-\delta}$ [90]) and with interface engineered junctions (effectively ion beam damaged ramp edges with no barrier material) [91]. These types of junctions are all somewhat different to grain boundary junctions and generally involve either a thin film of another material or a damaged layer of $YBa_2Cu_3O_{7-\delta}$, so the theory seems more applicable in these cases than in the case of a single grain boundary. The scaling of the resistance area product with the critical current appears to indicate that this model might apply for deoxygenated grain boundaries — although this is not definitively established. Similarly the ratio of the resistance noise to the critical current noise appears to imply some form of resonant tunneling although it is not clear whether the noise data comes from fully oxygenated grain boundaries with large critical currents.

The second school of thought proposes that the local band structure is

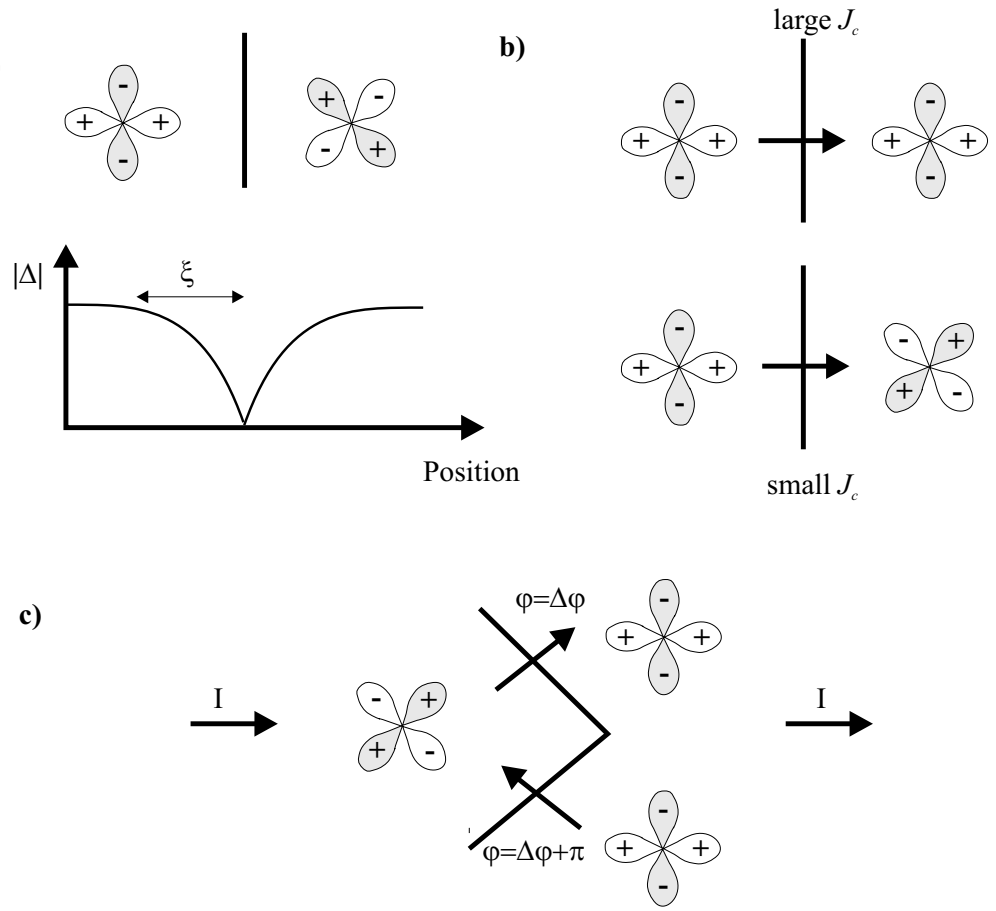


Figure 2.21: Illustration of mechanisms related to the $d_{x^2-y^2}$ pairing that reduce the critical current density at the grain boundary. a) The magnitude of the order parameter ($|\Delta|$) is depressed over a distance of approximately one coherence length ($\xi$) due to frustration caused by the orientation of the crystallographic axis and their alignment with different signs of the order parameter. b) For a highly directional tunnelling process the number of pairs available for tunneling across the barrier changes with the orientation of the order parameter to the grain boundary plane. c) For a facetted boundary the geometry of the facets can lead to frustration effects and the formation of $\pi$ junctions. In arrays of 0 and $\pi$ junctions the local Josephson current flows in the opposite direction to the applied bias for some facets. Based on [82].

distorted by charge residing on the boundary, resulting in a phenomenon referred to as 'band bending' [92], which is known to control the properties of semiconductor interfaces [93, 94, 95] and also occurs at grain boundaries in Mn doped $SrTiO_3$ [96]. Within a band bending picture charge is trapped on the grain boundary at localised states. The local bandstructure is distorted by the potential associated with this trapped charge and the bands are shifted in energy as a function of distance from the grain boundary. The presence of the trapped charge on the boundary leads to a carrier depleted region adjacent to it, the width of which is given by the electrostatic screening length $\lambda_{el}$ (which is in the range of several Å to 1 nm for the cuprates [1]). $\lambda_{el}$ is determined by the charge on the boundary, $Q$, and the carrier density, $n$, giving $\lambda_{el} \approx Q/2ne$, assuming a completely charge depleted layer ($e$ is the electron charge). Since the electrostatic screening length and the distance between the mobile charge carriers is comparable, the charge screening is not governed by a simple solution of Poisson's equation as in the semiconductor case, but the barrier energy $E_b$ will be of a similar order of magnitude to the Poisson result $E_b = Q^2/8n\varepsilon$, where $\varepsilon$ is the dielectric constant. These equations give reasonable estimates of both the normal resistance area product and the capacitance of the boundary with a barrier height of order 0.1 eV [92]. They also predict an unconventional shape for the tunnel barrier (see Fig. 2.22).

The sign of the charge trapped on the boundary determines the direction of band bending. In Fig. 2.22 the boundary is assumed to trap holes and therefore to cause a reduction in the local potential. There has recently been some contention over the sign of the band bending [97]. Bending of the band in the opposite direction is expected if the boundary traps electrons. It is difficult to assess which scenario occurs because the situation depends heavily on the poorly understood physics of the bulk material. If the material can be treated as a conventional Fermi-liquid at optimum doping then it the fact that the Fermi level is close to the bottom of the band in Fig. 2.4 would seem to point to electron trapping at the boundary. However if a picture in terms of a hole doped Hubbard band is more appropriate then the diagram in Fig. 2.22 is probably more accurate. Such a scheme appears to be upheld by the sign of field effect experiments, which show an enhancement of the grain boundary critical current when the gate voltage produces hole accumulation near the surface of the electrode [98, 99, 100]. Note that there is an isolated result that disagrees with the sign of the effect observed in these studies [101], but in this case there was a rather large leakage current.

The band bending model also predicts increases in the grain boundary critical current with increases in the carrier density, and was the motivation for performing the Calcium doping experiments. Such band bending is not

significant in conventional superconductors because the carrier density in these materials is significantly larger than it is in the cuprates, so the length scales involved are negligible.

In addition to these two views as to the nature of the grain boundary barrier there is some debate as to whether the boundary contains pinholes at all grain boundary angles, as proposed by Sarnelli and Testa [102]. Superconducting pin-holes (also known as ScS junctions or Dayem bridges [103, 104]) are clearly important in the intermediate angle boundaries defined in section 2.3, but Sarnelli and Testa propose that they persist at grain boundary angles where the disordered region observed by transmission electron microscopy is continuous. They propose a two channel model of conductivity, with transport of quasiparticles by resonant tunneling through the insulating regions of the boundary and transport of pairs and quasiparticles through the pinholes (the insulating regions are assumed to be of the same form as the grain boundary barrier in the resonant tunneling model). For fully oxygenated samples they predict that the transport will be dominated by the channels. As the oxygen content is reduced the channel contributions are reduced and the normal resistance is dominated by resonant tunneling whilst the critical current is severely depressed.

In summary there are three possibilities for the current transfer through the insulating grain boundary. The first is resonant and direct tunneling through an insulator with a 1 eV gap, the second is direct tunneling through a 0.1 eV barrier induced by band bending and the third is current transfer through pinholes in the insulating seam at the boundary.

### 2.5.3 The Role of Oxygen

The oxygen content of the boundary has been shown to be important by a number of experiments involving annealing and electromigration [66]. As discussed above, it seems likely that the local oxygen content at the grain boundary is reduced in 24° [001] tilt boundaries which show resonant tunneling type behaviour. This would make sense as the underdoped phase proposed for the boundary in this model occurs in severely oxygen depleted $YBa_2Cu_3O_{7-\delta}$. Within a band bending picture the local oxygen content will determine the carrier density and therefore deoxygenated grain boundaries will be wider and correspondingly have a reduced critical current and normal resistance area product. Both models predict that oxygen depletion leads to a wider barrier.

Some authors propose that changes in the oxygenation lead to changes in the effective area of the grain boundaries [105]. Such a filamentary model proposes that the oxygen disorder forms filamentary structures that change the

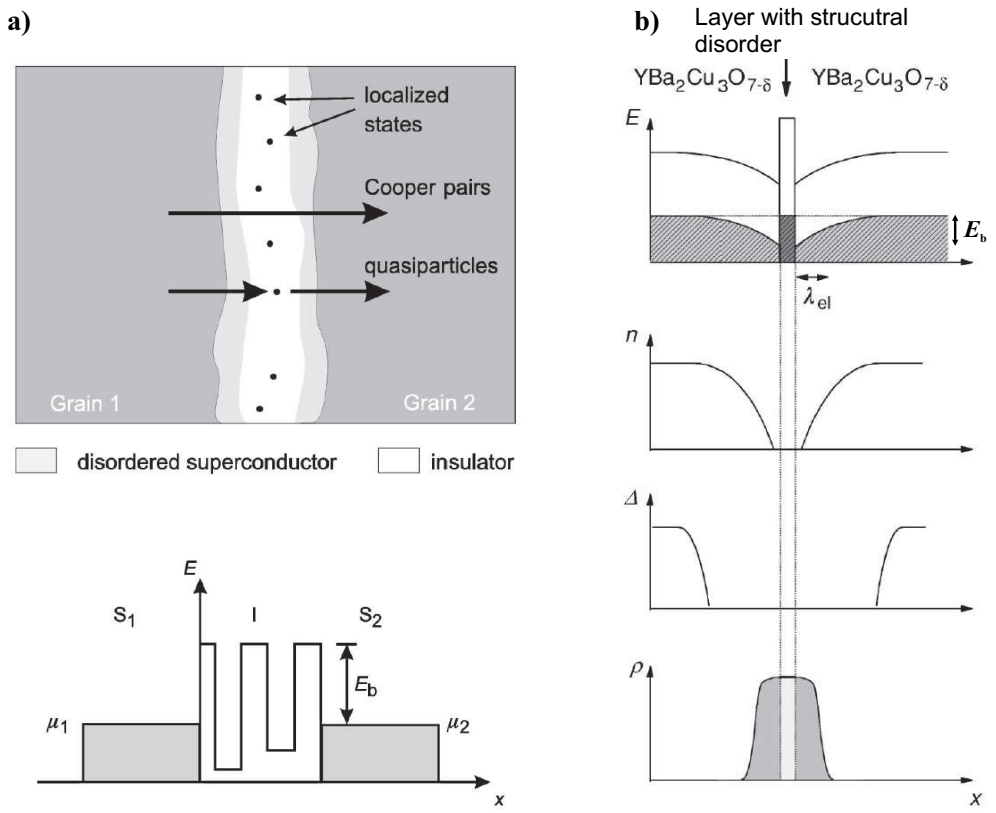


Figure 2.22: a) Resonant tunneling model of the barrier at a high $T_c$ grain boundary. The interface is characterised by a seam of the insulating parent compound ($I$) containing a high density of localised states. Quasiparticles tunnel resonantly via these localised states whilst the Cooper pairs must tunnel directly. The barrier energy $E_b$ is approximately 2 eV above the Fermi energy ($\mu_1$ on side $S_1$ and $\mu_2 = \mu_1 - eV$ on side $S_2$). b) A possible scenario for the band bending model for the potential barrier at the interface. The band is distorted over the electrostatic screening length $\lambda_{el}$, leading to a local insulator (due to a full band) with a characteristic energy scale, $E_b$, of order 0.1 eV. The number of free carriers $n$ is reduced in the region surrounding the boundary leading to a rapid suppression of the order parameter $\Delta$. The charge density on the barrier, $\rho$, is high in the carrier depleted regions of the boundary and a corresponding opposite charge is located on the structurally disordered layer of the grain boundary (not shown).

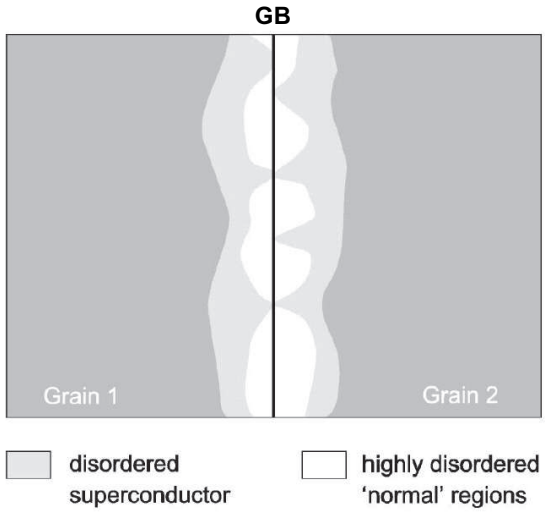


Figure 2.23: Schematic showing a proposed filamentary microstructure for a grain boundary. Filaments of material with reduced oxygen order such that the material has a suppressed but finite critical temperature are interspersed between more oxygen depleted regions that do not superconduct. The critical current of the boundary is determined by the overlap of filaments from either side of the grain boundary.

effective area of the grain boundary, as illustrated in Fig. 2.23. This model has a number of similarities in its predictions to the ScS model discussed above. Its major difficulty is that the structures proposed seem somewhat arbitrary, and, while they explain some of the transport properties there is no direct evidence for their existence. It seems unlikely to this author that these filamentary structures could exist in the oxygen sublattice of a grain boundary that is similar in form to that shown in Fig. 2.10.

As discussed in the previous section, capacitance measurements from large numbers of [001] tilt boundaries grown with a range of critical currents appear to indicate changes in effective area, but these changes could be related to microstructural differences as they are measured on different films. As yet there is no published data on the capacitance of a single grain boundary that has been oxygen depleted — such an experiment might help to clear up the question of effective area.

## 2.6 Summary

In this chapter a survey of the $YBa_2Cu_3O_{7-\delta}$ grain boundary literature has been performed. Initially the properties of bulk $YBa_2Cu_3O_{7-\delta}$ relevant to grain boundaries were discussed. The relationship between the structure and the electronic properties as well as the high $T_c$ phase diagram were highlighted. The properties of the superconducting condensate were also briefly discussed and in particular the $d_{x^2-y^2}$ order parameter was highlighted.

The properties of the grain boundaries themselves were then discussed in some detail, focusing particularly on high angle boundaries. The grain boundary microstructure is complex on a number of length scales, with microscale meandering and nanoscale facetting contributing to the rich variety of structural features. On atomic scales high angle boundaries consist of structural units, which also make up the dislocation cores in low angle boundaries. The grain boundary structure is remarkably small and Z-contrast images show that the lattice appears undistorted just a few atomic spacings away from the grain boundary line.

The literature on electrical measurements of grain boundaries was then reviewed. The situation is complex and no coherent picture emerges from the experiments reported to date. The current voltage characteristics highlight the Josephson coupling across high angle boundaries and these boundaries appear to conform well to the RCSJ model at low voltage bias. At higher biases non-linear current voltage characteristics are observed. The critical current is found to decrease approximately linearly as the sample is warmed towards $T_c$ from low temperatures. The normal state properties are typically temperature independent below the critical temperature. The magnetic field dependence of the critical current points to inhomogeneous grain boundaries and in some cases anomalous Fraunhofer patterns are caused by the interaction of the facetted microstructure with the $d_{x^2-y^2}$ order parameter. The strong relationship between grain boundary orientation and the current through the boundary appears indicative of tunneling behaviour. The observation of Fiske resonances in the boundary indicates that the boundary layer is insulating, further supporting a tunneling model. The relationships between the different junction properties are complex and are best assessed in the context of single grain boundaries which are treated to modify their oxygen content. Experiments on 24° symmetric [001] tilt boundaries indicate that the deoxygenated grain boundaries obey the scaling law $I_c R_n \approx J_c^{1/2}$. Similar scaling of the critical voltage is implied by the noise data, although the range of critical currents over which this observation is valid is uncertain. In the noise experiments the grain boundary barrier is modified by charge trapping in the boundary region implying a link between the charge

on the boundary (which changes in noise experiments) and the local doping (which is altered in experiments where the boundaries are deoxygenated). Well oxygenated (higher critical current) boundaries obey the scaling law $I_c R_n \approx$ constant [66]. The Calcium doping experiments can be interpreted in a number of ways — but may indicate that the charge and the local carrier density determine the properties of the barrier, by a band bending mechanism. Many of the experiments are difficult to interpret and compare because of the irreproducibility of the properties of the grain boundaries. In order to make further experimental progress a focus on fabricating more controlled grain boundary structures may be necessary. Alternatively focusing a number of experiments on a single, well characterised, grain boundary, may help clarify some of the issues. In addition the controlled alteration of single grain boundaries may be a better way to understand the scatter in the data in the literature than the fabrication of large numbers of different boundaries with varying microstructures.

The present theoretical understanding of grain boundaries was also discussed. The interaction of the $d_{x^2-y^2}$ order parameter symmetry with the grain boundary microstructure was mentioned since such effects are well established. They cannot however account for all the transport properties and in particular the strong suppression of the critical current and normal resistance with the misorientation angle is not explained. The competing theories for the nature of the current transfer across the grain boundary were then highlighted. Three possibilities were discussed: resonant and direct tunneling through an insulator with a 1 eV gap, direct tunneling through a 0.1 eV barrier induced by band bending and current transfer through pinholes in the insulating seam at the boundary. The issues surrounding what occurs when the grain boundary is oxygen depleted were also highlighted. The lack of a consensus as to the mechanism that controls the grain boundary properties is indicative that, despite all the work carried out to date, a full understanding of these complex defects is yet to emerge.

# Bibliography


[1] H. Hilgenkamp and J. Mannhart, Reviews of Modern Physics **74**, 485 (2002).

[2] M. K. Wu et al., Physical Review Letters **58**, 908 (1987).

[3] R. J. Cava et al., Physical Review Letters **58**, 1676 (1987).

[4] J. G. Bednorz and K. A. Müller, Zeitschrift für Physik B **54**, 189 (1986).

[5] J. D. Jorgensen et al., Physical Review B **41**, 1863 (1990).

[6] Y. Tokura, J. B. Torrance, T. C. Huang, and A. I. Nazzal, Physical Review B **38**, 7156 (1988).

[7] J. L. Tallon et al., Physical Review B **53**, 11972 (1996).

[8] J. Nam, R. A. Hughes, A. Dabkowski, and J. S. Preston, Applied Physics Letters **82**, 3728 (2003).

[9] J. Tallon and J. Loram, Physica C **349**, 53 (2001).

[10] T. Timusk and B. Statt, Reports on Progress in Physics **62**, 61 (1999).

[11] A. Damascelli, Z. Hussain, and Z. Shen, Reviews of Modern Physics **75**, 473 (2003).

[12] N. E. Hussey, M. Abdel-Jawad, A. Carrington, A. P. Mackenzie, and L. Balicas, Nature **425**, 815 (2003).

[13] R. E. C. W. E. Pickett and H. Krakauer, Physical Review B **42**, 8764 (1990).

[14] C. E. Gough et al., Nature **326**, 855 (1987).

[15] J. R. Waldram, *Superconductivity of Metals and Cuprates*, Institute of Physics Publishing, Bristol, 1996.

[16] G. Blatter, M. V. Feigel'man, V. B. Geshkenbein, A. I. Larkin, and V. M. Vinokur, Reviews of Modern Physics **66**, 1125 (1994).

[17] M. J. Hogg, *The Electronic Properties of Thin Film $YBa_2Cu_3O_{7-\delta}$ Low Angle Grain Boundaries*, PhD thesis, Cambridge University, Cambridge, UK, 2002.

[18] J. H. Durrell et al., Physical Review Letters **90**, 247006 (2003).

[19] C. C. Tsuei and J. R. Kirtley, Reviews of Modern Physics **72**, 969 (2000).

[20] D. Dimos, P. Chaudhari, J. Mannhart, and F. K. Legoues, Physical Review Letters **61**, 219 (1988).

[21] R. Wördenweber, Superconductor Science and Technology **12**, R86 (1999).

[22] B. Dam and B. Stäuble-Pümpin, Journal of Materials Science: Materials in Electronics **9**, 217 (1998).

[23] J. H. Durrell, *Critical Current Anisotropy in High Temperature Superconductors*, PhD thesis, Cambridge University, Cambridge, UK, 2001.

[24] D. J. Miller et al., Applied Physics Letters **66**, 2561 (1995).

[25] J. L. Alarco et al., Physica C **247**, 263 (1993).

[26] J. Ayache, A. Thorel, J. Lesueur, and U. Dahmen, Journal of Applied Physics **84**, 4921 (1998).

[27] C. Tæholt, J. G. Wen, H. W. Zandebergen, Y. Shen, and J. W. M. Hilgenkamp, Physica C **230**, 425 (1994).

[28] X. F. Zhang, D. J. Milkler, and J. Talvacchio, Applied Physics Letters **11**, 2440 (1996).

[29] Q. Jin and S.-W. Chan, Journal of Materials Research **17**, 323 (2002).

[30] S.-W. Chan, Q. Jin, J. W. H. Tsai, S. C. Tidrow, and Q. Jiang, IEEE Transactions on Applied Superconductivity **13**, 2829 (2003).

[31] N. D. Browning, J. P. Burban, C. Prouteau, G. Duscher, and S. J. Pennycook, Micron **30**, 425 (1999).

[32] S. E. Babcock and J. L. Vargas, Annual Review of Materials Science **25**, 193 (1995).

[33] J. G. Wen, T. Takagi, and N. Koshizuka, Superconductor Science and Technology **13**, 820 (2000).

[34] U. Poppe et al., IEEE Transactions on Applied Superconductivity **11**, 3768 (2001).

[35] Y. Y. Divin, U. Poppe, J. L. Jia, P. M. Shadrin, and K. Urban, Physica C **372-376**, 115 (2002).

[36] L. Asalamazov and A. I. Larkin, Soviet Physics JETP **9**, 87 (1969).

[37] K. K. Likharev, Reviews of Modern Physics **51**, 101 (1979).

[38] R. D. Redwing et al., Applied Physics Letters **75**, 3171 (1999).

[39] M. F. Chisholm and S. J. Pennycook, Nature **351**, 47 (1991).

[40] A. Gurevich and E. A. Pashitskii, Physical Review B **57**, 13878 (1998).

[41] D. T. nad R. P. J. Ijsselstein and H. Rogalla, Applied Physics Letters **66**, 2286 (1995).

[42] O. M. Froehlich, P. Richter, A. Beck, R. Gross, and G. Koren, Journal of Low Temperature Physics **106**, 243 (1997).

[43] C. W. Schneider et al., cond-mat/0307470, 2003.

[44] K. A. Delin and A. W. Kliensasser, Superconductor Science and Technology **9**, 227 (1996).

[45] R. Gross, P. Chaudhari, M. Kawasaki, and A. Gupta, Physical Review B **42**, 10736 (1990).

[46] P. A. Rosentahl, M. R. Beasley, K. Char, M. S. Colclough, and G. Zaharchuk, Applied Physics Letters **59**, 3482 (1991).

[47] R. G. Humphreys and J. A. Edwards, Physica C **210**, 42 (1993).

[48] O. Nesher and E. N. Ribak, Applied Physics Letters **71**, 1249 (1997).

[49] M. Carmody, B. H. Moeckly, K. L. Merkle, and L. D. Marks, Journal of Applied Physics **87**, 2454 (2000).

[50] J. Mannhart et al., Physical Review Letters **77**, 2782 (1996).

[51] Y. F. Eltsev et al., IEEE Transactions on Applied Superconductivity **11**, 3784 (2001).

[52] Y. F. Eltsev et al., Physica C **357-360**, 1572 (2001).

[53] H. Hilgenkamp and J. Mannhart, Applied Physics Letters **73**, 265 (1998).

[54] Z. G. Ivanov et al., Physical Review B **57**, 602 (1998).

[55] D. Winkler, Y. M. Zhang, P. A. Nilsson, E. A. Sperantsov, and T. Claeson, Physical Review Letters **72**, 1260 (1994).

[56] A. Beck et al., IEEE Transactions on Applied Superconductivity **5**, 2192 (1995).

[57] Y. M. Zhang, D. Winkler, G. Brorsson, and T. Claeson, IEEE Transactions on Applied Superconductivity **5**, 2200 (1995).

[58] K. Nakajima, K. Yokota, H. Myoren, J. Chen, and T. Yamashita, IEEE Transactions on Applied Superconductivity **5**, 2861 (1995).

[59] E. J. Tarte et al., IEEE Transactions on Applied Superconductivity **11**, 3662 (1997).

[60] M. G. Medici et al., Journal of Superconductivity **11**, 225 (1998).

[61] P. F. McBrien et al., Physica C **339**, 88 (2000).

[62] E. J. Tarte et al., Physica B **284-288**, 628 (2000).

[63] E. J. Tarte et al., IEEE Transactions on Applied Superconductivity **11**, 418 (2001).

[64] J. Halbritter, IEEE Transactions on Applied Superconductivity **13**, 1158 (2002).

[65] P. F. McBrien, *Novel applications of the Josephson effect: Ferroelectric characterisation and capacitively shunted grain boundary junctions*, PhD thesis, Cambridge University, Cambridge, UK, 2000.

[66] J. P. Sydow, M. Berninger, R. A. Buhrman, and B. H. Moeckly, Superconductor Science and Technology **12**, 723 (1999).

[67] R. Gross et al., IEEE Transactions on Applied Superconductivity **7**, 2929 (1997).

[68] A. Y. Tzalenchuk et al., Physical Review B **68**, 100501 (2003).

[69] L. Hao, J. C. Macfarlane, and C. M. Pegrum, Superconductor Science and Technology **9**, 678 (1996).

[70] K. K. Likharev, *Dynamics of Josephson Junctions and Circuits*, Gordon and Breach Publishers, Amsterdam, 1986.

[71] M. Kawasaki, P. Chaudhari, and A. Gupta, Physical Review Letters **68**, 1065 (1992).

[72] A. Marx, U. Fath, L. Alff, and R. Gross, Applied Physics Letters **67**, 1929 (1995).

[73] S. G. Hammond et al., IEEE Transactions on Applied Superconductivity **3**, 2319 (2003).

[74] F. Herbstritt, T. Kemen, L. Alff, A. Marx, and R. Gross, Applied Physics Letters **78**, 955 (2001).

[75] A. Schmehl et al., Europhysics Letters **47**, 110 (1999).

[76] C. W. Schneider et al., Applied Physics Letters **75**, 850 (1999).

[77] G. Hammerl et al., Nature **407**, 162 (2000).

[78] G. A. Daniels, A. Guerevich, and D. C. Larbalestier, Applied Physics Letters **77**, 3251 (2000).

[79] K. Guth, H. U. Krebs, H. C. Freyhardt, and C. Jooss, Physical Review B **64**, 140508(R) (2001).

[80] J. T. Kucera and J. C. Bravman, Physical Review B **51**, 8582 (1995).

[81] J. P. Buban, *Symposium S — MRS Fall 2002*, December 2002.

[82] J. Mannhart et al., Philosophical Magazine B **80**, 827 (2000).

[83] O. M. Froehlich, P. Richter, A. Beck, D. Koelle, and R. Gross, IEEE Transactions on Applied Superconductivity **7**, 3189 (1997).

[84] Y. S. Barash, H. Burkhardt, and D. Rainer, IEEE Transactions on Applied Superconductivity **77**, 4070 (1996).

[85] M. Sigrist and T. M. Rice, Reviews of Modern Physics **67**, 503 (1995).

[86] H. Hilgenkamp, J. Mannhart, and B. Mayer, Physical Review B **53**, 14586 (1996).

[87] R. Gross, *Interfaces in Superconducting Systems*, chapter Grain-Boundary Josephson Junctions in the High-Temperature Superconductors, pages 176–209, Springer, New York, 1994.

[88] L. I. Glazman and K. A. Matveev, Soviet Physics JETP **67**, 1276 (1988).

[89] R. Dömel, C. Horstmann, M. Siegel, A. I. Braginski, and M. Y. Kupriyanov, Applied Physics Letters **67**, 1775 (1995).

[90] M. A. J. Verhoeven, G. J. Gerritsma, H. Rogalla, and A. A. Golubov, Applied Physics Letters **69**, 848 (1996).

[91] J.-K. Heinsohn et al., Journal of Applied Physics **89**, 3852 (2001).

[92] J. Mannhart and H. Hilgenkamp, Materials Science and Engineering B **56**, 77 (1998).

[93] W. E. Taylor, N. H. Odell, and H. Y. Fan, Physical Review **88**, 867 (1952).

[94] H. F. Mataré, Journal of Applied Physics **56**, 2605 (1984).

[95] C. R. M. Grovenor, Journal of Physics C **18**, 4079 (1985).

[96] V. R. Ravikumar, R. P. Rodrigues, and V. P. Dravid, Physical Review Letters **75**, 4063 (1995).

[97] For example at MRS Fall 2002, R. F. Klie (talk Z1.1) and Y. Zhu (talk Z1.8) presented conflicting transmission electron microscopy results on the sign of the band bending in $YBa_2Cu_3O_{7-\delta}$.

[98] K. Nakajima, K. Yokota, J. Chen, H. Myoren, and T. Yamashita, Japanese Journal of Applied Physics **33**, L934 (1994).

[99] K. Petersen et al., Applied Physics Letters **67**, 1477 (1995).

[100] B. Mayer, J. Mannhart, and H. Hilgenkamp, Applied Physics Letters **68**, 3031 (1996).

[101] Z. G. Ivanov, E. A. Stepantsov, A. Y. Tzalenchuk, R. I. Shekhter, and T. Claeson, IEEE Transactions on Applied Superconductivity **3**, 2925 (1993).

[102] A. Sarnelli and G. Testa, Physica C **371**, 10 (2002).

[103] P. W. Anderson and A. H. Dayem, Physical Review Letters **13**, 195 (1964).

[104] A. H. Dayem and J. J. Wiegand, Physival Review **155**, 419 (1966).

[105] B. Moeckly, D. K. Lathrop, and R. A. Buhrman, Physical Review B **47**, 400 (1993).

# Chapter 3

# Experimental Methods

This chapter details the experimental techniques used to fabricate, characterise and measure the devices that were investigated during this work. Fabrication involved the deposition of thin films by pulsed laser deposition and the subsequent patterning of devices by photolithography and Argon ion milling. Characterisation consisted of atomic force microscopy, transmission electron microscopy and electrical measurements using a standard dip probe.

## 3.1 Pulsed Laser Deposition

Pulsed laser deposition is widely used for the deposition of high temperature superconducting thin films. The basic principle is that a target is ablated by an focused laser beam (typically an excimer laser with $\lambda = 308$ or 248 nm with an energy density of between 1 and 3 $\mathrm{J\,cm^2}$ per shot and a frequency of several Hz). Because of the short wavelength of the laser, the photons of the beam are immediately converted into electronic excitations which subsequently transfer their energy to the lattice via electron-phonon interactions. This leads to a sudden increase of the local temperature and, for a high enough power density ($> 10^7$-$10^8$ $\mathrm{Wcm^{-2}}$), an explosive removal of material. Two length scales are particularly important for the ablation process, the thermal diffusion length and the optical absorbtion depth. The larger of these determines the length scale of heating in the surface of the target (for high $T_c$ superconductors the thermal diffusion length is usually largest). Provided that the energy per pulse exceeds the latent heat of vaporisation for the heated volume of material, the material is vaporised congruently and stoichiometry is maintained. For lower pulse energies the target surface is melted and vaporised in a similar manner to conventional thermal evaporation and multi-element targets are not ablated stoichiometrically. There

is therefore a threshold power density for stoichiometric ablation, which is 1 $\mathrm{J\,cm^{-2}}$ for $YBa_2Cu_3O_{7-\delta}$[1].

For practical ablation yields the ablated particulates cannot escape the surface collisionlessly. There is therefore a layer in contact with the target in which reflections and collisions occur. This layer is referred to as the Knudsen layer. As a result of the Knudsen layer there is a significant transfer of energy from the ablated material back to the target surface. The energy transfer is both thermal and mechanical and results in the formation of a thin liquid layer on the target surface. Interaction of this liquid with the laser and/or Knudsen layer can produce ejected molten droplets of liquid. In addition, the ejection of larger, solid particulates can also occur, due to roughening of the target surface by repeated melt-freeze cycles of the irradiated material or due to defects in the target making it vulnerable to fracture. It is therefore important to use a smooth and dense target. The occurrence of particulates and droplets in the ablation plume is intrinsic to the deposition process and it can be very hard to eliminate them from thin films. Both droplets and particulates can be observed in $YBa_2Cu_3O_{7-\delta}$ films grown by pulsed laser deposition [2]. Particulates are common in the films grown in this study and a major part of the optimisation of the growth process was to minimise the particulate density on the films.

In the system used to grow the films used in this study the films are grown in an oxygen atmosphere. As the ablated plume moves towards the substrate reactive and non-reactive collisions take place within the plume itself, at the contact between the plume and the ambient atmosphere (the collision front) and near the substrate surface. The background pressure affects both the geometry of the plume and oxygen content of the film and is therefore a critical deposition parameter. The growth rate is also strongly dependent on the background pressure.

Species impinging onto the substrate from the plume require a certain amount of time for surface diffusion and incorporation into proper lattice sites. The diffusion and growth mechanisms of the films on the substrate surface are particularly important for the formation of the grain boundary microstructure and were discussed in more detail in section 2.2. The deposition rate and the energy of the impinging species both contribute to the film growth process. These are in turn determined by the background pressure, the target-substrate distance and the laser repetition rate. The optimum distance between the target and the substrate at a given pressure is often found to be close to the tip of the visible plasma plume, which provides a useful starting point when optimising the pressure for a given target substrate distance. The substrate temperature determines the diffusion rate on the substrate and is therefore also critical to the deposition process.

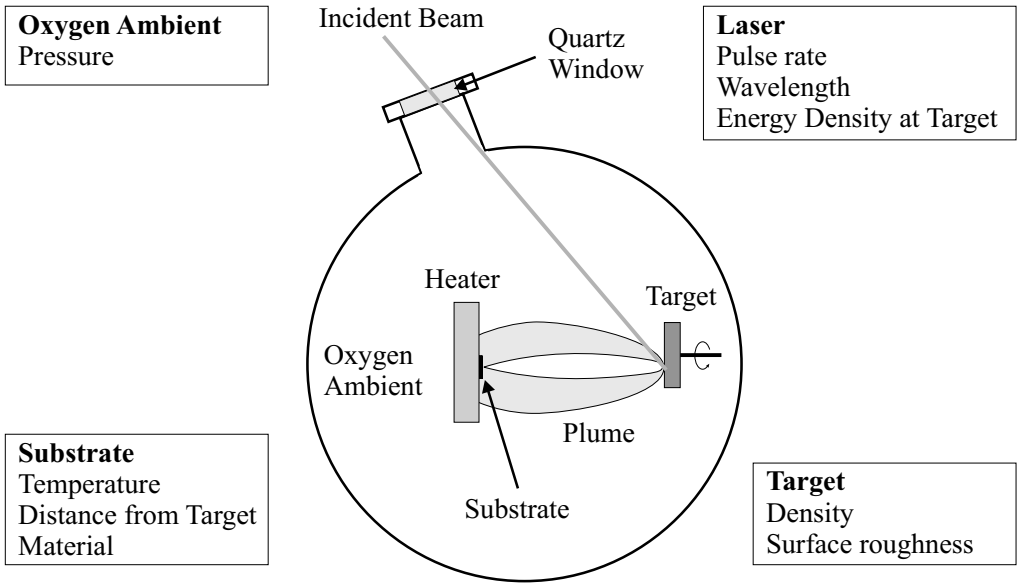


Figure 3.1: A schematic pulsed laser deposition system, shown together with the most critical process parameters.

A schematic pulsed laser deposition system, together with the key process parameters for deposition is shown in Fig. 3.1. Detailed reviews of the PLD process can be found in references [3, 4, 5, 6]. The system used in Cambridge is similar to the system depicted here. In the following sections the detailed deposition procedure that was developed during the course of this work is described. This procedure was used for the growth of the Cambridge films. The deposition procedures for films produced at the University of Augsburg and at LG Electronics are described in references [7] and [8] respectively.

### 3.1.1 Substrates and Substrate Preparation

The substrates used in this study are manufactured by Shinkosha Ltd, Pi-Kem Ltd and Crystal GmbH. In this work all the single crystal films used were grown on polished (100) surfaces of $SrTiO_3$. Artificial grain boundaries were grown on [001] tilt bicrystal substrates.

Before the films were deposited the substrates were cleaned ultrasonically in acetone. The polished surface of the substrate was then placed face down on an Anticon gold sealed cleanroom wipe, which had been saturated with isopropanol. The surface of the substrate was rubbed on the wipe for 1-3 minutes, taking care to ensure that the isopropanol did not dry out. The sample was then returned to the acetone, and cleaned ultrasonically for a further 10

minutes, followed by 10 minutes of ultrasonic cleaning in isopropanol. The substrate was then dried with an air gun. Careful cleaning of the substrate in this manner was found to be an important part of a reproducible growth process.

### 3.1.2 Pulsed Laser Deposition Process

The on axis pulsed laser deposition system used for the growth of the Cambridge films in this study is similar in design to the schematic system shown in Fig. 3.1. The laser used was a Lambda Physik Compex 201 KrF eximer laser (wavelength 248 nm). The laser beam is guided into the chamber with a series of mirrors and just before it enters the vacuum system it passes through a rectangular aperture (24 mm by 10 mm) and a lens. The lens focuses the beam so that the beam cross sectional area is typically reduced to approximately 4 $mm^2$ at the target surface. The vacuum system in which the deposition occurs has a base pressure of less than $10^{-6}$ mBar. Within the vacuum system, the target is mounted in a carousel that allows it to be moved behind a water cooled shield while the substrate is heated to the deposition temperature and during the post deposition anneal. The target itself is rotated during deposition. Next to the carousel is a shutter that can be placed between the target and the substrate to prevent deposition during pre-ablation. The heater is mounted opposite the target and its position can be varied so as to alter the target – substrate distance. The heater consists of two Whatlow Firerod FRE1J42A cartridge heaters mounted in an oxidation resistent stainless steel block. The heater temperature is monitored by means of a commercial thermocouple embedded in the block. The reading of the thermocouple will be significantly greater than the surface temperature of the substrate but as long as the temperature is maintained at a consistent value this makes little difference from the point of view of optimising the deposition process.

For the films used in this thesis Praxair, sintered, $YBa_2Cu_3O_{7-\delta}$ targets were used with a density of greater than 5.95 $g\,cm^{-3}$. These targets were glued with silver paint to a target holder which fitted into the target carousel. Before each deposition run the target carousel was removed from the system and the target holder was removed from the carousel. The target was re-polished using metallography paper (the final stages of polishing used grit 1000 paper). Care was taken to ensure that the target was flat and that the pressure on it was even during polishing — to ensure the surface of the target is perpendicular to the laser beam when it is mounted in the system. Excess dust was removed with an air gun. The surface of the water cooled shield of the carousel was also cleaned, with dilute phosphoric acid solution, to remove

$YBa_2Cu_3O_{7-\delta}$ deposits from the previous run. The target was replaced in the carousel and carefully aligned with the edge of the carousel, so that the target substrate distance was fixed from run to run.

After re-mounting the target the carousel was then replaced in the vacuum system and the target was moved into the correct position for deposition. The beam profile was measured outside the chamber by placing a piece of fax paper in front of the focusing lens and firing the laser, to ensure that the laser beam was aligned properly with the aperture. The energy of the beam was then measured both outside and inside the chamber (using a Fieldmaster energy meter) and noted for comparison with previous runs — it was therefore possible to track the transmissivity of the lens as a function of time, and to determine when the lens needed cleaning. A small piece of fax paper was then pressed up against the target's face and the laser was fired once more. The spot size was measured at the target and this area was used to determine the energy density of the laser at the surface of the target. Typically the energy density at the target was 2 $Jcm^{-2}$.

After the substrate had been cleaned, silver paint (Acheson Electrodag 1415M) was applied to its reverse side using a fine paintbrush. The substrate was then gently placed onto the heater. Gentle pressure was applied to the corners of the substrate to ensure only a thin layer of paint remained between the substrate and the heater. At this stage it was critical to ensure no air bubbles formed under the substrate. A small piece of lens tissue was then placed on the polished surface of the substrate and on top of this a small weight was placed – to keep the substrate in good contact with the heater. The heater was then warmed to 90°C to dry the glue.

After approximately 30 minutes the weight and lens tissue were removed and the heater was remounted in the vacuum system. The chamber was pumped down to a pressure of less than $10^{-6}$ mBar. At this point a constant flow of oxygen (regulated by an MKS mass flow controller) was switched on. The oxygen pressure was controlled by regulating the mass flow controller and by the continued operation of the backing pump on the system. Typically the pressure was maintained at 0.25 mBar throughout the deposition process (measured by means of a Leybold CM1 capacitance manometer gauge). The flow of water to the cooled shield in the target carousel was switched on and the target was moved behind the shield. The heater was then switched on and set to ramp the temperature up to the deposition temperature (for a typical deposition this was 765°C) at 30°C/min.

Once the heater had reached temperature the target was moved into place and the pre-ablation shutter was moved between the target and the substrate. The motor to rotate the target was switched on. The laser was fired 500 times to pre-ablate the target. The shutter was removed and once the temperature

had re-stabilised, the deposition was started. In a typical run the laser was fired 8000 times which produced approximately 100 nm thick $YBa_2Cu_3O_{7-\delta}$ films.

When the deposition was finished the target rotation was turned off and the target was moved behind the water cooled shield. The chamber was then filled with close to 1 atmosphere of oxygen for the post deposition anneal. The film was then cooled to 540°C at 15°C/min and then from 540°C to 450°C at 4°C/min. The substrate was held at a temperature of 450°C for 20 minutes and then cooled to 430°C at 4°C/min. After a period of 30 minutes the heater was switched off, to facilitate rapid cooling to room temperature. Once the heater had cooled to close to room temperature, the system was opened up to air and the heater was removed. Finally, the substrate was detached from the heater using a razor blade.

## 3.2 Film Characterisation

The as grown films were primarily characterised by transport measurements. However, because the film microstructure plays a significant role in determining the properties of the devices, the surface properties of the films were carefully studied by atomic force microscopy. For bicrystal samples the grain boundary microstructure was characterised at the surface of the film with this technique, which enabled an assessment of the grain boundary meander. Atomic force microscopy was also used to characterise devices fabricated from the films. In addition a transmission electron microscopy cross section was fabricated from a grain boundary sample grown in Cambridge and imaged at the Dutch National Centre for High Resolution Electron Microscopy. This enabled the microstructure of the boundary to be characterised throughout the thickness of the film.

### 3.2.1 Atomic Force Microscopy

Atomic force microscopy (AFM) measurements were performed on all the bicrystal films measured in this study, in order to assess the quality of the films and to characterise the meandering path of the grain boundary at the film surface. A Digital Instruments Nanoscope III was used in tapping mode for the purposes of this characterisation (for full technical details of the AFM see reference [9]).

The basic operating principles of the tapping mode AFM are illustrated in Fig. 3.2. The sample is mounted beneath the cantilever and is moved with respect to it by means of piezoelectric crystals in the scanner. The cantilever

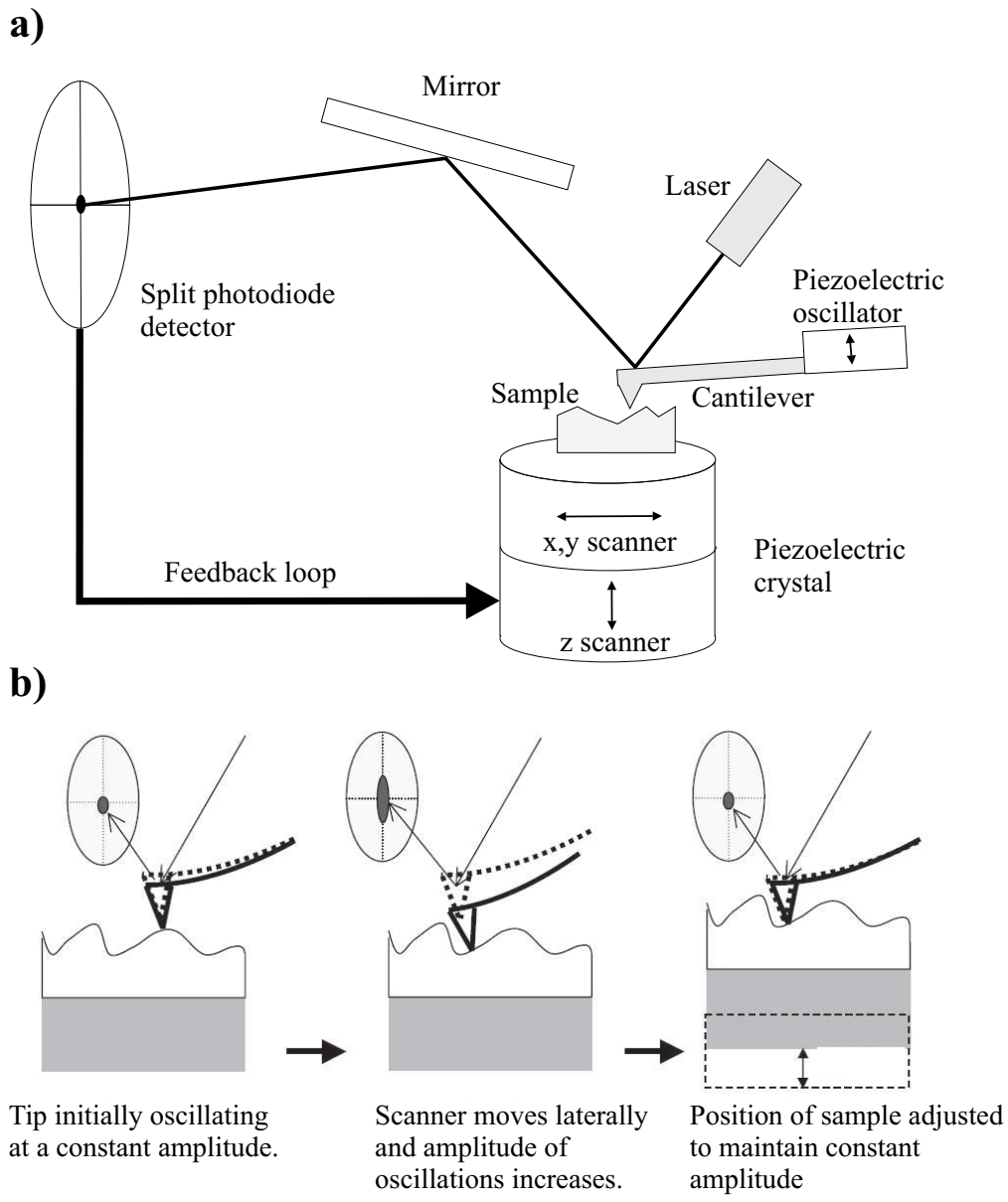


Figure 3.2: Schematic showing the basic principles of tapping mode atomic force microscopy. a) Basic features of a typical scanning probe microscope. b) Schematic showing the basic principle of tapping mode operation.

is oscillated at its resonant frequency by a separate piezoelectric crystal. A laser is reflected off the tip of the cantilever and the intensity of the reflected beam is detected by a split photomultiplier. As the cantilever oscillates the differential signal at the photomultiplier also oscillates. A feedback loop adjusts the position of the sample so that the amplitude of the signal is maintained at a constant value. The value of the $z$ signal (calibrated to give an accurate height) is recorded as the tip is rastered across the sample in the $x$–$y$ plane to produce an image of the sample topography. The velocity of the tip across the surface is determined by the scan rate (the frequency associated with a raster forwards and backwards of the tip) and the image dimensions. The lateral resolution of the instrument and the quality of the images obtained is dependent on the details of the feedback parameters, the tip velocity, and the type of tip used, as well as on the imaging environment (images in this study were all obtained in air). The AFM used for this work was well calibrated in the z-direction — a maximum error of $\pm 2$ nm was observed imaging 180 nm deep pits on a calibration sample. The AFM tips used were Nanoworld NCH standard tips, with typical tip radius of curvature less than 10 nm.

A typical AFM image of one of the samples used in this study is shown in Fig. 3.3 (this was a single crystal film, grown at LG Electronics and subsequently fabricated into bridge structures for the investigation described in section 5.3). The growth islands are clearly visible and a large particulate is also visible in the lower part of the image. Within the individual growth islands, steps of approximately unit cell dimension are visible. In addition to characterising the film surface and the grain boundary topography, AFM is a useful tool for studying devices and was also used for measuring the thicknesses of the thin films, as described below.

### 3.2.2 Transmission Electron Microscopy

The samples used in the transmission electron microscopy investigation of the grain boundary were prepared and imaged at the Dutch National Centre for High Resolution Electron Microscopy (Delft, the Netherlands) in the laboratory of Henny Zandbergen. The sample preparation was performed by Sorin Lazar and the images were produced by Sibe Mennema. Only the important technical details of the sample preparation and imaging are given here.

The samples were prepared with a FEI Company dual beam SEM/FIB nanofabrication facility. Lamellae are cut perpendicular to the grain boundary plane and to the film surface using SEM/FIB and are thinned to approximately 100 nm. The microscope used to produce the images is a Philips

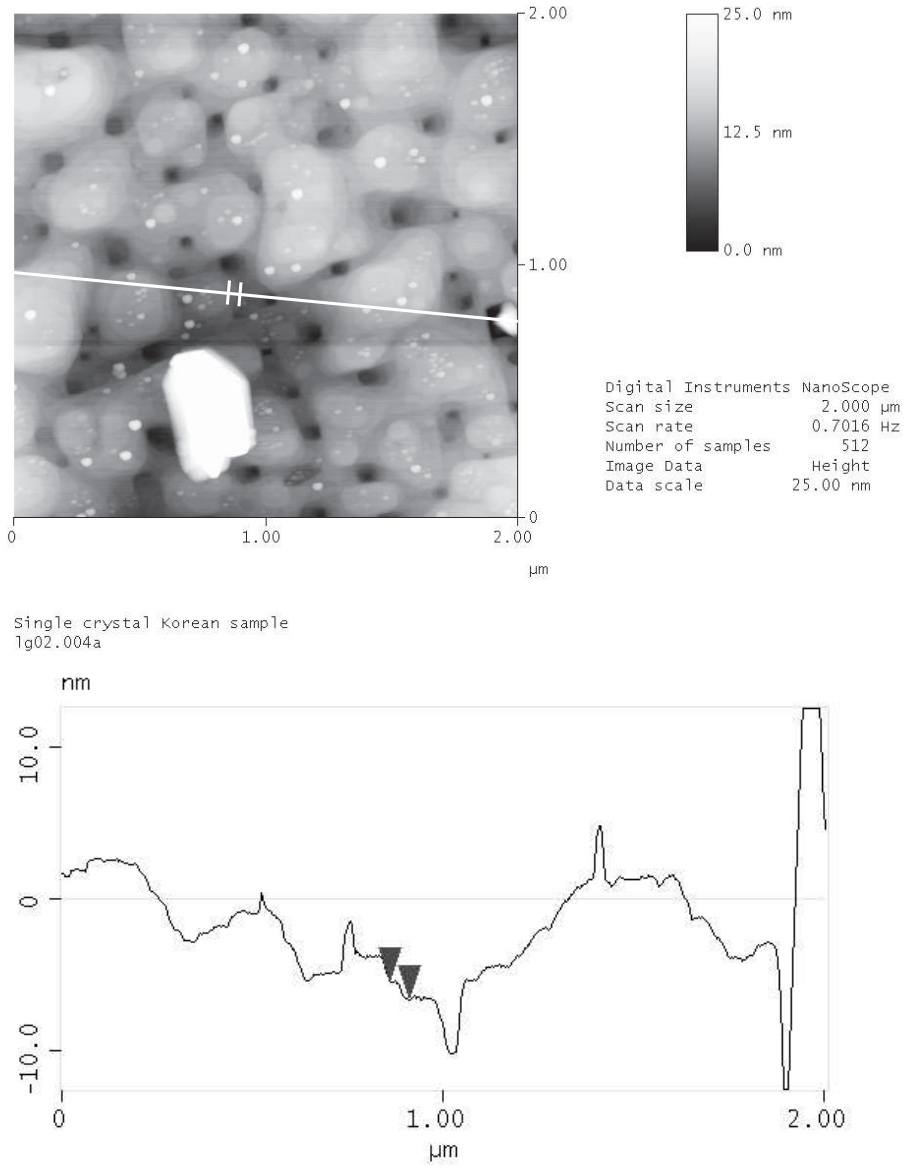


Figure 3.3: AFM image of a c-axis orientated single crystal film grown at LG electronics. The growth islands are clearly visible and growth steps, with dimensions of approximately unit cell size, are visible. A cross section (marked by a white line across the image) is also shown. The two arrows (marked by perpendicular lines on the image) are separated in the z-direction by 1.1 nm, which is approximately equal to the c-axis unit cell dimension.

CM30T Transmission Electron Microscope with a thermionic electron gun. The cathode material was $LaB_6$ and the acceleration voltage was 300 kV. The microscope has a point to point resolution of 0.23 nm.

## 3.3 Device Fabrication

In this section the various stages of device fabrication are described in detail. Note that for some films not all the stages were necessary — for example, for single crystal samples it was not necessary to perform an HF etch to reveal the bicrystal line.

### 3.3.1 Preparation of Films Before Patterning

In the case of the high resistance Wheatstone bridge devices particular care needed to be taken to avoid shorts during measurement. Therefore, before these devices were patterned the silver paint that was used to attach the substrate to the heater was removed. Firstly the film was covered with a layer of photoresist (Clariant AZ1529, spun for 30 s at 6000 rpm and baked for 1 minute at 100°C). This layer of resist was used as a protective layer to prevent damage to the sample. To remove the silver paint, the sample was carefully rubbed on a piece of metallography paper with the substrate side down. The edges of the film were also carefully cleaned, using a piece of metallography paper wrapped around a pair of tweezers. Provided sufficient care was taken the film was not damaged by this process since it was protected by the photoresist. The protective layer of resist was removed by ultrasounding (for 2 minutes) and airbrushing with acetone and rinsing in isopropanol. The sample is dried with filtered compressed air from an air gun. This procedure for removing the resist was used throughout the fabrication process.

For films grown at LG Electronics 10 mm by 10 mm substrates were used and these films were diced into two parts before processing. After removal of the silver paint, a new protective layer of resist was produced as described above and the films are mounted on a glass block with wax which is in turn mounted in a diamond dicing saw. The saw was then carefully aligned with the center of the film and the film was cut into two. The resist was then removed as described above.

### 3.3.2 HF Etch

The artificial grain boundary of a bicrystal substrate is not easily visible, except under strong backlighting or when viewed at an oblique angle. It

was therefore necessary to etch the substrate so that the grain boundary can be clearly viewed and aligned with the mask that was used to pattern the devices. In an HF etch the grain boundary is preferentially etched and becomes clearly visible.

Before etching the substrate part of the $YBa_2Cu_3O_{7-\delta}$ film was removed. A small region of the film was removed where the bicrystal line meets the edge of the film. This was done by first patterning the film with a mask that exposes this region and then removing the exposed $YBa_2Cu_3O_{7-\delta}$ with a wet etch. Clariant AZ1529 resist was spun onto the film and baked as described in the previous section. A mask with two notches at the edge of the film was then projected onto the film surface for 3 minutes, using a Cannon PPC 210 projection print camera fitted with a UV light source. The regions of the resist exposed to the light undergo a photochemical reaction and become soluble in a developer solution. A mixture of 4 parts of Clariant AZ photoresist developer to 1 part water (by volume) was used to develop the resist. The film was left in the developer solution until the exposed resist had been removed (this was determined by eye). The sample was rinsed in distilled water and blown dry with a compressed air gun. The same procedure for patterning with the Cannon projection camera was used for fabricating most large features. Having removed two notches from the resist the film was then placed in a solution of 2.5% Phosphoric acid, which chemically etches the $YBa_2Cu_3O_{7-\delta}$ in these regions, revealing the underlying substrate.

After the $YBa_2Cu_3O_{7-\delta}$ etch the photoresist was not removed from the film and it was taken directly to the department's dedicated HF etch facility. It was then etched for 30 s in 7% HF solution and rinsed in two stages by distilled water, to remove any acid residues. The photoresist was removed as described above. The film was then ready for the patterning of devices.

### 3.3.3 Patterning of Devices

For the fabrication of devices a thinner layer of resist was used to achieve sharper small features. Clariant AZ5214 resist was applied as described previously and spun onto the film at 6000 rpm for 30 s. Particular care needed to be taken to ensure a smooth resist layer and it was often necessary to spin the resist on several times before baking. During the spinning of a resist a thicker layer of resist forms at the edge of the sample — the so called 'edge bead'. For the contact lithography process used to fabricate devices this needed to be removed before processing.

The edge bead was usually removed using the Cannon projection camera, as described above. A rectangular mask with truncated corners was used as the edge bead is typically largest at the corners of the film. The next stage

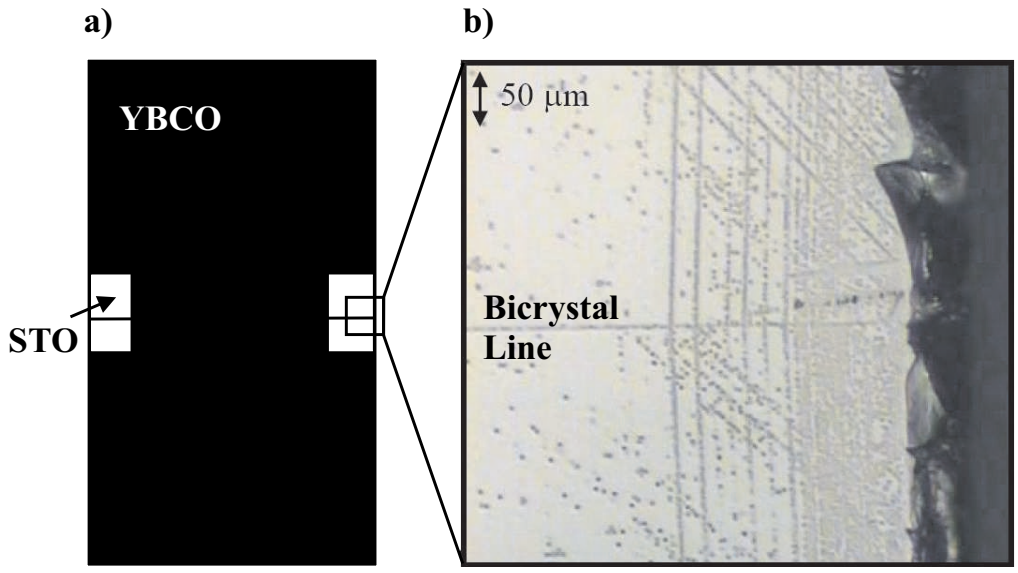


Figure 3.4: The effect of an HF Etch on a bicrystal. a) Schematic of the bicrystal after the $YBa_2Cu_3O_{7-\delta}$ has been removed in the grain boundary vicinity and the substrate has been etched with HF. b) Optical micrograph (from [10]) of an etched grain boundary.

of patterning was performed in a Karl Suss MJB3 mask aligner. The film was mounted in the mask aligner and brought into direct contact with the mask. The mask aligner was used in a soft contact configuration, and good contact between the sample and the mask was achieved by applying pressure by raising the chuck beneath the film. The device mask usually contains alignment marks that were lined up with the bicrystal line of grain boundary samples. For the bridge devices used in Chapters 5 and 6 the alignment was critical and the procedure could often take several hours. Once the sample was aligned with the mask and in good contact the resist was exposed, typically for 4 s (note that exposure times needed to be lengthened a little as the lamp in the mask aligner aged). The film was removed from the mask aligner and the resist was developed in a mixture of 2 parts of Clariant AZ photoresist developer to 1 part water (by volume). The time taken to develop the resist was typically 30 s although this needed to be judged by eye as it was critical not to over-develop — which led to a rounded resist profile and poorer definition features.

Once the resist was developed the pattern in the resist was transferred to the film by argon ion milling. During the milling process argon ions from a plasma are accelerated at the sample which mills the film away. The regions of the film beneath the photoresist are protected by the layer of resist above them whilst exposed regions are milled. Because of the highly

directional nature of the milling process the features produced are much cleaner than those produced by a chemical etch and so a greater resolution can be achieved. For the devices fabricated for Chapter 4 a large diffusion pump based vacuum system was used for the milling. The system base pressure was $\leq 4 \times 10^{-6}$ mBar. During milling an Ar / 2% $O_2$ mixture was introduced into the chamber at a pressure of $2.1 \times 10^{-4}$ mBar (maintained by a needle valve to regulate the flow of gas into the chamber), the beam voltage was maintained at 500 V, the beam current at 10 mA the discharge voltage at 42 V and the accelerator voltage was maintained at 70 V. For the remainder of this work a turbo-pump based system with a load lock chamber was used — this considerably reduced the pumping time to reach the base pressure and the improved ion gun milled at a greater rate. The base pressure of this system was $< 1 \times 10^{-7}$ mBar. The milling parameters were: Ar / 2% $O_2$ pressure of $2.1 \times 10^{-4}$ mBar, beam voltage of 500 V, beam current of 20 mA, the discharge voltage of 42 V and accelerator voltage of 100 V. In both systems the sample stage is water cooled and rotated during the milling process, to ensure uniform milling.

When the film was milled through (confirmed by visual inspection of the sample and checked by measuring the resistance between two corners of the insulating substrate) the resist was stripped as described previously. This process is illustrated in Fig. 3.5. In the next stage of processing gold contacts were sputtered onto the sample.

### 3.3.4 Gold Contact Deposition

Gold contacts were deposited onto the samples by a lift off process. A photoresist layer was patterned so that holes were present in the regions where gold contacts are desired, using the cannon projection mask system and Clariant AZ1524 resist, as described above. The film was then mounted into the gold deposition system which was pumped down to $\leq 4 \times 10^{-6}$ mBar (note that the vacuum system used for gold deposition was also equipped with an ion gun and was used for the ion milling of the samples in Chapter 4, as described above). A pure argon pressure of $5 \times 10^{-2}$ mBar was introduced into the chamber and the gold was deposited by DC sputtering. During DC sputtering a large DC voltage is applied between the gold target (connected as the cathode) and ground. The argon ions are produced in the gas and accelerated towards the gold cathode, colliding with it and sputtering the gold atoms which move towards the substrate. More details of the sputtering process are given in reference [11]. Sputtering was performed at 30 W power, leading to a gold deposition rate of 3.3 $\mathrm{nm\,s^{-1}}$. The target was presputtered for 30 s to remove contaminant before the film was deposited. Again, the

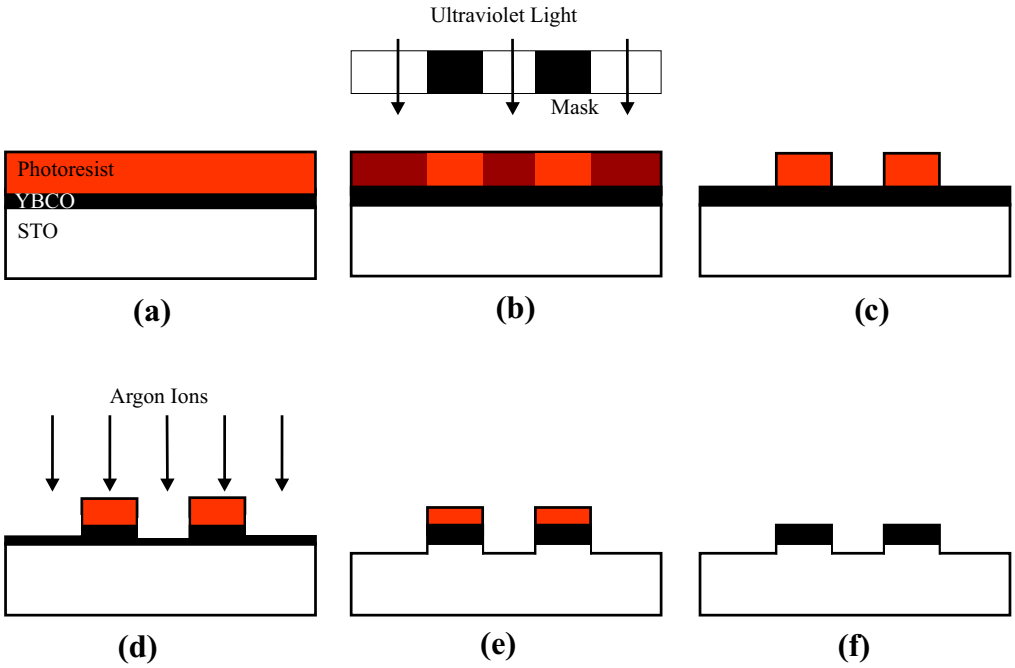


Figure 3.5: Schematic showing the patterning process to produce the $YBa_2Cu_3O_{7-\delta}$ devices. a) Photoresist is spun onto the film and baked. Resist is exposed to ultraviolet light (b) and developed (c). The sample is then ion milled to remove material in the exposed area (d). After ion milling (e), the resist is removed leaving the patterned $YBa_2Cu_3O_{7-\delta}$ (f).

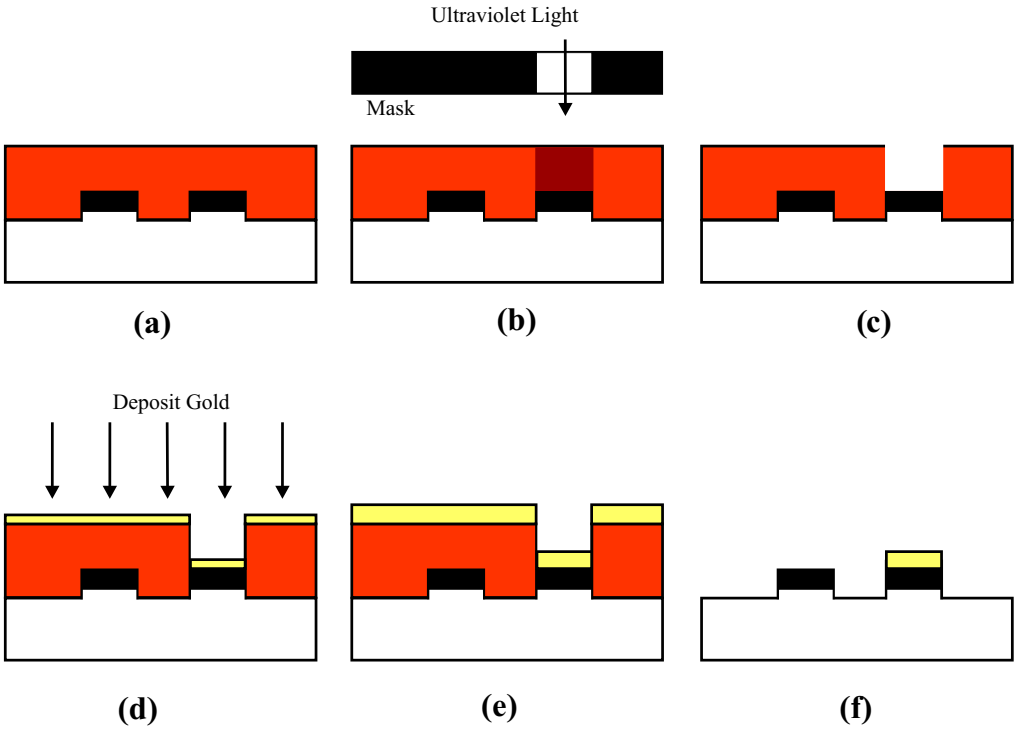


Figure 3.6: Schematic showing the lift off process used to produce the contact pads. a) Photoresist is spun onto the patterned film and baked. Resist is exposed to ultraviolet light in the regions where contact pads are required (b) and developed (c). Gold is then deposited onto the sample (d). After deposition (e), the resist is removed along with the gold on top of it, leaving behind gold in only those regions that were not covered with resist (f).

sample holder was water cooled to ensure the film was not heated too much during the deposition.

After deposition the system was brought up to air and the sample was placed into a beaker of acetone. As the photoresist is dissolved, the regions of gold that were deposited on top of it are removed, leaving behind gold on only the exposed areas of the contact. To remove the resist the beaker of acetone was usually placed in an ultrasound bath for several seconds. When the resist had been completely removed the film was dried as described previously and the sample was ready for measurement. The lift-off process is illustrated in Fig. 3.6.

### 3.3.5 Film Thickness Measurement

The film thickness was measured by patterning and wet etching a small notch in the leads running to the devices. A wet etch was used to avoid the removal of any of the substrate, as for example, ion milling would. This notch was usually located close to the devices to minimise errors due to variations in thickness across the film. A mask with a small square opening was used to pattern a notch over one of the tracks using the cannon projection system and Clariant AZ1524 resist, as described above. The $YBa_2Cu_3O_{7-\delta}$ in this region was removed by a wet etch in phosphoric acid, using the same procedure as was employed to remove the film before the grain boundary HF etch. The photoresist layer was then stripped in the usual manner. The substrate step height was then measured with either a profilometer (for the work in Chapter 4) or by Atomic Force Microscopy, as described above.

## 3.4 Electrical Characterisation

After sample fabrication the chip was mounted on a copper sample holder designed to fit into the custom built dip probe used for the measurements of this thesis. A thin layer of nail varnish was used to attach the sample to the copper block and electrical connections to the sample were made by ultrasonic wedge bonding with 25 $\mu$m diameter aluminium and gold wire. The sample block was then measured in a dip probe built by Phil McBrien and modified by the author. The lower end of the probe consists of a diode thermometer, heater and a coil mounted in a copper block (the coil can be wired in series with an additional coil to apply a magnetic field to the sample). Measurement lines running to the sample are wired through capacitive lead through filters (RS part number DLT 1000) to attenuate high frequency noise. The lines are not thermally grounded or twisted in pairs (twisted pairs are not

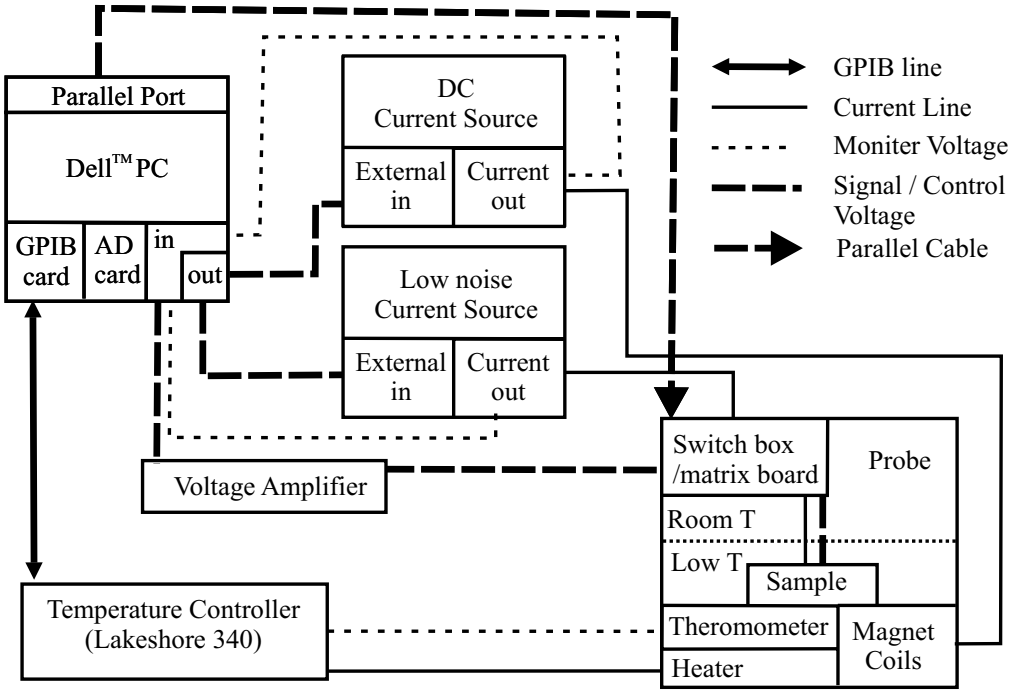


Figure 3.7: Schematic showing the standard setup used for electrical measurements in this thesis.

used to ensure maximum flexibility in the measurement configuration). 19 measurement lines run down through the probe. These wires are connected via shielded twisted pairs to a voltage amplifier or current source by a matrix board or alternatively by a computer driven switch array. While the switch array increased the signal noise it offered considerable time savings for the measurement as several devices could be measured simultaneously through a single cool down. Current was applied to the devices by means of a quasi-DC ($\sim$15 Hz) low noise current and voltage source (a typical noise level was 0.5-1 $\mu$V in a 10 kHz bandwidth). In the standard setup, the output voltage was amplified by a low noise amplifier and detected by 16 bit National Instruments analogue-to-digital (AD) card. The signal is also filtered by a band pass filter. All the measurements reported in this thesis are carried out with a four point technique.

Temperature control is performed by a Lakeshore 340 temperature controller. For temperature dependent measurements the sample was cooled at 4 K per minute — at this cooling rate the difference between measurements performed on cooling down and heating up the sample is less than 0.5 K. In addition by measuring a sample on a cool down at this rate and measuring

the same sample immersed in liquid nitrogen, it was possible to determine that the temperature lag between the sample and the thermometer during cooling at this rate was less than 2 K (this is the approximate accuracy of the temperature measurements for the data in Chapter 6). Note that it was found that, for measurements of critical currents, the best procedure was to cool the sample through the critical temperature in helium vapour with the temperature controller switched off and the devices shorted. In this way trapped flux in the grain boundary junctions was avoided.

For the capacitance measurements, magnetic field was applied to the sample using a 1000 turn coil wound by the author and mounted to produce a field in the c-axis direction. This coil was used in conjunction with a smaller coil already mounted in the probe. This arrangement allowed the application of field of up to 4 mT using a second computer controlled precision current source set up to apply a DC current.

The standard measurement setup is illustrated in Fig. 3.7.

For low noise voltage measurements (in particular the measurements of critical current distributions presented in Chapter 6), an EG & G Princeton Applied Research 5320L lock-in amplifier was used. A 1 kHz reference voltage signal (typically with amplitude 5 mV) was combined with the DC offset voltage output from the AD card used to control the current source using a unity gain op-amp adder box. The combined signal was then amplified using the current source employed in the standard setup, whilst the output voltage was amplified and then detected by the lock in amplifier. The measurement setup for lock-in measurements is illustrated in Fig. 3.8.

For all the above measurements the apparatus was computer controlled and driven by the Dualscope software written in LabVIEW$^{TM}$ by Gavin Burnell. The use of this software to control and record the measurements saved a considerable amount of time in performing the measurements.

## 3.5 Annealing

The annealing experiment described in Chapter 6 was carried out using a specially designed quench furnace. For samples that were annealed it was found that wire bonds needed to be made using gold wire, to avoid contamination of the contact pads by aluminium residues left after the removal of wire bonds. Such contamination caused severe degradation of the contact between the gold and $YBa_2Cu_3O_{7-\delta}$.

The basic configuration of the furnace is shown in Fig 3.9. Before the anneal the sample was placed in a small bucket made from high purity gold foil and platinum wire. It was then suspended within the glass tube of

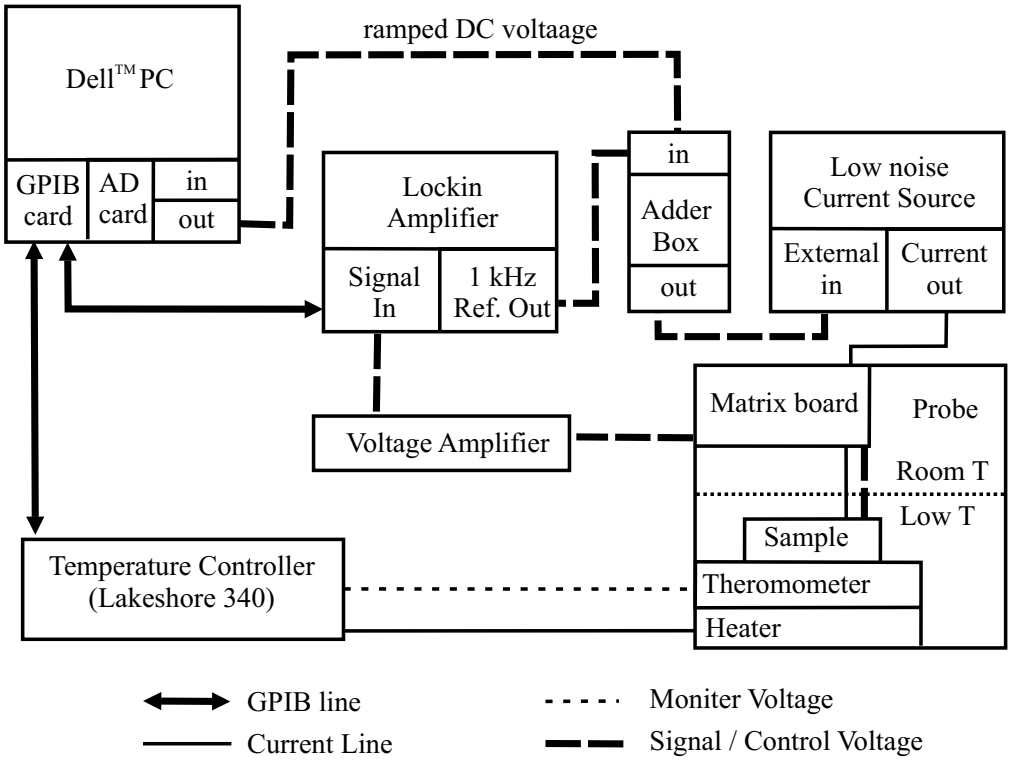


Figure 3.8: Schematic showing the experimental setup used for low noise electrical measurements with a lock-in amplifier.

the furnace as shown in Fig. 3.9. The tube was sealed and an oxygen nitrogen mixture was flowed through it. The furnace was then heated to the anneal temperature. The temperature and the ratio of nitrogen to oxygen was chosen to produce the desired oxygen concentration [12, 13]. The samples were annealed in argon-oxygen mixtures at constant temperature for periods of greater than 7 hours. After the anneal the lower seal was removed from the tube and a small thermos filled with liquid nitrogen was placed under the tube. The magnet holding the sample in the centre of the tube furnace was then removed and the sample drops into the liquid nitrogen, resulting in a rapid quench (see Fig. 3.9). The sample was then removed and warmed to room temperature under flowing nitrogen-oxygen mix, to prevent any water condensing on it as it heated up.

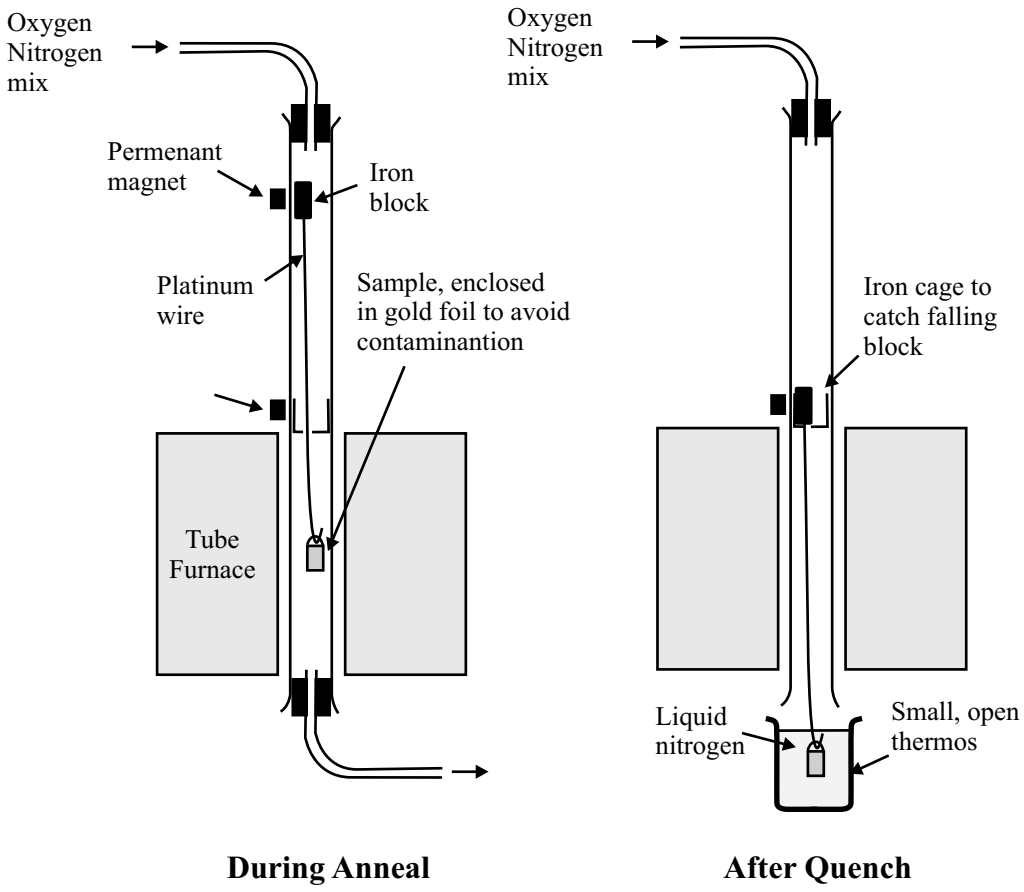


Figure 3.9: Schematic showing the quench furnace used to anneal some films after measurement. During the anneal the sample is held at temperature in a flowing oxygen-nitrogen mix at atmospheric pressure. After the anneal period the bung at the bottom end of the furnace is removed and a small thermos containing liquid nitrogen is placed under the tube containing the sample. The magnet holding the sample in place is released and the sample drops into the liquid nitrogen.

# Bibliography


[1] B. Dam et al., Applied Physics Letters **65**, 1581 (1994).

[2] S. Proyer, E. Stangl, M. Borz, B. Hellebrand, and D. Bauerle, Physica C **257**, 1 (1996).

[3] P. R. Willmott and J. R. Huber, Reviews of Modern Physics **72**, 315 (2000).

[4] D. Bäuerle, *Laser processing and chemistry*, Springer-Verlag, Berlin, 1996.

[5] K. L. Saenger, Processing of Advanced Materials **2**, 1 (1993).

[6] K. L. Saenger, Processing of Advanced Materials **3**, 63 (1993).

[7] A. Schmehl et al., Europhysics Letters **47**, 110 (1999).

[8] W. K. Park et al., IEEE Transactions on Applied Superconductivity **11**, 147 (2001).

[9] Digital Instruments, *Nanoscope III manual*, 1999.

[10] M. J. Hogg, *The Electronic Properties of Thin Film $YBa_2Cu_3O_{7-\delta}$ Low Angle Grain Boundaries*, PhD thesis, Cambridge University, Cambridge, UK, 2002.

[11] M. Ohring, *Materials Science of Thin Films*, Academic Press, New York, 2002.

[12] K. Conder, C. Koyer, and E. Kaldis, unpublished, data courtesy of John Cooper.

[13] K. Conder, J. Karpinski, E. Kaldis, S. Rusiecki, and E. Jilek, Physica C **196**, 164 (1992).

# Chapter 4

# The Capacitance of $Y_{1-x}Ca_xBa_2Cu_3O_{7-\delta}$ Grain Boundaries

As discussed in Chapter 2, the early work of the IBM group demonstrated that grain boundaries were the limiting factor determining the critical current in bulk high-$T_c$ samples [1, 2, 3]. Since then there has been a major effort to increase the grain boundary critical currents in these materials [4]. Recently it has been demonstrated that improvement in the critical currents attainable in the technologically promising superconductor $YBa_2Cu_3O_{7-\delta}$, can be achieved by doping the grain boundaries with calcium [5, 6, 7, 8, 9, 10]. Local Calcum doping has been successfully employed to improve the critical currents of ion-beam-assisted-deposition coated conductors [11]. While this discovery was met with significant excitement in the applied superconductivity community, the mechanisms by which Calcium doping improves the critical current are not established. The role of grain boundary charging, overdoping and band bending [12] has not yet been unequivocally demonstrated and the microstructural evidence is still disputed [13]. In this chapter experiments to determine the variation of the grain boundary capacitance with Calcium doping are reported. These measurements were performed in order to gain insight into the manner in which Calcium doping alters the grain boundary properties. The capacitance of the boundary is determined by the width of the potential barrier and is not dependent on the barrier height — unlike the other transport properties, such as the normal state resistance and the critical current. Such measurements therefore give an additional insight into the nature of Calcium doping.

In this chapter the results obtained from a study of the capacitance of 24° [001] tilt Calcium doped grain boundaries are presented. The capaci-

tance of high angle grain boundaries has previously been determined from measurements of current–voltage characteristic hysteresis and by measuring the voltages of Fiske resonances [14, 15, 16, 17, 18, 19, 20, 21, 22]. This study is the first time the technique has been applied to $Y_{1-x}Ca_xBa_2Cu_3O_{7-\delta}$. Capacitance as a function of doping was determined from hysteresis in the current–voltage characteristics of Josephson junctions fabricated from thin film bicrystals. The properties of the films are examined and the technique is described in detail. Considerable care was taken to eliminate the effect of parasitic contributions to the capacitance from the substrate [22] and increases in the apparent capacitance due heating effects [23], so that the grain boundary capacitance alone is measured. The effect of thermal noise, which can reduce the measured capacitance [24], is also assessed. In addition to the capacitance, the normal resistance and the critical current is measured. The values of all these parameters are compared to gain insight into the nature of Calcium doping.

## 4.1 Properties of the films used in this study

Epitaxial thin films were deposited by pulsed laser deposition from polycrystalline $Y_{1-x}Ca_xBa_2Cu_3O_{7-\delta}$ targets onto 24°[001] tilt $SrTiO_3$ bicrystal substrates. Five films were grown: one for each of the dopings $x = 0.0$, $x = 0.1$, $x = 0.2$, and two with doping $x = 0.3$. Film thicknesses were measured by atomic force microscopy on a wet etched step and were in the range 120–180 nm. The films used in this study were grown at the University of Augsburg and the deposition conditions are described in detail in a previous publication [5]. Films grown under identical conditions in the same laboratory have been extensively characterised [5, 6, 7] so in this study only limited characterisation was performed. Details of the film properties are given in Table 4.1.

The surface properties of the films were characterised by atomic force microscopy. Representative images of samples with each doping are shown in Figs. 4.1 and 4.2. All the films are very smooth with few or no particulates on the surface. In the case of the 0% Calcium doped sample there are a few, micron wide, irregularly shaped particulates that are most likely 'boulders' — larger pieces of target material ablated in the deposition process and subsequently embedded in the film [25]. The addition of calcium appears to have a significant effect on the growth of the films. In general the grain size in the calcium doped films is smaller. The 10% doped sample has an unusual surface morphology, with some much larger grains forming between the smaller, more typical grains. There are not likely to be secondary phases in this film,

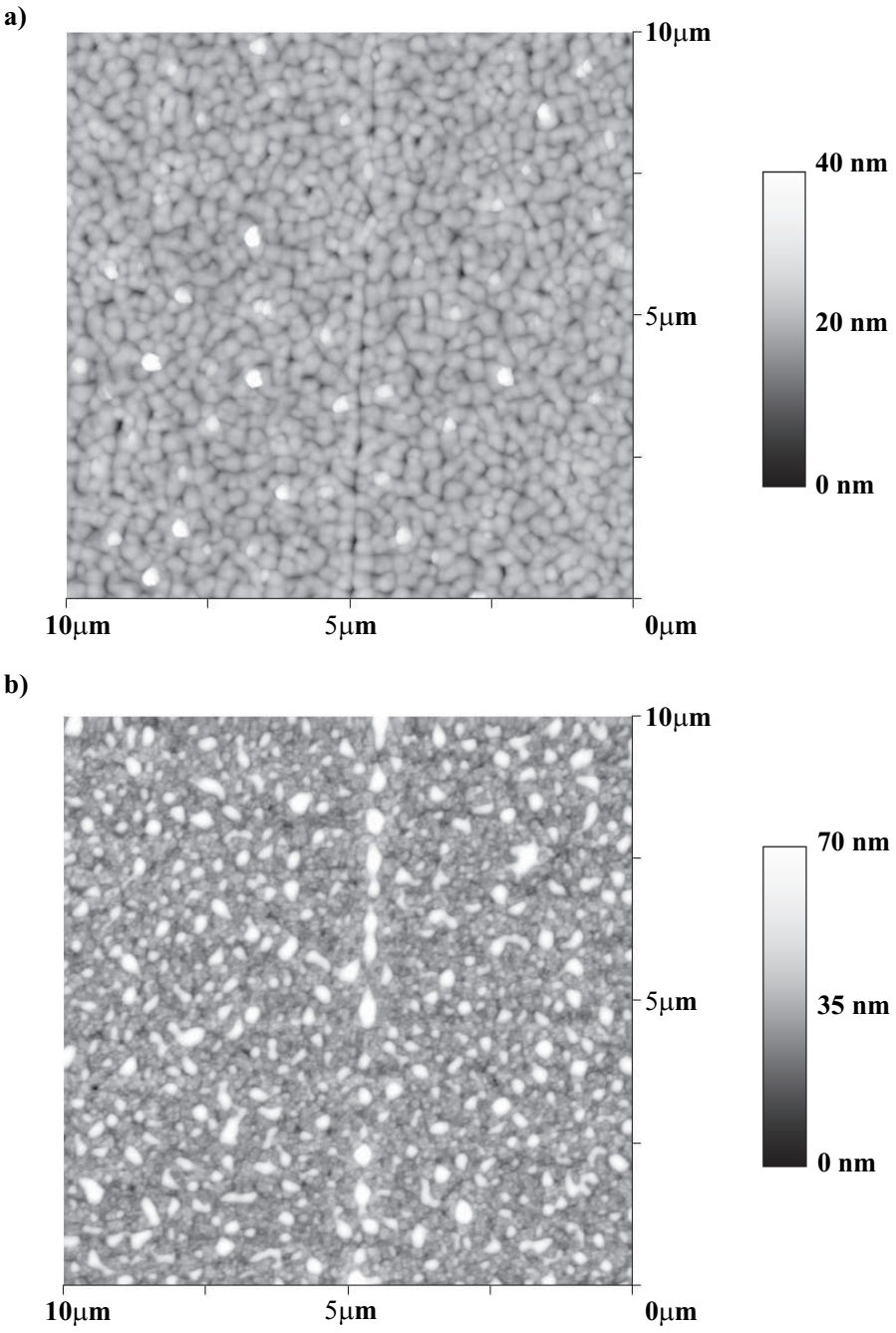


Figure 4.1: Atomic force microscope images of Calcium doped bicrystal films grown at the University of Augsburg. a) 0% Ca doped film, B190 (image scanned at 0.7 Hz). b) 10% Ca doped film, B191 (image scanned at 0.6 Hz). In both cases image resolution is 512 samples per line. Both films are grown on 24° [001] tilt bicrystals. Both images were obtained with the assistance of Michael Hogg.

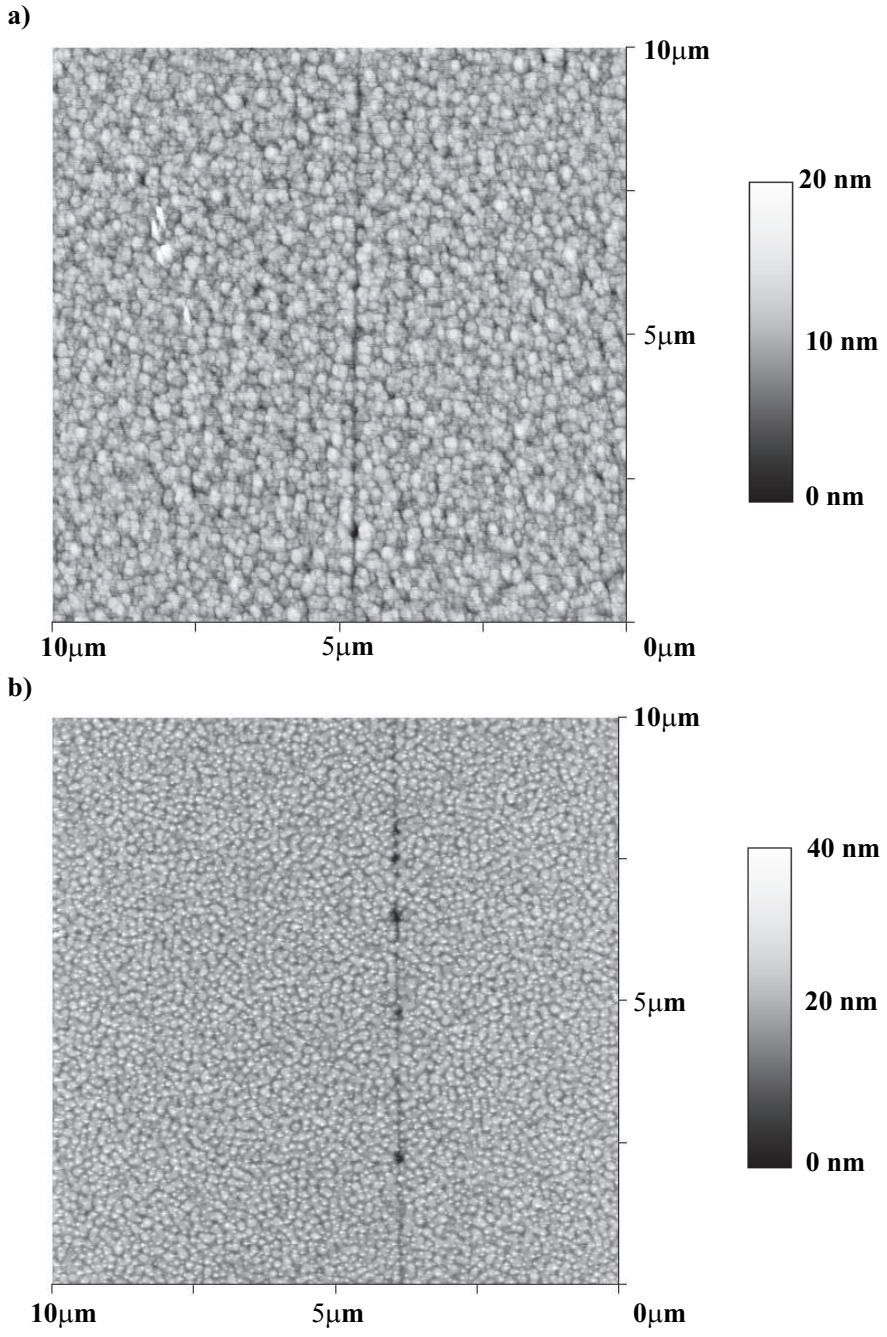


Figure 4.2: Atomic force microscope images of Calcium doped bicrystal films grown at the University of Augsburg. a) 20% Ca doped film, B274 (image scanned at 0.76 Hz). b) 30% Ca doped film, B294 (image scanned at 0.86 Hz). In both cases image resolution is 512 samples per line. Both films are grown on 24° [001] tilt bicrystals. Image a) was obtained with the assistance of Michael Hogg.

Table 4.1: Properties of the films used in this study. The films were grown at the University of Augsburg and the growth conditions are described in a previous publication [5]. All the films were grown on 24° symmetric [001] tilt bicrystals. Film thicknesses were measured by either atomic force microscopy or profilometery, on wet etched steps.

| Calcium Doping | Augsburg Growth Run | Critical Temperature | Film Thickness |
|---|---|---|---|
| 0% | B190 | 92 K | 160 nm |
| 10% | B191 | 84 K | 170 nm |
| 20%† | B274 | 78 K | 134 nm |
| 30%‡ | B192 | 80 K | 175 nm |
| 30% | B294 | 82 K | 120 nm |

† *There were no hysteretic junctions on this sample, so the grain boundary capacitance was not measured.*
‡ *This sample was measured with the assistance of Phil McBrien. It was destroyed during the first set of measurements and so is not referred to extensively below.*

since 10% is well below the solubility limit for Calcium in $YBa_2Cu_3O_{7-\delta}$ [26, 27, 28, 29]. The transport properties of this film were also intermediate between those of the 0% and the 20% samples, suggesting that the different microstructure does not alter the transport properties significantly. The 20% and 30% doped films have similar grain sizes and a series of small holes are present at the boundary. Such holes are often observed at bicrystal grain boundaries and are also present in the substrate [30, 31, 32, 33]. The observation of these holes on a specially fabricated 0° bicrystal demonstrates that they result from the bicrystal fusion process [33]. The principle effect of such holes will be to reduce the effective area of the boundary.

Films grown under the same conditions as those used in this study have been studied extensively. It is clear from Rutherford backscattering experiments that the transfer of the doped target material to the film is stoichiometric [5] and from annealing experiments that the films are overdoped [5]. The critical temperatures of these films are consistent with those reported by Schneider *et al.* [6].

In conclusion the properties of the films used in this study are consistent with those observed by the Augsburg group in their original study of Calcium doped bicrystals [5, 6, 7]. The surface morphology of the films is found to vary with Calcium doping and, in particular the grain size appears to be

reduced by the addition of Calcium — this is consistent with the previous observations of the Augsburg group [5]. The films have a low density of particulates and are in general very smooth.

## 4.2 Preparation and measurement of the devices

The films were patterned into micro-bridges by photolithography and argon ion milling, as described in Chapter 3. The mask design used is shown in Fig. 4.3. This mask was designed for 5 mm ×10 mm samples, and the films supplied by the University of Augsburg were approximately 3 mm ×10 mm, so not all the devices shown could be fabricated. The widths of the bridges in this study were therefore between 2 $\mu$m and 6 $\mu$m, and only the lower part of the mask was employed — this is shown in an expanded view in Fig. 4.3. The widths of the bridges were measured after patterning by optical microscopy. The grain boundary is aligned with the mask so that each microbridge contains a single, Josephson coupled, boundary.

Current biased current-voltage characteristics were measured by the standard four point technique, with the sample immersed in liquid helium or in helium vapour, at atmospheric pressure. The apparatus used is described in Chapter 3. Fig. 4.4 shows a series of typical current density-voltage characteristics for the 3 $\mu$m wide junctions, as well as the detail of the hysteresis for the 30% calcium doped 2 $\mu$m junction. The critical current criterion adopted was a significant increase above the noise level (typically 1 $\mu$V). The same criterion was used to define the return currents. Junction normal resistances were obtained from current-voltage characteristics with large applied bias, such as those shown in Fig. 4.4(a).

## 4.3 Determining the Intrinsic Capacitance of the Grain Boundaries

The capacitance of the grain boundaries can be measured by taking advantage of the Josephson coupling that occurs across them. Josephson junction capacitances can be determined from values of the return current and the critical current extracted from current voltage characteristics such as those shown in Fig. 4.4(b). Within the resistively and capacitively shunted junction (RCSJ) model it is possible to determine the McCumber parameter, $\beta_c$, from the ratio of the critical current, $I_c$, to the return current, $I_r$, using the

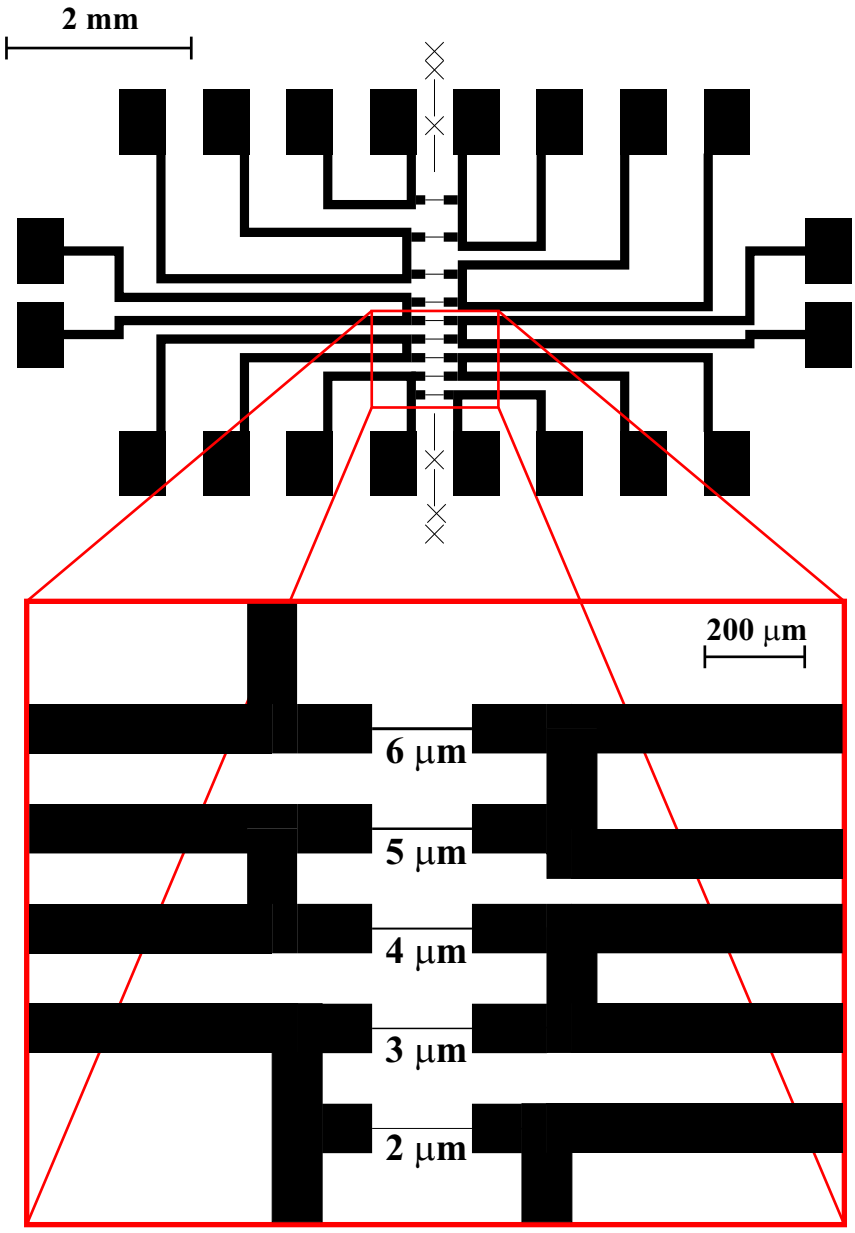


Figure 4.3: Mask design used for the fabrication of microbridges with different widths on Calcium doped films. The grain boundary was aligned with the dashed and crossed line in the center of the mask. Due to the reduced size of the samples only the smaller microbridges were fabricated, these are shown in an expanded view.

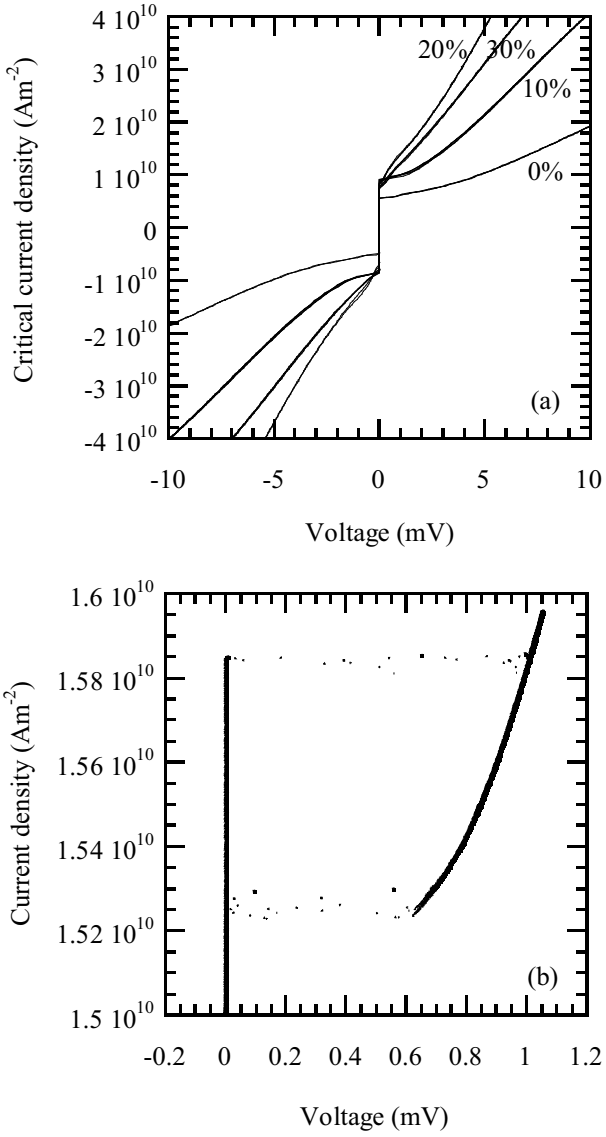


Figure 4.4: (a) Current density-voltage characteristics for 3 $\mu$m wide junctions of each of the 3 dopings, measured at 4.2 K with the sample immersed in liquid helium. (b) Detail of the hysteresis for the 30% doped 2 $\mu$m wide junction. 10 consecutive measurements are shown to give an indication of the noise level.

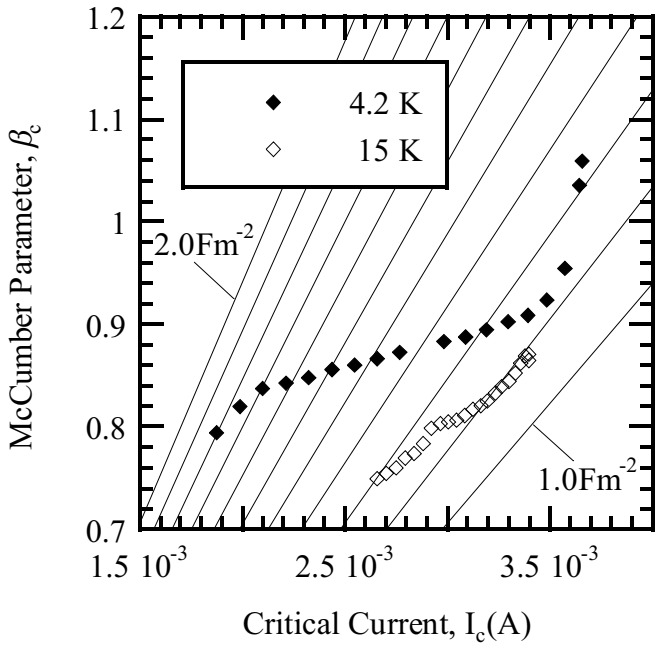


Figure 4.5: Plot of the McCumber parameter, $\beta_c$, against the critical current, $I_c$ for the 30% Calcium doped 2 $\mu$m junction at two different temperatures. Equation 4.1 predicts a linear relationship between $\beta_c$ and $I_c$ for a constant capacitance. Lines of constant capacitance per unit area, spaced at intervals of 0.1 Fm$^{-2}$ are also shown.

numerical result of McCumber [34]. $\beta_c$ is in turn related to the capacitance by the following equation:

$$\beta_c = \frac{2eI_cR_n^2C}{\hbar}, \tag{4.1}$$

where $e$ is the electronic charge, $\hbar$ is Planck's constant divided by $2\pi$, $R_n$ is the normal resistance of the junction and $C$ is its capacitance.

This equation predicts a linear relationship between $\beta_c$ and $I_c$ given that all the other parameters are constant. It is possible to suppress the critical current of a junction by applying a DC magnetic field in the junction plane so the relationship between $\beta_c$ and $I_c$ can be measured experimentally. Figure 4.5 shows such a relationship for one of the grain boundary junctions measured in this study. It is clear that the relationship between these two quantities is not linear for this device at either 4.2 K or 15 K. As expected, the normal resistance is found to be independent of the applied magnetic field and therefore the capacitance must be increasing at lower critical currents or the hysteresis must be due to some other effect.

The reduction of the critical current by the application of a magnetic field results in a reduction of the return voltage at which the junction switches back into the superconducting state. When a voltage is dropped across the Josephson junction the current oscillates at a frequency proportional to the applied voltage. So reducing the critical current also has the effect of reducing the frequency of the Josephson oscillations. The dielectric properties of the $SrTiO_3$ substrate are frequency dependent and at lower frequencies the relative dielectric constant can be extremely large. It is therefore possible that a parasitic capacitance is added to the system at lower voltages as electric field is diverted into the high dielectric constant substrate. This situation is illustrated in Fig. 4.6(a). As shown in Fig. 4.6(b), the dielectric constant of $SrTiO_3$ is a function of both frequency and temperature [35]. The Josephson voltages equivalent to the frequencies are shown as an alternative $x$-axis in Fig. 4.6(b). It is clear that in the 0-1 mV voltage range the parasitic capacitance is likely to increase at lower voltages (and hence reduced critical currents).

A second possible explanation for the non-linear curves observed in Fig. 4.5 is that the hysteresis observed is dominated by heating [23]. Self-heating of the junction can cause a reduction in the return current and can lead to hysteresis even in the absence of capacitance. To understand this effect consider traversing a single hysteresis loop in the $I$–$V$ curve. As the current is initially increased the sample is in the superconducting state and there is no dissipation or heating. Once the sample switches into the normal state there is a voltage across the junction and power is dissipated as heat. The junction temperature rises. Provided this rise in temperature is significant there will be a corresponding decrease in the critical current. The junction will switch back at the reduced critical current, appropriate for its increased temperature. For junctions that are already hysteretic heating effects will increase the amount of hysteresis.

Finally there is the possibility that the hysteresis is suppressed by thermal noise in the junction, which leads to switching out of the superconducting state at a reduced current and switching back at an increased current. While this cannot explain the results of Fig. 4.5 it is nonetheless important to assess its effect on the measurement as it is likely to be a major source of error.

The effects of both the substrate and heating must be ruled out in any measurement of the grain boundary capacitance and the error due to thermal noise should be estimated. In the remainder of this section the experiments performed to ensure that the measured capacitance is that intrinsic to the grain boundary and to assess the effect of thermal noise are described.

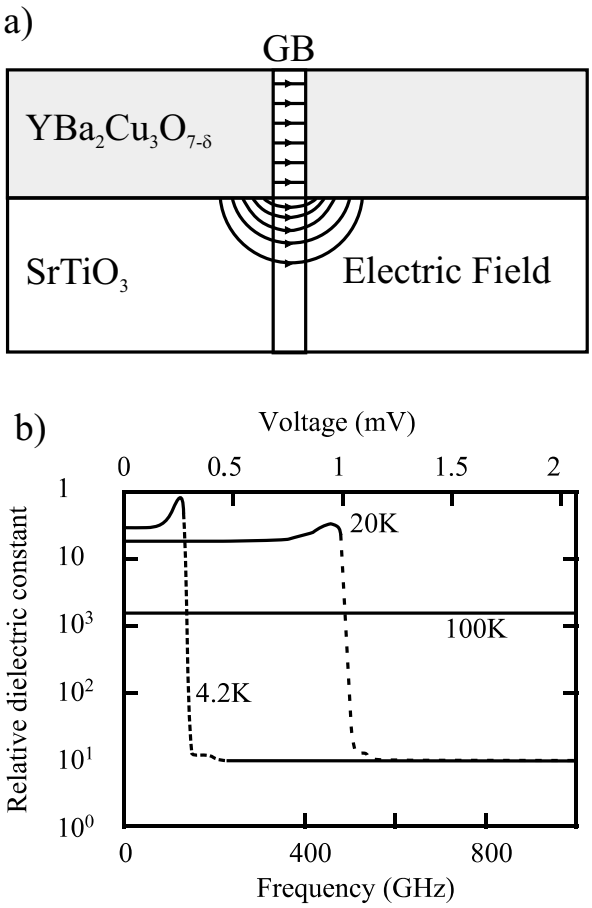


Figure 4.6: a) Diagram illustrating the effect of a large substrate capacitance on the electric field distribution in the vicinity of the grain boundary. The substrate contributes parasitically to the overall capacitance. b) Schematic temperature and frequency dependance of the dielectric constant of single domain $SrTiO_3$. The equivalent Josephson voltage for a given frequency is shown as an alternative $x$-axis. Based on Neville, Hoeneisen and Mead [35].

### 4.3.1 Eliminating Substrate Effects from the Capacitance Measurement

To rule out substrate effects it is necessary to demonstrate that the junction properties are measured at a sufficiently large frequency that the dielectric constant of the substrate is low. The detailed behaviour of the dielectric constant of $SrTiO_3$ is shown schematically in Fig. 4.6(b). At 4.2 K and at low frequencies the relative dielectric constant ($\varepsilon_r$) is very high (approximately 20,000). $\varepsilon_r$ remains high until the soft optic phonon frequency, $\nu_{so}$, is reached. At this point there is a rapid drop in $\varepsilon_r$ with increasing frequency and at high frequencies $\varepsilon_r \approx 10$. As the temperature is increased the zero frequency value of $\varepsilon_r$ is reduced, whilst $\nu_{so}$ increases, but similar behavior is observed. The location of the sharp drop in the dielectric constant is also dependent on the domain structure in the $SrTiO_3$, which forms as the sample is cooled below 110 K [36], so the diagram is necessarily a schematic representation of the behaviour of the substrate.

If the substrate does cause the variations in capacitance shown in Fig. 4.5 then it should be possible to observe voltage (effectively frequency) and temperature dependencies of the capacitance that reflect the behaviour of the dielectric constant. Figure 4.7 shows the data from Fig. 4.5 plotted in an alternative manner, as capacitance versus return voltage. The return voltage is the appropriate voltage for the re-trapping process and so reflects the frequency at which the capacitance is measured (frequency is shown as an alternative $x$-axis). In addition to the data from the 30% Calcium doped, 2 $\mu$m junction, results from other devices on the same sample are also shown. A sharp increase in the capacitance at low frequencies is apparent for all the junctions and in addition occurs at the same frequency as the sharp rise in the dielectric constant of $SrTiO_3$ (see Fig. 4.6). At larger voltages and hence frequencies the capacitance of both the 2 and 3 $\mu$m junctions levels out to a constant value, indicative of a negligible substrate contribution. The same behaviour was observed from an additional 5 $\mu$m junction on the same sample. The capacitance of the 4 $\mu$m junction varies continuously over the measurable range so there is always some substrate capacitance. It is therefore not possible to measure the grain boundary capacitance of this junction by this technique. The high frequency capacitance of the 2 $\mu$m junction measured at 15 K is the same as the 4.2 K value, in very different thermal conditions. The onset of the increase in the capacitance due to parasitic substrate contributions occurs at a higher frequency at 15 K than at 4.2 K. The magnitude of the parasitic contributions is also reduced, as expected from Fig. 4.6(b).

This consistency of the results in Fig. 4.7 with the behaviour of the

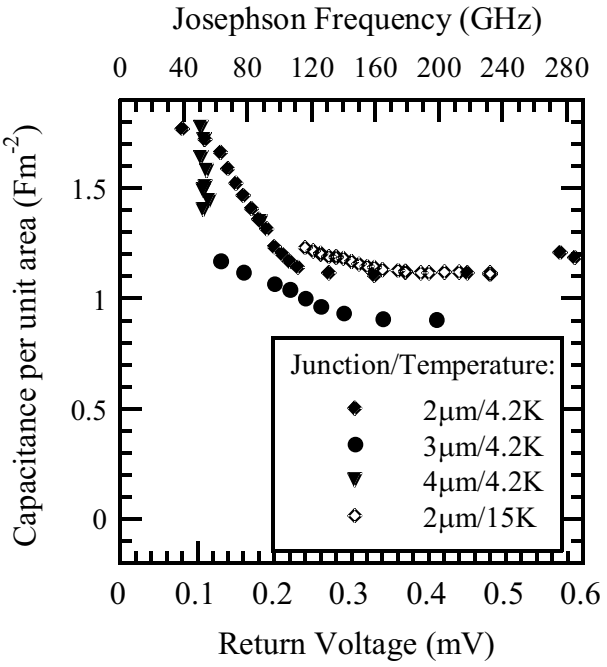


Figure 4.7: Measured capacitance per unit area, $C/A$, shown against the return voltage for 30% Calcium doped junctions. At 4.2 K the sample is immersed in liquid helium, at 15 K it is held in helium vapour. The Josephson frequency is shown as an alternative $x$-axis and is effectively the frequency at which the capacitance is measured. The sharp rise in the capacitance at low frequencies is due to parasitic components from the substrate. At higher frequencies the capacitance is constant and temperature independent.

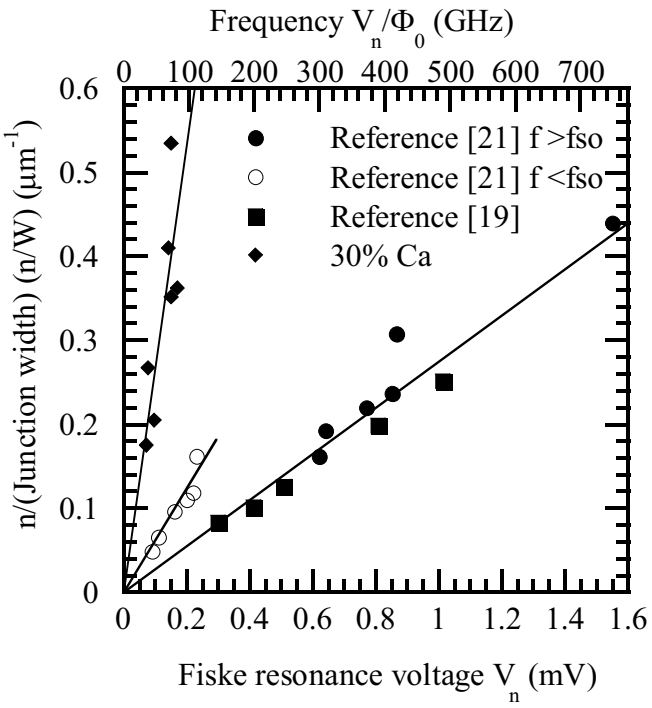


Figure 4.8: Fiske resonance dispersion relations for undoped junctions from Tarte *et al.* [21], from Medici *et al.* [19] and for the 30% doped junctions from this study.

substrate shown in Fig. 4.6(b) shows that the effects of the substrate on the measurement are observed. Other authors have observed similar, enhanced grain boundary capacitances in hysteresis [17] and Fiske resonance [17, 15] measurements of $YBa_2Cu_3O_{7-\delta}$ (on $SrTiO_3$) grain boundary capacitance at low frequencies. Nakajima, Yokota, Myoren, Chen and Yamashita confirmed that this effect was due to the substrate capacitance by demonstrating a large electric field effect [17]. Tarte *et al.* have observed a similar transition in the capacitance of $YBa_2Cu_3O_{7-\delta}$ grain boundaries on $SrTiO_3$ at a voltage of 0.25 mV (equivalent to a frequency of 130 GHz), by observations of the Fiske resonance dispersion relation [21]. Their results are discussed in more detail below. The parasitic substrate contribution to the capacitance can be eliminated by measuring the capacitance in the high frequency region. Notice that the measured capacitance of the 2 $\mu$m junction at the highest return voltages is slightly increased. This increase is not observed in the same junction at 15 K and may result from the onset of heating effects. The effect of heating on the measurement is assessed in more detail below.

Fiske resonances have been frequently used to determine the capacitance

of $YBa_2Cu_3O_{7-\delta}$ grain boundaries [14, 15, 16, 17, 22]. The voltage ($V_n$) at which an $n$th order Fiske resonance occurs is given by the following equation:

$$V_n = \frac{n\Phi_0}{2l\sqrt{L'C'}}, \tag{4.2}$$

where $\Phi_0$ is the flux quantum, $l$ is the width of the junction and $L'$ and $C'$ are the inductance and capacitance, per unit length of the junction. An $n$th order Fiske resonance corresponds to a cavity resonance in which $n/2$ wavelengths fit into the junction cavity.

Using equation 4.2 the inductance per unit length of the junction can be determined from the Fiske resonance voltage. If the inductance of the junction is dominated by the superconducting electrodes, then the value of the inductance can be simply related to the London penetration depth. By plotting the Fiske resonance voltage against the inverse junction width (effectively a dispersion relation for the junction cavity) the junction inductance can be determined from the gradient if the capacitance is known from the hysteresis. Fig. 4.8 shows a plot of data from several undoped junctions from the literature, together with the data obtained from the 30% doped junction. It is clear that the dispersion relation for the undoped data has two linear regimes—one at low voltages (below 0.3 mV) and one at high voltages (above 0.3 mV). Analysis of the data in the high voltage regime produces a reasonable penetration depth of 180 nm for the junction region [22]. The lower voltage regime, however, has an increased gradient and does not produce a consistent penetration depth. This is because, at these reduced voltages (and hence reduced Josephson frequencies) the dielectric constant of the substrate is extremely large and substrate effects increase both the inductance and capacitance per unit length of the junction (see Fig. 4.6).

It is clear that the data obtained for the 30% doped sample is all in this low frequency, substrate dominated, region. Although this means a quantitative analysis of the Fiske resonances is not possible, qualitative observations can be made. The gradient of the curve for the 30% doped sample is approximately 5 times greater than that previously observed for an undoped sample in the same low frequency regime. This indicates that the junction capacitance has increased significantly. The fact that the resonances occur at such low voltages is a further indication of an increased capacitance and is consistent with the observations from the hysteresis measurements.

In addition to measuring the frequency dependence of the capacitance by suppressing the critical current with a magnetic field the temperature dependance of the zero field capacitance was measured. The data from this experiment is shown in Fig. 4.9. In addition to the measured capacitance per unit area the variation of the return voltage with temperature is shown.

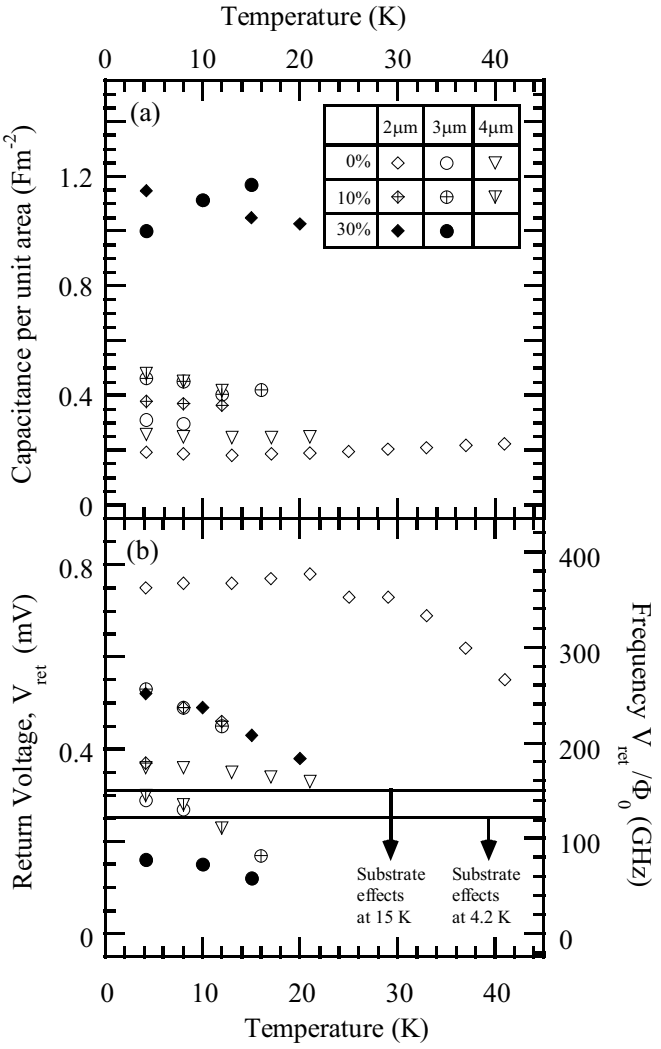


Figure 4.9: a) Temperature dependence of the zero field capacitance of a number of junctions in the study. The capacitance is determined from the hysteresis in the $I$-$V$ curve with the sample in helium vapour, or immersed in liquid helium at 4.2 K. In most cases the capacitance is independent of temperature to within the error associated with the measurement (approximately 10% if the systematic errors are ignored). b) Return voltage of these junctions as a function of temperature. With the exception of the 3 $\mu$m 30% Calcium doped junction the return voltages are all above the substrate dominated regime at 4.2 K.

In general the return voltage decreases as the temperature increases, since at higher temperatures the critical current is reduced. It is clear that in most cases the capacitance is approximately temperature-independent over the measurable range. At 4.2 K the return voltages of all the samples with the exception of the 3 $\mu$m 30% doped junction are out of the substrate dominated regime — determined from Fig. 4.7. The effect of the substrate for this junction is to cause a rise in the capacitance, since as the temperature is increased the location of the drop in the substrate dielectric constant moves up in frequency and the return voltage drops further into the substrate dominated regime. The decreasing capacitance of the 2 $\mu$m junction may be associated with heating effects at low temperatures causing an artificially inflated low temperature capacitance value. The temperature independence of the 2 $\mu$m undoped junction capacitance provides further evidence that the technique is consistent — a temperature independent capacitance would not be observed up to 40 K if the measured capacitance were dominated by the substrate or if the hysteresis were caused by heating. The effect of heating is assessed in more detail in the next part of this section.

### 4.3.2 Eliminating Heating Effects

The discussion in the previous section highlighted the possibility that heating may contribute significantly to the measured hysteresis. In order to investigate this possibility a detailed model for heating in the high-$T_c$ grain boundary was developed, in collaboration with E. J. Tarte. This model is described in full in appendix A. By adapting the model of Skockpol, Beasley and Tinkham [23] to the geometry of our bicrystal grain boundaries it is possible to calculate the temperature rise expected at any point in the $I$–$V$ curve.

Table 4.2 shows the calculated temperature increases for all the hysteretic junctions measured in this study, at key points on the $I$–$V$ curve. The power dissipated in these junctions typically leads to temperature increases of the order of 1 K at the return current. For the junctions measured in this study the critical current is found to be temperature independent at low temperatures, so small variations in temperature are unlikely to make a significant difference to the hysteresis.

The expected hysteresis ($\alpha = I_{ret}/I_c$) due to a small temperature rise at the junction is $\alpha = 1 + (\Delta T/I_c) \times dI_c/dT$. A typical value for $1/I_c \times dI_c/dT$ is -3×10$^{-3}$ K$^{-1}$ for an optimally doped 24° [001] tilt $YBa_2Cu_3O_{7-\delta}$ grain boundary [4]. For temperature rises of order 1 K this leads to $\alpha = 0.997$, which should be compared to the measured values in this study, in the range 0.95 to 0.995. The temperature increases associated with heating in the

Table 4.2: Temperature rise associated with heating of the junction in the normal state at the return current, $\Delta T_{ret}$, and at the critical current, $\Delta T_{crit}$. Values are calculated for different values of $x$ in $Y_{1-x}Ca_xBa_2Cu_3O_{7-\delta}$, different junction widths $w$ and different temperatures, $T$. The return voltage, $V_{ret}$, is also shown for easy comparison with Fig. 4.7. The calculations were performed using the model outlined in the appendix. Note that the predicted temperature increase is approximately the same for all the junctions in the study and that it is strongly reduced as the temperature is increased.

| $x$ | $w(\mu\text{m})$ | $T$ (K) | $V_{ret}$ (mV) | $\Delta T_{crit}$ (K) | $\Delta T_{ret}$ (K) |
|---|---|---|---|---|---|
| 0 | 4 | 4.2 | 0.6 | 1.0 | 0.9 |
| 0 | 3 | 4.2 | 0.5 | 1.0 | 0.7 |
| 0 | 2 | 4.2 | 0.7 | 1.7 | 1.0 |
| 10 | 4 | 4.2 | 0.3 | 0.9 | 0.7 |
| 10 | 3 | 4.2 | 0.6 | 1.9 | 1.3 |
| 10 | 2 | 4.2 | 0.4 | 0.9 | 0.8 |
| 30 | 5 | 4.2 | 0.2 | 0.6 | 0.5 |
| 30 | 4 | 4.2 | 0.1 | 0.5 | 0.4 |
| 30 | 3 | 4.2 | 0.2 | 0.7 | 0.6 |
| 30 | 2 | 4.2 | 0.6 | 2.3 | 1.6 |
| 30 | 2 | 15.0 | 0.5 | 0.3 | 0.2 |

2 $\mu$m 30% Calcium doped junction are the largest. This was the junction in which heating effects were expected from the rise in the capacitance observed at high return voltages in Fig. 4.7 and the temperature dependance of the capacitance in Fig. 4.9. The observation of the onset of heating effects in this junction gives confidence that such effects do not occur in the other junctions, in which less power is dissipated at the return current. In the case of this junction the capacitance could be extracted from measurements at 15 K, where the heating is significantly reduced. In addition most of the junctions measured in this study had a temperature independent capacitance, as shown in Fig. 4.9. The observation of a temperature independent capacitance suggests that heating effects are negligible — it is clear from the data in Table 4.2 that the effects of heating are strongly reduced at higher temperatures.

Heating effects can therefore be eliminated by careful consideration of the temperature and magnetic field dependence of the critical current. A self-consistent picture emerges from these measurements and indicates that it is possible to measure the grain boundary capacitance using the junction hysteresis. Further evidence for the consistency of the technique comes from the scaling of the measured capacitance with junction width, shown in Fig. 4.10. Having demonstrated that the capacitance measured is due to the grain boundary itself, the next section assesses the systematic effect of thermal noise on the measured hysteresis.

### 4.3.3 The Effect of Thermal Noise on the Measured Capacitance

Thermal or other noise sources cause a reduction in the measured critical current and an increase in the return current, producing a systematic underestimate of the capacitance. The washboard analogue for the resistively and capacitively shunted Josephson Junction provides a simple explanation for this effect (see chapter 1) . In the presence of a noise source the superconducting state becomes metastable at currents just below the critical current, when the size of the washboard potential well becomes comparable to $kT$ (where $k$ is Boltzmann's constant and $T$ is the noise temperature). The junction switches into the normal state prematurely as a result of noise excitation out of the potential well. Similarly the return process can occur at currents greater than the return current, with the noise source leading to premature re-trapping into the washboard potential well. As a consequence of the noise the junction does not switch out at a fixed current, but rather the observed critical currents are distributed across a finite range of currents. By measuring the distribution of the observed critical currents it is possible

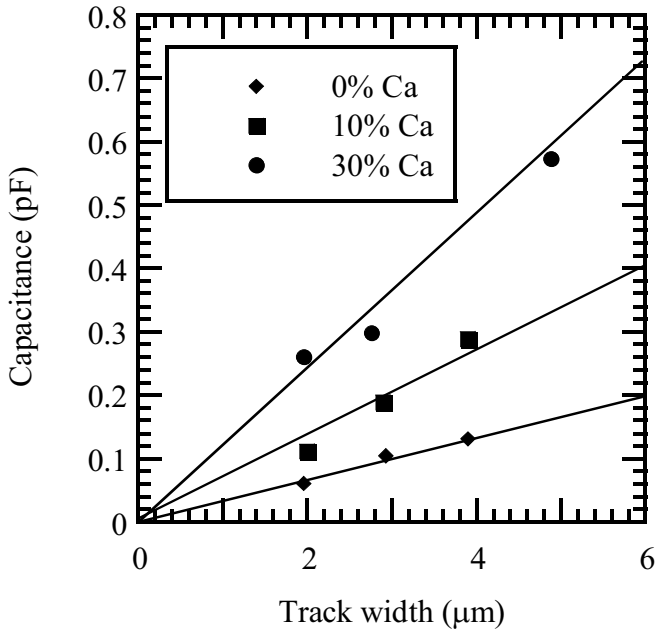


Figure 4.10: Junction capacitance at 4.2 K shown against width of the device for the different samples measured. The straight lines serve as a guide to the eye.

to determine the lifetime of the states corresponding to the observed currents and the true critical current can then be determined from the distribution of these lifetimes [24].

Kramers [37] showed that in the intermediately damped (or the transition state) regime the lifetime, $\tau$, of the state corresponding to a current just below the critical current is given by:

$$\tau^{-1} = \frac{\omega}{2\pi} \exp\left(-\frac{E}{kT}\right), \tag{4.3}$$

where $\omega/2\pi$ is the frequency of escape attempts from the potential well, $E$ is the energy of the washboard potential barrier, $k$ is Boltzmann's constant and $T$ is the temperature. For a Josephson junction tilted washboard the values of $E$ and $\omega$ are:

$$E = \frac{I_c \Phi_0}{\pi} \left( \sqrt{1 - \left(\frac{I}{I_c}\right)^2} - \frac{I}{I_c} \arccos\left(\frac{I}{I_c}\right) \right), \tag{4.4}$$

$$\omega = \left(\frac{2\pi I_c}{\Phi_0 C}\right)^{\frac{1}{2}} \left(1 - \left(\frac{I}{I_c}\right)^2\right)^{\frac{1}{4}}, \tag{4.5}$$

where $I$ is the current of the metastable state, $I_c$ is the true (zero noise) critical current, $C$ is the junction capacitance and $\Phi_0$ is the flux quantum. The assumptions implicit in the above analysis are that $\omega\tau \gg 1$ and that $E/kT > RC\omega > 0.8$. The junctions in this work satisfy these requirements.

To calculate the inverse lifetime of a given current state, the critical current data is reduced to the form of a histogram with $N$ current bins. The lifetime of the state corresponding to each current bin, $\tau^{-1}(K)$ (where $K = 1...N$) can then be determined. The $K = 1$ bin is defined as that with largest critical current and the $K = N$ bin as that with the smallest. Fulton and Dunkleberger showed that $\tau^{-1}(K)$ is given by [24]:

$$\tau^{-1}(K) = \frac{dI}{dt}\frac{1}{\Delta I} \ln\left(\frac{\sum_{j=1}^{K} P(j)}{\sum_{i=1}^{K-1} P(i)}\right), \tag{4.6}$$

where $dI/dt$ is the current sweep rate at the $K$th current bin, $\Delta I$ is the width of the current bin and $P(i)$ is the number of switching events that occur within the $i$th current bin. In deriving this equation it is assumed that $\dot{I}/I_c \ll \omega, \tau^{-1}$ and that the current applied can be approximated as increasing linearly with time over the period corresponding to a single current interval. Again these approximations are valid for our experimental conditions.

Having calculated $\tau^{-1}$ for a number of current intervals it is possible to produce a plot of $\ln(2\pi\tau^{-1}/\omega)$ versus $E/k$, provided a value for the true (zero noise) critical current, $I_c$, is assumed. Initially this is fixed at the value of the largest critical current observed. From equation 4.3 it is clear that such a graph should have an intercept of zero and a gradient of $1/T$, where $T$ is the noise temperature. The value of $I_c$ is increased until the condition of zero intercept for the graph is satisfied. In this way the true critical current is determined and the noise temperature can also be extracted from the gradient of the graph.

Fig. 4.11(a) shows the distribution of critical currents obtained for the 2 $\mu$m 30% Ca doped junction, together with the theoretical distribution obtained from the above analysis. Fig. 4.11(b) shows the plot of $\ln(2\pi\tau^{-1}/\omega)$

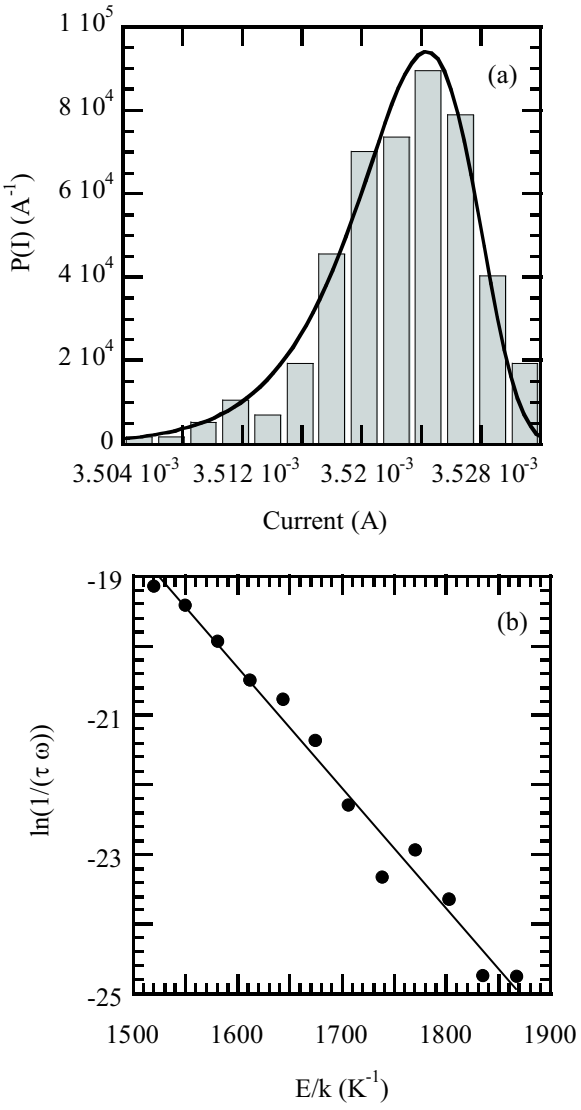


Figure 4.11: (a) Distribution of critical currents for the 30% doped 2 $\mu$m junction at 4.2 K. The continuous line shows a fit corresponding to a noise temperature of 54 K. (b) $\ln(1/\omega\tau)$ versus $E/k$ (see equation 4.3). The gradient of this graph is used to extract the noise temperature of the measurement and the condition of zero intercept can be used to extract the zero noise critical current. The linear relationship indicates a thermal distribution.

versus $E/k$ that was used to calculate the true critical current and the noise temperature. For this data the noise temperature is 54 K, significantly above the measurement temperature of 4.2 K. This excess noise could be due to Johnson noise transmitted down the wires in the measurement probe to the device, and indeed in previous experiments to measure critical current distributions special precautions had to be adopted to prevent this [24, 38]. The bandwidth of this measurement (effectively the inverse total measurement time to the attempt frequency $\omega$) is sufficiently large that the contribution of $1/f$ noise to the switching distribution is expected to be negligible in comparison to the white noise. The fact that Fig. 4.11(b) is linear indicates that the noise is frequency independent, so the above analysis is applicable. The value of the true critical current was found to be 3.67 mA, so the value measured is approximately 4% lower than the true value. The effect of this systematic under-estimate is discussed below.

The return currents can also be treated by a similar analysis to estimate the effect of the noise [39, 40]. Generally the return currents are less susceptible to thermal noise than the critical currents [41], so it is more difficult to measure their distribution. The 2 $\mu$m 30% Ca doped junction was found to have a non-thermal current distribution. A possible cause of this problem is that shot noise makes a significant contribution to the noise across the junction. Likharev identifies the limit at which shot noise becomes important as voltages above 0.5 mV at 4.2 K [41]. This is comparable to the return voltage across the junction when it switches back (0.48 mV in zero field).

Assuming that the effect of the noise on the return current is comparable to its effect on the critical current (i.e. the measured return current is 4% above the true return current) the systematic error in the capacitance can be estimated. This assumption will over-estimate the effect of noise on the measurement, since the critical current distribution is generally broader than the return current distribution for a given noise temperature. The 4% errors in both the critical and return current translate to a 25% systematic under-estimate of the capacitance. While this is significant, it is much less than the 500% increases in the capacitance observed as the calcium doping is increased from 0% to 30% (see Fig. 4.12). The error is also consistent, as the capacitance of the junctions scales well with the track width (see Fig. 4.10) and is approximately temperature independent (see Fig. 4.9). This consistency occurs because the noise temperature is larger than the measurement temperature in all cases and indicates that the noise is fundamental to our measurement apparatus.

Thermal noise therefore produces a significant, but consistent underestimate of the capacitance. The measured capacitance is likely to be approximately 75% of the true value in the absence of thermal noise. This is

significantly less than the 500% increase in the capacitance observed as the Ca doping is changed.

In summary measurements of the junction capacitance from the current–voltage hysteresis demonstrate that it is dominated by the substrate at low frequencies. By measuring the capacitance at higher frequencies the intrinsic grain boundary capacitance can be determined. The results obtained from hysteresis measurements on the 30% Calcium doped junctions are in qualitative agreement with the data from Fiske resonances, although the resonances themselves all occur in the low frequency, substrate dominated regime and so cannot be used to extract the capacitance. The temperature dependence of the capacitance was measured for all the junctions in this study. For the undoped 2 $\mu$m wide junction the capacitance was measured up to 40 K and was found to be temperature independent, this is further evidence that the technique is viable. There was some indication that heating may be significant, particularly in the case of the 30% Calcium doped 2 $\mu$m junction which had the highest critical current density of all the junctions measured in this study. Calculations of the temperature rises associated with heating of the junctions revealed that this junction had the largest heating effect. A self-consistent picture emerges from these measurements and indicates that it is possible to measure the grain boundary capacitance using the junction hysteresis. The major error associated with this technique is due to suppression of the junction hysteresis by thermal noise. The effect of thermal noise can be estimated by measuring the distribution of critical currents obtained from sequential measurements. Such a measurement demonstrates that thermal noise produces a systematic under-estimate of the capacitance of approximately 25%, which is much less than the 500% increase in the capacitance observed in the next section.

## 4.4 Capacitance as a Function of Doping

Fig. 4.12 shows the transport and normal state properties of the films measured at 4.2 K, together with the capacitance, as measured by the junction hysteresis. The previous discussion has demonstrated that both heating and parasitic substrate capacitances do not effect the results. The effect of thermal noise is that the measured capacitances are approximately 25% less than the true values, and this should be considered when interpreting the results. Note also that there are further systematic errors associated with the accuracy of measuring the size of the tracks and the film thickness, which, together with the random errors associated with determining the return cur-

rent and the critical current, amount to approximately 15% of the measured capacitance values.

There is a clear trend of increasing capacitance per unit area, decreasing resistance-area product and increasing critical current density as the calcium doping in the films is increased. The results, including the scatter in the data, are consistent with the previous work by Schneider *et al.* [6]. The capacitance of the junctions increases from 0.2 $\mathrm{Fm}^{-2}$ for the undoped sample to a maximum value of 1.2 $\mathrm{Fm}^{-2}$ for the 30% doped sample.

## 4.5 Discussion

The measured values of the grain boundary capacitance for doped and undoped samples can now be compared with the other properties of the boundaries — to gain further insight into their nature.

The undoped boundaries had a capacitance of 0.2 $\mathrm{Fm}^{-2}$, similar to the value of 0.1 $\mathrm{Fm}^{-2}$ predicted by Mannhart and Hilgenkamp using the band bending model [12]. A similar approach is used to consider the results from the undoped film. The capacitance per unit area, $C/A$, is related to the barrier thickness, $t$, by the simple relation: $C/A = (\varepsilon_r \varepsilon_0)/t$, where $\varepsilon_r$ is the relative dielectric constant, and $\varepsilon_0$ is the permittivity of free space. The barrier thickness, $t$, is made up of two depletion regions, width $l_d$, and the structural width of the boundary, $d$ ($t = 2l_d + d$). $d$ has been measured by TEM and was found to be a few atomic spacings, independent of misorientation angle [42]. The width of the boundary is assumed to be $d \approx 0.2$ nm and the dielectric constant is taken as $\varepsilon_r \approx 20$, a value well within the range of values in the literature [12]. The capacitance per unit area measured in this study for undoped boundaries is 0.2 $\mathrm{Fm}^{-2}$. Assuming a uniform barrier it is possible to calculate the width of the depletion region: $l_d = 0.3$ nm. The built in voltage, $V_{bi}$, is related to $l_d$ by $V_{bi} = l_d^2 en/2\varepsilon_0\varepsilon_r$, where $e$ is the electronic charge and n is the carrier density ($4.5 \times 10^{27}$ $\mathrm{m}^{-3}$ for $YBa_2Cu_3O_{7-\delta}$). Using this relation a value of $V_{bi} = 0.2$ V is calculated. The built in voltage and the measured capacitance can be used to calculate the charge on the boundary, which in turn enables an estimate of the number of charge trapping sites per unit area of the boundary, $S_{GB}$. In this case $S_{GB} = 3 \times 10^{17}$ $\mathrm{m}^{-2}$ (using $S_{GB} = CV/eA$). This value is within an order of magnitude of that predicted by Browning on the basis of the structural unit model [43].

A uniform boundary with a capacitance per unit area of 1.0 $\mathrm{Fm}^2$ (the capacitance of the 30% doped boundaries) has a total width, $t$, of 0.2 nm, if $\varepsilon_r$ is 20. However it is not possible to conclude that the Ca doping has completely eliminated the charge on the boundary (leaving just the structural

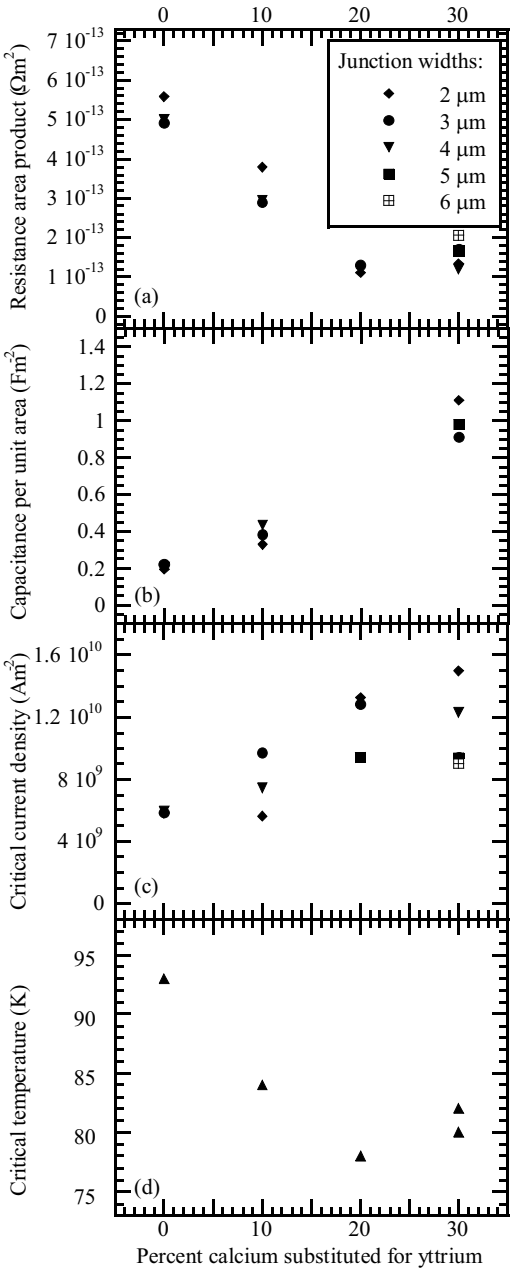


Figure 4.12: Dependence of (a) the normal resistance area product, (b) the capacitance per unit area, (c) the critical current density and (d) the critical temperature, on the amount of calcium doping. (a) to (c) were measured with the samples immersed in liquid helium at atmospheric pressure. The different symbols correspond to junctions of different widths. Experimental errors are approximately 15% of the measured value in (a) and (c) and 1 K in (d). The errors in (b) are discussed in more detail in sections 4.3 - 4.4.

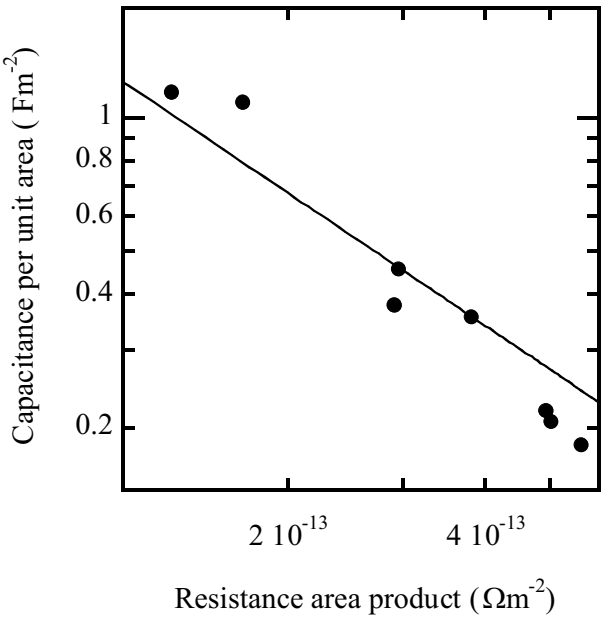


Figure 4.13: Capacitance per unit area shown against resistance area product at 4.2 K for all the junctions measured in this study. The solid line shows the relation $C/A \propto 1/R_nA$.

width of the boundary), since the observed decrease in resistance is too small. A four fold decrease in the width of the barrier would produce an extremely large decrease in the barrier resistance, which is exponentially dependent on the barrier width. The relationship between the resistance and the capacitance as the doping is varied is shown in Fig. 4.13. This relationship is well approximated by the following equation:

$$C/A \propto \frac{1}{R_n A}. \tag{4.7}$$

Such a relationship is inconsistent with a simple model of the grain boundary in which the tunnel barrier is homogenous across the width of the junction. The change in the capacitance is much too large for the observed changes in the normal state resistance. The data does not, however, rule out a tunnelling model because of the extremely inhomogeneous nature of grain boundaries in $YBa_2Cu_3O_{7-\delta}$. The microstructure of grain boundaries in thin film samples is typically very complex [44, 45], with structures that include nanoscale facetting [46, 42] and microscale meandering [47] of the grain boundary. The capacitance per unit area of the grain boundary scales as the inverse of the boundary thickness ($C/A = (\varepsilon_r \varepsilon_0)/t$) whilst the resistance area product will, to a good approximation, scale as $R_n A \propto \mathrm{e}^{-At}$, where $A$ is some tunneling constant. The resistance area product will therefore be dominated by contributions from the narrowest regions of the barrier [48], whilst the capacitance is sensitive to the entire width of the barrier. With inhomogeneities on many length scales it is difficult to predict the expected relationship between the normal resistance area product and the capacitance per unit area, but it is clear that the capacitance will change more rapidly in relation to the resistance area product than a simple one dimensional model would predict. The relationship between capacitance per unit area and resistance area product given in Equation 4.7 has been observed by a number of authors with various grain boundary geometries [22, 49]. Such a relationship is consistent with changes in the effective area of the boundary. This may imply that the narrowest regions of the boundary dominate both the capacitance and the normal resistance and that the proportion of these regions is increasing as calcium is added. Such a conclusion is necessarily tentative. A possibility within a band bending context is that the charge on the boundary is inhomogeneous along its length — with some parts of the electrical barrier being relatively unaffected by band bending. The addition of Calcium may reduce the charge and hence the boundary width on the other areas of the boundary and therefore effectively increase the active area of the boundary.

The interpretation of the capacitance data is further complicated since it is not clear how the addition of Calcium alters the dielectric constant

of the barrier region. Despite such difficulties in interpretation, it is clear that calcium doping produces a definite increase in the capacitance of the boundary.

## 4.6 Summary

The capacitance of 24° [001] tilt Calcium doped $Y_{1-x}Ca_xBa_2Cu_3O_{7-\delta}$ grain boundaries has been measured for thin films with $x$ in the range 0.0 to 0.3. The capacitance was determined from the hysteresis in the $I$–$V$ characteristic. By measuring the capacitance as a function of the voltage across the junction it was possible to observe the contribution of both parasitic substrate capacitance and heating to the hysteresis. At 4.2 K, the substrate contributes to the capacitance at return voltages below approximately 0.25 mV. Heating can increase the measured capacitance at high bias voltages and heating effects were observed in one of the junctions measured. However, since the effects of heating and the substrate could be observed in the measurement it was possible to eliminate them by using values of the measured capacitance in the regime where they had no effect. The effect of thermal noise on the measurement was assessed and is an order of magnitude less than the observed changes in capacitance. The grain boundary capacitance increased from 0.2 $\mathrm{Fm}^{-2}$ for $x = 0$ to a maximum value of 1.2 $\mathrm{Fm}^{-2}$ for $x = 0.3$. Due to the complex structure of the boundaries, and in the absence of knowledge of how doping effects the dielectric constant, it is difficult to make definite conclusions about how these capacitance changes relate to changes in the boundary's electrical structure. However, the results do seem consistent with changes in the effective area of the boundary occurring as Calcium is added.

# Bibliography


[1] D. Dimos, P. Chaudhari, J. Mannhart, and F. K. Legoues, Physical Review Letters **61**, 219 (1988).

[2] D. Dimos, P. Chaudhari, and J. Mannhart, Physical Review B **41**, 4038 (1990).

[3] P. Chaudhari et al., Physical Review Letters **53**, 1653 (1988).

[4] H. Hilgenkamp and J. Mannhart, Reviews of Modern Physics **74**, 485 (2002).

[5] A. Schmehl et al., Europhysics Letters **47**, 110 (1999).

[6] C. W. Schneider et al., Applied Physics Letters **75**, 850 (1999).

[7] J. Mannhart et al., Physica C **341-348**, 1393 (2000).

[8] G. Hammerl et al., Nature **407**, 162 (2000).

[9] G. A. Daniels, A. Guerevich, and D. C. Larbalestier, Applied Physics Letters **77**, 3251 (2000).

[10] K. Guth, H. U. Krebs, H. C. Freyhardt, and C. Jooss, Physical Review B **64**, 140508(R) (2001).

[11] A. Weber et al., Applied Physics Letters **82**, 772 (2003).

[12] J. Mannhart and H. Hilgenkamp, Materials Science and Engineering B **56**, 77 (1998).

[13] For example at MRS Fall 2002, R. F. Klie (talk Z1.1) and Y. Zhu (talk Z1.8) presented conflicting transmission electron microscopy results on the sign of the band bending in $YBa_2Cu_3O_{7-\delta}$.

[14] D. Winkler, Y. M. Zhang, P. A. Nilsson, E. A. Sperantsov, and T. Claeson, Physical Review Letters **72**, 1260 (1994).

[15] A. Beck et al., IEEE Transactions on Applied Superconductivity **5**, 2192 (1995).

[16] Y. M. Zhang, D. Winkler, G. Brorsson, and T. Claeson, IEEE Transactions on Applied Superconductivity **5**, 2200 (1995).

[17] K. Nakajima, K. Yokota, H. Myoren, J. Chen, and T. Yamashita, IEEE Transactions on Applied Superconductivity **5**, 2861 (1995).

[18] E. J. Tarte et al., IEEE Transactions on Applied Superconductivity **11**, 3662 (1997).

[19] M. G. Medici et al., Journal of Superconductivity **11**, 225 (1998).

[20] P. F. McBrien et al., Physica C **339**, 88 (2000).

[21] E. J. Tarte et al., Physica B **284-288**, 628 (2000).

[22] E. J. Tarte et al., IEEE Transactions on Applied Superconductivity **11**, 418 (2001).

[23] W. J. Skockpol, M. R. Beasley, and M. Tinkham, Journal of Applied Physics **45**, 4054 (1974).

[24] T. A. Fulton and L. N. Dunkleberger, Physical Review B **9**, 4760 (1968).

[25] S. Proyer, E. Stangl, M. Borz, B. Hellebrand, and D. Bauerle, Physica C **257**, 1 (1996).

[26] R. G. Buckley et al., Physica C **174**, 383 (1991).

[27] J. T. Kucera and J. C. Bravman, Physical Review B **51**, 8582 (1995).

[28] C. Greaves and P. R. Slater, Superconductor Science and Technology **2**, 5 (1989).

[29] A. Manthiram, S. J. Lee, and J. B. Goodenough, Journal of Solid State Chemistry **73**, 278 (1988).

[30] Q. D. Jiang et al., Physical Review B **56**, 6947 (1997).

[31] E. B. McDaniel, S. C. Gausepohl, C.-T. Li, M. Lee, and J. W. P. Hsu, Applied Physics Letters **70**, 1882 (1997).

[32] E. B. McDaniel and J. W. P. Hsu, Journal of Applied Physics **84**, 189 (1998).

[33] J. W. P. Hsu et al., IEEE Transactions on Applied Superconductivity **9**, 3413 (1999).

[34] D. E. McCumber, Journal of Applied Physics **39**, 3113 (1968).

[35] R. C. Neville, B. Hoeneisen, and C. A. Mead, Journal of Applied Physics **43**, 2124 (1972).

[36] R. C. Neville, B. Hoeneisen, and C. A. Mead, Journal of Applied Physics **43**, 3903 (1972).

[37] H. A. Kramers, Physica **7**, 284 (1968).

[38] M. G. Castellano et al., Journal of Applied Physics **80**, 2922 (1996).

[39] J. R. Kirtley et al., Physical Review Letters **61**, 2372 (1988).

[40] M. G. Castellano et al., Journal of Applied Physics **86**, 6405 (1999).

[41] K. K. Likharev, *Dynamics of Josephson Junctions and Circuits*, Gordon and Breach Publishers, Amsterdam, 1986.

[42] Q. Jin and S.-W. Chan, Journal of Materials Research **17**, 323 (2002).

[43] N. D. Browning, J. P. Burban, C. Prouteau, G. Duscher, and S. J. Pennycook, Micron **30**, 425 (1999).

[44] C. Tæholt, J. G. Wen, H. W. Zandebergen, Y. Shen, and J. W. M. Hilgenkamp, Physica C **230**, 425 (1994).

[45] J. L. Alarco et al., Physica C **247**, 263 (1993).

[46] S.-W. Chan, Q. Jin, J. W. H. Tsai, S. C. Tidrow, and Q. Jiang, IEEE Transactions on Applied Superconductivity **13**, 2829 (2003).

[47] D. J. Miller et al., Applied Physics Letters **66**, 2561 (1995).

[48] J. Mannhart, A. Kleinsasser, J. Strobel, and A. Baratoff, Physica C **216**, 401 (1993).

[49] B. Moeckly and R. A. Buhrman, Applied Physics Letters **65**, 3126 (1994).

# Chapter 5

# Measuring the Normal State Properties of $YBa_2Cu_3O_{7-\delta}$ Grain Boundaries

In previous studies of the transport properties of $YBa_2Cu_3O_{7-\delta}$ grain boundaries measurements have been performed below the critical temperature, $T_c$ [1]. The absence of any data for the normal state properties of $YBa_2Cu_3O_{7-\delta}$ grain boundaries was the motivation for developing a technique to measure grain boundary properties above $T_c$. This is not a simple task, since the resistance of a $0.1 \times 2\,\mu m^2$ 24 °[001] tilt grain boundary ($4\,\Omega$ at 290 K, as measured in this work) is significantly less than the resistance of even very short adjoining tracks ($\approx 33\,\Omega$ for a 0.1 $\mu$m thick square section at 290 K [2]). The normal state properties cannot, therefore, be accurately measured with the standard four point technique. However, if the resistance of the adjoining tracks is compensated, by means of a Wheatstone bridge structure [3, 4, 5], it is possible to measure accurately the properties of isolated grain boundaries. In this chapter the development of this technique for use on $YBa_2Cu_3O_{7-\delta}$ grain boundaries is described.

## 5.1 The Wheatstone Bridge Technique

The technique employed to isolate the grain boundary resistance is derived from the simple concept of a Wheatstone bridge. As shown in Fig. 5.1a, if a bridge is fabricated with identical arms (resistance $R$) then in the standard configuration the measured voltage is zero. This can be realised in practice by fabricating a bridge in which each of the four arms are composed of identically patterned regions of a uniform thin film.

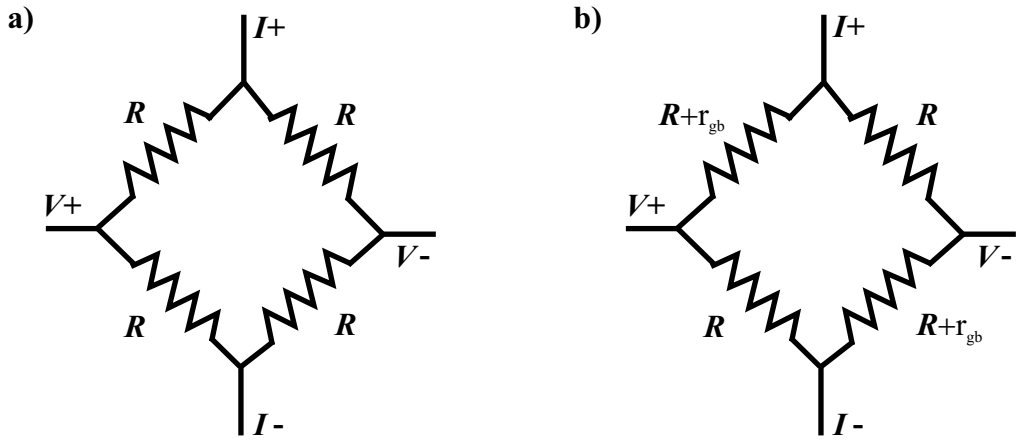


Figure 5.1: Diagrams illustrating the concept of the Wheatstone bridge device. a) If a bridge is fabricated with arms of identical resistance, $R$, then the measured voltage is zero. b) If an additional grain boundary resistance, $r_{gb}$, is added in each arm the voltage measured is $Ir_{gb}/2$ for applied current $I$.

If an additional grain boundary resistance, $r_{gb}$, is added in series with two arms of the bridge in a non symmetric manner, as shown in Fig 5.1b, then a voltage is developed across the structure. In practice this is achieved by carefully aligning a patterned bridge across a grain boundary, so that the grain boundary contributes additional resistance asymmetrically to two arms of the bridge. It is straightforward to show that the ratio of the measured voltage, $V$, to the applied current, $I$, is then given by:

$$\frac{V}{I} = -\frac{r_{gb}}{2} \tag{5.1}$$

This technique was first used by Mathur *et al.* [3] to measure the magnetoresistance of $La_{0.7}Ca_{0.3}MnO_3$ grain boundaries. We performed several experiments to find the best structure for use with $YBa_2Cu_3O_{7-\delta}$ grain boundaries and to understand the sources of error in the technique. These experiments are discussed in the next section.

## 5.2 Optimising the Properties of the Bridges

In practice it is not possible to fabricate perfectly symmetric bridge structures. In the absence of the grain boundary, imbalance is caused by asymmetries due to film inhomogeneity and the lithographic resolution. Fabricating sufficiently balanced bridges in $YBa_2Cu_3O_{7-\delta}$ is more challenging than doing

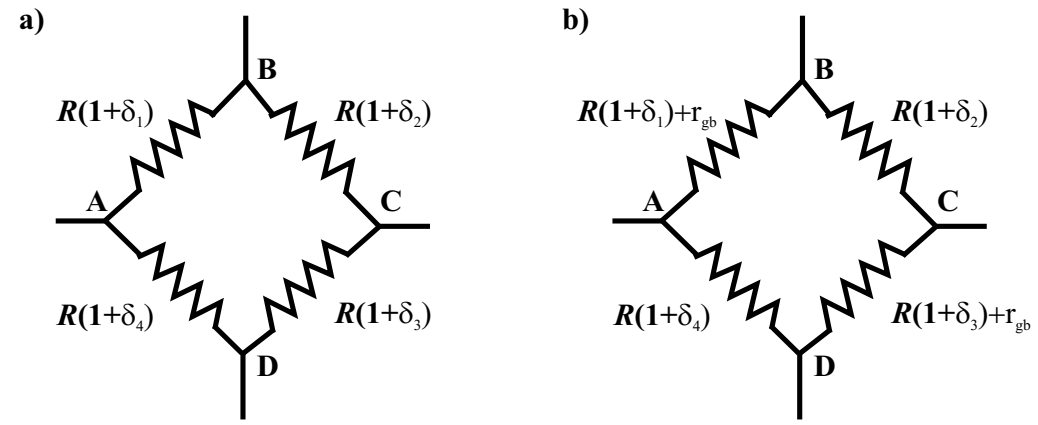


Figure 5.2: Circuit diagram for bridges containing imperfections. a) An off grain boundary bridge. b) A bridge aligned with a grain boundary. Each arm of the bridge contains a small imperfection, changing its resistance from the mean value $R$ to $R(1+\delta_x)$, where $\delta_x \ll 1$.

so for $La_{0.7}Ca_{0.3}MnO_3$ boundaries, because the bulk material has a higher resistance (so that lithographic inhomogeneities in the bridges produce a greater absolute change in their resistance) and the grain boundaries have a lower resistance (which means that the bridges must be better balanced for the grain boundary signal to be greater than that of the bridge alone). It is therefore necessary to consider in detail the effect of such asymmetries on the signal measured by a bridge and to understand their source in our experiments.

### 5.2.1 Imperfect Bridges

Figure 5.2a shows the circuit diagram for a bridge with small asymmetries due to imperfections in fabrication. Each arm of the bridge contains a small imperfection, changing its resistance from the mean value $R$ to $R(1+\delta_x)$, where $\delta_x \ll 1$. A current $I$ is applied between the points B and D. The voltage $V_{AC}$ measured between points A and C is given by:

$$V_{AC} = IR\frac{(2+\delta_1+\delta_4)(2+\delta_2+\delta_3)}{4+\delta_1+\delta_2+\delta_3+\delta_4}\left(\frac{1+\delta_4}{2+\delta_4+\delta_1}-\frac{1+\delta_3}{2+\delta_2+\delta_3}\right) \qquad (5.2)$$

By Taylor expanding the quotients and neglecting terms of order $\delta_x^2$ the following result is obtained:

$$V_{AC} \approx \frac{IR}{4}(\delta_2+\delta_4-\delta_1-\delta_3) \qquad (5.3)$$

Similarly, if current $I$ is applied between points A and B the voltage measured between D and C, $V^*_{DC}$, is given by:

$$V^*_{DC} \approx \frac{IR}{4}\left(1 + \frac{3}{4}(\delta_1 + \delta_3) - \frac{1}{4}(\delta_2 + \delta_4)\right) \tag{5.4}$$

If the same current is applied between B and C, the voltage measured between A and D, $V^*_{AD}$, is:

$$V^*_{AD} \approx \frac{IR}{4}\left(1 + \frac{3}{4}(\delta_2 + \delta_3) - \frac{1}{4}(\delta_1 + \delta_3)\right) \tag{5.5}$$

Since by definition $\delta_1 + \delta_2 + \delta_3 + \delta_4 = 0$, the mean resistance of an arm $R$ is given by:

$$R = 2\frac{V^*_{AD} + V^*_{DC}}{I} \tag{5.6}$$

We define the quantity $\Delta R$:

$$\Delta R = 4\frac{V_{AC}}{I} \tag{5.7}$$

It is clear from Equation 5.3 that $\Delta R$ is of the same order as the quantities $R\delta_x$. It is therefore possible to measure the mean resistance of a single arm and to estimate the size of the resistance deviations from measurements of the bridge in different configurations.

When the bridge is aligned with a grain boundary as shown in Fig. 5.2b the voltage measured between A and C when current is applied between B and D is given by:

$$V_{AC} \approx -\frac{I}{2}\left(r_{gb} + \frac{R}{2}\left(\delta_1 + \delta_3 - \delta_2 - \delta_4\right)\right) \tag{5.8}$$

to first order in $\delta_x$. The resistance, $V_{AC}/I$, of a bridge away from the boundary is therefore a good estimate of the error in $r_{gb}/2$ for an identical bridge patterned on the boundary.

The results derived in this section give useful insights into the properties of the bridge system. Using the above results it is possible to evaluate the properties of single crystal bridges in a non-destructive manner. Both the resistance of a single arm and the magnitude of the differences in resistance between the arms can be determined from measurements of the bridge in different configurations. It is also shown that the errors obtained are applicable when a grain boundary is aligned with the device. In the next section these results are applied to different bridge structures fabricated on single crystal $YBa_2Cu_3O_{7-\delta}$ films.

Table 5.1: Resistance of bridges with different geometries fabricated on a single crystal $YBa_2Cu_3O_{7-\delta}$ film, nominally 100nm thick. The various bridge geometries are illustrated in Fig. 5.3. The resistance is measured at 290 K.

| **Bridge geometry** | **Fig. 5.3a** | **Fig. 5.3b** | **Fig. 5.3c** | **Fig. 5.3d** |
|---|---|---|---|---|
| $V_{AC}/I$ ($\Omega$) | -6 | $\approx 9^{\dagger}$ | 11 | 69 |
| $R$ ($\Omega$) | 879 | - | 69 | 1232 |
| $\Delta R$ ($\Omega$) | 24 | - | 43 | 275 |

$^{\dagger}$ This bridge was damaged by application of too large a current before the controlled temperature measurement was performed, so the temperature for this measurement is not accurately known, although it is likely to be within a few degrees of 290 K.

### 5.2.2 Bridge Geometry

Bridges of various geometries were fabricated and measured in order to obtain estimates of realistic experimental values of $\Delta R$ in relation to $R$, given our fabrication procedure (the fabrication and measurement procedures are described in chapter 3). The geometries investigated are illustrated in Fig. 5.3, together with the intended location of the grain boundary. Devices were fabricated on a single crystal $YBa_2Cu_3O_{7-\delta}$ film, nominally 100 nm thick and the resistance was measured at 290 K. The results obtained from this preliminary study are shown in Table 5.1.

Several conclusions can be drawn from the results in Table 5.1. Firstly it is clear that the device structure shown in Fig. 5.3a outperforms the other geometries considerably. The quantity of relevance for comparison with the grain boundary resistance is $V_{AC}/I$ (and not $\Delta R$), since it is this measured resistance that will compete with the signal from the grain boundary on a bicrystal sample. The resistance of a single $0.1 \times 2\,\mu$m 24°symmetric boundary is approximately $4\,\Omega$ at 290 K — so a single boundary crossing two arms would contribute a signal of $2\,\Omega$ to each of the bridges (see Equation 5.1). The bridge in Fig. 5.3a is designed so that there are 19 such boundaries in each arm. The estimated total signal obtainable from a device aligned with a grain boundary (34 $\Omega$) is therefore significantly greater than the error signal obtained from this measurement of a single crystal sample. It is equally clear that the bridges shown in Figs. 5.3 c and d are unsuitable - as the measured signal in the case of these devices is significantly greater than the $2\,\Omega$ signal that the single grain boundary per arm would generate. The device shown in Fig. 5.3b may have been damaged during processing, or possibly the bridge

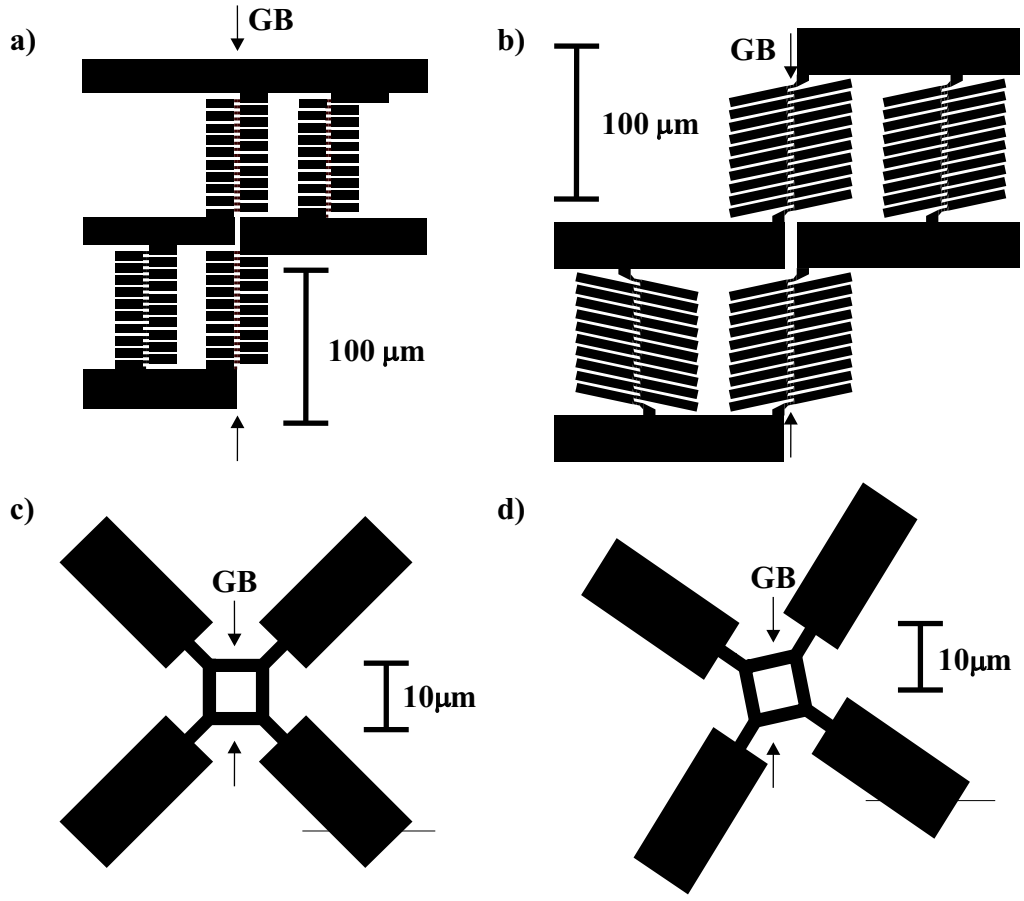


Figure 5.3: Initial devices used to investigate the feasibility of using bridges to measure the normal state properties of the boundary. Bridges with a number of crossings were investigated, running both perpendicular (a) and at an angle to (b) the grain boundary plane. Small bridges consisting of single track arms were also investigated (c and d). For each device the position of the grain boundary is marked by two arrows labelled 'GB'.

arms at different angles milled in an asymmetric manner, producing a large imbalance.

In order to understand the origins of the asymmetries in the bridges we performed a detailed analysis of the resistance of the bridge shown in Fig. 5.3c. On the length scale of this device (10 $\mu$m) the film properties were expected to be uniform, so the principle source of error should be the lithography. We therefore imaged the bridge using an atomic force microscope (Fig. 5.4a) and estimated from this image the resistance of the bridge.

The atomic force microscope (AFM) image in Fig. 5.4a was converted to a black and white image, so that regions above 0.8 $\mu$m in height appeared black, whilst those below appeared white (Fig. 5.4b). The bridge was then split into four different arms (Fig. 5.4c) and these images were resampled to increase their resolution. A vertical array of lines, spaced at intervals of one pixel in the original image, was superimposed on top of these images, producing a bitmap like that shown in Fig. 5.4d. The software package 'Scion Image' was then used to extract the areas of all $n$ segments of the $i$th arm, $A^i_j$ where $j = 1 \ldots n$. The areas $A^i_j$ are proportional to the widths, $w^i_j$, of the individual segments since the segments are all 1 pixel wide. A reasonable approximation to the total resistance of the $i$th arm will be given by the expression:

$$R^i \approx \frac{\rho l}{t} \sum_{j=1}^{n} \frac{1}{w^i_j} \tag{5.9}$$

where $\rho$ is the resistivity of the film, $l$ is the length of a single pixel in the original AFM image and $t$ is the thickness of the film (assumed to be uniform across the device). This expression assumes that the resistance of each segment can be simply added to that of the previous segment. It therefore completely ignores current redistribution effects, but should, nonetheless, produce an order of magnitude estimate of the bridge imbalance. Since in this case the film resistivity was not measured, but the mean resistance of the bridge arms, $R$, was known (see Table 5.1) — it was simpler to normalise the results in the following manner:

$$R^i \approx \frac{4 \sum_{j=1}^{n} \frac{1}{w^i_j}}{\sum_{k=1}^{4} \sum_{j=1}^{n} \frac{1}{w^k_j}} R \tag{5.10}$$

Using Equation 5.5 and 5.7 the value of $\Delta R$ can be estimated from the image using the following expression:

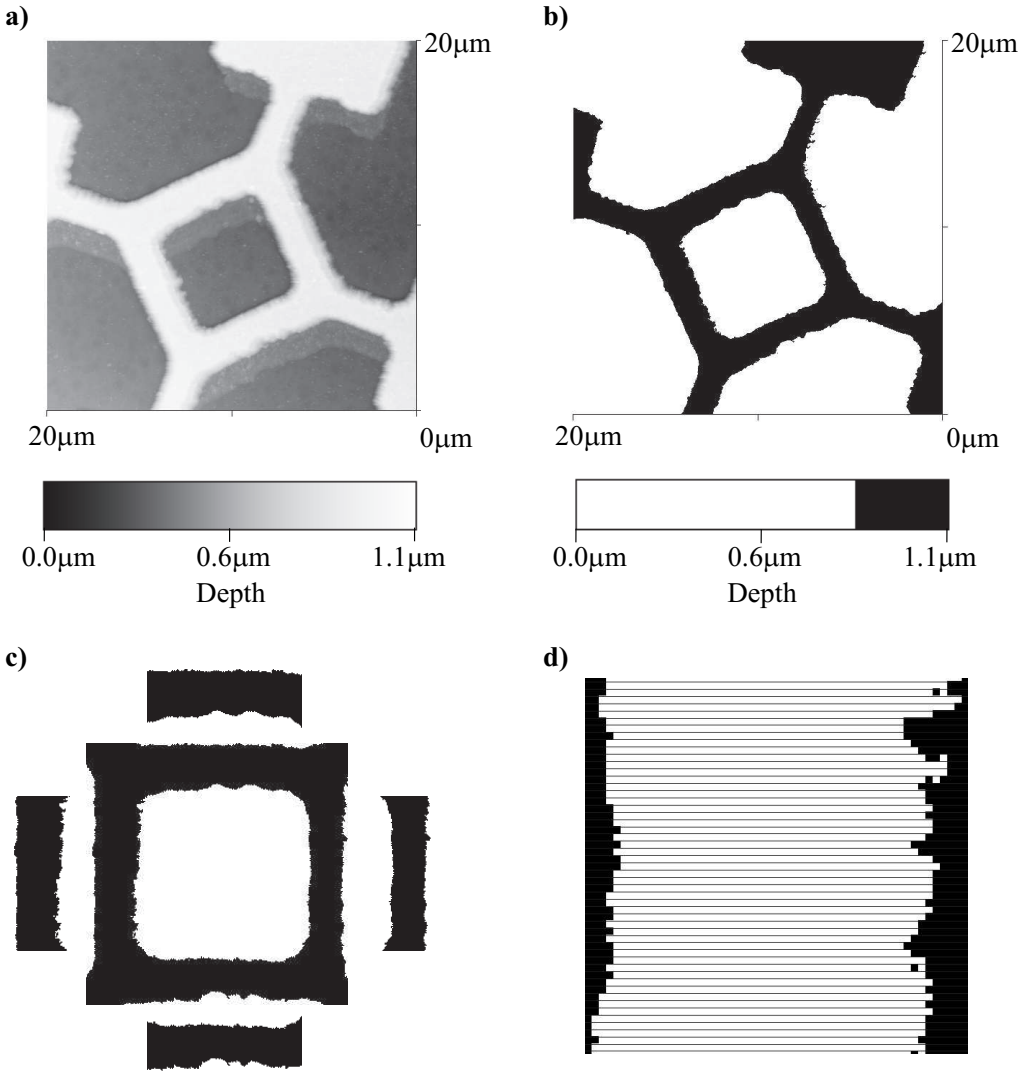


Figure 5.4: Analysis of the small bridge resistance. a) An atomic force microscope image is made of the bridge (image resolution: 512 samples per line, scan rate: 0.5 Hz). b) The image is processed so that the flat regions of the bridge appear black. c) The bridge is separated into individual arms. d) Each bridge is divided into sections and the area of each of these sections is then computed. This area is proportional to the width of the section.

$$\Delta R \approx \frac{4\left(\sum_{j=1}^{n}\frac{1}{w_j^2}+\sum_{j=1}^{n}\frac{1}{w_j^3}-\sum_{j=1}^{n}\frac{1}{w_j^1}-\sum_{j=1}^{n}\frac{1}{w_j^4}-\Gamma\right)}{\Gamma}R \qquad (5.11)$$

where $\Gamma = \sum_{k=1}^{4}\sum_{j=1}^{n}\frac{1}{w_j^k}$.

Applying the above analysis to the device shown in Fig. 5.4, leads to an estimated $\Delta R$ of 19 Ω (or equivalently an estimated $V_{AC}/I$ of 5 Ω) which is approximately half the measured value in Table 5.1. This agreement is relatively good considering the approximations made in the analysis — furthermore the estimated $\Delta R$ is less than the measured value, as expected. An underestimate occurs because the resistance of the corners in Fig. 5.4c was ignored. In addition current redistribution effects will also increase the measured resistance.

The previous discussion demonstrates that, in the case of small bridges, the principle sources of error are asymmetries in the lithography. With a short track these inhomogeneities can lead to relatively large changes in the resistance of the track and so small devices are not optimum. The device shown in Figure 5.3a, consists of a $n$ smaller tracks in series, with a total grain boundary resistance of $nr_{gb}$. As the value of $n$ increases, the standard deviation of the total resistance increases as $\sqrt{n}$ but the total grain boundary resistance increases as $n$. The signal to noise ratio is therefore predicted to increase as $\sqrt{n}$. For this reason we decided to investigate bridges similar to that shown in Fig. 5.3a, but of increasing length, to further improve the technique.

### 5.2.3 Bridge Length

A mask with a number of similar bridges, each with a different number of grain boundary crossings per arm, was designed in order to further optimise the bridge structure. The 3 device geometries investigated are illustrated in Fig. 5.5. Note that these structures have several improvements over the device shown in Fig. 5.3a. The voltage taps in the center of the device are located symmetrically with respect to the arms above and below them. The region of track with these voltage taps has also been lengthened, to ensure that current redistribution effects do not cause asymmetry in the resistance of the arms above and below it (current coming into the left hand track follows a 'u' shaped path, turning back on itself, whilst current leaving the track follows a dogleg). In addition to this, many of the sharp corners in the device have been rounded, to facilitate more consistent processing (this is difficult to see in the figure).

Table 5.2: Effect of varying the number of grain boundary crossings on the spread in resistance of bridges fabricated on single crystal films. The standard deviation of the resistance of bridges of each type, $\sigma_{n-1}$, is given.

| **Bridge Geometry** | **Fig. 5.5a** | **Fig. 5.5b** | **Fig. 5.5c** |
|---|---|---|---|
| **Crossings per arm of bridge** | 11 | 21 | 41 |
| $\sigma_{n-1}$ **at 250 K** ($\Omega$) | 33.8 | 5.8 | 62.3 |
| $\sigma_{n-1}$ **at 150 K** ($\Omega$) | 22.0 | 3.7 | 40.6 |

These structures were patterned onto a number of films grown under identical conditions. The resistance of the devices was then measured as a function of temperature (the fabrication and measurement of these devices was performed by S. H. Mennema, using the procedures described in chapter 3). For this experiment 8 devices were fabricated on each substrate so more detailed statistics could be obtained. The best estimate of the population standard deviation for the resistance of this group of bridges, $\sigma_{n-1}$, is shown in Table 5.2. The resistance of the devices was found to vary with temperature in the same way as a $YBa_2Cu_3O_{7-\delta}$ track (the critical temperatures of the films were between 87 and 89 K). This indicates that the inhomogeneities in the structure result from normal $YBa_2Cu_3O_{7-\delta}$.

The results from Table 5.2 indicate that the geometry in 5.5b is optimum. As the device size increases a larger portion of the film is sampled so film inhomogeneities become an increasing problem. This is the likely reason for the larger standard deviation of the devices depicted in Fig. 5.5c. The standard deviation of the devices shown in Fig. 5.5a is significantly greater than $\sqrt{2}$ times those in 5.5b (as would be expected from the statistics discussed in the previous section). It therefore seems that the signal to noise ratio does not follow the simple $\sqrt{n}$ relationship proposed in the previous section. It is likely that there is a more complex interplay between film homogeneity, lithography and device design for these larger structures.

The structure in Fig. 5.5b, with 21 crossings per arm of the bridge, was used as the basis for the remainder of this investigation, since the results above indicate that such a structure is optimal. Figure 5.6 shows the final mask design adopted for the remainder of this study. 8 Bridges in total are arranged on the mask, 5 aligned with the grain boundary and 3 away from it (to serve as controls). In addition to these there are 3 tracks (2 crossing the boundary and 1 not) to facilitate standard, 4 point, measurements of the both the grain boundary $I$–$V$ characteristics and the single crystal $R$–$T$ characteristics. The bridges are labelled B1 to B8 and the tracks T1 to T3.

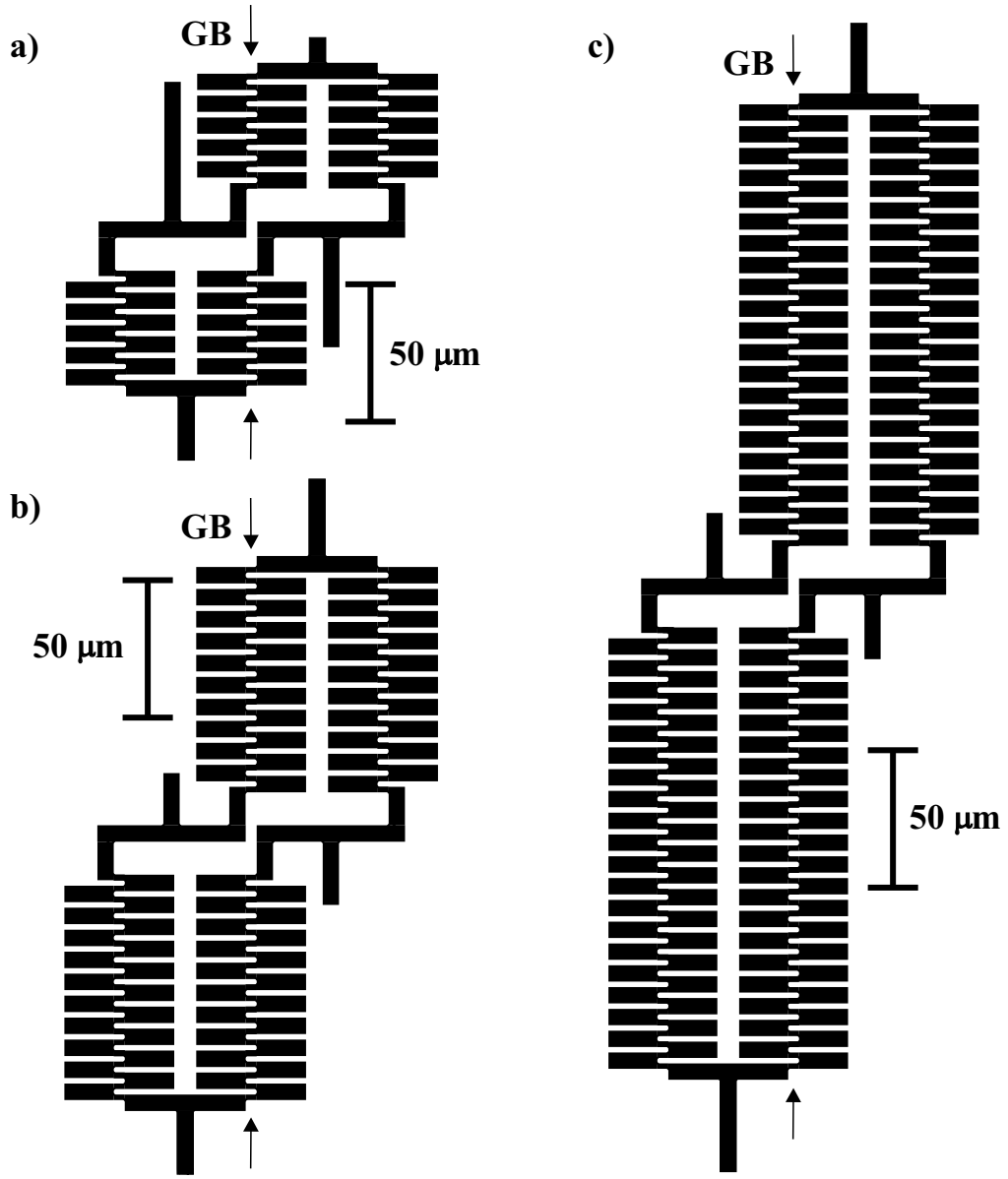


Figure 5.5: Mask design used to investigate the effect of varying the length of the bridges. Bridges with a) 11, b) 21 and c) 41 traverses of the grain boundary per arm were investigated. In each case the position of the grain boundary is marked by two arrows labelled 'GB'.

The resolution of the bridge technique, using this mask, is assessed in the next section.

## 5.3 Resolution of the Technique

A single crystal film was grown at LG Electronics, in order to determine the resolution of the technique with devices fabricated in our experimental facilities. This film was patterned with the mask design shown in Fig. 5.6 and the resistance of each bridge was measured between room temperature and the critical temperature with a current bias of 5 $\mu$A (the equipment used is described in Chapter 3). The measured resistance ($R_m$) was then normalised as it would be were a grain boundary present in the bridge to produce the equivalent resistance area product $R_{eq}A$, defined by:

$$R_{eq}A = \frac{2R_m wt}{n} \tag{5.12}$$

where $w$ is the width of the narrow tracks in the center of each bridge arm (measured by atomic force microscopy), $t$ is the film thickness (measured by atomic force microscopy on a wet-etched step) and $n$ is the number of crossings per arm of the grain boundary (in this case 21). The factor $n$ is present because, were the pattern to be aligned with a grain boundary, there would be $n$ boundary resistances contributing in series to the additional resistance in each grain boundary arm. By normalising the data in this manner the results obtained are directly comparable to the resistance area product of a grain boundary.

The mean resistance of the devices in Fig. 5.7 at 250 K is $(-5 \pm 4) \times 10^{-14}$ $\Omega$m$^2$. This value is sufficiently close to zero to indicate that there is no significant systematic imbalance in the bridge structure adopted. The variation of the bridge resistance is also not correlated with the position of the bridge on the sample (see Fig. 5.6 for the positions of bridges 1 to 8 along the grain boundary), which indicates that systematics associated with variations in film properties are also not significant. For the bridges with larger resistance, the variation of the resistance with temperature is similar in form to that characteristic of bulk, optimally doped $YBa_2Cu_3O_{7-\delta}$, which indicates that the main contribution to the imbalance is from such material. It is clear that the technique is sensitive to resistance area products of order $1 \times 10^{-13}$ $\Omega$m$^2$, which corresponds to 15° [001] tilt boundaries [6]. It should be noted that this is not necessarily the ultimate resolution of the technique — with improved lithography and film homogeneity it may be possible to significantly improve the quality of the bridges.

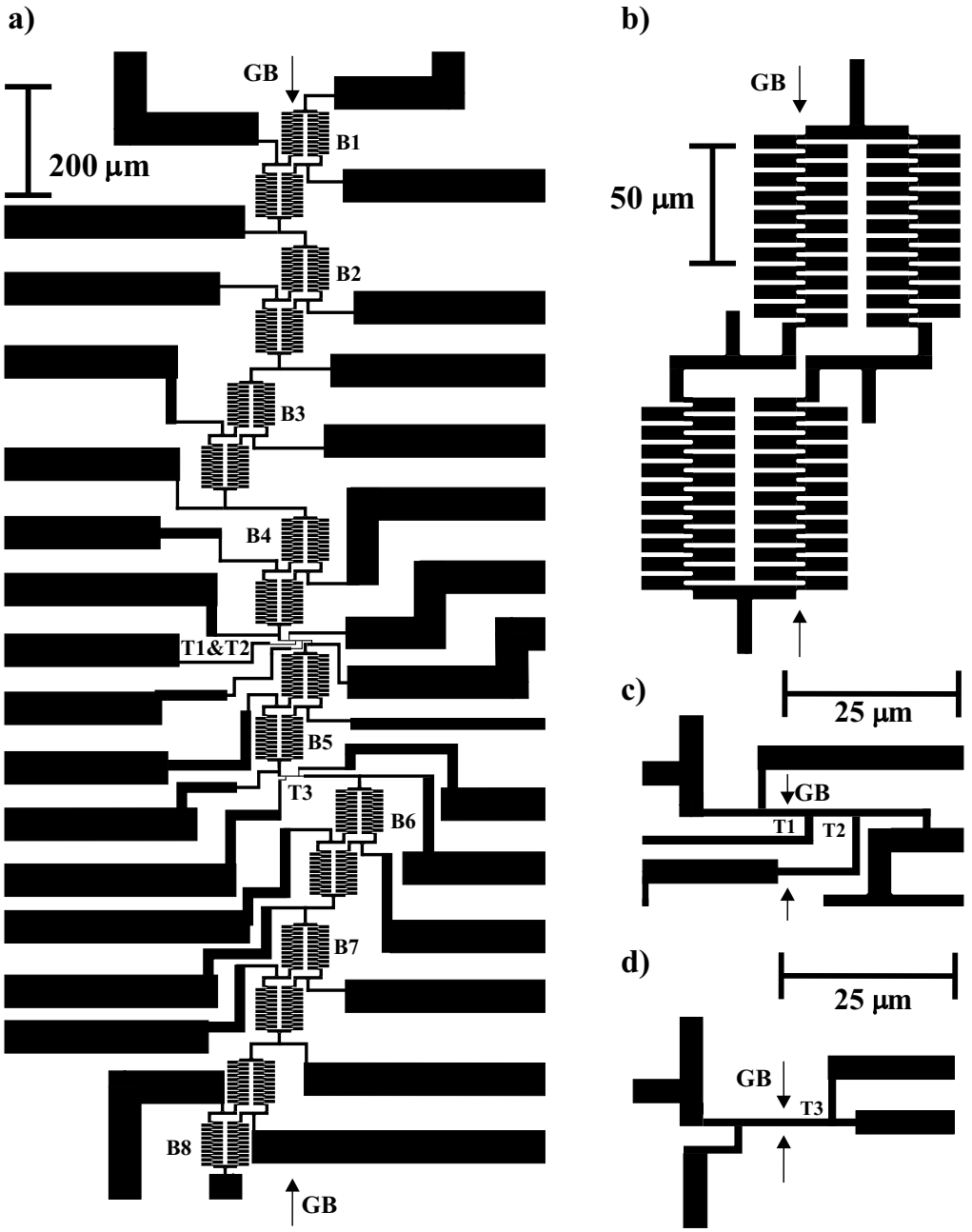


Figure 5.6: Chip layout and device structure adopted for the experiments reported in the remainder of this chapter. a) Detail of the central region of the chip, showing the individual bridges and tracks as they are arranged down the grain boundary. Bridges are marked B1, B2... whilst tracks are marked T1, T2... b) Detail of the bridge structure. c) Detail of tracks 1 and 2. d) Detail of track 3. In all panels the position of the grain boundary is marked by two arrows labelled 'GB'.

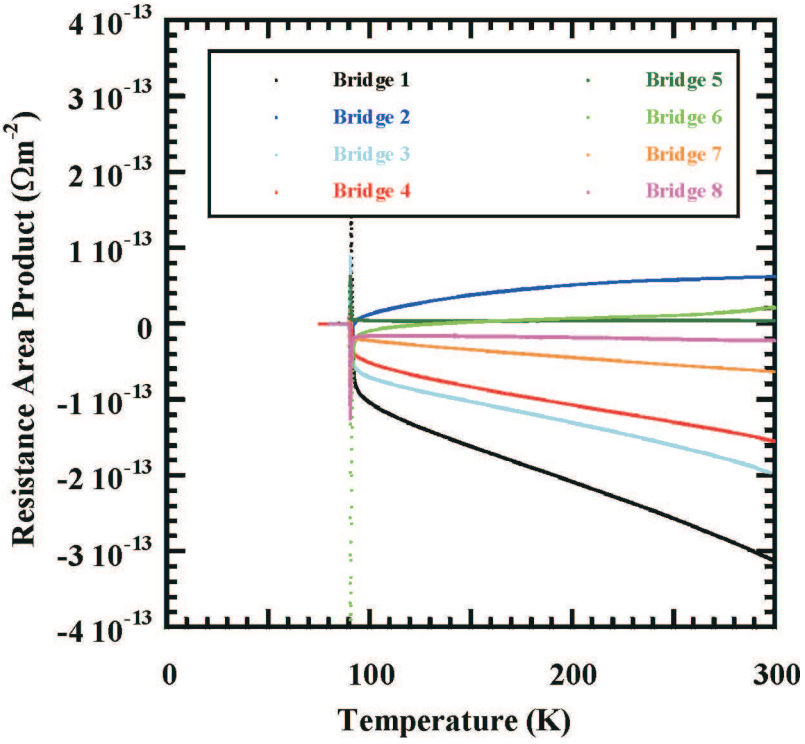


Figure 5.7: Equivalent resistance area product shown against temperature for 8 devices patterned on a single crystal substrate. The devices are named according to the convention set out in Fig. 5.6.

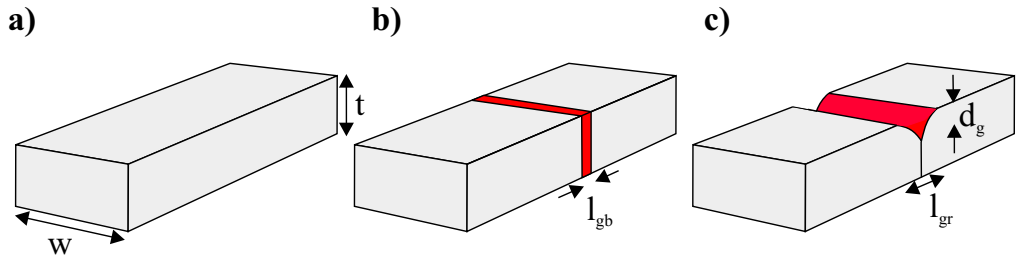


Figure 5.8: Grain boundary related sources of systematic error in a bridge. The figures show cross sections of tracks from part of a Wheatstone bridge structure. a) A track on a compensating bridge arm away from the boundary. b) When a grain boundary is aligned with the track the boundary itself occupies a small volume of the track (shown in red). There is thus a missing volume of normal track that is over-compensated by the balancing arm of the bridge. c) Since there is a groove associated with the boundary — the film thickness in the region of the boundary is slightly depressed. This means that there is a higher resistance portion of track associated with each grain boundary.

In conclusion the results from single crystal bridges indicate that, given the currently available facilities, it is possible to measure resistance area products of order $1\times10^{-13}\ \Omega\mathrm{m}^2$, with a signal to noise ratio of 1. However, the addition of a grain boundary to the system may add additional, systematic errors to the bridge devices. These sources of error are discussed in the next section.

## 5.4 Further Possible Sources of Error

In addition to the sources of error discussed above, further systematics occur when a grain boundary is aligned with the bridges. Errors are caused by the finite volume of the grain boundary itself, and by the inter-grain groove associated with the boundary. These sources of error are illustrated in Fig. 5.8. Additionally heating of the grain boundary may lead to errors.

The finite volume of the grain boundary means that a small volume of normal track is missing from the track that the boundary crosses. This means that the measured resistance area product, $R_mA$, of the boundary is given by:

$$R_mA = R_nA - l_{gb}\rho \tag{5.13}$$

where $\rho$ is the resistivity of the film and the other symbols are as defined in Fig. 5.8.

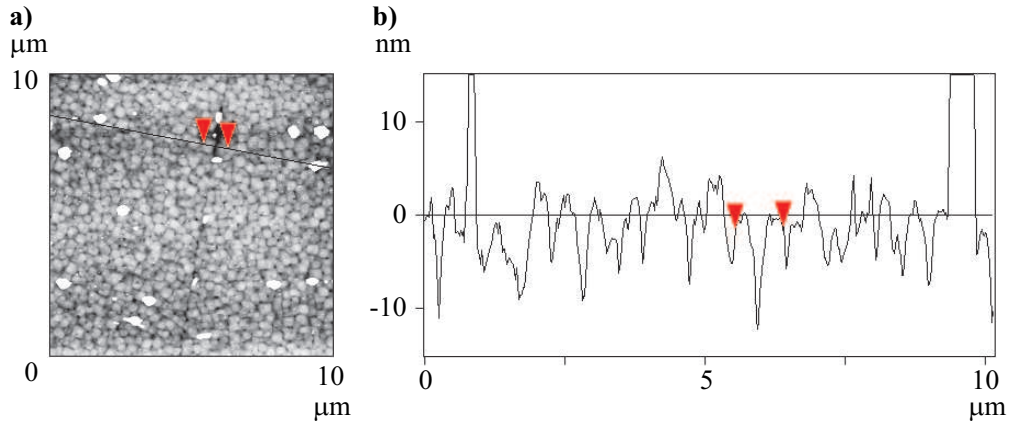


Figure 5.9: Atomic force microscope cross section through a grain boundary, illustrating the grain boundary groove. a) The line along which the cross section is taken. b) Film height shown against distance along the cross section. The two red arrows in both a) and b) are positioned either side of the boundary. The image was scanned at 0.88 Hz with a resolution of 512 samples per line. The image in a) has a height scale of 30 nm (0 nm shown in black, 30 nm shown in white).

At 300 K for optimally doped $YBa_2Cu_3O_{7-\delta}$ the quantity $l_{gb}\rho$ is approximately $10^{-14}$ $\Omega m^2$, assuming $l_{gb}$ is 1 nm and $\rho$ is 0.15 m$\Omega$cm [2]. This is an order of magnitude less than the equivalent resistance area product shown in Fig. 5.7.

The groove associated with the grain boundary extends over distances considerably larger than the boundary itself. Figure 5.9 shows that such a groove is typically comparable in depth to the grooves associated with different grains. However the presence of the boundary forces a groove to be present along the length of the bicrystal line.

The reduced cross section of the track near the boundary increases the measured resistance area product. Provided the size of the groove is small compared to the film thickness the measured resistance area product is approximately:

$$R_m A \approx R_n A + l_{gr}\rho\frac{d_g}{t} \tag{5.14}$$

where the terms are defined in Fig. 5.8.

Fig. 5.9 shows that $d_g \approx 10\ nm$ and $l_d \approx 100nm$. $l_{gr}\rho d_g/t$ is therefore approximately $5 \times 10^{-14}\Omega m^2$ at 300 K, assuming $\rho$ is 0.15 m$\Omega$cm [2]. This is of a similar order to the equivalent resistance area products shown in Fig. 5.7 and is therefore not likely to significantly change the resolution of the technique. However it should be noted that this is a systematic error, and it

does provide a limit on the available resolution, given the film microstructure.

A further possible source of error is heating of the boundary. The heat transfer across the grain boundary is determined by both the thermal conductivity, $\kappa$, and the heat transfer coefficient across the substrate-film boundary, $\alpha$, as discussed in Chapter 4. $\kappa$ is strongly dependent on temperature below 100 K [7], as is $\alpha$ below 30 K [8, 9] — so it is possible that the grain boundary heating associated with the dissipation occurring at the boundary changes with temperature and therefore effects the results. The effect of this potential source of error is dependent on both the bias current and on the temperature variation of the resistance itself. Above the critical temperature, $T_c$, it is unlikely to be a significant source of error, as the bias current used (5 $\mu$A) is small. Below $T_c$ the critical current makes it necessary to use a higher bias current for measuring the normal resistance. However, the normal resistance of grain boundaries below $T_c$ has been observed to be temperature independent in previous studies [10] and in the work presented in the next chapter. Given a temperature independent normal state resistance, heating is not significant a problem — as the resistance of the boundary is not changed by heating. In addition the observation of a temperature independent normal state resistance is evidence for the absence of heating effects, as the heating of the boundary is likely to be strongly temperature dependent at low temperatures.

In summary the additional systematic effects that occur when a grain boundary is aligned with the bridge device have been assessed and are all comparable to or less than the resolution of the technique. In the next section the results obtained from applying the technique on a single bicrystal sample are described.

## 5.5 Application of the technique to a $YBa_2Cu_3O_{7-\delta}$ Grain Boundary

In order to test the technique on a $YBa_2Cu_3O_{7-\delta}$ grain boundary a film was grown on a 30°symmetric [001] tilt $SrTiO_3$ bicrystal. This film was grown at LG Electronics under identical conditions to the film used in Section 5.3. It was patterned in Cambridge and the grain boundary was carefully aligned with the devices as shown in Fig. 5.6. Above the critical temperature, $T_c$, the normal resistance is obtained by the application of a small current bias of 5 $\mu$A to the bridge. Below $T_c$ the normal resistance is more difficult to determine, because of the critical current of the film. The critical current can be suppressed by the application of a low frequency (<10 GHz) microwave

signal to the boundary [5]. In the absence of a microwave source it was found that good values of the resistance area product are obtained by measuring at a sufficiently large voltage that the film critical current causes a negligible effect. This is illustrated in Fig. 5.10. If the quasiparticle current voltage ($I$–$V$) characteristic is linear, then it is expected that the static ($I/V$) and dynamic $dI/dV$) resistances should be equivalent. The figure shows that this is the case provided that the data is analysed at sufficiently high voltages.

The results in Fig. 5.11 show the measured normal resistance area product of the five grain boundary devices on the 30° bicrystal. It is clear that the temperature dependance of the resistance area product is markedly different from that in Fig. 5.7. The resistance is fairly temperature independent for this grain boundary — this result implies that there is no large contribution from normal $YBa_2Cu_3O_{7-\delta}$ tracks. Note that the data in the vicinity of $T_c$ is omitted for clarity — the resistance simply drops to zero for the data obtained above $T_c$ at low current bias, whilst the high current bias data below $T_c$ diverges due to flux flow in the connecting tracks. For some devices large peaks or troughs in the resistance are also observed as the sample is cooled though $T_c$ — these are simply due to small differences in $T_c$ between different arms of the bridges producing imbalance in the bridge structure. The consistency of this data (together with the consistency of the data obtained for other grain boundary angles in Chapter 6) is convincing evidence for the viability of the technique discussed in this chapter.

Figure 5.12 shows the resistance area product from bridge 4 subtracted from that of bridge 7. The resulting temperature dependance is markedly similar to that of normal $YBa_2Cu_3O_{7-\delta}$ and is of a similar magnitude to the signals obtained from the control bridges shown in Fig. 5.7. This is what is expected from the bridges and is further evidence that the technique is well understood. The offset in the resistance is likely caused by differences in the grain boundary properties from bridge to bridge. Note that the form of this curve suggests that this offset is temperature independent. This is important since if such an offset is present from device to device it is possible that there is a difference between the additional grain boundary resistances on opposite arms of the same bridge. For a bridge in which the two grain boundary contributions $r_{gb}(T)$ and $r(T)_{gb}(1+\Delta)$ differ by a constant percentage it is straightforward to show that the voltage measured in the same configuration as in Fig. 5.1 is given by:

$$\frac{V}{I} = -\frac{r_{gb}}{2}\left(1+\frac{\Delta}{2}\right) \tag{5.15}$$

provided that $\Delta r_{gb}/(2R+r_{gb}) \ll 1$ (in fact this is essentially a limiting case of equation 5.8). So the measured resistance is simply scaled by a factor

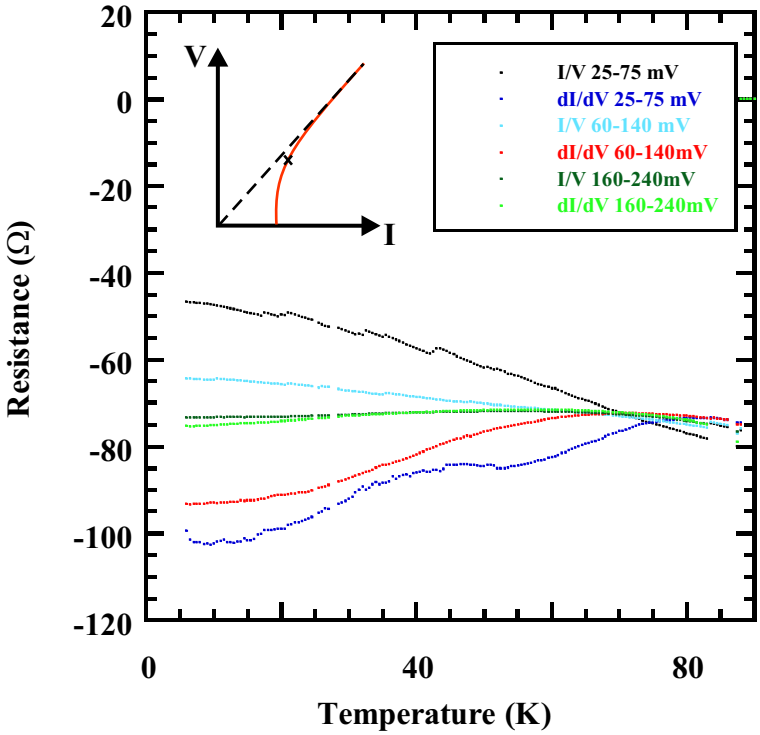


Figure 5.10: Defining a consistent value for the normal state resistance below the critical temperature. The insert shows a schematic $I$–$V$ curve. At the point marked 'x' it is clear that the static resistance, $V/I$, is less than the true normal resistance and the dynamic resistance, $dV/dI$, is greater. The main figure shows the static and dynamic resistance calculated from raw data obtained from bridge 1 on the 30° misorientated sample. These values are calculated from straight line fits to the $I$–$V$ curves in the voltage range indicated. As the voltage is increased the two values converge. Note that the resistance is negative in this unprocessed data as expected from Equation 5.1.

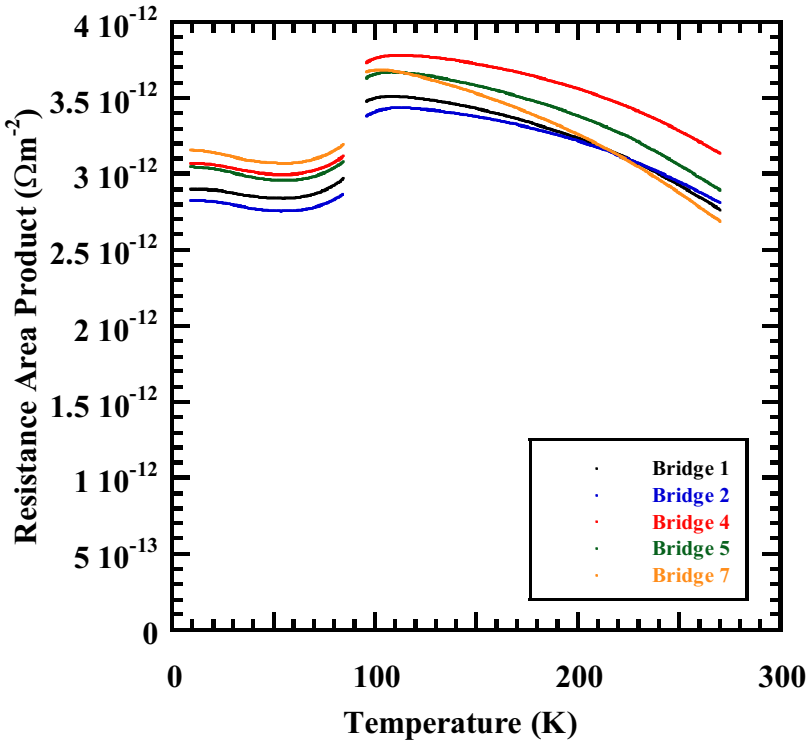


Figure 5.11: Temperature dependance of the Resistance Area Product obtained from devices on a 30° symmetric [001] tilt boundary. Below the critical temperature the resistance area product is obtained from the gradient of a linear fit to the data at large voltage (see Fig. 5.10).

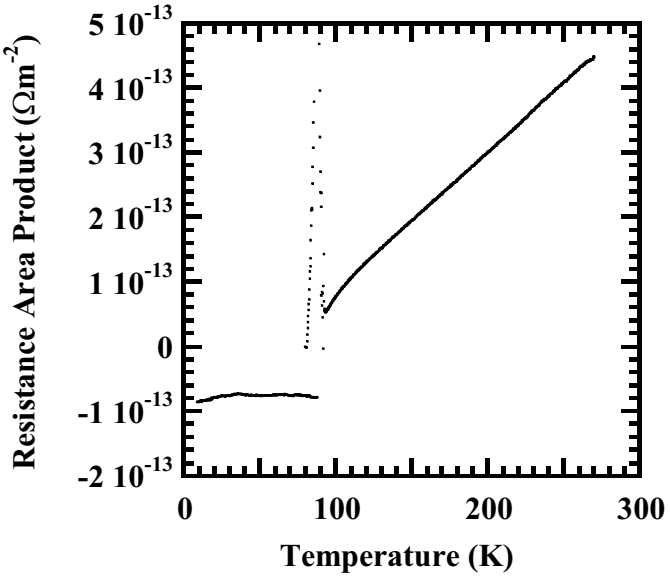


Figure 5.12: Temperature dependance of the difference between the Resistance Area Product of bridge 7 and bridge 4 on the 30° symmetric [001] tilt boundary. The form of the temperature dependence is similar to that of optimally doped $YBa_2Cu_3O_{7-\delta}$, and so is associated with an imbalance in the bridge.

of $(1 + \Delta/2)$ if there is an offset of this form between the two arms of a bridge. The overall temperature dependance of the signal is unaffected, and the mean properties of the grain boundaries are measured.

A consistent decrease in the grain boundary resistance as the sample is cooled through $T_c$ is observed. Its magnitude (approximately $0.5\times10^{-13}\ \Omega m^2$) appears an order of magnitude too large to be accounted for by the grain boundary groove. Since the resistance of this grain boundary is largely temperature independent the jump cannot be well explained by heating effects either. Schneider *et al.* have observed that this difference is not consistent from device to device and furthermore that it can be eliminated altogether [5]. There are several possible explanations for this behaviour. Firstly, because of the critical current of the junctions, it is necessary to measure the resistance of the junction at a finite voltage below the critical temperature, $T_c$, and at zero voltage above $T_c$. If there is some small difference in the resistance between these two voltages this will result in an offset at the critical temperature. Schneider *et al.* use a low frequency microwave source to suppress the critical current of the samples so that they can measure the resistance at zero bias below the critical temperature. They found that using other criteria for the normal resistance produced discontinuities similar

to those observed in our study [11]. It is also possible that there are higher resistance regions of film associated with the grain boundary that are shorted out in the superconducting state but that contribute an additional resistance in the normal state. The presence of such regions may be dependent on the growth conditions, and a different film microstructure could explain why Schneider *et al.* do not observe such a discontinuity.

In summary the data in Figs. 5.7 and 5.11 indicate that it is possible to use the Wheatstone bridge technique on $YBa_2Cu_3O_{7-\delta}$ and that consistent results may be obtained from bridges patterned over grain boundaries. The properties of five wheatstone bridge devices patterned on the same sample are consistent, with small differences from bridge to bridge. The device to device variation is consistent with the error signals observed from bridges patterned on a single crystal sample, which indicates that the technique is well understood. In the next section a new technique proposed by another group is described, and compared with the results discussed in this section.

## 5.6 An Alternative Technique

Schneider *et al.* have recently introduced an alternative technique to the bridge technique described above [5]. Instead of using a bridge to compensate the resistance of the adjoining tracks they employ reference tracks adjacent to the boundary. A single track is patterned across the grain boundary and in addition two identical tracks are patterned either side of this track. The voltage signal obtained from the adjacent tracks can then be compared (to ensure that it is equal) and then subtracted from that of the grain boundary track to obtain the grain boundary signal. The experimental arrangement that they used is shown in Fig. 5.13. The grain boundary resistance, $R_{\rm gb}$, is obtained in the following manner:

$$R_{\rm gb} \approx \frac{1}{I}\left(V_{\rm meas} - \frac{V^*_{\rm g1} + V^*_{\rm g2}}{2}\right) \tag{5.16}$$

where the terms are defined in Fig. 5.13.

Schneider *et al.* report that they obtain significantly improved results over the bridge technique by using this method. However, their bridges seem to be significantly less well balanced than those measured in this study. The bridges they use appear to be 3 times larger than those in Fig. 5.6 — and so may be subject to the variations in film properties discussed above. It is clear however, that their alternative technique produces good results for high angle boundaries. In addition the authors do not observe a significant

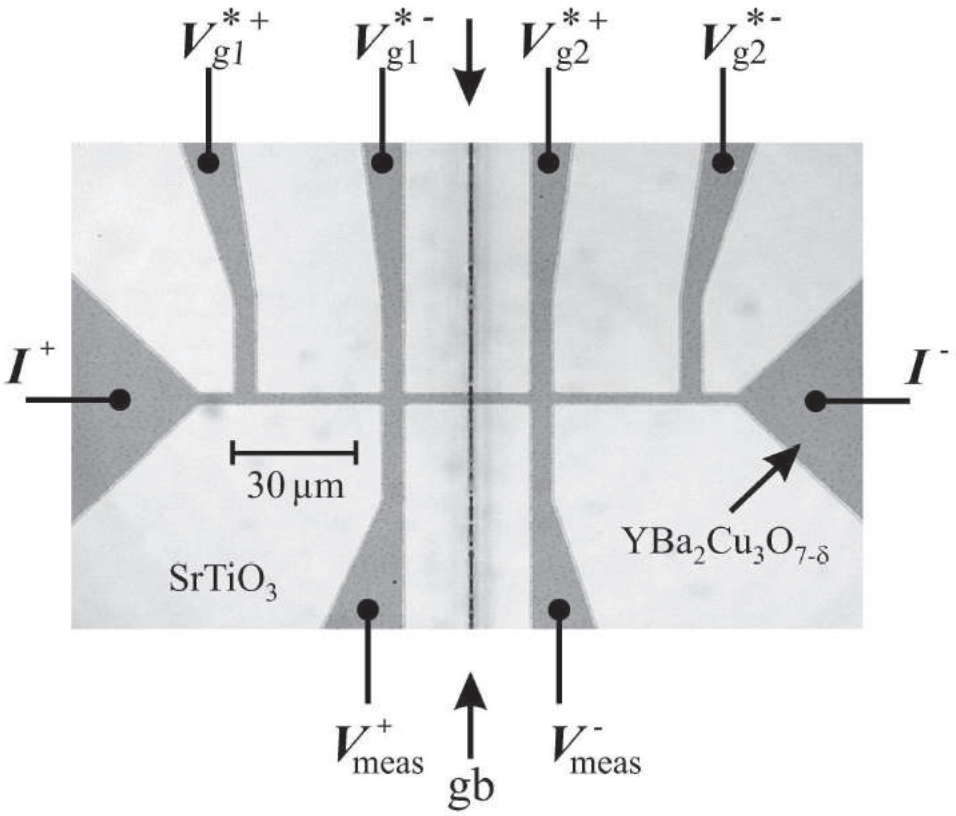


Figure 5.13: The structure used by Schneider *et al.* to measure the resistance of a 45° symmetric [001] tilt boundary [5]. The grain boundary resistance is obtained by subtracting the mean resistance of the two adjacent tracts from the grain boundary tracks.

discontinuity in the measured resistance at the critical temperature on grain boundary samples — unlike that observed in this study.

## 5.7 Summary

In this chapter a bridge technique to measure the normal state resistance of grain boundaries in $YBa_2Cu_3O_{7-\delta}$ has been introduced. The technique has been analysed in detail and a number of useful results for characterising the bridges have been derived. A preliminary study on a number of bridges indicated that the use of smaller bridge structures is limited by the quality of the lithography, whilst larger structures are limited by both the lithography and the film homogeneity. The device structure adopted as a result of these preliminary studies was a meandering bridge that crosses the grain boundary 21 times in two of the four bridge arms. A study on single crystal bridges shows that these devices can be used to measure resistance area products greater than $1 \times 10^{-13}$ $\Omega m^2$ (equivalent to the resistance of 15° [001] tilt boundaries [6]), as fabricated in our experimental facilities. Further systematic errors due to the presence of the grain boundary in the device are discussed and shown to be the same order as, or less than $1 \times 10^{-13}$ $\Omega m^2$. The application of the method to a 30° [001] tilt grain boundary demonstrates consistent results both above and below the critical temperature. The device to device variation is consistent with the error signals observed from bridges patterned on a single crystal sample, which indicates that the technique is well understood. Finally an alternative method for measuring the normal state resistance of large angle grain boundaries was compared with the technique described in this chapter.

# Bibliography


[1] H. Hilgenkamp and J. Mannhart, Reviews of Modern Physics **74**, 485 (2002).

[2] C. P. Poole, *Handbook of Superconductivity*, Academic Press, San Diego, 2000.

[3] N. D. Mathur et al., Nature **387**, 266 (1997).

[4] S. P. Isaac, N. D. Mathur, J. E. Evetts, and M. G. Blamire, Applied Physics Letters **72**, 2038 (1998).

[5] C. W. Schneider et al., cond-mat/0307470, 2003.

[6] H. Hilgenkamp and J. Mannhart, Applied Physics Letters **73**, 265 (1998).

[7] R. C. Yu, M. B. Salamon, J. P. Lu, and W. C. Lee, Physical Review Letters **69**, 1431 (1992).

[8] M. Nahum, S. Verghesse, P. L. Richards, and K. Char, Applied Physics Letters **59**, 2034 (1991).

[9] J. D. N. Cheeke, H. Ettinger, and B. Hebral, Canadian Journal of Physics **54**, 1749 (1976).

[10] R. Gross, P. Chaudhari, M. Kawasaki, and A. Gupta, Physical Review B **42**, 10736 (1990).

[11] C. W. Schneider, personal communication.

# Chapter 6

# Normal State Properties of $YBa_2Cu_3O_{7-\delta}$ Grain Boundaries as a function of Misorientation

In this chapter the technique developed in Chapter 5 is applied in a study of the properties of $YBa_2Cu_3O_{7-\delta}$ grain boundaries as a function of misorientation. The first measurements of the normal state properties of a number of grain boundary orientations are described. As mentioned previously, there is little data available in the literature for the normal state properties [1] — the only other work is an unpublished study on 45° symmetric and asymmetric [001] tilt boundaries [2]. The data presented provides a valuable tool in distinguishing between the various models proposed for high $T_c$ grain boundaries (see reference [1] and Chapter 2 for a detailed analysis of the current models for high $T_c$ grain boundaries).

A series of 4 films was grown on bicrystalline samples of different misorientations. 24°symmetric, 37°symmetric and 45°asymmetric [001] tilt grain boundaries were grown in Cambridge (using the procedure described in chapter 3) and a 30°symmetric boundary was grown at LG Electronics. These films were patterned into bridges using the mask illustrated in Fig. 5.6 and following the procedure outlined in Chapter 3. The properties of devices from each film were then measured in detail — so that information on both the normal state properties and the technique itself was obtained.

Table 6.1: Growth conditions for films used in this chapter. The films were all grown in Cambridge with the exception of the 30° symmetric [001] tilt boundary, which was grown by LG Electronics. Full details of the Cambridge growth procedure are given in Chapter 3.

| **Bicrystal Angle** | **Growth Temper -ature** | **Power Density at Target** | **Target Substrate Distance** | **Oxygen Pressure** | **Film Thickness** |
|---|---|---|---|---|---|
| 45°† | 765 °C | 2.2 $Jcm^{-2}$ | 57 mm | 200 mBar | 135 nm |
| 36°‡ | 765 °C | 3.3 $Jcm^{-2}$ | 57 mm | 200 mBar | 77 nm |
| 30°‡ | 800 °C | 1.4 $Jcm^{-2}$ | 43 mm | 1000 mBar | 210 nm |
| 24°‡ | 765 °C | 3.7 $Jcm^{-2}$ | 57 mm | 200 mBar | 120 nm |

† *Asymmetric [001] tilt*
‡ *Symmetric [001] tilt*

## 6.1 Properties of the films used in this study

Table 6.1 summarises the growth conditions and the thicknesses of the films used in this study. These films were characterised electrically by resistivity measurements and their surface properties were measured by Atomic Force Microscopy (AFM). In addition Transmission Electron Microscopy (TEM) samples were prepared from one of the samples (the 24°symmetric [001] tilt bicrystal) and subsequently imaged. A good understanding of both the surface and the bulk properties of the films was obtained in this way.

Figure 6.1 shows Atomic Force Microscope images of films grown at both the I. R. C. in Superconductivity and LG Electronics (note that Fig. 6.1b is typical of the surface properties of the films grown in Cambridge). As discussed in Section 5.4 the grain boundary is associated with a groove of approximately 10 nm in depth — similar in magnitude to the inter-grain grooves. The boundary is therefore visible in both images. Due to their large size and irregular shapes the particulates on the films are most likely 'boulders' — larger pieces of target material ablated in the deposition process and subsequently embedded in the film [3]. These boulders will reduce the effective area of the grain boundary slightly (if they happen to lie over it) but should not effect the measurements significantly in other ways. The particulate density of the Cambridge film is higher than that of the LG film and the grain size is somewhat larger — this is probably due to differences in the growth conditions.

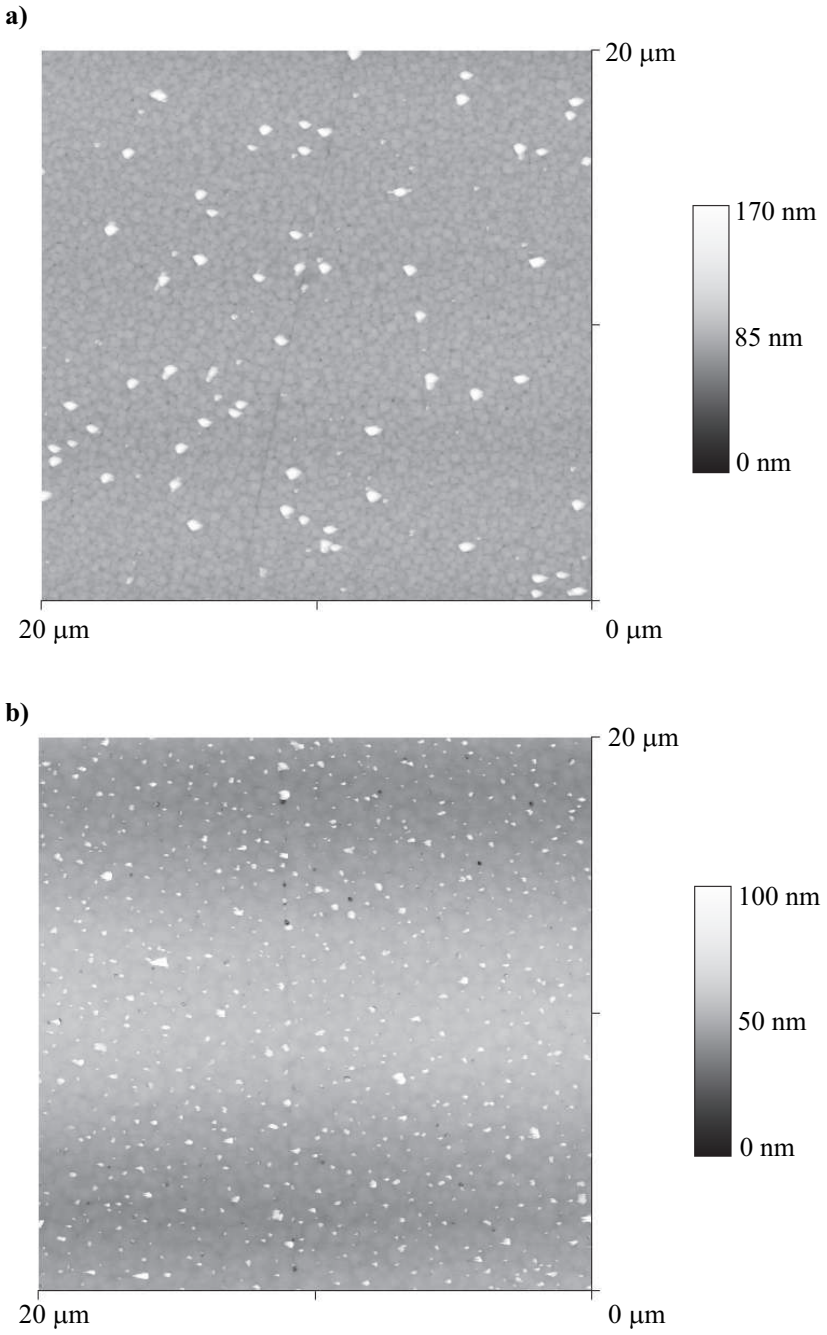


Figure 6.1: Atomic force microscope images of bicrystal films used in this study grown at LG Electronics and at the I. R. C. in Superconductivity. a) The 30°bicrystal (grown at LG Electronics). b) The 37°bicrystal (grown at the I. R. C. in Superconductivity). In both cases the image is scanned at 0.7 Hz and the resolution is 512 samples per line.

The detailed microstructure of the grain boundaries themselves is clearly important for this investigation. For this reason Transmission Electron Microscopy was performed on a cross sections of the film through the 24° grain boundary. The samples were prepared by Sorin Lazar and imaged by Sibe Mennema in the laboratory of Henny Zandbergen. A dual beam scanning electron microsope/focused ion beam (SEM/FIB) was used to cut the lamellae, which meant that it was possible to prepare sections perpendicular to both the grain boundary and the substrate surface. This non-standard geometry provides a unique view of the grain boundary microstructure throughout the film. Full experimental details are given in Chapter 3.

Figure 6.2 shows the TEM images obtained from the film. Panels a) and b) illustrate the geometry of the lamellae with respect to the grain boundary. Panels c) and d) show two sections at different point through the boundary. Both images are bright field images taken along the [100] direction of the darker side of the bicrystal — this is why there is a strong contrast between the two sides of the bicrystal. In both cases the grain boundary itself is clearly visible. Panel c) shows that in some regions of the boundary individual grains extend across the bicrystal line and grow non-epitaxially on the opposite side of the bicrystal. Such a microstructure has been observed previously on $YZrO_2$ bicrystals [4]. It is possible that the non-epitaxial regions of the $YBa_2Cu_3O_{7-\delta}$ are significantly strained as a result of a large mismatch with the underlying substrate lattice parameters (particularly close to the interface with the substrate). If this is the case they will have a reduced critical current and critical temperature and may even be non-superconducting. The grain boundary 3 dimensional microstructure is illustrated schematically in Fig. 6.3. The projected structure is similar in form to the model of Moeckly *et al.* [5]. The overgrowth mechanism is a plausible means of producing the kind of microstructure that Moeckly *et al.* envisage and would limit the active area of the boundary. Such inhomogeneities in the grain boundary structure are typical of the complexity of these defects, with structures that also include nanoscale facetting [6, 7] and microscale meandering [8] of the grain boundary. It is interesting to note that the overgrowth of these grain boundaries contrasts with the results on different films in which the grain boundary essentially follows the bicrystal line along the substrate/film interface and then deviates away from this line through the thickness of the film [9, 10]. This indicates that the model proposed by Ayache *et al.* [11] for the grain boundary three dimensional topography is not universal and that the properties of these complex defects can depend strongly on the growth conditions. Miller *et al.* have observed that the grain boundary meander depends on the growth conditions [8, 12], so it is not surprising that other structural features are also effected. It is clear from the image in panel d)

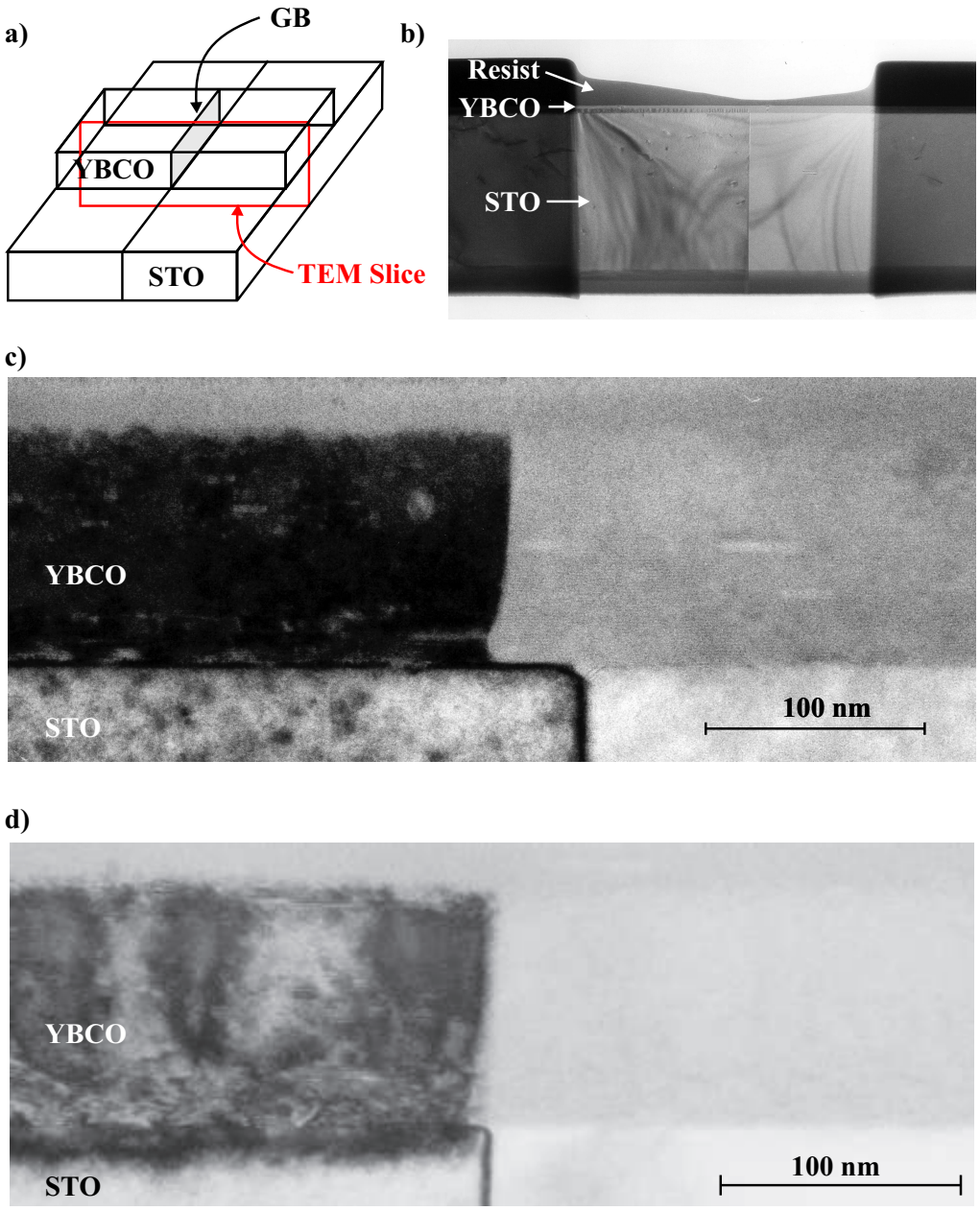


Figure 6.2: Transmission Electron Micrograph (TEM) of cross sections through the 24° bicrystal. a) Diagram showing the plane of the TEM lamella (shown in red). b) Image obtained from the dual beam scanning electron microscope/focused ion beam used to prepare the sample. An entire lamella is shown. c) and d) Transverse TEM images through the grain boundary at different points. In both cases the images are bright field images taken along the (100) direction of the darker side of the bicrystal. The $YBa_2Cu_3O_{7-\delta}$ film is marked 'YBCO' and the $SrTiO_3$ substrate is marked 'STO'.

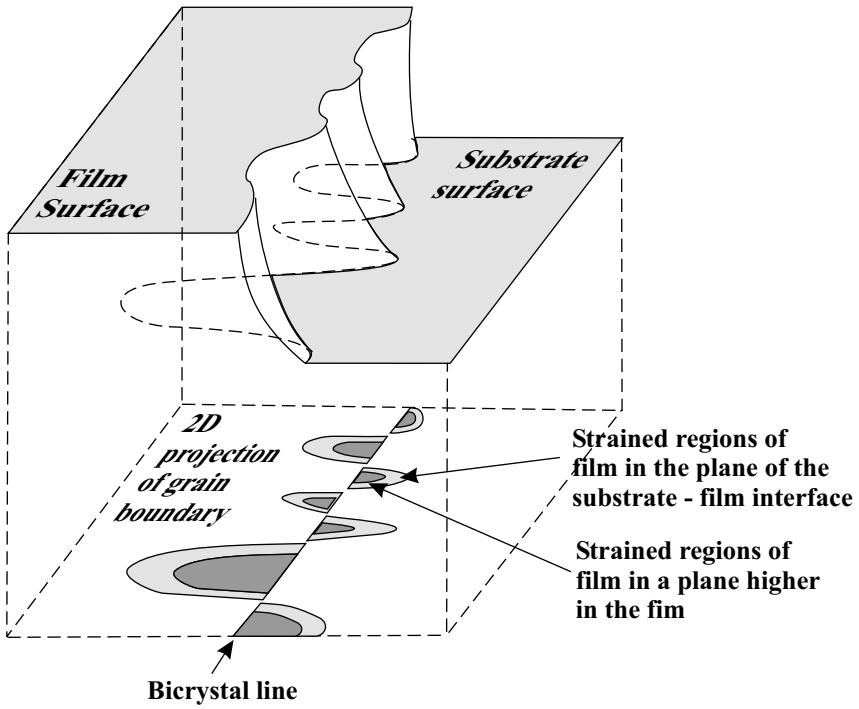


Figure 6.3: Schematic showing the effect of overgrown grains on the grain boundary 3 dimensional structure. The film on the right hand side of the boundary has been removed from the diagram to reveal the boundary topography. In a single plain of the boundary the current is limited to narrow constrictions in which the film is not excessively stressed. As the film grows away from the substrate the size of these constrictions increases. This is a reasonable mechanism to produce the microstructure proposed by Moeckly *et al.* [5] and would mean that the effective area of the grain boundary was limited by the grain size.

that the $YBa_2Cu_3O_{7-\delta}$ grain boundary does not always deviate significantly from the substrate boundary along its length — in some regions the two grain boundaries are essentially coincident.

In addition to characterising the structure of the films, measurements of the film resistivity were performed. Track 2 in Fig. 5.6c was used in order to characterise the properties of a section of single crystal $YBa_2Cu_3O_{7-\delta}$ track. This device is one aspect of the mask that could be significantly improved — the track is too short and narrow for accurate measurements of the resistivity of the material. A longer, wider section of track would be more appropriate, since then it would be possible to accurately define the location of the voltage contacts and lithographic inhomogeneities will play less of a role.

Figure 6.4 shows the results obtained for the film resistance-temperature characteristics. The form of the curves in a), b) and d) is similar to that observed in thin films [13, 14, 15, 16] and single crystal samples [17, 18] with $\delta = 0.05$. The estimated values of the resistivity are approximately 50% higher than those reported. It is likely that this discrepancy results from systematic errors in measuring the film thickness, track width and contact separation (in this case the voltage contacts were 2 $\mu$m wide and were only separated by 5 $\mu$m). The curve in c) is more consistent with $\delta \approx 0.19$, so this film is likely to be somewhat underdoped. This film was also significantly thinner than the others used in this study, which may be related to its non-optimal doping. It appears that a mistake was made in the growth and subsequent oxygenation of this sample.

In summary the films employed in this investigation have been characterised by AFM, TEM and electrical resistivity measurements. The AFM images reveal that the films are reasonably flat and contain particulates that are most likely 'boulders', chunks of target material removed during the ablation process. The TEM studies revealed that in some regions of the film the grain boundary overgrows the bicrystal line producing regions of non-epitaxial growth. The resistivity measurements show that the electrical characteristics of the films are comparable and consistent with optimal doping, with the exception of the 36° symmetric boundary, which is slightly underdoped.

These films were fabricated into Wheatstone bridge and single track devices. These devices were also characterised by AFM, as described in the next section.

## 6.2 Devices Characterisation

Each of the films described above were patterned into devices using the mask shown in Fig. 5.6. Particular care was taken in order to align the pattern accurately to the grain boundary — the alignment stage of the lithography often taking several hours. Figure 6.5 shows part of a fabricated device on the 24° bicrystal. This device was typical of those fabricated in this study. The 2 $\mu$m tracks in the centre of the bridge arm are faithfully reproduced from the mask by the lithographic process. The quality of these tracks is critical for the successful operation of the devices as they contribute a good proportion of the resistance of the device and in addition run across the grain boundary itself. Although there are occasional defects (for example in the very top track shown there is a small notch missing) in general the tracks are of consistent width. It is clearly possible to fabricate high quality devices

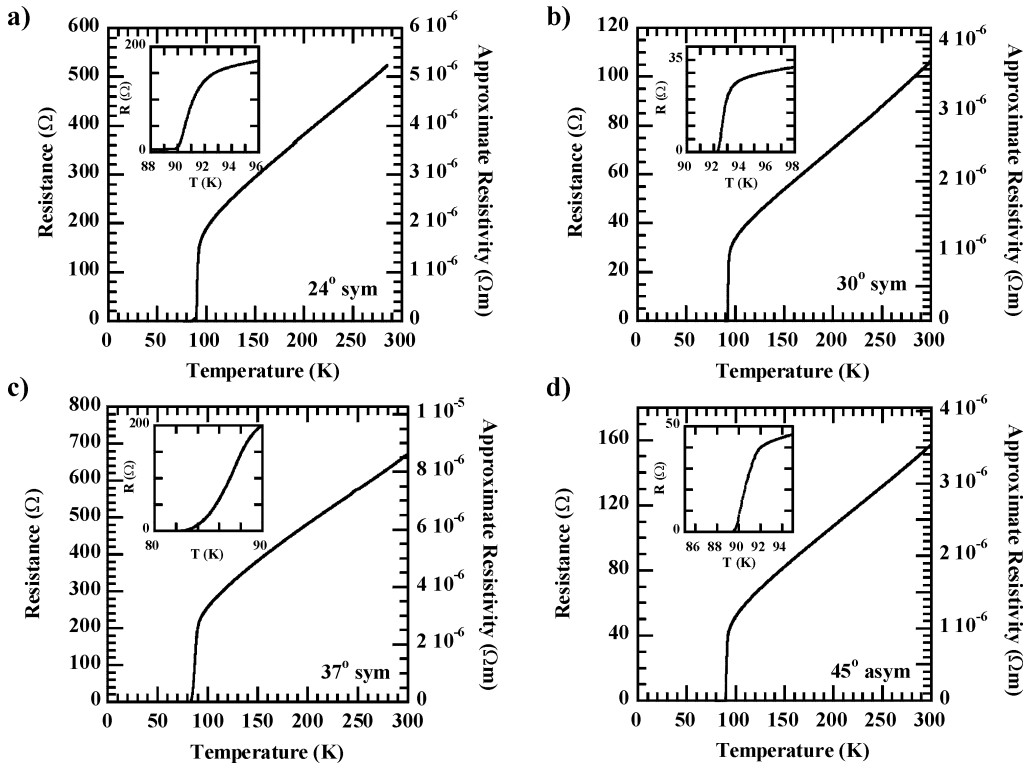


Figure 6.4: Bulk resistance-temperature characteristics for the films measured in this study. Data is shown for: a) 24° symmetric boundary, b) the 30° symmetric boundary, c) the 37° symmetric boundary and (d) the 45° asymmetric boundary. The insets show detail of the region close to the critical temperature, $T_c$. The approximate resistivity is shown as an alternative $y$-axis. Note that, because the electrically conducting thickness of the film is not known, the resistivity is necessarily an estimate. In this case the track width was measured only in the case of the 45° boundary (2 $\mu$m wide), in all other cases it was assumed to be 2 $\mu$m. Note also that a track containing a grain boundary was measured for the 24° boundary, since on this bicrystal the non-grain boundary track was damaged during processing.

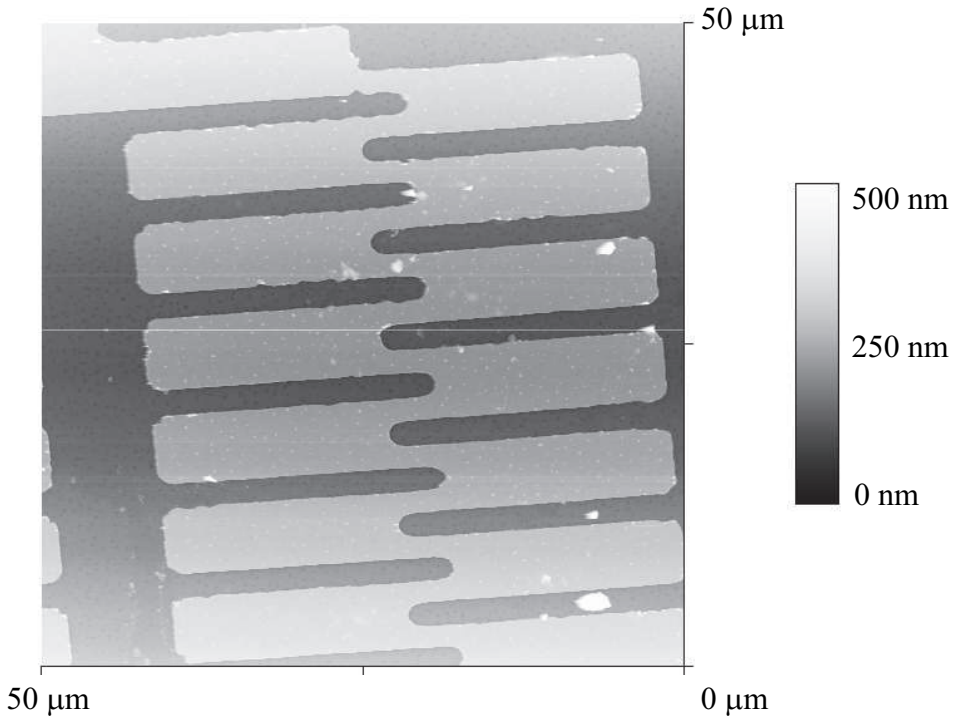


Figure 6.5: Atomic force microscope image of part of a bridge device on the 24° bicrystal. The image is scanned at 0.3 Hz and the resolution is 512 samples per line.

of this size using our, standard UV–lithography, process. It is nonetheless likely that the technique will be improved by the use of a higher resolution mask aligner with a lower wavelength UV source or by the use of an electron beam lithography system.

Having discussed the properties of both the films and the devices, the next section describes the measurements of the normal state properties of the grain boundaries themselves.

## 6.3 Normal State Resistance as a function of Misorientation

The principle aim of this investigation was to measure the normal state resistance of a series of grain boundaries of different misorientations and to correlate the normal state properties with other transport characteristics. In this section the normal state measurements above the critical temperature, $T_c$, are presented.

Figure 6.6 shows the normal state resistance above $T_c$ for all the samples measured in this study. Panels a to d show the data from the 24°, 30° and 36° symmetric and from the 45° asymmetric samples respectively. Panel e shows the data obtained from a single crystal control sample (also shown in Fig. 5.7) for comparison with the grain boundary results. The marked difference between the behaviour in a to d and that in e is further evidence that the technique is viable. Note that one device is missing from the 24° sample as this device was damaged during processing. The results from a given sample are typically very consistent from device to device. The functional form of the resistance is very similar, although there is approximately a 20% variation in its magnitude. Such variations are not too surprising — the boundaries themselves are extremely inhomogeneous and previous work on bicrystal junction arrays has shown that macroscopic transport properties (in particular the critical current) can vary greatly along the length of a single grain boundary [19, 20, 21, 22]. For the 24° and 30° samples it is also possible to observe a small device to device error that is due to bridge imbalance — this can be revealed by plotting the difference between the curves obtained from different devices — as illustrated in Fig. 5.12. Such errors can be eliminated by taking an mean over all the devices on a single boundary — since the bridge imbalance itself has been shown to have a random sign (see panel e). The panel in f shows such a mean over all devices from each misorientation angle.

There is a clear transition in the data from behaviour in which the resistance remains almost temperature independent at low misorientation to an almost linearly decreasing resistance at larger misorientation. In the case of the 24° and the 30° symmetric samples the resistance levels off at lower temperatures — this is consistent with the current–voltage data below $T_c$ presented below — the normal state properties are essentially temperature independent below 80 K. Although a similar trend is not visible in the data above $T_c$ for the 37° symmetric and 45° asymmetric samples the current-voltage curves from these devices are also temperature independent below 80 K — indicating that a levelling off occurs. A transition from a constant resistance at lower temperatures to a roughly linearly decreasing resistance at higher temperatures has also been reported for a 45° symmetric bicrystal [2] and is consistent with all the other available data (see below). Since the 37° symmetric sample was slightly underdoped it is expected that its resistance is larger than would be the case for optimally doped samples. This is the likely reason why its room temperature resistance area product is greater than that of the 45° asymmetric boundary from the same growth series.

Figure 6.7 shows all the other data currently available on optimally doped $YBa_2Cu_3O_{7-\delta}$ grain boundaries. Data from a subsequent study in Cambridge

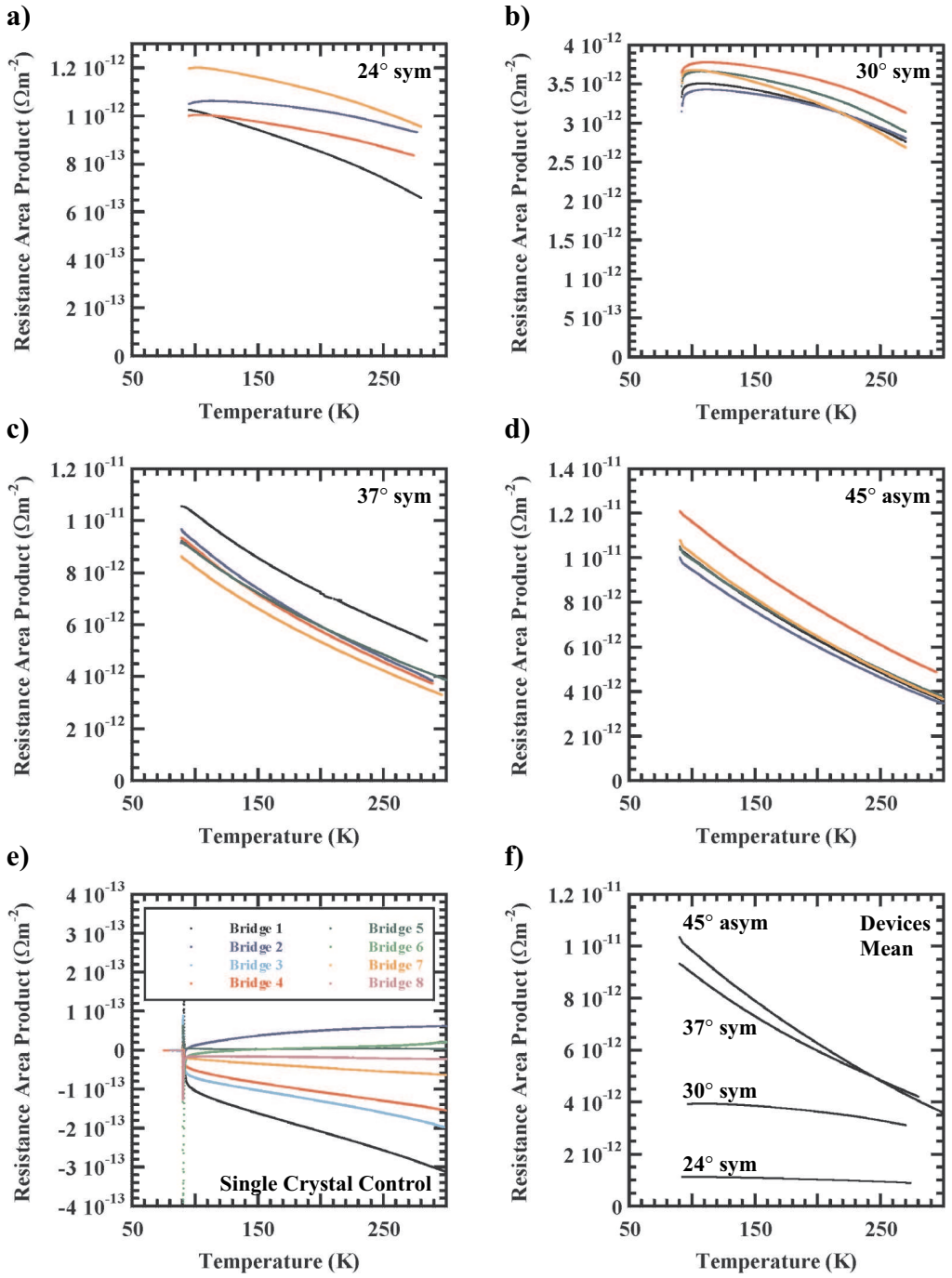


Figure 6.6: Zero bias resistance area product shown against temperature for the devices measured in this work (as grown). a)–d) Data from each of the devices measured on 24°, 30°, 37°symmetric and 45°asymmetric grain boundaries respectively. The devices are named according to the convention set out in Fig. 5.6. e) Data from control sample with no grain boundary. f) Comparison of data from different grain boundary angles, showing the mean over all the devices for each sample. Note that in each case the data is normalised so that it is comparable to single junction data.

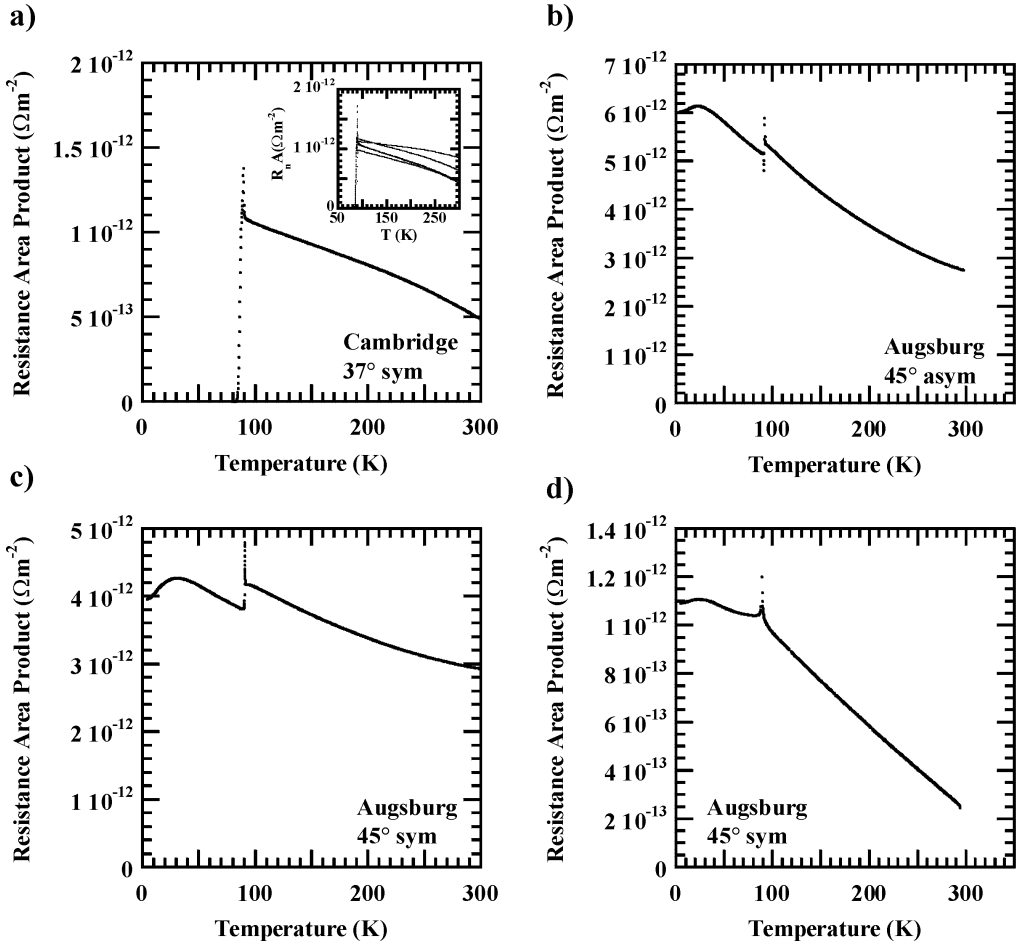


Figure 6.7: Other measurements of $YBa_2Cu_3O_{7-\delta}$ grain boundary normal state resistance area product. a) Mean resistance area product of 5 bridges on a 37° bicrystal grown in Cambridge (measured by Sibe Mennema) [23]. The insert shows the characteristics of the five devices used in this study. Note that the growth conditions for this film are different from those used for the films reported in this study, which is why the resistance area product has decreased significantly. b) and c) Results obtained by Christof Schneider on single bridges fabricated on bicrystal samples grown in Augsburg [24]. d) Results obtained from an alternative technique (described in section 5.6) by the Augsburg group [2]. Note that in each case the data is normalised so that it is comparable to single junction data.

(with films grown under different conditions to those in this study) and from an additional study in Augsburg are reported. The Augsburg group are able to continue the normal state resistance measurements below $T_c$ since they use a low frequency microwave source to suppress the critical current [2]. The results are generally consistent with those reported in this study, although the resistance area products are all significantly lower. The reason for this difference is probably differences in the growth conditions for the different samples. Large variations in the properties of grain boundaries of a fixed misorientation have been reported in the literature [1] — these are primarily attributed to differences in the growth conditions and corresponding grain boundary microstructure. It is clear that although the magnitude of the resistance area product is not the same for these additional studies, the functional form of the variation is comparable. This may indicate that the grain boundary effective area is largely responsible for the differences in the transport properties for a fixed misorientation angle. In the preceding discussion the overgrowth of the grain boundary, and corresponding non-epitaxial, highly stressed, growth was highlighted as a possible mechanism for changes in the effective area of the grain boundary. A further possibility is that a single facet orientation is responsible for the bulk of the current carrying capability of the grain boundary. The facet and meander structure is known to be highly dependent on the growth conditions of the film [8, 12].

In conclusion, the measured normal state resistance of these grain boundaries is self consistent and consistent with other studies in the literature. The magnitude of the normal state resistance is higher than that measured in other studies, but is nonetheless within the spread reported in the literature. For the two higher angle boundaries (36° symmetric and 45° asymmetric) the resistance area product decreases approximately linearly above $T_c$, whilst for the lower angle boundaries (24° and 30° symmetric) it is almost temperature independent. Below $T_c$ it is possible to investigate the entire current–voltage characteristic of the devices. The next section describes these measurements in detail.

## 6.4 Current Density–Voltage Characteristics as a Function of Misorientation

Below the critical temperature ($T_c$) the current density–voltage ($J$–$V$) curves were measured for all the devices as a function of temperature. Although there is some variation from device to device the data in Fig. 6.8 shows that the behaviour at 10 K is reasonably consistent for each sample. The

differences between the $J$–$V$ curves correlate with the differences observed in the normal state results and most likely reflect variations in the grain boundary properties along its length, as discussed in the previous section. The functional form of the $J$–$V$ curves, like those of the $R_nA$–$T$ curves is consistent from device to device.

The 24° and 30° symmetric boundaries have current density–voltage characteristics similar to the majority of those reported in the literature and consistent with the early work by the I. B. M. Group [25]. The absence of excess currents is usually observed in short junctions less than 3 $\mu$m wide [1]. The $J$–$V$ characteristic is essentially linear over the measurable range of ±20 mV. The $J$–$V$ characteristic of the 36° symmetric and the 45° asymmetric boundaries can be measured over a much greater range (±150 mV) because of their higher resistance. The reason for this is that flux flow in the film adjacent to the boundary occurs at a roughly constant current for a fixed temperature — so the measurements of the grain boundaries are limited by a maximum current bias at a given temperature. For the lower resistance samples the obtainable voltage range is therefore much smaller than for the higher resistance samples. The higher angle boundaries have clearly non-linear current density–voltage characteristics in the voltage range of ±150 mV. Such characteristics are also observable in single tracks across the grain boundary (see Fig. 6.10), and have been observed by other authors in both optimally doped [2] and underdoped [26] $YBa_2Cu_3O_{7-\delta}$ grain boundaries.

Figure 6.10 shows the current density–voltage characteristics for two single track devices on the 36° symmetric and 45° asymmetric samples. The non-linear current voltage characteristics observed in the bridges are also observed in these devices. The conductance–voltage characteristics calculated from the $J$–$V$ curves are also shown. These characteristics are not parabolic (see the detailed analysis in the next chapter). Froehlich *et al.* maintain that they have observed parabolic conductance–voltage characteristics in their deoxygenated 24° [001] tilt grain boundary [26], however they observe the current voltage characteristics over a limited range and the barrier height they obtain from their fit ($eV = 20$ meV) is far too low to be consistent with the other transport properties. In particular the grain boundary resistance has previously been shown to be constant up to 100 K for 24° symmetric [001] tilt boundaries [27], and in this work such a temperature independent resistance is observed up to 300 K for similar boundaries. With such a low barrier height, quasiparticle thermal emission should be significant even below $T_c$ ($eV/k_b = 270$ K, where $k_b$ is Boltzmann's constant). Below approximately 30 mV a reduction in the conductivity is observed. This may be a feature caused by the superconducting gap although further investigation is necessary to confirm this. The presence of this feature makes it difficult to extract

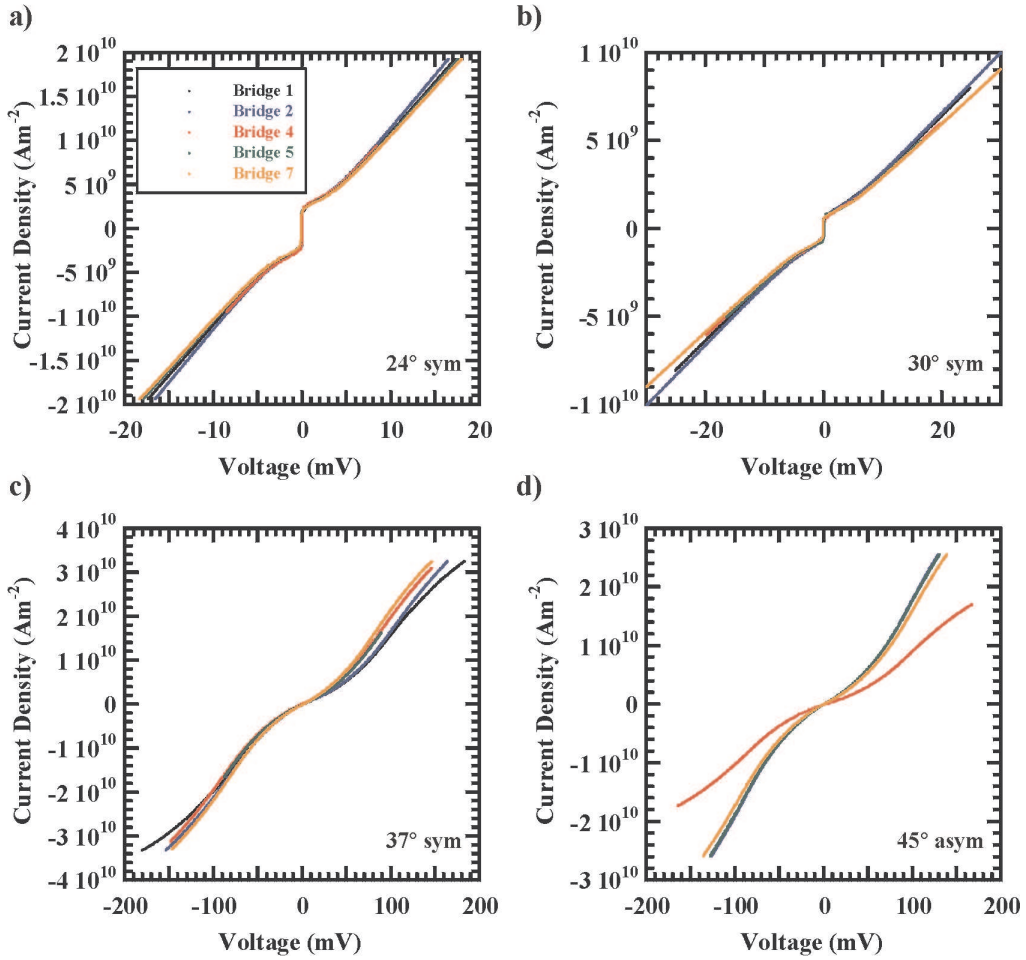


Figure 6.8: 10 K current density – voltage characteristics for all the devices on each bicrystal sample (measured as grown). a)–d) shows data from each of the devices measured on 24°, 30°, 37°symmetric and 45°asymmetric grain boundaries respectively. The data has been normalised so that it is comparable to single junction data.

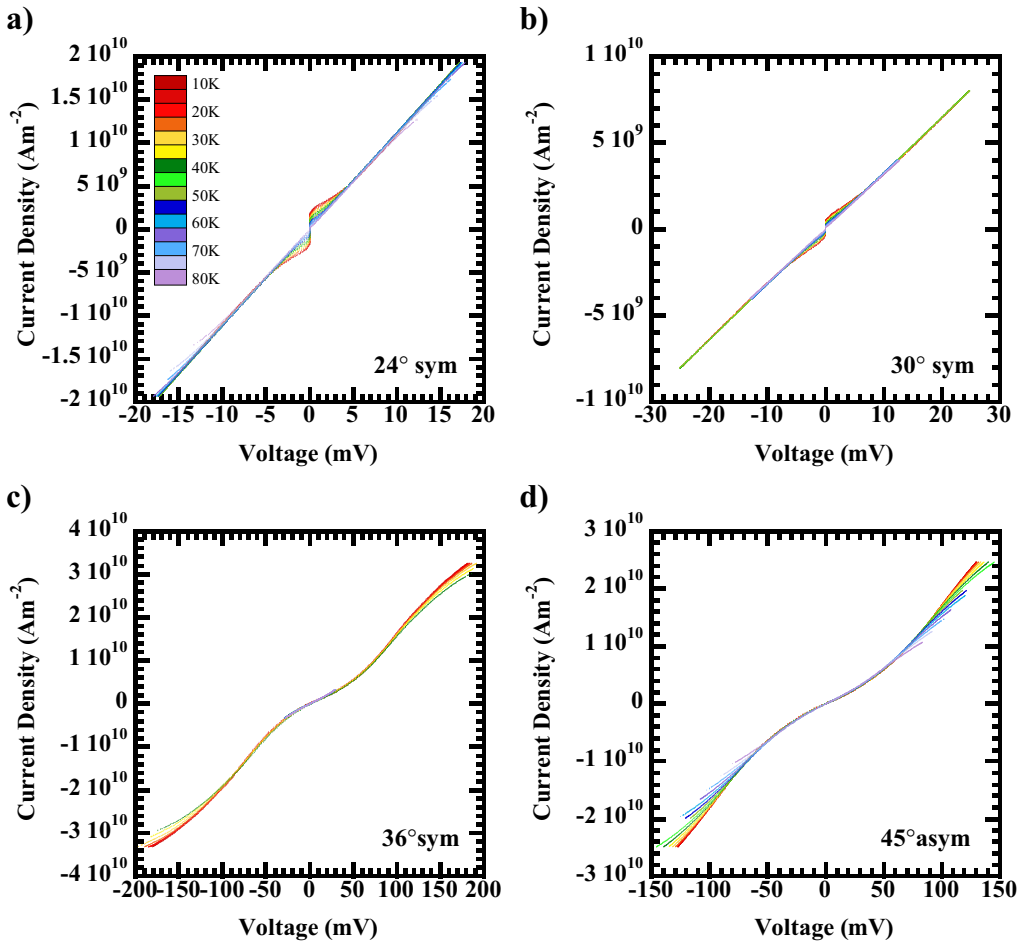


Figure 6.9: Current density voltage characteristics as a function of temperature, for each misorientation angle measured (measured as grown). a)–d) shows data from each of the devices measured on 24°, 30°, 37°symmetric and 45°asymmetric grain boundaries respectively. The data shown is obtained from bridge 1 on each of the samples and has been normalised so that it is comparable to single junction data. As shown in Fig. 6.8, there is some variation in the characteristics between devices, but all devices produce results that are essentially temperature independent.

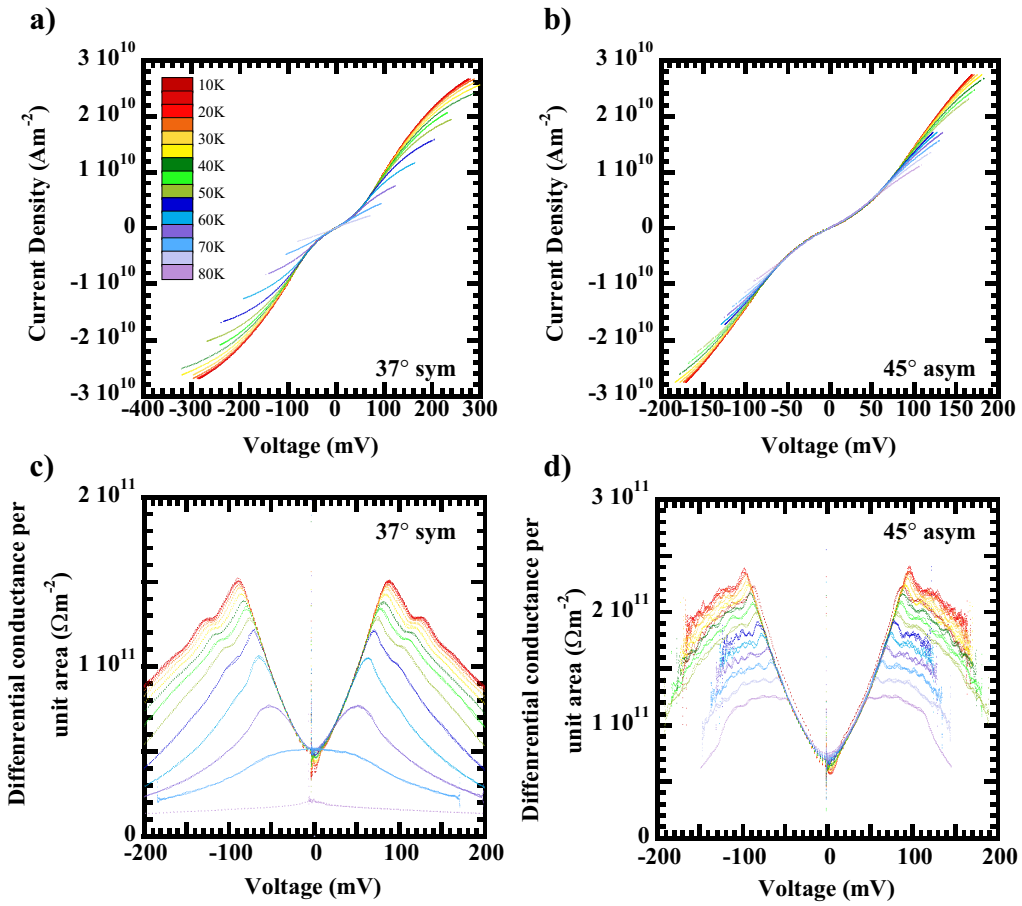


Figure 6.10: Current density voltage characteristics as a function of temperature, for single 36° symmetric and 45° asymmetric grain boundary junctions. a) and b) show data normalised data from Track 3 on the 36° and the 45° samples. c) and d) show the differential conductance as a function of voltage for the same devices.

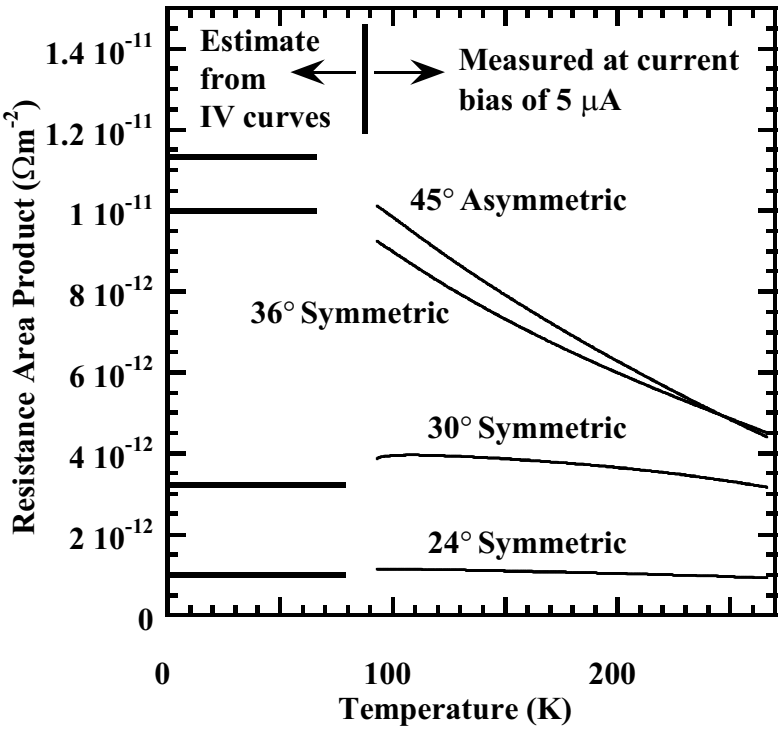


Figure 6.11: Approximate form of the zero bias normal state resistance area product–temperature curve. Above the critical temperature the zero bias resistance area product is measured directly with a low current bias. Below 80 K the value is constant (see figure 6.8) and has been estimated by linear fits to the current voltage characteristics.

the zero bias resistance area product from the data at low temperatures.

The $J$–$V$ characteristics show that below 80 K the normal state properties of all the grain boundaries studied are essentially temperature independent. Thus the zero bias normal state resistance must be constant at low temperatures, for all the samples. Figure 6.11 shows the form of the complete $R_nA$-$T$ curve that is measured in this study. The value of the zero bias resistance below $T_c$ is obtained from linear fits to the $J$–$V$ curves close to the origin. This is done by eye for each device to avoid the difficulties due to the critical current of low bias measurements of the normal state resistance below $T_c$. The resistance area product is then averaged over the devices (note that in the case of the 45° junction the data from bridge 4 is treated as an outlier). It is clear that the zero bias resistance area product of the 36° symmetric and 45° asymmetric boundaries is constant below $T_c$ and decreases approximately linearly above $T_c$. The resistance of the 24° symmetric boundary is almost temperature independent between 4 K and room temperature and the 30°

symmetric sample shows behaviour intermediate between the 45° asymmetric and the 24° symmetric boundary.

Since the $J$–$V$ characteristic is temperature independent for all the devices, heating is not likely to have a significant effect on the measured characteristics. However, it is nonetheless worthwhile to consider the temperature rises expected at large voltages, where the heating is expected to be most significant. At the maximum current bias (typically 1-5 mA) the voltages across the individual junctions range from 20 mV for the 24° boundary to 170 mV for the 36° boundary. The heating at each grain boundary can be estimated using the model from Appendix A. This is necessarily an approximation because the model assumes that the thermal conductivity is proportional to $T^2$, where $T$ is the temperature. While this assumption is accurate below 10 K it is less accurate (although not entirely unreasonable) between 10 and 20 K. The 10 K current–voltage characteristics shown in Fig. 6.9 were analysed using the model at the maximum current bias. The predicted temperature rises were 6 K, 6 K, 21 K and 9 K for the 24°, 30°, 36° and 45° samples respectively. Note that the value of 21 K predicted for the 36° sample is so large that the model is unlikely to be accurate. This approximate calculation shows that heating is significant at large bias in these devices. Fortunately the properties of the grain boundaries are temperature independent, so this heating does not effect the measured $J$–$V$ characteristic. It is clear from the analysis of the heating that temperature independent $J$–$V$ curves are unlikely to result from a measurement where the characteristic was severely effected by heating. Both the thermal boundary resistance and the thermal conductivity, which are critical parameters in the model, vary rapidly with temperature over the range explored in this investigation [28, 29]. The heating of the grain boundaries does explain why flux flow occurs in the film at applied currents significantly less than the critical current of $YBa_2Cu_3O_{7-\delta}$ ($YBa_2Cu_3O_{7-\delta}$ critical currents are typically in the range of $10^{11}$ $Am^{-2}$ to $10^{12}$ $Am^{-2}$ at helium temperatures [30]).

In conclusion, non-linear current density–voltage characteristics have been observed for the 36° symmetric and the 45° asymmetric grain boundaries below $T_c$. These characteristics have been confirmed in both single track and bridge devices. Straight line fits to the curves at voltages greater than the critical current but sufficiently low that the current density–voltage characteristic is linear, were performed. The values obtained from these fits were used to estimate the temperature dependance of the grain boundary resistance area product at low temperatures. In all cases the low temperature resistance area product was found to be temperature independent. Such temperature independent behaviour indicates that heating, while estimated to be significant at large bias, does not alter the results obtained. Both the

current density–voltage curves and the resistance area product–temperature data provide new insights into the grain boundary problem. In particular this data set provides an excellent testing ground for the various models of grain boundaries in high $T_c$ superconductors, since two independent curves must be fitted. These results are analysed in the context of the existing models of grain boundaries in the next chapter. In the next section we discuss in detail the spread in the properties of grain boundaries in a single bridge, and its implications for the analysis of this data.

## 6.5 Spread in Grain Boundary Properties within a Bridge

The previous discussion has highlighted the inhomogeneous nature of grain boundaries in $YBa_2Cu_3O_{7-\delta}$. Both the critical current density and the normal resistance area product have been observed to vary over an order of magnitude for a given grain boundary misorientation [1]. The complex structure of the boundaries includes nanoscale facetting [4, 6, 7] and microscale meandering [8] and the resulting microstructure is heavily dependent on the growth conditions of the thin films [8, 12]. It is this complex microstructure that produces inhomogeneities in the transport properties at both the nanoscale and the microscale and that leads to the observed irreproducibility of the macroscopic transport properties. The critical current of grain boundary arrays has also been observed to be very inhomogeneous with a number of studies showing large variations across a grain boundary in a single sample [19, 20, 21, 22]. Since the bridge technique measures the average properties of two arrays of grain boundaries it is important to understand the spread in the properties of the boundaries in the individual arrays in the device.

The grain boundary critical currents provide a useful means of assessing the spread in the transport properties of junctions fabricated on a single device. The critical current spread can be estimated by performing sensitive measurements of the current–resistance characteristics using a lock-in amplifier. The full experimental setup is described in Chapter 3. The switching of individual junctions can be detected as a sudden increase in the resistance at a given applied current. In the Wheatstone bridge device geometry the current is split between two parallel arrays of grain boundary Josephson junctions. The equivalent circuit in the superconducting state is shown in Figure 6.12a). When a current less than the sum of the critical currents of the lowest critical current junctions in the left and right hand arrays ($I_1^l + I_1^r$) is applied, no voltage is measured. As the current approaches $I_1^l + I_1^r$ it re-

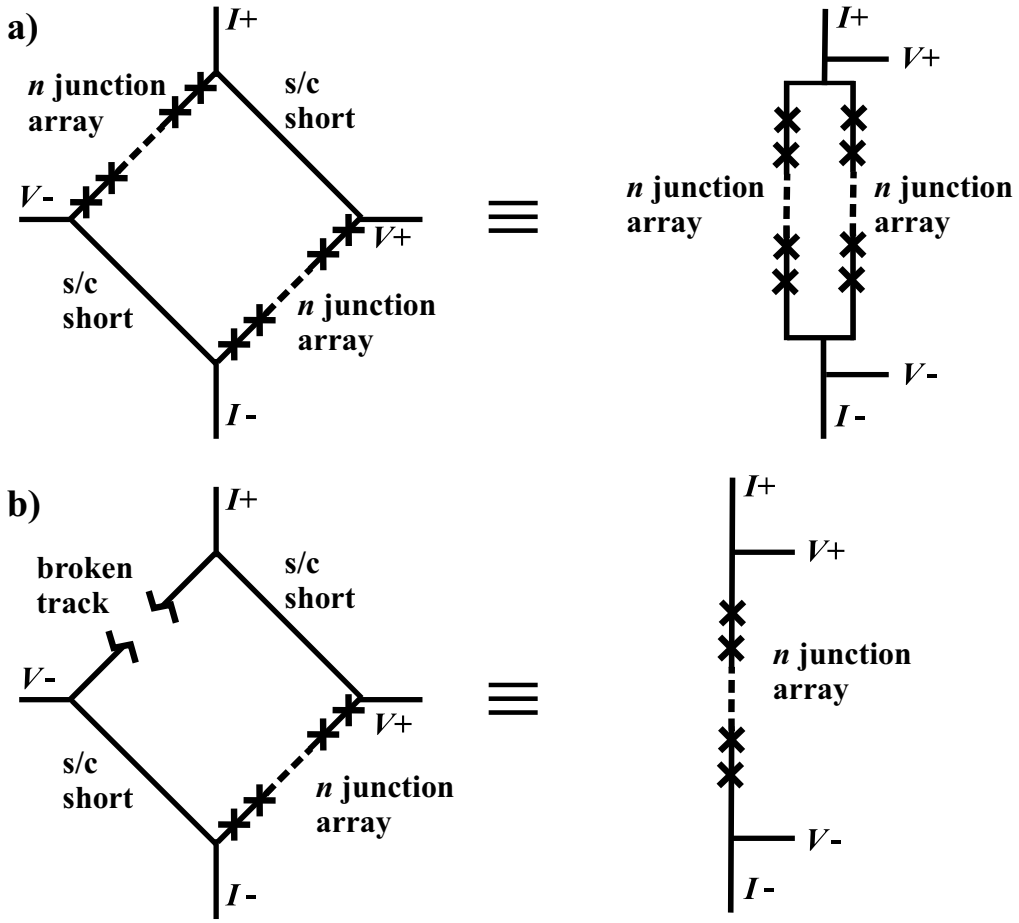


Figure 6.12: Equivalent circuits for a) a bridge and b) a broken bridge in the superconducting state.

distributes such that the current in the left hand arm is $I_1^l$ and the current in the right hand arm is $I_1^r$. At this point the two junctions switch together and the current is redistributed according to the resistances of the two junctions. The resistance of the device increases from zero to some finite value at this current. Further discontinuities in the measured resistance occur as different junctions switch and the current is redistributed accordingly. In some cases several junctions will switch simultaneously, either because their critical currents are extremely close or because the sudden increase in the resistance of one arm leads to a sudden increase in the current flowing through the opposite arm. It is clear that the applied current is not always an accurate measure of the critical currents of the junctions, but that, particularly after a number of junctions in each arm have switched, the current will redistribute fairly evenly down the left hand and right hand arms of the bridge. Half the applied current is therefore a reasonable estimate of the critical current. The total spread in the critical currents of the junctions in each device can therefore be obtained from this method.

In order to ensure that the technique produces valid results a number of experiments were performed. The results obtained from both the positive and the negative sides of the resistance–current curve were compared, along with the results from a subsequent cool down. Figure 6.13 shows that these results are consistent with small differences occurring between subsequent cool-downs. If the distribution of switching events is plotted these differences are relatively minor and a fairly consistent picture emerges. Note that the number of switching events is typically significantly less than the number of junctions, so the distributions cannot be treated simply as critical current distributions. It is possible to measure the discontinuity in the resistance at each switch and to estimate the number of junctions that switch. There is some indication in the distribution of these discontinuities that this approach may be valid. However the results obtained from such an analysis are ultimately somewhat over-analysed — in the text below the distributions of the switching events themselves are shown as this was considered to be a more transparent way of analysing the data. This means that the distributions observed may be suppressed somewhat from the true critical current distribution — particularly in current ranges where large numbers of junctions switch — as in these regions it is likely that several junctions will switch together. Provided these limitations are kept in mind the switching event distributions may be used to derive useful information about the devices.

To confirm the assumption that the current divides approximately evenly between the two junction arrays bridge devices were severed as shown in Fig 6.12b. Bridge 1 on the 45° asymmetric sample and bridge 2 on an additional 30° sample were used for this experiment (the 30° sample grown

Table 6.2: Approximate spread of critical current densities in each of the samples measured in this investigation. These critical current ranges are necessarily approximate because of the bridge geometry. They are obtained from the data in Fig. 6.15.

| Bicrystal Sample | Range of Critical Currents |
|---|---|
| 45° asymmetric [001] tilt | $2\times10^{9}$ – $5\times10^{10}$ $Am^{-2}$ |
| 36° symmetric [001] tilt | $2\times10^{10}$ – $2\times10^{11}$ $Am^{-2}$ |
| 30° symmetric [001] tilt | $5\times10^{11}$ – $3\times10^{12}$ $Am^{-2}$ |
| 24° symmetric [001] tilt | $2\times10^{12}$ – $5\times10^{12}$ $Am^{-2}$ |

at LG Electronics was on a $10 \times 10$ mm substrate and was cut into 2 parts — the second part was used for this experiment, the first for the remainder of this study). A single bridge is measured before and after one of the junction arrays is severed — by photolithographically patterning a small hole over the array and wet etching to remove the $YBa_2Cu_3O_{7-\delta}$. For both of these samples the results in Fig. 6.14 show that the technique is remarkably consistent. The detailed form of the curves is discussed in further detail below.

Figure 6.15 shows representative resistance voltage characteristics near the critical current from each of the samples measured in this study. In each case the data is taken from bridge 1 on the sample. As with the normal resistance data there is a clear distinction between the behaviour of the 24° and 30° samples and that of the 36° and 45° samples. The large peaks in the data of the 36° and 45° samples are associated with the abrupt switching of these junctions, which indicates that these junctions' McCumber parameters are sufficiently large that abrupt switching occurs out of the superconducting state [31, 32]. Such abrupt switching behaviour is also observed in single tracks patterned across the grain boundaries in these two samples — as shown in panels e and f. Unfortunately the large changes in the resistance that occur appear to induce other junctions in the bridges to switch, making the data very difficult to analyse, especially at lower currents. For this reason the detailed distribution of switching events cannot be unambiguously investigated for these two samples. Nevertheless the approximate range of critical current densities present in each sample can reasonably be estimated from the data. Table 6.2 shows the approximate range of critical currents present in each sample — obtained from the data in Fig. 6.15. These critical currents are within the range of values in the literature [1].

For the 24° and 30° samples the currents at which switching events occur were extracted from the data. As discussed above this was not possible in the case of the 36° and 45° samples since the results at low currents are not

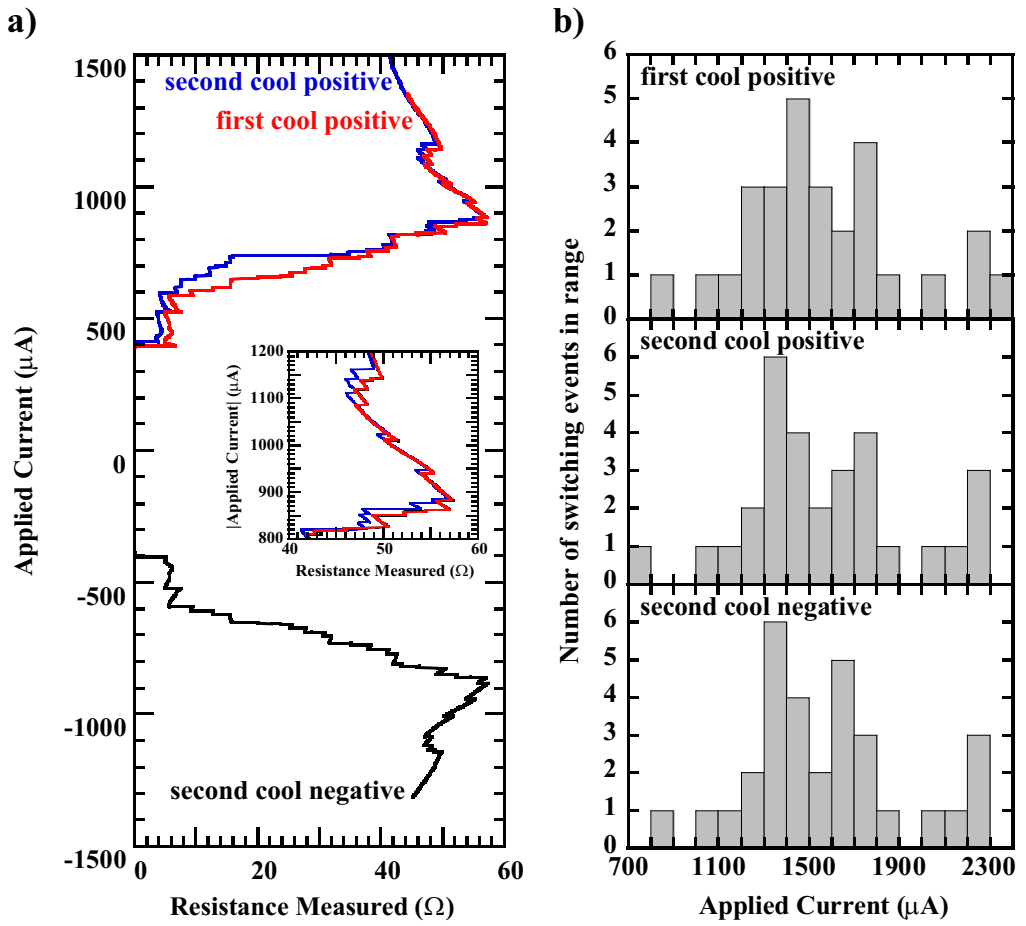


Figure 6.13: Current voltage characteristics and switching distributions shown on consecutive measurements of a bridge on the 24° symmetric boundary. a) The current–resistance characteristic measured on two consecutive cool downs. On the second cool down both the positive and negative branches of the current–resistance curve were measured. The inset shows detail of all three curves plotted together — there is good consistency between the results from the negative branch and the positive branch and between the consecutive cool-downs. b) Switching distributions extracted from the data — all three distributions are similar.

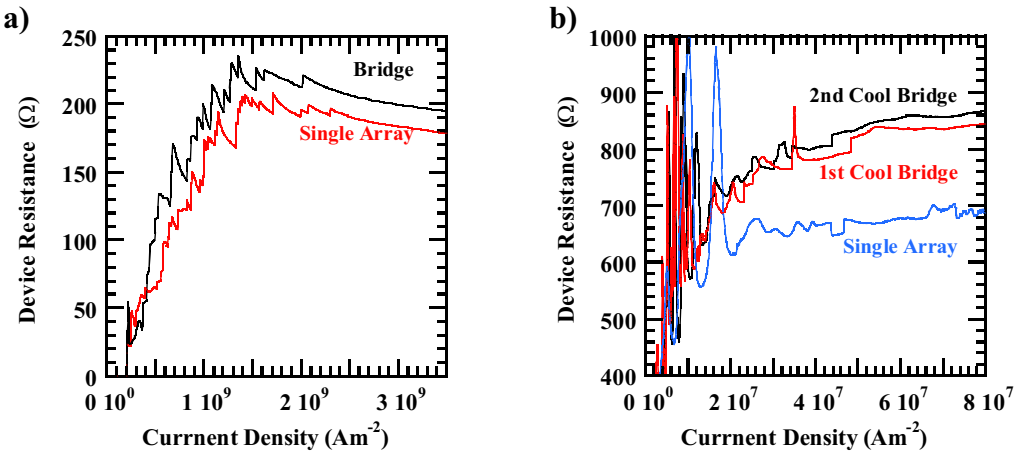


Figure 6.14: Current density–resistance characteristic of a bridge on a) 30° and b) 45° samples before and after the bridge has been broken open to form a single array. The correspondence between the different curves is good.

straightforwardly interpretable. Figure 6.16 shows the distribution of switching events versus current density on both linear and logarithmic scales — for both of the measurable samples. These distributions are consistent with other measurements in the literature [19, 20, 21, 22]. Some authors claim that the distribution of critical currents observed is normal [19, 20] — this data does not appear to support this view. There is some evidence for the log-normal distributions proposed by Shadrin, Jia and Divin [21, 22]. However, the switching distribution data should not be interpreted too heavily — the technique does not make it possible to observe the switching of all the junctions individually so there is necessarily some bias in the distributions observed. The majority of the switching events occur within the ranges set out in Table 6.2, this data is therefore a good indication of the overall spread in the junction properties within individual bridges.

Having considered the range of critical currents present in each sample it is important to note that the measurements of the previous two sections are necessarily averaged over grain boundaries with quite variable properties. This is a particular problem with almost all experiments on grain boundaries — since with conventional samples it is simply not possible to fabricate sufficiently narrow tracks that there are no microstructural variations along the boundary. Although these experiments highlight the problems inherent with grain boundaries, it is at least clear that there is no difference between this study and the vast majority of the literature (in which measurements of single tracks are performed). The bridges involve averaging the properties of grain boundaries over a number of tracks but even measurements on

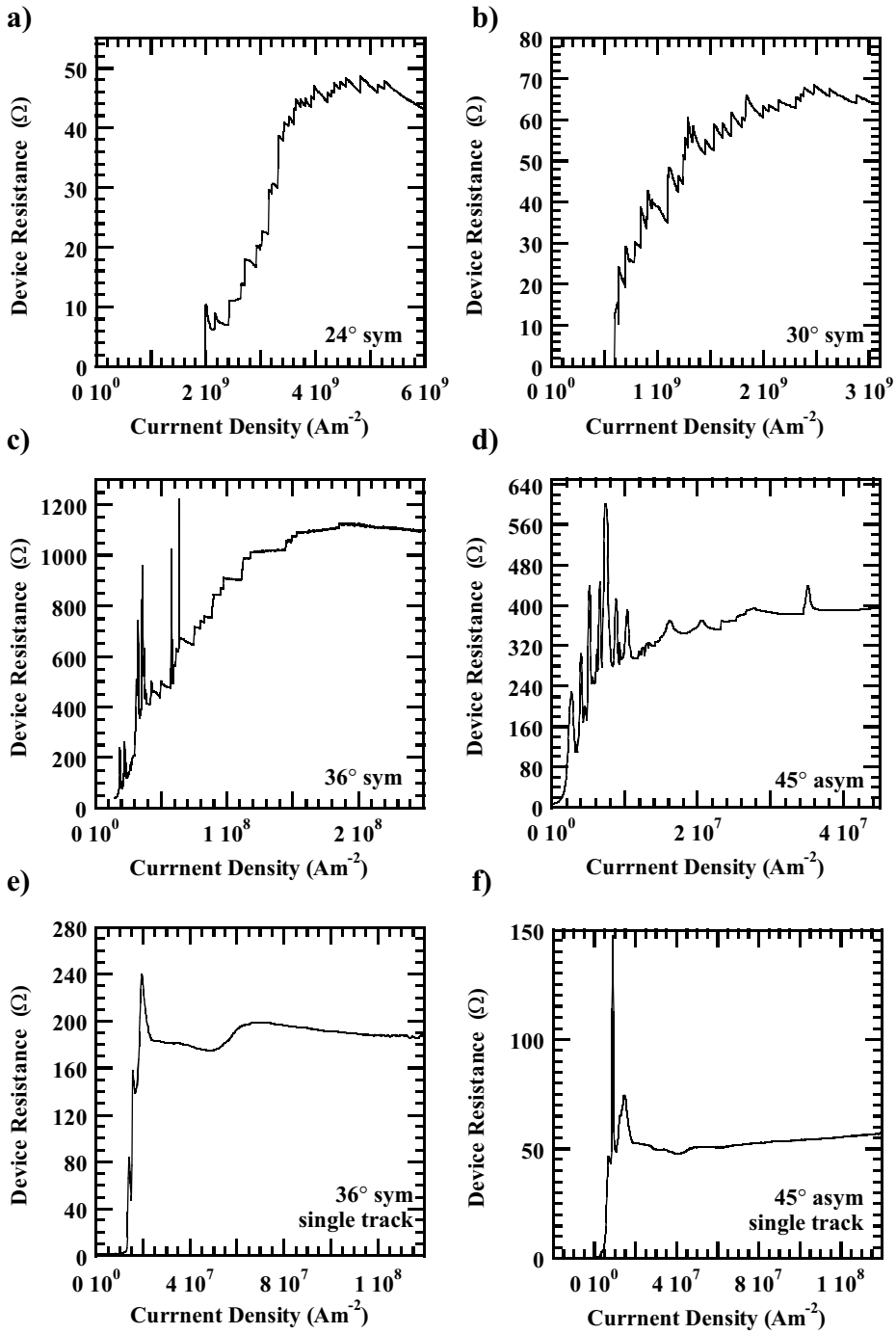


Figure 6.15: a) to d) — Representative current–resistance characteristics close to the critical current for each grain boundary measured in this study. In each case the data is taken from bridge 1. e) and f) — Current–Resistance characteristics for two single track devices, on the 36° symmetric and the 45° asymmetric grain boundaries respectively. The large spikes observable in c) and d) are also apparent in the single track data and are associated with the switching of the junctions.

individual tracks involve averaging over a number of facets and meanders.

The facet and meander structures are the source of the inhomogeneities reflected in the critical current measurements. The TEM investigation above shows that individual meanders can overgrow the bicrystal line producing non-epitaxial regions of film. This mechanism may lead to changes in the effective area of the boundary as discussed previously. The facets add an additional element of complexity to the system. The critical current through individual facets has been shown to depend on the orientation of the facets with respect to the grains either side (the so called inclination angles) as well as on the total misorientation (which is essentially unchanged across the entire facetting structure) [6]. The individual facets themselves may vary significantly in their electrical widths. Since the transport through the boundaries is almost certainly tunneling (see the discussion in Chapter 2) the effect of variations in the facet width would be that the narrowest facets would dominate the transport properties (due to the exponential decay of the tunnel current with width). The facetting therefore produces another mechanism by which the effective area of the boundaries can be reduced. Facetting adds an additional element of complexity to measurements of the critical current, since the $d_{x^2-y^2}$ order parameter can interact with the facet structure to produce a significant decrease in the observed critical current [33, 34]. This may mean that the critical current spreads measured are an over-estimate of the spread in the normal state transport properties on which this study focuses. There is some evidence that this is the case from the close agreement of the single track current density–voltage characteristics in Fig. 6.10 with those of the bridges in Fig. 6.9. The other sources of variation discussed change the effective area of the boundary and so the transport properties measured are at least proportional to those of single facet boundaries. A liquid phase epitaxy technique has recently been employed to grow macroscopic single facet grain boundaries [35] of certain misorientations. Such single facet grain boundaries are highly desirable for fundamental studies of transport properties, as they remove many of these difficulties. It would be interesting to repeat some of this work with such samples.

In summary the distributions of the critical currents in each of the bridges have been estimated by accurate measurements of the bridge resistance–voltage curves in the region close to the critical current. Experiments in which a bridge device is measured on multiple occasions, in which the positive and negative branches of the same curve are compared and in which individual bridges are severed so as to measure a single array, confirm that the technique is a reasonable way of investigating the critical current spread. The spread in the critical currents occurs over half to one order of magnitude for the different samples in this investigation. For the two lower angle

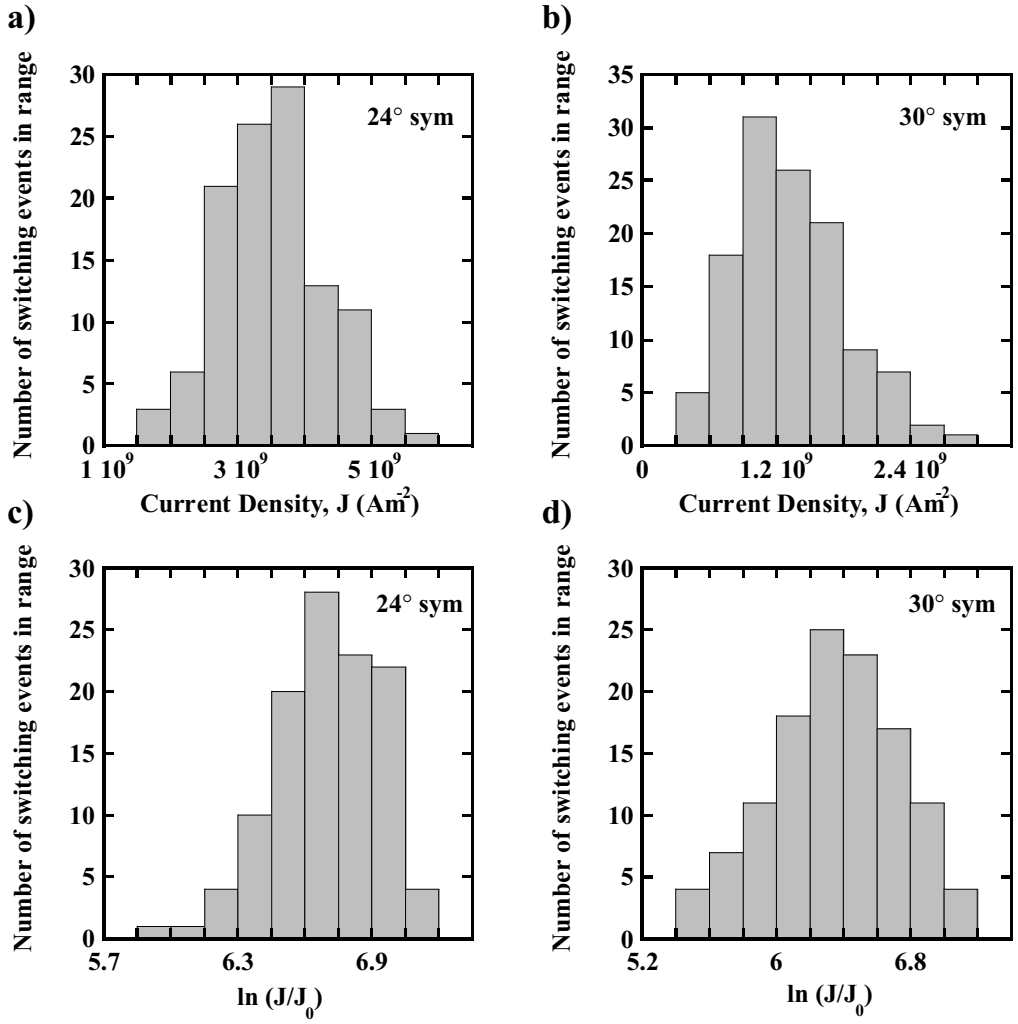


Figure 6.16: Distribution of switching current densities for a) the 24° and b) the 30° symmetric samples. This distribution should be a reasonable approximation to the critical current distribution. The two distributions are also shown with a logarithmic current scale (panels c) and d) — note that $J_0$ is an arbitrary constant).The 30° symmetric sample in particular shows evidence for the log normal distribution proposed by Shadrin, Jia and Divin [21, 22].

samples the critical current distribution could be investigated. While the results are not sufficiently quantitative to be conclusive, there is some indication that the critical currents obey the log normal distribution proposed by Shadrin, Jia and Divin [21, 22]. The implications of the spread in the critical currents were considered in some detail. The variations in the grain boundary properties are likely to be associated with variations in the effective area of the boundary or with the $d_{x^2-y^2}$ order parameter. The averaging process inherent to macroscopic measurements of normal state properties is therefore less complex than it might initially seem. However it would nonetheless be useful to repeat these experiments on single facet boundaries in which the microstructure is significantly less complex [35].

Both the normal state and other transport properties of these samples have been characterised in considerable detail. In the next section the effect of a controlled anneal on the 30° sample is discussed. By annealing the samples it is possible to alter the properties of the surrounding film without changing the grain boundary structure.

## 6.6 Properties as a Function of Oxygenation

A final experiment was performed in order to investigate the properties of de-oxygenated grain boundaries. The 30° symmetric grain boundary was annealed in a mixture of 0.2% Oxygen in Nitrogen (i.e. 0.2% of the total number of molecules in the gas mixture were Oxygen molecules) at 500°C for 7 hours. This time is sufficient to underdope the entire sample homogenously. The sample was then quenched into Liquid Nitrogen (the apparatus used for this experiment is described in detail in Chapter 3). The properties of the sample were measured in detail both before and after this annealing procedure so that a detailed comparison could be made.

Figure 6.17 summarises the results obtained from this experiment. The critical temperature of the sample is reduced from 92 K to 43 K and the bulk resistance–temperature curves are consistent with a decrease in the doping from $\delta \approx 0.05$ to $\delta \approx 0.45$ [13] (note that, as discussed in section 6.1, the estimated absolute values of the resistivity are high). The form of the resistance temperature curve suggests that the sample is strongly underdoped after annealing. The effect of underdoping is to bring the sample into the pseudogap regime of the high–$T_c$ phase diagram [36, 37] (see the discussion in chapter 2). Since it is likely that the transport mechanism for high angle boundaries involves tunneling of some form (as concluded in chapter 2) the presence of a (direction dependent) gap in the normal state density of states will almost certainly alter the tunnel current in some directions.

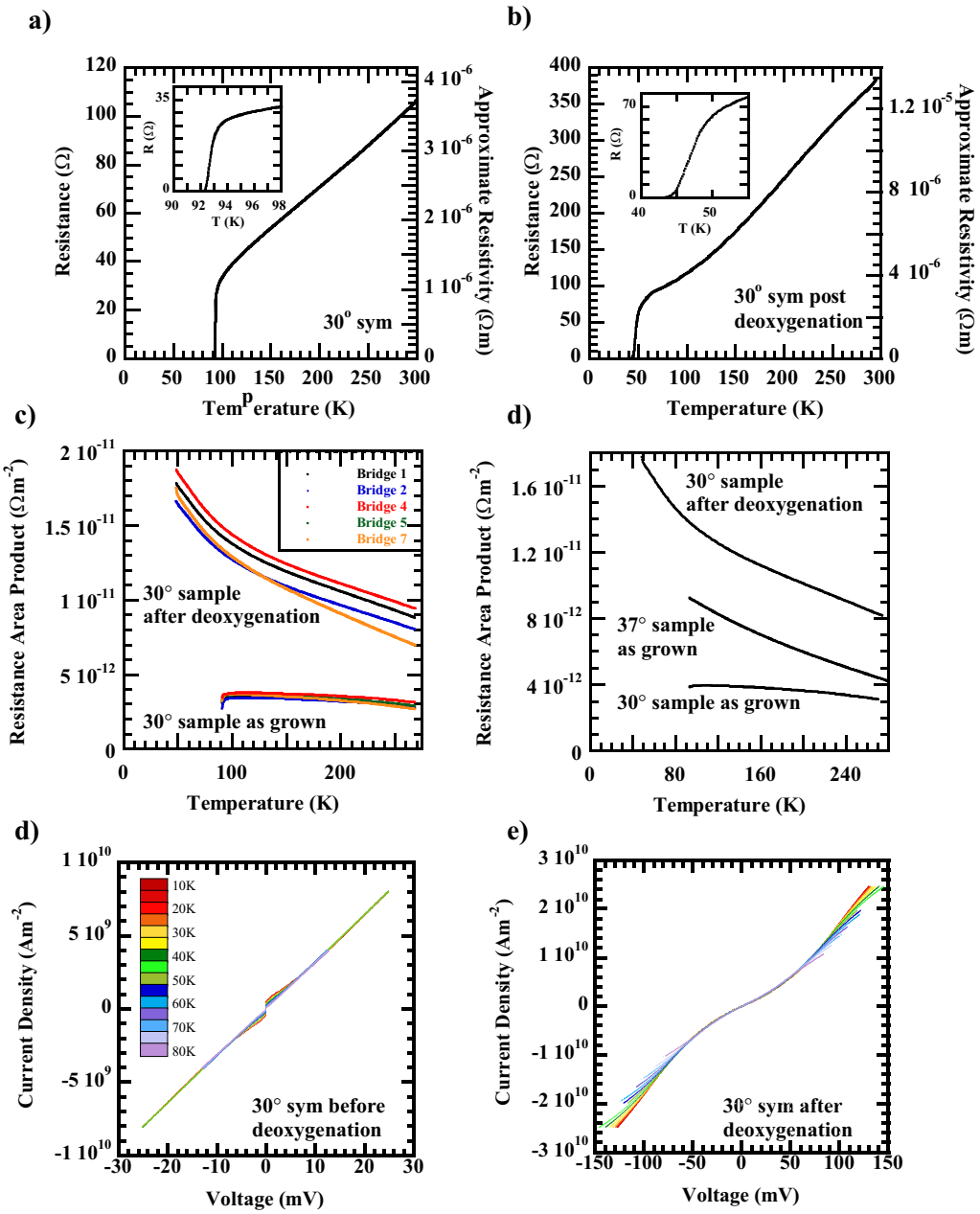


Figure 6.17: The effect of de-oxygenating one of the samples. Bulk resistance-temperature characteristics of the 30° film a) before and b) after deoxygenation. The insets show detail of the region close to the critical temperature, $T_c$. c) Resistance area product shown against temperature for all the wheatstone devices patterned over the 30° symmetric boundary before and after the film was deoxygenated. d) Comparison with the as grown 37° symmetric boundary (Tc=82 K)—in this case the mean over all the devices is shown. The current density–voltage characteristic for bridge 1 is also shown both before (e) and after (f) de-oxygenation. Note that for the bridge measurements the data is normalised so that it is comparable to single junction data.

Panels c and d in Figure 6.17 show the change in the behaviour of the zero bias normal state resistance as a function of temperature. There is a striking difference between the pre and post anneal characteristics. At higher temperatures the post anneal characteristics are markedly similar to those of the 36° symmetric and 45° asymmetric boundaries. At low temperatures the zero bias resistance increases rapidly with decreasing temperature — this may be a sign of a gap opening up in the density of states. The Pseudogap is zero along the $k_x = \pm k_y$ directions and maximum along the $k_x = 0$ and $k_y = 0$ directions [36]. The normal to the grain boundary plane in the 30° symmetric sample is tilted at ±15° to the $k_x = 0$ direction on the two sides of the boundary. The tunnel current is highly dependent on the density of states in these normal directions [38, 39] so it should be possible to observe the pseudogap in the underdoped state (assuming that tunneling is the transport mechanism).

The current density–voltage ($J$–$V$) characteristics are measurable over a significantly greater voltage range and are clearly non-linear. Interestingly the value of the resistance obtained from a fit to the $J$–$V$ characteristic shown in Figure 6.17 e is $1 \times 10^{-11}$ $\Omega\mathrm{m}^{-2}$ — significantly lower than the value of the zero-bias resistance measured close to the critical temperature (the fit is performed at sufficiently low voltages that the curve is linear). The $J$–$V$ curves are measured below $T_c$ so the pseudogap is replaced by the anisotropic superconducting gap, which has $d_{x^2-y^2}$ symmetry [40] and therefore maxima and minima in the same locations as those of the pseudogap. The gap energy scale is of order 10 meV and is too small to be observed clearly in the $J$–$V$ characteristics. Above the critical temperature the normal resistance is measured with a constant current bias of 5 $\mu A$. The maximum voltage measured is therefore approximately 0.1 mV. The pseudogap energy scale is similar to that of the superconducting gap — approximately 10 meV [36] and these low bias measurements will therefore be highly sensitive to it. While the pseudogap is the most obvious explanation for the observed sharp increase in the resistance area product at low temperatures, further work is necessary to convincingly confirm this. If the pseudogap is being probed, high angle grain boundaries may prove to be a useful means of studying the normal state gap in $YBa_2Cu_3O_{7-\delta}$ and other high temperature superconductors.

The effect of the anneals on the critical currents of the grain boundaries in the bridge is shown in the current–resistance characteristic in Fig. 6.18. The critical current is decreased by two orders of magnitude and its spread is increased slightly by de-oxygenation. The large peaks characteristic of abrupt switching appear in the underdoped sample. The fact that the critical current spread remains reasonable in this sample after annealing indicates that it may be possible to anneal a single sample multiple times. In this case the anneal

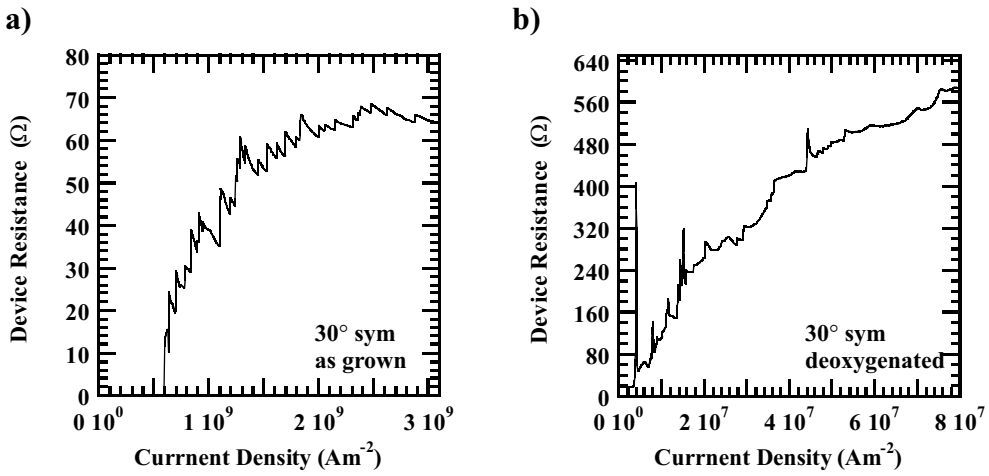


Figure 6.18: Current–resistance characteristic close to the critical current for bridge 1 on 30° sample a) before and b) after deoxygenation.

conditions dramatically changed the doping of the sample so the change in the grain boundary properties should be an extreme case. It is particularly interesting to anneal a single sample multiple times because the doping can then be altered progressively without changing the detailed microstructure of the grain boundary. The sample to sample irreproducibility is a major problem in the study of grain boundaries in $YBa_2Cu_3O_{7-\delta}$, so performing repeated experiments on a single sample is desirable.

In this section the effect of homogenously deoxygenating the 30° symmetric sample was examined. The transport properties measured are consistent with a reduction in the doping of the $YBa_2Cu_3O_{7-\delta}$ from $\delta \approx 0.05$ to $\delta \approx 0.45$. At higher temperatures the properties of the grain boundary change from the almost temperature independent lower angle behaviour to that more characteristic of the higher angle boundaries. As the sample is cooled towards $T_c$, the resistance increases rapidly at low bias, most likely as a result of the normal state gap. Further work is necessary to confirm this. The critical current of the grain boundaries was reduced by almost two orders of magnitude, whilst the spread in the critical currents was increased. The promise of repeated annealing experiments was highlighted — by exploring a range of doping levels with a single sample experiments can be performed with the same grain boundary microstructure. This may lead to a more systematic understanding of grain boundary properties and in addition should establish whether the technique is suitable for investigating the pseudogap in the normal state.

## 6.7 Summary

In this chapter a detailed study of the transport properties of grain boundaries of various misorientations has been reported. 24°, 30° and 36° symmetric and 45° asymmetric [001] tilt grain boundaries were investigated. The transport properties have been correlated with the previously unmeasured normal state resistance of these grain boundaries.

Initially the films used in this investigation were characterised in detail by AFM, TEM and by measuring their electrical resistivity. The films were reasonably flat, with some particulates on their surface. The grain boundary has been shown to overgrow the substrate bicrystal in some regions — producing regions of non-epitaxial growth. The resistivity measurements show that the electrical characteristics of the films are consistent with optimal doping, with the exception of the 36° symmetric boundary, which is slightly underdoped. The fabrication of devices from the films was also characterised by atomic force microscopy and the devices were found to be of good quality.

The normal state resistance of the grain boundaries was measured using a number of devices on each sample and was found to be self consistent and consistent with other studies. The magnitude of the low temperature normal state resistance was found to be within the spread reported in the literature. The resistance area product of the higher angle boundaries (36° symmetric and 45° asymmetric) decreased approximately linearly above $T_c$, whilst that of the lower angle boundaries (24° and 30° symmetric) was almost temperature independent. Below $T_c$ the current–voltage characteristics of the devices were measured. Devices on the higher angle samples showed non-linear current voltage characteristics that were also observed in single track devices. The conductance–voltage characteristics were not quadratic for the single track devices, so a standard, spherical Fermi surface picture does not apply.

The bridges used in this investigation were found to consist of grain boundaries with a significant spread in critical currents. The critical currents were estimated by careful resistance measurements using a lock-in amplifier and were typically spread over half to one order of magnitude about the mean. The effect of this variation in critical currents on the validity of the normal resistance measurements was discussed. It is likely that the variations reflect changes in the effective area of the grain boundary, or that they result from the d-wave order parameter and so overestimate the variations in the normal state resistance. The potential of liquid phase epitaxy grown single facet grain boundaries [35] for eliminating these problems was highlighted.

While the critical current spread leads to some difficulties in interpretation, this data is nonetheless a useful body of knowledge with which to test

the various models of $YBa_2Cu_3O_{7-\delta}$ grain boundaries. The current density–voltage curves and the resistance area product–temperature data represent two, essentially independent sets of data which must be explained by any model for high $T_c$ grain boundaries. The data are analysed in the context of different models in the next chapter.

The experiment in which a single grain boundary was underdoped highlighted the potential of annealing experiments on a single grain boundary. Such experiments allow changes in the bulk properties of the sample without changes in the microstructure of the grain boundary itself. The effect of underdoping the 30° symmetric boundary was dramatic, with behaviour in the resistance area product characteristic of higher angle samples at higher temperatures and a sharp increase in the normal state conductance at lower temperatures (possibly due to the pseudogap opening up). The results showed that it may be possible to use grain boundaries as a means of investigating the normal state pseudogap.

In the next chapter a detailed analysis of both the normal state resistance and the current voltage characteristics is performed. The results are analysed in the context of the various transport models for high-$T_c$ grain boundaries.

# Bibliography


[1] H. Hilgenkamp and J. Mannhart, Reviews of Modern Physics **74**, 485 (2002).

[2] C. W. Schneider et al., cond-mat/0307470, 2003.

[3] S. Proyer, E. Stangl, M. Borz, B. Hellebrand, and D. Bauerle, Physica C **257**, 1 (1996).

[4] J. L. Alarco et al., Physica C **247**, 263 (1993).

[5] B. Moeckly, D. K. Lathrop, and R. A. Buhrman, Physical Review B **47**, 400 (1993).

[6] S.-W. Chan, Q. Jin, J. W. H. Tsai, S. C. Tidrow, and Q. Jiang, IEEE Transactions on Applied Superconductivity **13**, 2829 (2003).

[7] Q. Jin and S.-W. Chan, Journal of Materials Research **17**, 323 (2002).

[8] D. J. Miller et al., Applied Physics Letters **66**, 2561 (1995).

[9] C. Tæholt, J. G. Wen, H. W. Zandebergen, Y. Shen, and J. W. M. Hilgenkamp, Physica C **230**, 425 (1994).

[10] M. J. Hogg, *The Electronic Properties of Thin Film* $YBa_2Cu_3O_{7-\delta}$ *Low Angle Grain Boundaries*, PhD thesis, Cambridge University, Cambridge, UK, 2002.

[11] J. Ayache, A. Thorel, J. Lesueur, and U. Dahmen, Journal of Applied Physics **84**, 4921 (1998).

[12] X. F. Zhang, D. J. Milkler, and J. Talvacchio, Applied Physics Letters **11**, 2440 (1996).

[13] A. Carrington, D. J. C. Walker, A. P. Mackenzie, and J. R. Cooper, Physical Review B **48**, 13051 (1993).

[14] B. Wuyts et al., Physical Review B **47**, 5512 (1993).

[15] E. C. Jones et al., Physical Review B **47**, 8986 (1993).

[16] P. Xiong, G. Xiao, and X. D. Wu, Physical Review B **47**, 5516 (1993).

[17] T. Ito, K. Takenaka, and S. Uchida, Physical Review Letters **70**, 3995 (1992).

[18] J. M. Harris, Y. F. Yan, and N. P. Ong, Physical Review B **46**, 14293 (1992).

[19] R. Gerdemann et al., Journal of Applied Physics **76**, 8005 (1992).

[20] H. Burkhardt, O. Bruhmann, A. Rauther, F. Schnell, and M. Schilling, IEEE Transactions on Applied Superconductivity **9**, 3153 (1999).

[21] P. Shadrin, C. L. Jia, and Y. Divin, Physica C **372-376**, 80 (2002).

[22] P. Shadrin, C. L. Jia, and Y. Divin, IEEE Transactions on Applied Superconductivity **13**, 603 (2003).

[23] S. H. Mennema, unpublished.

[24] C. W. Schneider, unpublished.

[25] D. Dimos, P. Chaudhari, and J. Mannhart, Physical Review B **41**, 4038 (1990).

[26] O. M. Froehlich, P. Richter, A. Beck, R. Gross, and G. Koren, Journal of Low Temperature Physics **106**, 243 (1997).

[27] R. Gross, P. Chaudhari, M. Kawasaki, and A. Gupta, Physical Review B **42**, 10736 (1990).

[28] M. Nahum, S. Verghesse, P. L. Richards, and K. Char, Applied Physics Letters **59**, 2034 (1991).

[29] C. Uher, *Physical Properties of High Temperature Superconductors II*, World Scientific, 1992.

[30] B. Dam et al., Nature **399**, 439 (1999).

[31] D. E. McCumber, Journal of Applied Physics **39**, 3113 (1968).

[32] K. K. Likharev, *Dynamics of Josephson Junctions and Circuits*, Gordon and Breach Publishers, Amsterdam, 1986.

[33] H. Hilgenkamp, J. Mannhart, and B. Mayer, Physical Review B **53**, 14586 (1996).

[34] J. Mannhart and H. Hilgenkamp, Superconductor Science and Technology **10**, 880 (1997).

[35] J. G. Wen, T. Takagi, and N. Koshizuka, Superconductor Science and Technology **13**, 820 (2000).

[36] T. Timusk and B. Statt, Reports on Progress in Physics **62**, 61 (1999).

[37] J. Tallon and J. Loram, Physica C **349**, 53 (2001).

[38] C. B. Duke, *Tunneling in Solids*, Solid State Physics, Supplement 10, Academic Press, New York, 1969.

[39] E. L. Wolf, *Principles of Electron Tunneling Spectroscopy*, International Series of Monographs on Physics, 71, Oxford Universtiy Press, New York, 1985.

[40] C. C. Tsuei and J. R. Kirtley, Reviews of Modern Physics **72**, 969 (2000).

# Chapter 7

# Analysis of the Normal State Results

In this chapter the results presented in the previous chapter are analysed in terms of the various models for high angle grain boundaries in the literature. This analysis is necessarily complicated by the inhomogeneities in the boundary highlighted in the work presented in Chapters 4 and 6. Since the analysis of the grain boundaries is complex even for a uniform barrier, the arguments in this chapter will be primarily focused on models that take no account of the barrier inhomogeneity. The inhomogeneous grain boundary structure cannot of itself explain the current voltage and the resistance temperature data of the previous chapter, since both measurements were performed on a single boundary with a fixed structure. However the results obtained are necessarily an average of the transport properties which are known to be non-uniform across the width of the barrier. Some experiments (such as those presented in Chapter 4) appear to indicate that the major effect of the inhomogeneities is to limit the grain boundary effective area. If this is the case then uniform barrier models are likely to produce reasonable fits to the data.

As discussed in Chapter 2, the electrical barrier present at a high angle grain boundary can be modelled in one of three ways:

- An insulating barrier with a low height of order 100 meV caused by a local distortion of the band structure (Band bending model [1]).

- A Mott insulating barrier with a gap of order 1 eV, containing a high density of localised states. Supercurrent transport occurs through the barrier by direct tunneling whilst the quasiparticles tunnel resonantly (Resonant tunneling type models [2, 3, 4, 5, 6, 7]).

- An insulating barrier perforated by pinholes through which the supercurrent transport occurs (ScS type models [8, 9, 10]).

The main focus of this chapter will be on the band bending model. The reason for this focus is that this is currently the most plausible model for high angle grain boundaries. The model developed in this chapter will show that the magnitude of the normal state resistances of [001] tilt grain boundaries are consistent with the lower barrier heights associated with a band bending model. A band bending framework is developed that accounts for the results of Chapter 6 in a reasonable way. The resonant tunneling model is associated with a multi-step tunneling process, with larger barrier heights than the band bending model. The direct tunneling model developed for the band bending calculations can be used to show that the thickness of the barrier required for direct tunneling with a 1 eV barrier height is less than the interatomic spacing, which demonstrates that a resonant tunneling model is implausible. It is also shown that the results of the previous chapter are inconsistent with transport that is dominated by narrow constrictions.

## 7.1 A Direct Tunneling Band Bending Model

The band bending model describes transport through the boundary as being dominated by tunneling. In this section a tunneling model with band-bending type potential barriers is developed. The spherical Fermi-surface results of Stratton [11] and others [12] cannot be applied to the essentially two dimensional Fermi surface topology of $YBa_2Cu_3O_{7-\delta}$. It is therefore necessary to account more completely for the bandstructure of the material within a tunneling model.

While the bandstructure is properly accounted for, a number of approximations are still implicit in the analysis that follows. Firstly, the bending of the band structure is modelled by the simplest approach of employing a trapezoidal barrier. The detailed physics of the band distortion is not contained within such an approach and a more difficult calculation would need to be carried out to include such effects. Secondly, the model assumes that the tunnel barrier is uniform along the length of the grain boundary. This is clearly not the case for the boundaries measured in this study, as discussed previously. Thirdly, as a result of the low resistance of the grain boundaries, the tunnel barriers that are employed are necessarily very narrow, typically of order 1 nm wide. The model that is used employs the WKB approximation to calculate the tunnel current, which implicitly assumes that the potential changes that occur do so over distances that are large compared to the

electron wavelength, which is also of order 1 nm. An estimate of the errors involved in using the WKB approximation may be obtained by comparing the exact value of the transmission probability with that given by the WKB approximation for a rectangular barrier. For an electron with a wavevector at the Fermi surface of $YBa_2Cu_3O_{7-\delta}$ (wavevector, $k = 2.04 \times 10^9$ m$^{-1}$ and effective mass, $m = 4.5m_e$, where $m_e$ is the electron mass) the exact expression gives a transmission probability of 0.09 for a tunnel barrier of width 0.5 nm and with height 100 meV above the Fermi energy. This is significantly greater than the WKB transmission probability of 0.03. However the model should predict the correct order of magnitude of the tunnel current and therefore provide a reasonable basis on which a more detailed formalism could be based. Finally the model is formulated within the independent electron approximation, which assumes that the electrons tunneling are independent particles [13]. Such an assumption may not apply to the Cuprates in the normal state, dependent on the validity of a Fermi-liquid picture. As a result of the independent electron assumption, it is necessary to perform the calculation for electrons in a band that is less than half full, which requires the assumption of a negative trapped charge on the boundary.

Despite these limitations, the model that is developed is a significant improvement over the currently available models for direct tunneling. Furthermore, it reproduces the form of the data well and therefore provides a reasonable basis on which more detailed calculations can proceed.

### 7.1.1 Theory of Tunneling in Metal-Insulator-Metal Junctions

In this section we describe the theory for tunneling through a metal-insulator-metal junction, within the independent electron approximation. We start by considering the case of a tunnel junction in which the two electrodes consist of an identical metal in the same orientation. The equations given below will need to be generalised subsequently, since the crystallographic axes on either side of the grain boundary are rotated with respect to one another. The net current through the tunnel junction is obtained by subtracting the current from side $b$ to side $a$ of the junction, $J_{b\to a}$, from that in the opposite direction, $J_{a\to b}$: $J = J_{a\to b} - J_{b\to a}$. Within the independent electron framework, the current in each direction is determined by the following equations [12, 14]:

$$J_{a\to b} = \frac{2e}{(2\pi)^3} \iiint_{\mathrm{BZ}} \mathbf{v}\cdot\mathbf{n}_\perp f_a(E_a)\left[1-f_b(E)\right] D(E,\mathbf{k}_\parallel,V)\,\mathrm{d}^3k \qquad (7.1)$$

$$J_{b\to a} = \frac{2e}{(2\pi)^3} \iiint_{\mathrm{BZ}} \mathbf{v}\cdot\mathbf{n}_\perp \left[1-f_a(E)\right] f_b(E) D(E,\mathbf{k}_\parallel,V)\,\mathrm{d}^3k \qquad (7.2)$$

where $e$ is the electron charge, $E$ is the total energies of electrons in state $\mathbf{k}$, $\mathbf{v}$ is the electron group velocity, $\mathbf{n}_\perp$ is a unit vector normal to the grain boundary plain, $f_a(E)$ and $f_b(E)$ are the Fermi functions defined on sides $a$ and $b$ of the boundary respectively, $\mathbf{k}_\parallel$ is the wavevector of the electron projected into the plain of the boundary, $V$ is the applied voltage and $D(E,\mathbf{k}_\parallel,V)$ is a transmission probability. The integral is carried out over the first Brillouin zone (BZ).

Equations 7.1 and 7.2 are derived by summing the expectation values of the current operator in the eigenstates of the Schrödinger equation. Duke gives a detailed derivation [12]. The physical origin of the terms in each equation can be understood straightforwardly. Consider, for example, Equation 7.1. In order for an electron to tunnel it must come from an occupied state on side a and enter an unoccupied state on side b. This is the origin of the two Fermi function terms. The number of electrons that tunnel is proportional to the rate at which electrons hit the barrier in a given $\mathbf{k}$-state, which in turn is proportional to $\mathbf{v}\cdot\mathbf{n}_\perp$. Finally the factor $D(E,\mathbf{k}_\parallel)$ is determined by the form of the potential barrier and represents the decay of the wavefunction in the barrier region. Harrison has shown that, within the WKB approximation, the value of $D(E,\mathbf{k}_\parallel,V)$ is given by:

$$\begin{aligned} D(E,\mathbf{k}_\parallel,V) &= \exp\left(-2\int_{x_1}^{x_2} |\mathbf{k}_\perp(x)|\mathrm{d}x\right) \\ &= \exp\left(-2\sqrt{\frac{2m^*}{\hbar^2}}\int_{x_1}^{x_2}\left(\phi(x,V)-E+\frac{\hbar^2|\mathbf{k}_\parallel|^2}{2m^*}\right)^{1/2}\mathrm{d}x\right) \end{aligned} \qquad (7.3)$$

where $\mathbf{k}_\perp$ is the momentum component parallel to the boundary normal, $x_1$ and $x_2$ are the classical turning points in regions 1 and 2 respectively (i.e. the points at which $|\mathbf{k}_\perp| = 0$), $\phi(x,V)$ is the potential of the tunnel barrier (which is a function of both position, $x$, and applied voltage, $V$) and $m^*$ is the effective mass of the electrons (throughout this work a band average of $m^* = 4.5m_e$, where $m_e$ is the electron mass was used). Here we have assumed conservation of total energy (i.e. an elastic scattering process) and conservation of transverse momentum, $\mathbf{k}_\parallel$, and used the relation

$E = \hbar^2(-|\mathbf{k}_\perp|^2 + |\mathbf{k}_\parallel|^2)/2m^* + \phi$ (from the Schrödinger equation) to determine $|\mathbf{k}_\perp|$ (the minus sign occurs because in the barrier region, where the wavefunction decays, $\mathbf{k}_\perp$ is imaginary).

When a voltage, $V$, is dropped across the barrier the Fermi level on side $b$ of the boundary drops in energy by an amount $eV$ (i.e. $\mu_a - \mu_b = eV$ where $\mu_a$ is the Fermi level on side a and $\mu_b$ is that on side b). The Fermi functions are therefore given by:

$$f_a(E) = \frac{1}{\exp\left(\frac{E-\mu_a}{k_B T}\right) + 1} = f(E) \tag{7.4}$$

$$f_b(E) = \frac{1}{\exp\left(\frac{E-\mu_b}{k_B T}\right) + 1} = f(E + eV) \tag{7.5}$$

where $k_B$ is Boltzmann's constant and $T$ is the temperature.

We can also use the relation $\mathbf{v} \cdot \mathbf{n}_\perp = \hbar^{-1}\partial E/\partial k_\perp$ to substitute for the group velocity. Since the two integrals are identical, we can combine the two terms to obtain the net current density $J$, which is given by:

$$J = \frac{2e}{(2\pi)^3\hbar} \iiint_{\mathrm{BZ}} \frac{\partial E}{\partial k_\perp} \left[f(E) - f(E + eV)\right] D(E, \mathbf{k}_\parallel, V)\, \mathrm{d}^3k \tag{7.6}$$

This expression forms the basis of the analysis in the subsequent sections.

### 7.1.2 One Dimensional Model

We consider first a one dimensional limit of this problem which displays the basic phenomenology observed in the more accurate calculations. Taking Equation 7.6 in a one dimensional limit, we obtain the following expression for the total current, $I$:

$$I = \frac{2e}{\hbar} \int_0^{E(\pi/a)} \left[f(E) - f(E + eV)\right] D(E, V)\, \mathrm{d}E \tag{7.7}$$

where $D(E, V)$ is given by:

$$D(E, V) = \exp\left(-2\sqrt{\frac{2m^*}{\hbar^2}} \int_{x_1}^{x_2} (\phi(x) - E)^{1/2}\, \mathrm{d}x\right) \tag{7.8}$$

A trapezoidal potential barrier function is employed, since by the use of different parameters both band bending and classical tunnel barriers can be investigated. The form of the potential used is:

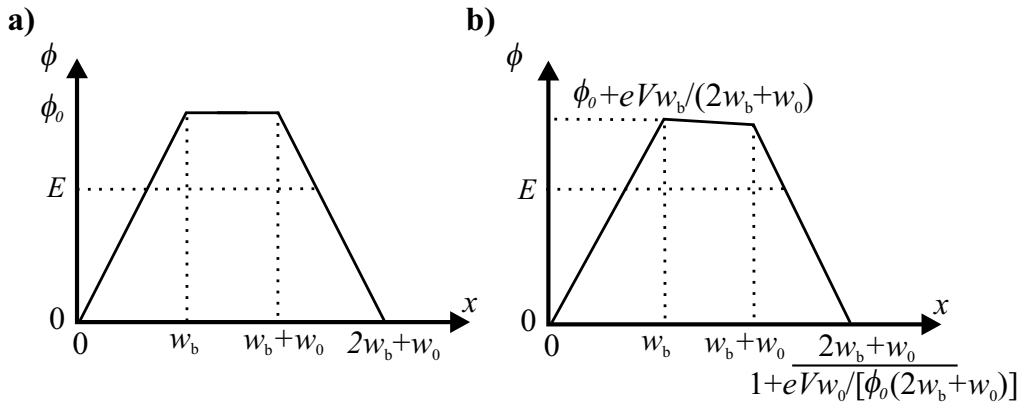


Figure 7.1: Trapezoidal tunnel barrier with a) no applied voltage and b) an applied voltage $V$. The barrier height $\phi$ is shown against position $x$. The various widths in Equation 7.9 are defined in the figure.

$$\phi(x,V) = \begin{cases} \dfrac{\phi_0 x}{w_b} - \dfrac{eVx}{2w_b+w_0}, & 0 \le x < w_b \\ \phi_0 - \dfrac{eVx}{2w_b+w_0}, & w_b \le x < w_b + w_0 \\ \dfrac{\phi_0(w_0+2w_b-x)}{w_b} - \dfrac{eVx}{2w_b+w_0}, & w_0 \le x \le 2w_b + w_0 \end{cases} \tag{7.9}$$

where $\phi_0$ is the zero voltage barrier height, $w_b$ is the width of the trapezoidal banks and $w_0$ is the width of the central, rectangular part of the boundary.

The form of $\phi(x,V)$ is illustrated in Fig. 7.1. It is clear from the figure that the limits of integration in Equation 7.8, $x_1$ and $x_2$, are a function of both $E$ and $V$, since the integral is carried out over the regions in which the barrier potential is greater than the initial energy of the electron $E$.

The values of $x_1$ and $x_2$ are given by:

$$x_1 = E\left(\frac{\phi_0}{w_b} - \frac{eV}{2w_b+w_0}\right)^{-1}, \qquad 0 \le E < E_2 \tag{7.10}$$

$$x_2 = \begin{cases} \left(\phi_0\dfrac{2w_b+w_0}{w_b} - E\right)\left(\dfrac{\phi_0}{w_b} + \dfrac{eV}{2w_b+w_0}\right)^{-1}, & 0 \le E < E_1 \\ \dfrac{\phi_0 - E}{eV}(2w_b+w_0), & E_1 \le E < E_2 \end{cases} \tag{7.11}$$

where $E_1$ and $E_2$ are given by:

$$E_1 = \phi_0 - eV\left(\frac{w_b + w_0}{2w_b + w_0}\right) \tag{7.12}$$

$$E_2 = \phi_0 - eV\left(\frac{w_b}{2w_b + w_0}\right) \tag{7.13}$$

Note that for $E > E_2$ thermal emission over the barrier occurs. This can be included in the model by assigning a transmission probability of 1 to energies greater than $E_2$. The integrals in Equation 7.8 can be evaluated analytically using these values for $x_1$ and $x_2$. The symbolic expressions obtained save a considerable amount of computation time in subsequent generalisations of the model. For completeness the complete form of $D(E, V)$ is given below:

$$D(E,V) = \begin{cases} \exp\left(-\frac{4}{3}\sqrt{\frac{2m^*}{\hbar^2}}g_1\right), & 0 \leq E < E_1 \\ \exp\left(-\frac{4}{3}\sqrt{\frac{2m^*}{\hbar^2}}g_1\right), & E_1 \leq E < E_2 \end{cases} \tag{7.14}$$

where:

$$\begin{aligned} g_1 =& \frac{(\phi_0 - E - eVw_b/(2w_b + w_0))^{3/2}}{\phi_0/w_b - eV/(2w_b + w_0)} + \frac{(\phi_0 - E - eV(w_b + w_0)/(2w_b + w_0))^{3/2}}{\phi_0/w_b + eV/(2w_b + w_0)} \\ &+ \frac{2w_b + w_0}{eV}\left[\left(\phi_0 - E - eV\frac{w_b}{2w_b + w_0}\right)^{3/2} - \left(\phi_0 - E - eV\frac{w_b + w_0}{2w_b + w_0}\right)^{3/2}\right] \end{aligned} \tag{7.15}$$

$$g_2 = \frac{(\phi_0 - E - eVw_b/(2w_b + w_0))^{3/2}}{\phi_0/w_b - eV/(2w_b + w_0)} + \frac{2w_b + w_0}{eV}\left(\phi_0 - E - eV\frac{w_b}{2w_b + w_0}\right)^{3/2} \tag{7.16}$$

These expressions have been checked against numerical evaluations of the integrals and shown to be correct.

The model can be understood conceptually in a reasonably straightforward manner. The important terms in the expression for the current, $I$, are the Fermi function terms $f(E) - f(E + eV)$ and the attenuation factor $D(E, V)$. The two Fermi functions define a 'window' of electron energies that can tunnel. This Fermi window broadens with increasing temperature, so at

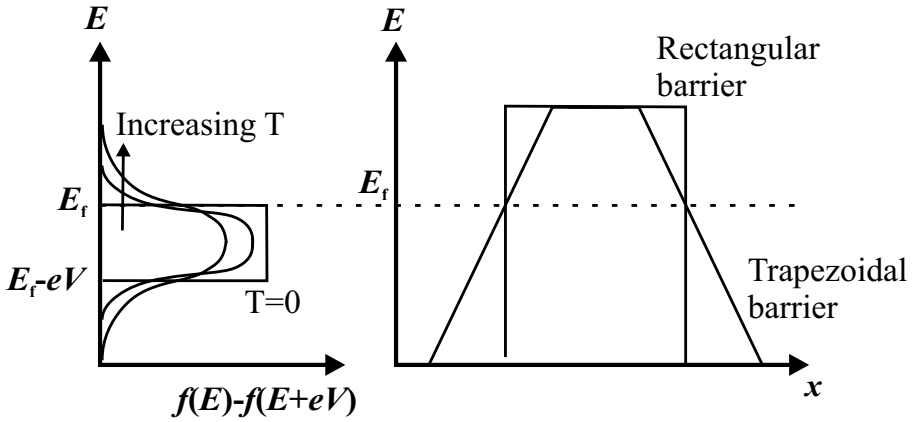


Figure 7.2: Diagram showing how the temperature dependence of the resistance is altered by the form of the barrier in a simple 1 dimensional tunneling model. The two Fermi functions define a 'window' of electron energies that can tunnel. The Fermi window broadens with increasing temperature. For a rectangular barrier the higher energy electrons see a barrier with the same width but a reduced height. For the case of a trapezoidal barrier the height and the width of the barrier are reduced. The temperature dependence for such barriers is therefore more pronounced.

higher temperatures higher energy electrons can tunnel. The exponent in $D(E, V)$ increases roughly as the product of the the barrier width with the square root of the barrier height. For a rectangular barrier, higher energy electrons see a barrier with the same width but a reduced height. In the case of a trapezoidal barrier, the height and the width of the barrier are reduced for higher energy electrons. The temperature dependence is therefore more pronounced for the trapezoid barrier. Figure 7.2 shows this principle schematically.

The current through the barrier can be calculated in specific cases by numerically evaluating the the integral in Equation 7.7. Results obtained from small trapezoidal barriers with heights of order 100 meV are shown in Figures 7.3 and 7.4. The reason this parameter range is employed becomes apparent in the next section, where it is shown that the barrier height must be in this range in order to explain the magnitude of the resistance area products of the grain boundaries. It is clear from the figures, that in this simple one dimensional picture, the behaviour of the resistance-temperature and the current voltage characteristics is similar to that observed in the experimental data presented in the previous chapter. In particular, the temperature dependence of the resistance area product seems consistent with a trapezoidal barrier, which suggests a band bending type picture. Note also that the ma-

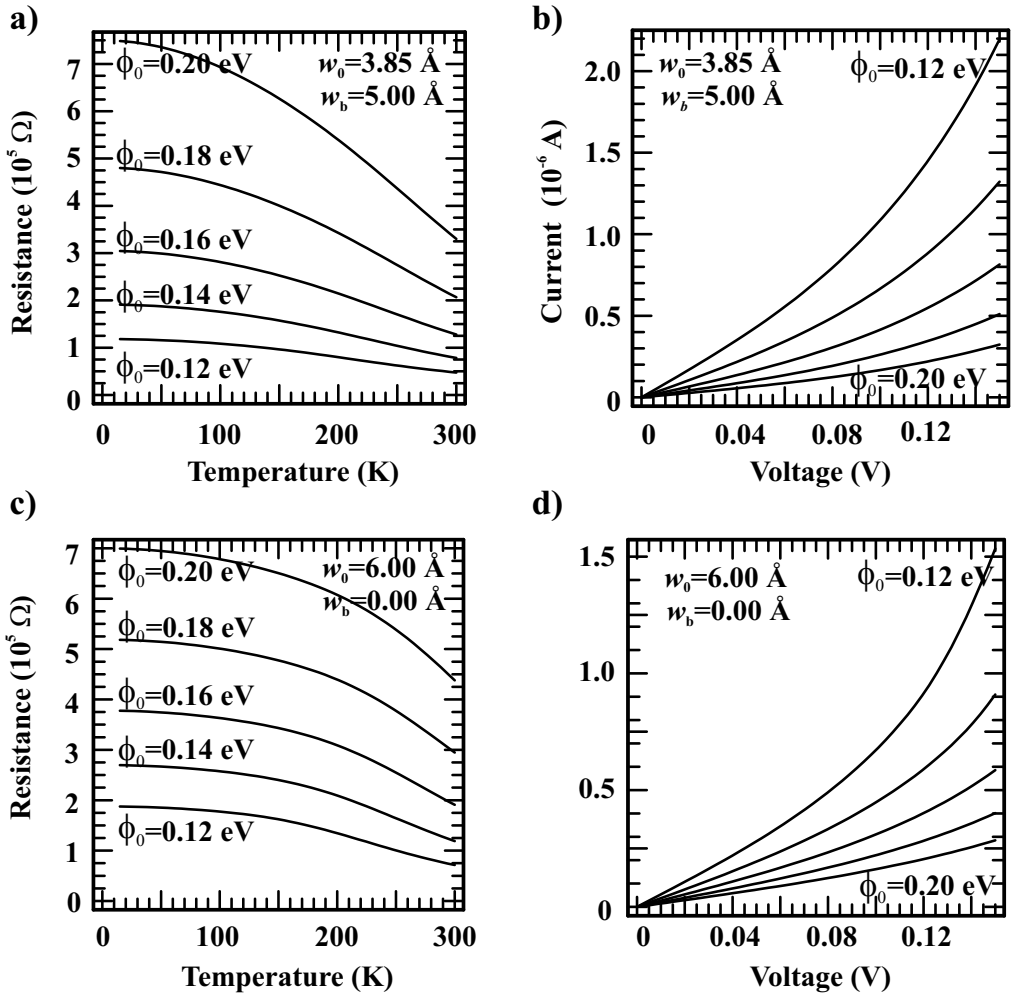


Figure 7.3: Variation of the resistance temperature and current voltage characteristics with barrier height in a simple 1 dimensional tunneling model with trapezoidal and rectangular barriers. a) Resistance temperature curves and b) current voltage curves for a trapezoidal barrier as the barrier height is increased in 0.02 eV increments from 0.12 to 0.20 eV. c) and d) Resistance temperature and current voltage characteristics for a rectangular barrier with a comparable resistance as the barrier height is increased in the same range. The terms $\phi_0$, $w_b$, and $w_0$, that describe the detailed barrier shape, are defined in Fig. 7.1.

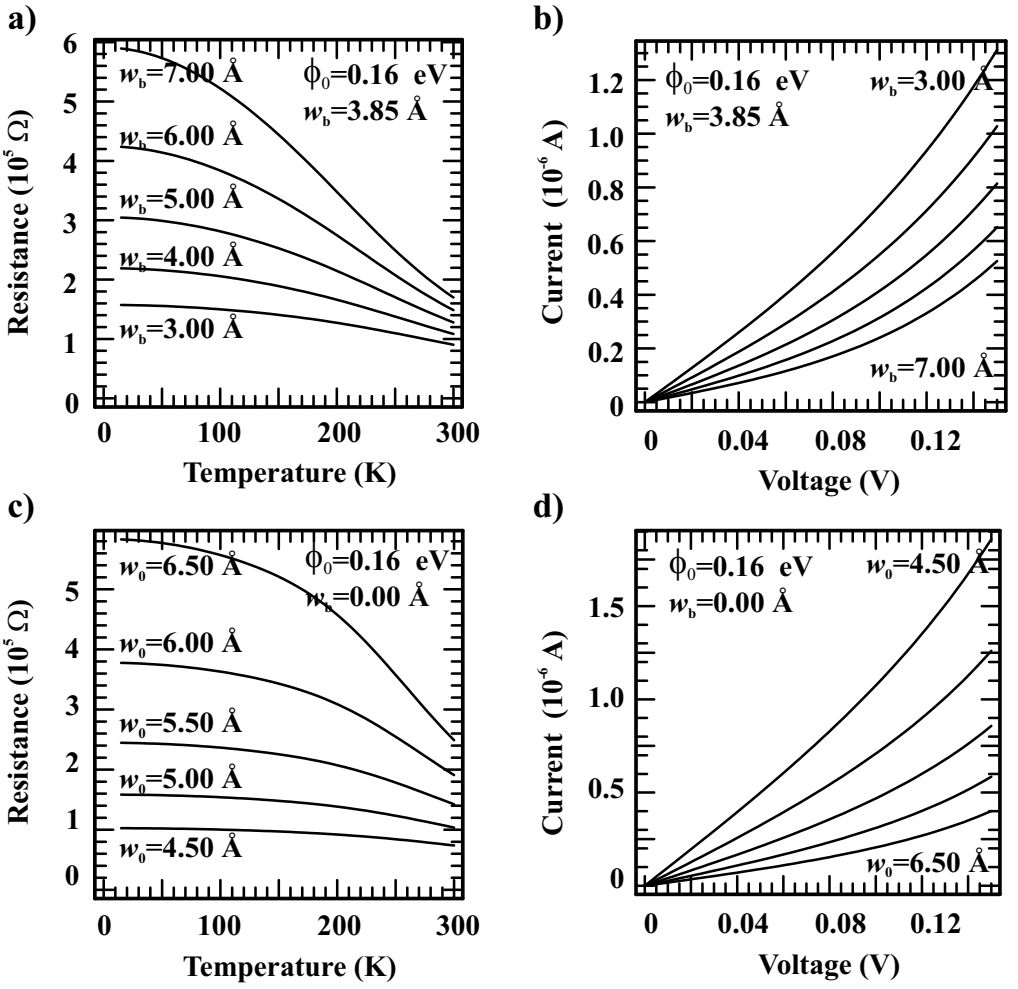


Figure 7.4: Variation of the resistance temperature and current voltage characteristics with barrier width in a simple 1 dimensional tunneling model with trapezoidal and rectangular barriers. a) Resistance temperature curves and b) current voltage curves for a trapezoidal barrier as the size of the trapezoidal bank is increased from 3 Å to 7 Å in 1 Å increments. c) and d) Resistance temperature and current voltage characteristics for a rectangular barrier with a comparable resistance as the barrier width is increased from 4.5 Å to 6.5 Å in 0.5 Å increments. The terms $\phi_0$, $w_b$, and $w_0$, that describe the detailed barrier shape are defined in Fig. 7.1.

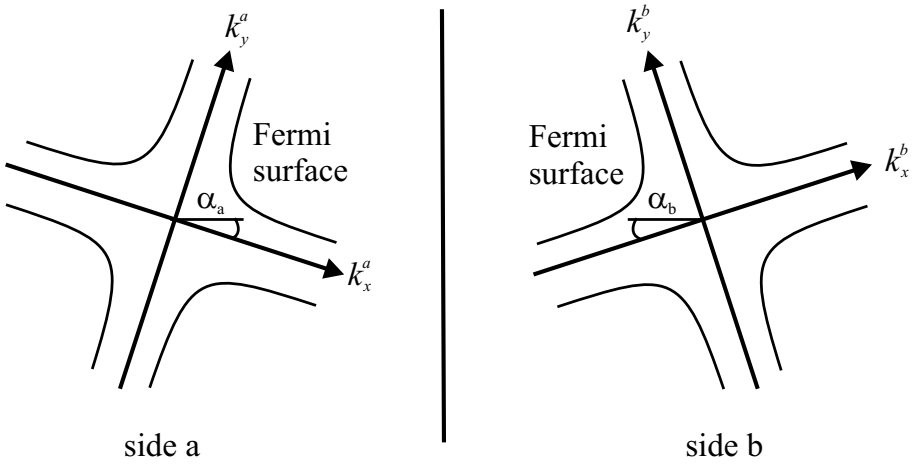


Figure 7.5: In a general tunneling calculation for grain boundaries, it is necessary to account for the rotation of the crystallographic axes on either side of the boundary. For the case of the [001] tilt boundary illustrated above, the axes have been rotated by angles $\alpha_a$ and $\alpha_b$ on sides a and b respectively. In the general case two sets of co-ordinates $[k_x^a, k_y^a, k_z^a]$ and $[k_x^b, k_y^b, k_z^b]$ are defined to describe the Fermi surface on either side of the boundary.

jority of the temperature dependence results from the mechanism depicted in figure 7.2 and not from thermal emission, since a barrier height of 150 meV corresponds to a temperature of approximately 1800 K.

The variation of both barrier height or barrier width independently could explain the change in the behaviour as the misorientation angle is changed. In a grain boundary it is likely that these two parameters are in fact linked, by a relationship of the form $\phi_0 \propto w_b^2$ [1, 15], so that a combination of the variation of $\phi_0$ and $w_b$ explains the experimental results. The form of the current voltage curves are also similar to those observed in the previous chapter. Unfortunately, these results cannot be directly compared to the experimental data, since it is not possible to predict the magnitude of the current density in a three dimensional scenario from this simple 1 dimensional picture. Nevertheless, a qualitative comparison with the data shows that this model has significant promise. For this reason the model was developed in three dimensions.

### 7.1.3 Tunneling Between Misorientated Crystals

In the simple one dimensional model presented above, it is not possible to account for detailed band structural effects. Although the model shows some

of the basic features of the data, quantitative fits to the data are not possible. A more detailed approach is therefore desirable. For any grain boundary, the tunnel current between misorientated crystals must be calculated, so a generalised form of Equation 7.6 is required. Figure 7.5 shows the typical scenario for an [001] tilt boundary. The generalised tunneling equation appropriate for the case where the crystallographic axis either side of the barrier are not aligned is:

$$J_{a\to b} = \frac{2e}{(2\pi)^3\hbar}\iiint_{\mathrm{BZ}} \frac{\partial E^a}{\partial k_\perp^a} f(E^a)\left[1 - f(E^a + eV)\right] D(E^a, \mathbf{k}_\parallel^a)\,\mathrm{d}k_x^a \mathrm{d}k_y^a \mathrm{d}k_z^a \tag{7.17}$$

$$J_{b\to a} = \frac{2e}{(2\pi)^3\hbar}\iiint_{\mathrm{BZ}} \frac{\partial E^b}{\partial k_\perp^b} \left[1 - f(E^b)\right] f(E^b + eV) D(E^b, \mathbf{k}_\parallel^b)\,\mathrm{d}k_x^b \mathrm{d}k_y^b \mathrm{d}k_z^b \tag{7.18}$$

where the $a$ or $b$ superscript refers to quantities defined on side $a$ or $b$. In the general case these two expressions cannot be straightforwardly combined and each contribution must be calculated separately. However in the particular case of a symmetric boundary the symmetry of the problem means that the equations can still be combined and Equation 7.6 is recovered. A model which takes advantage of this symmetry has been developed with a simple, but representative, two dimensional band structure. This is described in the next section.

### 7.1.4 A Model for Symmetric [001] Tilt Boundaries

For the particular case of a symmetric [001] tilt boundary the integrands in Equations 7.17 and 7.18 are identical with the exception of the Fermi-function terms. The two expressions can therefore be combined and Equation 7.6 is recovered. If in addition a simple band structure is employed, the problem is simplified significantly. The $YBa_2Cu_3O_{7-\delta}$ band structure illustrated in Fig. 2.4 can be reasonably approximated by an extruded square Fermi surface, as illustrated in Fig. 7.6. The $E - \mathbf{k}$ relationship is assumed to be linear in the region close to the Fermi-level and therefore takes the form:

$$E(k_x, k_y, k_z) = \begin{cases} \beta|k_y| + \eta, & |k_x| > |k_y| \\ \beta|k_x| + \eta, & |k_x| < |k_y| \end{cases} \tag{7.19}$$

where $\beta$ and $\eta$ are constants. The value of $\beta$ is taken as $7 \times 10^{-29}$ Jm, in agreement with band structure calculations [16]. A quantity $\gamma$ is defined such

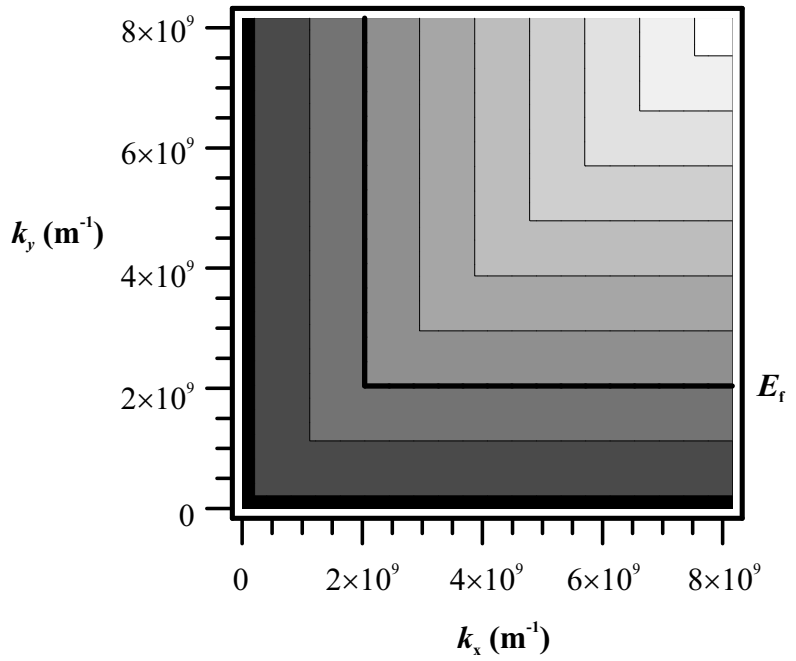


Figure 7.6: Simplified 2-Dimensional band structure for $YBa_2Cu_3O_{7-\delta}$ planes. The figure shows the $+k_x$, $+k_y$ quadrant of the Brillouin zone. The unit cell parameters used are $a = 0.385$ nm $b = 0.385$ nm and $c = 1.168$ nm. Energy contours are shown at 400 eV intervals around the Fermi energy, which is marked $E_f$. The Fermi surface is shown as the bold contour.

that the Fermi surface intersects the $k_x$ axis at $k_x = \gamma\pi/a$, where $a$ is the unit cell dimension in the $x$ direction. $\gamma$ is taken as $1/4$ and $\eta$ is defined via the relation $\eta = E_f - \beta\gamma\pi/a$. The unit cell is assumed to be tetragonal, with dimensions $a = b = 0.385$ nm and $c = 1.168$ nm.

The angle between the grain boundary normal and the $k_x$ direction, $\alpha$, is simply half the misorientation angle for a symmetric grain boundary. Figure 7.7 shows the definitions of key directions in k-space for the calculation. With this simple Fermi surface it is straightforward to show that the quantity $\partial E/\partial k_\perp$ is given by:

$$\frac{\partial E}{\partial k_\perp} = \begin{cases} \dfrac{k_y}{|k_y|}\beta\cos(\alpha), & |k_x| > |k_y| \\ \dfrac{k_x}{|k_x|}\beta\sin(\alpha), & |k_x| < |k_y| \end{cases} \tag{7.20}$$

It is clear from Equation 7.20 that the regions of Fermi surface with group

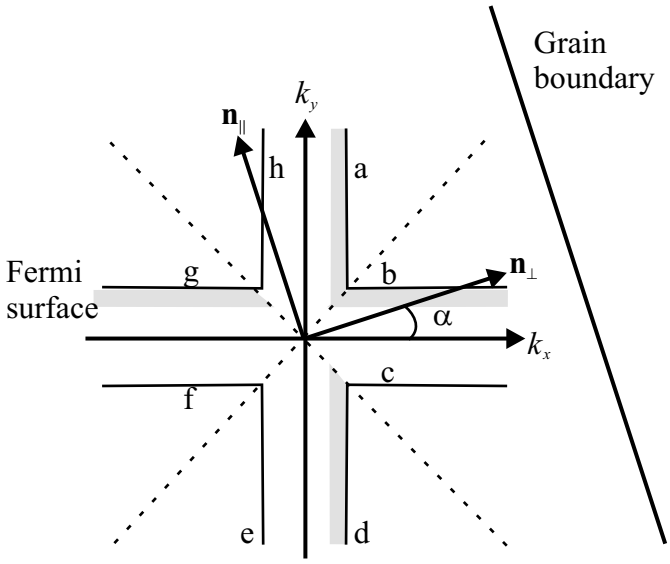


Figure 7.7: Fermi surface and important k-space directions for the simple model of a $YBa_2Cu_3O_{7-\delta}$ grain boundary. The grain boundary plane has normal $\mathbf{n}_{\perp}$. Regions of the Fermi surface have been marked $a$ to $h$ respectively depending on which region of $k$-space they are in. The shaded areas show regions of $k$-space that contribute to the current across the grain boundary at zero temperature.

velocity towards the barrier are regions $a$, $b$, $d$, and $g$ as defined in Fig. 7.7. These four regions of Fermi surface contribute to the net current across the grain boundary. While regions $a$ and $d$ have the same group velocity, the $k_\parallel$ contributions from points located symmetrically with respect to the $k_x$-axis are different, so the tunnel current from these parts of the Fermi surface is not the same (the same applies to regions $b$ and $g$). $\mathbf{k}_\parallel$ is given by:

$$\begin{aligned}\mathbf{k}_\parallel &= \mathbf{k} - \mathbf{k}_\perp = [k_x, k_y, k_z] - (k_x\cos(\alpha) + k_y\sin(\alpha))\,[\cos(\alpha), \sin(\alpha), 0] \\ &= [\sin(\alpha)\,(k_x\sin(\alpha) - k_y\cos(\alpha))\,, \cos(\alpha)\,(k_y\cos(\alpha) + k_x\sin(\alpha))\,, k_z]\end{aligned} \tag{7.21}$$

therefore $|\mathbf{k}_\parallel|^2$ is given by:

$$|\mathbf{k}_\parallel|^2 = k_z^2 + (k_x\sin(\alpha) - k_y\cos(\alpha))^2\,. \tag{7.22}$$

Consider first the zero temperature limit of Equation 7.6. In this limit the Fermi function terms $f(E) - f(E+eV)$ become a unit step that is 1 between $E_f - eV$ and $E_f$ and is zero at other energies. Equation 7.6 becomes:

$$\begin{aligned}J(T=0,V) =& \frac{2e}{(2\pi)^3\hbar}\left(\int_{k_z=-\pi/c}^{\pi/c}\int_{k_y=k_x}^{\pi/a}\int_{k_x=\gamma\pi/a-V/\beta}^{\gamma\pi/a}\beta\cos(\alpha)D\left(E - \frac{\hbar^2|\mathbf{k}_\parallel|^2}{2m^*}, V\right)\mathrm{d}^3k\right. \\ &+ \int_{k_z=-\pi/c}^{\pi/c}\int_{k_x=k_y}^{\pi/a}\int_{k_y=\gamma\pi/a-V/\beta}^{\gamma\pi/a}\beta\sin(\alpha)D\left(E - \frac{\hbar^2|\mathbf{k}_\parallel|^2}{2m^*}, V\right)\mathrm{d}^3k \\ &+ \int_{k_z=-\pi/c}^{\pi/c}\int_{k_y=-\pi/a}^{-k_x}\int_{k_x=\gamma\pi/a-V/\beta}^{\gamma\pi/a}\beta\cos(\alpha)D\left(E - \frac{\hbar^2|\mathbf{k}_\parallel|^2}{2m^*}, V\right)\mathrm{d}^3k \\ &\left.+ \int_{k_z=-\pi/c}^{\pi/c}\int_{k_x=-\pi/a}^{-k_y}\int_{k_y=\gamma\pi/a-V/\beta}^{\gamma\pi/a}\beta\sin(\alpha)D\left(E - \frac{\hbar^2|\mathbf{k}_\parallel|^2}{2m^*}, V\right)\mathrm{d}^3k\right)\end{aligned} \tag{7.23}$$

where $D(E - \hbar^2|\mathbf{k}_\parallel|^2/2m^*, V)$ is defined as in Equation 7.14 with the substitution $E \to E - \hbar^2|\mathbf{k}_\parallel|^2/2m^*$. The integration areas are shaded in grey in Fig. 7.7. These expressions are used to calculate the zero temperature resistance area product and the zero temperature current voltage characteristics presented below.

At finite temperatures the Fermi function terms do not simply alter the integration limits and the form of Equation 7.23 is altered. The calculation

time can be limited by making the integration limits temperature dependent. For the calculations below the following expression for $J$ is used:

$$\begin{aligned} J(T,V) =& \frac{2e}{(2\pi)^3\hbar}\left(\int_{k_z=-\pi/c}^{\pi/c}\int_{k_y=k_x}^{\pi/a}\int_{k_x=A}^{B}\beta\cos(\alpha)g(E)D\left(E-\frac{\hbar^2|\mathbf{k}_\parallel|^2}{2m^*},V\right)\,\mathrm{d}^3k\right. \\ &+\int_{k_z=-\pi/c}^{\pi/c}\int_{k_x=k_y}^{\pi/a}\int_{k_y=A}^{B}\beta\sin(\alpha)g(E)D\left(E-\frac{\hbar^2|\mathbf{k}_\parallel|^2}{2m^*},V\right)\,\mathrm{d}^3k \\ &+\int_{k_z=-\pi/c}^{\pi/c}\int_{k_y=-\pi/a}^{-k_x}\int_{k_x=A}^{B}\beta\cos(\alpha)g(E)D\left(E-\frac{\hbar^2|\mathbf{k}_\parallel|^2}{2m^*},V\right)\,\mathrm{d}^3k \\ &\left.+\int_{k_z=-\pi/c}^{\pi/c}\int_{k_x=-\pi/a}^{-k_y}\int_{k_y=A}^{B}\beta\sin(\alpha)g(E)D\left(E-\frac{\hbar^2|\mathbf{k}_\parallel|^2}{2m^*},V\right)\,\mathrm{d}^3k\right) \end{aligned} \tag{7.24}$$

where:

$$g(E) = f(E) - f(E+eV) \tag{7.25}$$

$$A = \frac{\gamma\pi}{a} - \frac{V+nk_BT}{\beta} \tag{7.26}$$

$$B = \frac{\gamma\pi}{a} + \frac{nk_BT}{\beta}. \tag{7.27}$$

By experimenting with different values of $n$ it was found that with $n = 10$ the value of the resistance is correct to within 3% in the high temperature limit and to less than 1% in the low temperature limit. This value of $n$ was used in subsequent calculations.

The value of $J$ is determined numerically from the above expressions using the Mathematica software package.

Representative results from this model with a variety of parameters are given in Fig. 7.8. Results obtained from a trapezoidal barrier shape are shown, as this shape reproduces the experimental data better than a rectangular barrier. These results are similar in form to those shown for the simple 1-dimensional model in Figs. 7.3 and 7.4, but the model allows the prediction of the magnitude of the current density and the resistance area product. The magnitude of the current density and the resistance area products with these model parameters is similar to the values measured in the previous chapter.

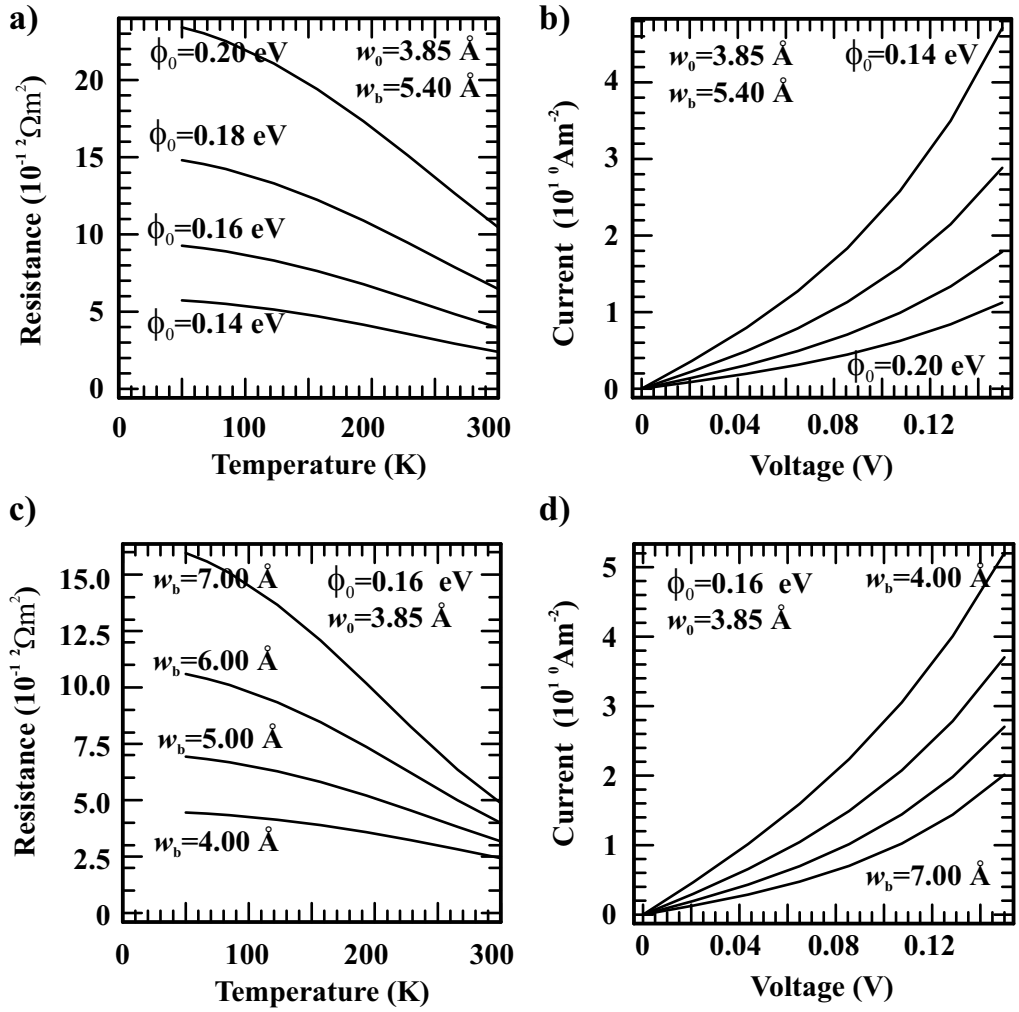


Figure 7.8: Variation of the resistance temperature and current voltage characteristics with changes in barrier shape for a model that accounts for the Fermi surface of the material. The results shown are obtained for a 36° symmetric [001] tilt boundary (which corresponds to $\alpha = 18°$, as defined in Fig. 7.7). a) Resistance temperature curves and b) current voltage curves for a trapezoidal barrier as the barrier height is changed. c) and d) Resistance temperature and current voltage characteristics as the width of the trapezoidal banks is changed. The terms $\phi_0$, $w_b$, and $w_0$, that describe the detailed barrier shape are defined in Fig. 7.1.

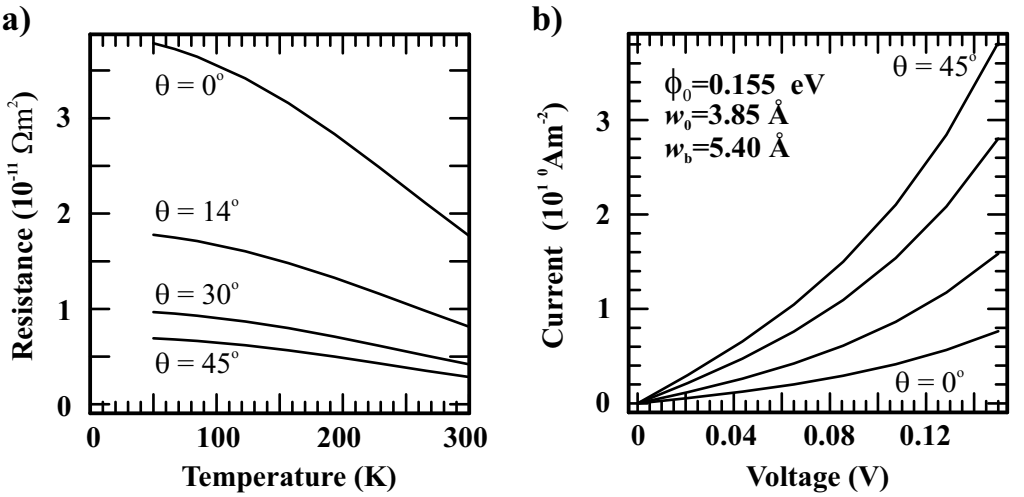


Figure 7.9: Predicted variation of the resistance area product-temperature and current density-voltage characteristics with grain boundary [001] tilt misorientation. a) Resistance temperature curves and b) current voltage curves for a trapezoidal barrier as the total misorientation angle, $\theta$, is changed (Note that $\theta = 2\alpha$ with $\alpha$ defined in Fig. 7.7). The terms $\phi_0$, $w_b$, and $w_0$, that describe the detailed barrier shape are defined in Fig. 7.1.

In addition to the effect of the barrier shape there is also a significant effect of the misorientation angle on the behaviour of these properties. For changes in the misorientation in the absence of changes in the barrier shape, the model predicts a three fold increase of the resistance area product at 4.2 K as the misorientation angle is decreased from 45° to 14°. This effect is primarily due to changes in the group velocity of the electrons towards the barrier, which increases by a similar factor as the misorientation is changed. With more complex band structures the effect may be different, due to a differences in the density of states around the Fermi surface. In the absence of changes in barrier shape the model predicts a resistance area product that decreases with increasing misorientation angle whilst the experimental observations in this thesis and elsewhere [17] show a clear trend of increasing resistance area product with increasing misorientation angle. Thus misorientation effects alone are not dominant. Within a band-bending picture the trapped charge on the boundary increases with the barrier width, which produces changes in the barrier shape with increasing misorientation angle. Such barrier shape effects will dominate over the changes due to the misorientation angle alone.

In order to fit the experimental data of chapter 6 a model in which the barrier width is related to the barrier height is adopted. According to the band bending model the two quantities $w_b$ and $\phi_0$ should be related

by by the equation $\phi_0 = ne^2 w_b^2/2\varepsilon$, where $e$ is the electronic charge, $n$ is the carrier density ($n \approx 4.5 \times 10^{27}$ m$^{-1}$) and $\varepsilon$ is the dielectric constant ($\varepsilon = \varepsilon_0 \varepsilon_r$). For the fits shown in Fig. 7.10 the parameters used in Table 7.1 are used. These parameters are constrained by the relation $w_b = K\phi_0^{1/2}$ where $K = 1.372 \times 10^{-9}$ V$^{-1/2}m$. This value of $K$ corresponds to $\varepsilon_r \approx 75$ and $n \approx 4.5 \times 10^{27}$ m$^{-1}$. This value of the dielectric constant is somewhat higher than that assumed in the calculations of the capacitance in Chapter 4, but is nonetheless within an acceptable range [1]. It is likely to be slightly inflated as a result of fitting the slightly underdoped data of the 36° boundary assuming an optimal carrier density. The fits to the data are in reasonable agreement with both the current voltage and the resistance temperature data. The agreement is not perfect, but the model reproduces the important features of the data, which, considering the spread in the properties of the boundaries within an individual bridge, is probably as much as could be expected. Importantly, the correct magnitude of the resistance area product is reproduced by the model. This is an important issue with the resonant tunneling model, which is discussed in detail in the next section. In addition a band bending and tunneling model provides a natural explanation for the experimental data obtained from the deoxygenated 30° symmetric [001] tilt boundary (see Fig. 6.17). The carrier density is expected to be reduced in the deoxygenated samples, increasing the extent of the band bending and leading to a barrier shape more characteristic of higher angle boundaries. In addition at lower temperatures the normal state psuedogap is expected to reduce the density of states at the Fermi-energy, leading to an increased normal state resistance, as is observed. Further modelling is necessary to confirm the consistency of the results with a psuedogap picture.

The model described in this section has been developed further in collaboration with Karl Sandeman. He has developed a model based on numerical solution of Equations 7.17 and 7.18 that can deal with both symmetric and asymmetric tilt boundaries and arbitrary band structures. This model is described in detail in a recent pre-print [18]. Similar barrier heights (of 0.19 eV above the Fermi energy) and widths (approximately 0.5 nm at the Fermi level) are obtained by fitting the same experimental data, using a more realistic band structure that accounts for the in plane features of the $YBa_2Cu_3O_{7-\delta}$ band structure.

In summary a band bending tunneling model has been developed which is in reasonable agreement with the experimental observations of this study. This model is in good agreement with the major features of the data and

Table 7.1: Parameters used for the direct tunneling band bending model fits to the data in Fig. 7.10. $\alpha$ is half the misorientation angle (see Fig. 7.7), $\phi_0$ is the barrier height, $w_b$ is the width of the band bending region and $w_0$ is the structural width of the boudnary (see Fig. 7.1).

| Grain Boundary | $\alpha$ (°) | $\phi_0$ (eV) | $w_b$ (nm) | $w_0$ (nm) |
|---|---|---|---|---|
| 36° symmetric [001] tilt | 18 | 0.155 | 0.540 | 0.385 |
| 30° symmetric [001] tilt | 15 | 0.130 | 0.495 | 0.385 |
| 24° symmetric [001] tilt | 12 | 0.080 | 0.388 | 0.385 |

reproduces the correct magnitude of the resistance area product. In the next two sections the data is compared to the predictions of two other models for low angle grain boundaries — the resonant tunneling model and ScS models.

## 7.2 Resonant Tunnelling

Within the resonant tunneling model the grain boundary is described as a disordered region with a high density of localised states [5, 6, 7, 2, 3, 4]. The quasiparticles tunnel through the boundary in a multi-step process via a number of intermediate states. Since the Cooper pairs cannot occupy these localised states, they must tunnel directly. The theory, and the experimental evidence that is cited in its support, are described in detail in Chapter 2. A particular point that is discussed in detail in this chapter is that of the scaling of the critical voltage, $I_cR_n$, with the critical current density, $J_c$. The resonant tunneling model predicts $I_cR_n \propto J_c^{0.5}$, but the experiments of Sydow *et al.* [19] show that such behaviour is only observed at critical current densities below approximately $J_c = 10^7$ Am$^{-2}$ to $J_c = 10^9$ Am$^{-2}$ for 24° symmetric [001] tilt boundaries. It is worth noting that in this study the 24° [001] tilt sample had a range of critical currents between 2 and 6 $\times$ $10^9$ Am$^{-2}$, which is above the range that the behaviour characteristic of resonant tunneling is observed.

Reasonable agreement can be obtained between the experimental data and models developed for resonant tunneling through amorphous barriers. Glazman and Matveev have predicted both the temperature dependence of the zero bias conductance and the current voltage characteristic at low temperatures for this scenario [20]. The Glazman-Matveev theory has been successfully applied to describe the properties of $YBa_2Cu_3O_{7-\delta}$ ramp-edge

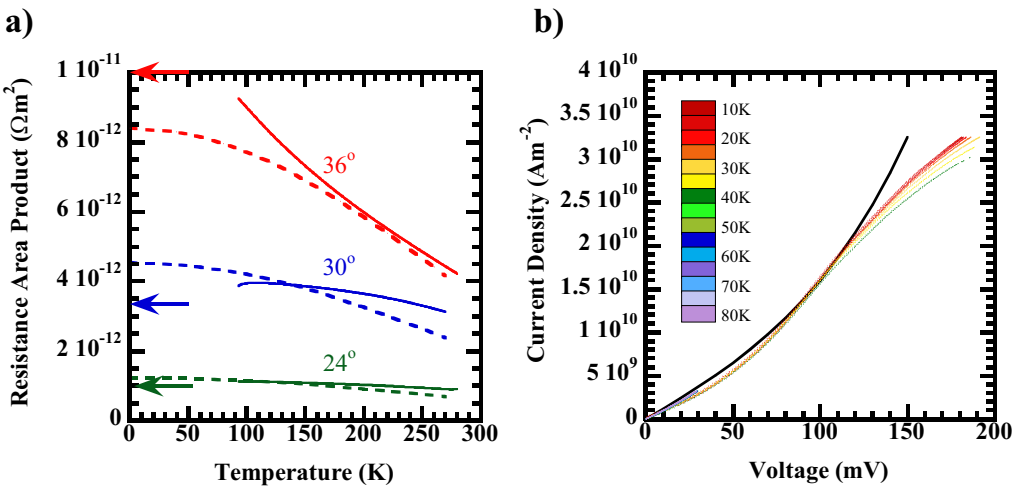


Figure 7.10: A band bending model fit to the normal state resistance-temperature and current-voltage characteristics of symmetric [001] tilt grain boundaries measured in this study. a) Resistance area product vs. temperature. Solid lines show the experimental data and dashed lines show the theoretically predicted values. The experimental data is an average over bridges for each misorientation value. The arrows indicate the experimental values of the resistance at low temperatures obtained from the current voltage characteristics. b) Current density-voltage curves for the 36° [001] tilt boundary. The coloured lines show experimental data (from bridge 1) obtained at various temperatures, whilst the black line shows the 0 K theoretical curve obtained with the same parameters as the fit in a). The fit parameters used to obtain the various curves are given in Table 7.1.

junctions with various barrier materials (e.g. $SrRuO_3$ [21] and $PrBa_2Cu_3O_{7-\delta}$ [22]) and with interface engineered junctions (effectively ion beam damaged ramp edges with no barrier material) [23]. The theory predicts power series forms for the conductance ($G = 1/R$) as a function of temperature and voltage in the low voltage and low temperature regimes respectively:

$$G(T) = A + \nu B(k_b T)^{4/3} + C(k_b T)^{5/2} + \ldots, \qquad eV \ll kT \tag{7.28}$$

$$G(V) = A + \xi B(eV)^{4/3} + \ldots, \qquad eV \gg kT \tag{7.29}$$

where $e$ is the electron charge, $V$ is the voltage, $k_b$ is Boltzmann's constant, $T$ is the temperature and $A$ to $C$ are constants. The terms preceded by $B$ and $C$ represent tunneling via two and three intermediate states respectively (direct tunneling and tunneling via one intermediate state produce temperature or voltage independent contributions within the model). $\nu$ and $\xi$ are numerical factors which are approximately 50 and 1 respectively.

These two equations can be compared against the temperature dependence of the normal state resistance and against the low temperature current voltage curves, where these are non-linear. Note that at 100 K, $kT/e = 8$ mV so the large bias current voltage curves of the 36° symmetric and the 45° asymmetric boundaries measured in the previous chapter satisfy the requirement $eV \gg kT$ and the zero bias resistance measurements above $T_c$ for all the samples satisfy $eV \ll kT$. Fig. 7.11 shows two plots to assess the data of the previous chapter against the resonant tunneling model. The low temperature conductance is linear when plotted against $V^{4/3}$, which is what is expected from the model. For the resistance temperature fit the value of the constant $A$ is determined by the zero temperature, zero bias resistance, whilst $B$ is constrained to agree with the corresponding value for the current voltage curve. Without a third order term the fit is almost temperature independent given these constraints.

A major problem with the Glazman-Matveev theory is that it is difficult to make quantitative predictions about the magnitude of the conductance, since there are so many undetermined parameters contained within the constants $A$, $B$ and $C$. Within a resonant tunneling model the relevant energy scales for tunneling are significantly different from those associated with a band bending model. The material is predicted to undergo a transition to a Mott insulating state with an insulating gap of the order of 1 eV in the vicinity of the grain boundary [3]. Application of the model of the previous section to a rectangular barrier of height 1 eV and width 0.385 nm (the unit cell size, which is the same order of magnitude as the inter-atomic spacing in the grain boundary region) yields a zero temperature resistance area product

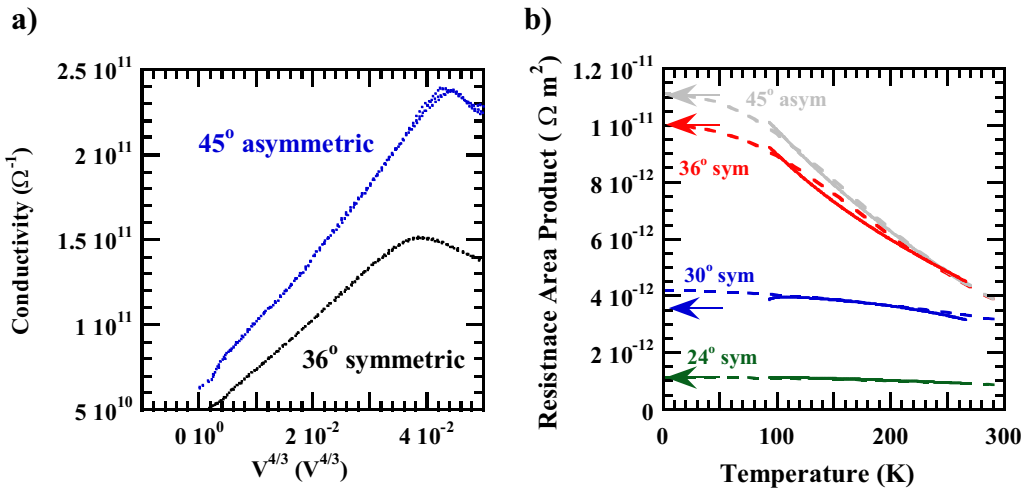


Figure 7.11: Resonant tunneling analysis of the temperature dependance of the normal state resistance area product and the current density voltage characteristics. a) The high bias conductivity takes the form $G = A + B(eV)^{4/3}$ at low temperatures. A plot of $G$ versus $V^{4/3}$ is expected to be linear if the model applies as indeed it is. The graph shows the data from Figure 6.10, obtained from single grain boundaries on the 36° and the 45° samples. b) Fits of the form $R_n A = 1/(A + 50B(k_bT)^{4/3} + C(k_bT)^{5/2})$ to the measured data, with $A$, $B$ and $C$ as the fitting parameters. $A$ is determined by the zero temperature, zero bias resistance, whilst $B$ is constrained to agree with gradient of the current voltage curve in a). The data is shown as a solid curve (and is obtained by averaging over bridges on each sample), whilst the theory is indicated by a dashed line. the zero temperature experimental results are indicated by arrows. The fit parameters used are as follows: 45°: A=$9.00\times10^{11}$ $\Omega^{-1}m^{-2}$, B=$4.60\times10^{6}$ $\Omega^{-1}m^{-2}J^{-4/3}$, C=$1.10\times10^{5}$ $\Omega^{-1}m^{-2}J^{-5/2}$, 36°: A=$1.00\times10^{11}$ $\Omega^{-1}m^{-2}$, B=$3.40\times10^{6}$ $\Omega^{-1}m^{-2}J^{-4/2}$, C=$1.05\times10^{5}$ $\Omega^{-1}m^{-2}J^{-5/2}$, 30°: A=$2.38\times10^{11}$ $\Omega^{-1}m^{-2}$, B=$1.18\times10^{7}$ $\Omega^{-1}m^{-2}J^{-4/3}$, C=$3.65\times10^{4}$ $\Omega^{-1}m^{-2}J^{-5/2}$, and 24°: A=$8.85\times10^{11}$ $\Omega^{-1}m^{-2}$, B=$5.54\times10^{6}$ $\Omega^{-1}m^{-2}J^{-4/3}$, C=$1.74\times10^{5}$ $\Omega^{-1}m^{-2}J^{-5/2}$.

of $4 \times 10^{-11}$ $\Omega m^{-2}$, which is four times larger than any of the experimental values measured in this study. Although the resonant tunneling process leads to lower resistances for barriers that are wide enough for tunneling via multiple states, tunneling between the states must occur through several 'hops' of interatomic distance. If a single tunneling stage produces too high a resistance then a multi-step process is not viable. This is a significant problem for resonant tunneling models and may suggest that if indeed resonant tunneling does occur, the energy scale associated with the localised states is smaller than expected. At present no grain boundary mechanism is proposed that accounts for such a scenario. Note also that resonant tunneling models cannot account for the de-oxygenated data shown in Fig. 6.17. This data seems more consistent with a direct tunneling model, although more detailed modelling is necessary to confirm this.

In conclusion the resonant tunneling model has been assessed in the context of the data of Chapter 6. While the Galzman-Matveev theory for resonant tunneling [20] is in reasonable agreement with the experimental data, the magnitude of the normal state resistance is too low to be consistent with the expected electronic structure within such a model. The resonant tunneling model is therefore tentatively ruled out, at least in its present form.

## 7.3 Constriction Models

The constriction model proposed by Sarnelli *et al.* [8, 9, 10] describes the grain boundary as an array of point contacts separated by insulating regions. As described in Chapter 2 this model must necessarily apply in some range of angles between the flux flow regime and the point at which a continuous barrier is established across the grain boundary (i. e. for intermediate angle boundaries, such as the 10° symmetric [001] tilt boundary observed by Redwing *et al.* [24]). The normal resistance data enables us to assess whether the model applies for grain boundary misorientation angles of 24° and greater, as is suggested by its proponents [10], or whether it is restricted to a limited range of grain boundary angles, large enough so that dislocations are sufficiently close together that Josephson coupling occurs, but below the misorientation angle at which the barrier becomes continuous.

The normal state properties of point contact arrays are determined by the size of the constrictions. Two limiting cases are of interest: constrictions with dimension, $a$, much larger than the mean free path, $l$, and those with much smaller dimensions. In these two limits the resistance of a singe constriction $R_c$ is given by:

$$R_c = \begin{cases} \dfrac{B\rho}{a} & \text{if } a \gg l, \\ \dfrac{Cm^* v_F}{ne^2 a^2} & \text{if } a \ll l, \end{cases} \tag{7.30}$$

where $B$ and $C$ are geometrical factors close to unity, $\rho$ is the bulk resistivity of the material, $v_F$ is the effective mean velocity of the electrons at the Fermi energy, $n$ is the number of electrons per unit volume of the material, $m^*$ is the effective mass of the electrons and $e$ is their charge. When $N$ such constrictions are added in parallel the resistance area product will be given by $R_n A = R_c A/N$.

In the former case the properties of the constriction are similar to those of the bulk (this is known as the Maxwell or diffusive regime). The expected temperature dependence of the normal state resistance is therefore that of a narrow track of normal $YBa_2Cu_3O_{7-\delta}$ — a linearly increasing resistance. In the latter case (known as the Sharvin or ballistic regime) the constriction effectively limits the passage of electrons in an analogous manner to the passage of a dilute gas through a hole [25]. In the optimally doped state (in the absence of psuedogap effects) the carrier density is temperature independent. The Fermi velocity is fixed by the details of the band-structure and is therefore also expected to be temperature independent. Therefore the Sharvin resistance is usually temperature independent. Between these two limits the properties have been shown to evolve continuously according to an expression derived by Wexler [26, 27].

A transition between the Maxwell and Sharvin temperature dependencies is also possible, since the mean free path varies with temperature. In this case it is expected that the resistance would be constant at low temperatures and at high temperatures it would increase linearly, with intermediate behaviour between the limits. Note that the mean free path of $YBa_2Cu_3O_{7-\delta}$ is approximately 10 nm at 90 K [28], so unit cell sized constrictions (such as those proposed by Sarnelli and Testa) are within the Sharvin regime at the critical temperature.

The data in Fig. 6.6 show a general trend of decreasing resistance area product with increasing temperature. This is not consistent with any of the above scenarios and therefore constriction dominated behaviour seems unlikely. The normal state resistance of the 24° symmetric boundary is approximately temperature independent, however, since the microstructure of a 24° boundary is similar to that of higher angle boundaries it seems unlikely that the behaviour observed is due to constrictions.

## 7.4 Summary

In this chapter a number of different models for grain boundaries have been compared with the experimental data obtained in Chapter 6. A direct tunneling, band bending model that properly accounts for the bandstructure of the $YBa_2Cu_3O_{7-\delta}$ was developed. This model produces results that are consistent with the experimental data, and also predicts the correct magnitude of the normal state resistance. Within the model the effects of changing the extent of the band bending and the barrier height separately were investigated. In addition it was shown that the effect of altering the misorientation independently of the potential barrier was opposite in sign to the experimentally observed changes in the normal state resistance. Reasonable fits to the experimental data were obtained by varying the barrier shape and height in a manner consistent with the band bending model. Importantly the correct magnitude of the normal resistance area product is predicted by this model, as well as the basic functional forms of the temperature dependence of both the zero bias resistance area product and the current voltage characteristic.

Two other models are compared with the experimental data. The resonant tunneling model is consistent with the functional form of both the current voltage and resistance temperature characteristics, provided that tunneling via, zero, one, two and three intermediate states are included within the model (the current voltage characteristic can be accounted for by tunneling via zero, one and two intermediate stages). The resonant tunneling model does, however, predict barrier heights of approximately 1 eV, which seem to be too large to be consistent with the observed magnitude of the resistance area product. For barriers of atomic thickness that have this height, the direct tunneling model developed in this chapter predicts resistance area products that are four times larger than any of the experimental values measured in this study (and more than an order of magnitude larger than the minimum values of the resistance area product measured). If direct tunneling produces a resistance that is too high then a resonant tunneling process consisting of several tunneling steps with similar barrier thicknesses must produce a resistance that is too large.

A constriction type model predicts either a temperature independent zero bias normal resistance for constrictions smaller than the mean free path, or, for larger constrictions, predicts that the resistance varies in the same manner as the bulk. Neither of these two scenarios can account for experimentally observed resistance–temperature characteristics for all misorientation angles, and the data therefore rules out the constriction models.

The direct tunneling, band bending, scenario therefore remains the most plausible model at the present time and accounts for the bulk of the ob-

servations in this thesis. The possibility of some other mechanism remains however, and further measurements and modelling are necessary to conclusively demonstrate that the band bending model applies.

# Bibliography


[1] J. Mannhart and H. Hilgenkamp, Materials Science and Engineering B **56**, 77 (1998).

[2] J. Halbritter, Physical Review B **46**, 14861 (1992).

[3] J. Halbritter, Physical Review B **48**, 9735 (1993).

[4] J. Halbritter, IEEE Transactions on Applied Superconductivity **13**, 1158 (2002).

[5] R. Gross, *Interfaces in Superconducting Systems*, chapter Grain-Boundary Josephson Junctions in the High-Temperature Superconductors, pages 176–209, Springer, New York, 1994.

[6] R. Gross et al., IEEE Transactions on Applied Superconductivity **7**, 2929 (1997).

[7] O. M. Froehlich, P. Richter, A. Beck, D. Koelle, and R. Gross, IEEE Transactions on Applied Superconductivity **7**, 3189 (1997).

[8] A. Sarnelli, P. Chaudhari, and J. Lacey, Applied Physics Letters **62**, 777 (1993).

[9] A. Sarnelli, G. Testa, and E. Eposito, Journal of Superconductivity **7**, 387 (1994).

[10] A. Sarnelli and G. Testa, Physica C **371**, 10 (2002).

[11] R. Stratton, Journal of the Physics and Chemistry of Solids **23**, 1177 (1962).

[12] C. B. Duke, *Tunneling in Solids*, Solid State Physics, Supplement 10, Academic Press, New York, 1969.

[13] W. A. Harrison, Physical Review **123**, 85 (1961).

[14] E. L. Wolf, *Principles of Electron Tunneling Spectroscopy*, International Series of Monographs on Physics, 71, Oxford Universtiy Press, New York, 1985.

[15] W. E. Taylor, N. H. Odell, and H. Y. Fan, Physical Review **88**, 867 (1952).

[16] R. E. C. W. E. Pickett and H. Krakauer, Physical Review B **42**, 8764 (1990).

[17] H. Hilgenkamp and J. Mannhart, Applied Physics Letters **73**, 265 (1998).

[18] J. H. T. Ransley et al., cond-mat/0311386, 2003.

[19] J. P. Sydow, M. Berninger, R. A. Buhrman, and B. H. Moeckly, Superconductor Science and Technology **12**, 723 (1999).

[20] L. I. Glazman and K. A. Matveev, Soviet Physics JETP **67**, 1276 (1988).

[21] R. Dömel, C. Horstmann, M. Siegel, A. I. Braginski, and M. Y. Kupriyanov, Applied Physics Letters **67**, 1775 (1995).

[22] M. A. J. Verhoeven, G. J. Gerritsma, H. Rogalla, and A. A. Golubov, Applied Physics Letters **69**, 848 (1996).

[23] J.-K. Heinsohn et al., Journal of Applied Physics **89**, 3852 (2001).

[24] R. D. Redwing et al., Applied Physics Letters **75**, 3171 (1999).

[25] Y. V. Sharvin, Soviet Physics JETP **21**, 655 (1965).

[26] G. Wexler, Proceedings of the Physical Society **89**, 927 (1966).

[27] D. Erts, H. Olin, L. Ryen, E. Olsson, and A. Thölén, Physical Review B **61**, 12725 (2000).

[28] K. Krishana, J. M. Harris, and N. P. Ong, Physical Review Letters **75**, 3529 (1995).

# Chapter 8

# Conclusions and Further Work

## 8.1 Conclusions

The major conclusions of this work are summarised below.

### The Capacitance of $Y_{1-x}Ca_xBa_2Cu_3O_{7-\delta}$ Grain Boundaries

In chapter 4 the first measurements of the grain boundary capacitance of 24°[001] tilt $Y_{1-x}Ca_xBa_2Cu_3O_{7-\delta}$ grain boundaries are presented. Measurements have been performed on films with $x$ in the range 0.0 to 0.3. The capacitance was determined from the hysteresis in the $I$–$V$ characteristic. The study highlighted the importance of eliminating systematic effects from the measurements and particular care was taken to eliminate effects due to the substrate, heating and thermal noise. By applying magnetic field to the junction it was possible to measure the capacitance as a function of return voltage (or equivalently as a function of the Josephson frequency). Such measurements show that at 4.2 K with return voltages below approximately 0.25 mV, the capacitance is dominated by the substrate, but that at higher voltages the intrinsic grain boundary capacitance can be measured. Heating effects were also observed in the junction in which the greatest power was dissipated. By measuring the critical current distribution of one of the junctions the effect of thermal noise on the measurement was assessed and, although it was significant, it was an order of magnitude less than the observed changes in capacitance. This work highlights the importance of assessing these effects in future capacitance measurements based on the Josephson effect.

The grain boundary capacitance was found to increase from 0.2 $\mathrm{Fm}^{-2}$ for $x = 0$ to a maximum value of 1.2 $\mathrm{Fm}^{-2}$ for $x = 0.3$. The magnitude of the capacitance for undoped samples is consistent with a band bending model.

However as the calcium doping is increased the capacitance per unit area, $C/A$ is found to increase as $C/A \propto 1/R_nA$, where $R_nA$ is the grain boundary normal resistance area product. This result is suggestive of changes in the effective area of the grain boundary. Since it is uncertain how the addition of dopants effects the dielectric constant, it is difficult to be certain that the major effect of Calcium doping is to increase the effective area of the boundary, and further evidence would be required to make such a conclusion. It is nonetheless clear that calcium doping leads to a definite increase in the grain boundary capacitance.

### The Normal State Resistance of $YBa_2Cu_3O_{7-\delta}$ Grain Boundaries

A Wheatstone bridge technique for measuring the normal state resistance of $YBa_2Cu_3O_{7-\delta}$ grain boundaries was developed in Chapter 5. Detailed characterisation highlighted that both the quality of the lithography and film inhomogeneities are the limiting factors for resolution of the technique for small and large bridges respectively. A bridge geometry consisting of a highly symmetric, meandering bridge that crosses the grain boundary 21 times in two of the four bridge arms was found to be optimal given the current fabrication facilities. Control bridges demonstrate that, for this geometry, the technique can be used to measure resistance area products greater than $1 \times 10^{-13}$ $\Omega m^2$. Further systematic errors due to the presence of the grain boundary were estimated to be the same order as, or less than $1 \times 10^{-13}$ $\Omega m^2$. Application of the technique to a grain boundary generated highly consistent results for a series of devices on the same sample, demonstrating its viability.

In Chapter 6, the bridge technique was applied to perform the first measurements of the normal state resistance of grain boundaries with various [001] tilt misorientations. 24°, 30° and 36° symmetric and 45° asymmetric [001] tilt grain boundaries were investigated. Below the critical temperature the resistance was estimated from the current voltage curves. For the higher angle boundaries (36° and 45°) the resistance was estimated to be approximately constant below the critical temperature, $T_c$. Above $T_c$ an almost linear decrease is observed up to room temperature. The lower angle boundaries (24° and 30°) had a normal state resistance that was approximately temperature independent between 4 K and room temperature. The results obtained are consistent with all the other available data and with published data in the literature below $T_c$ [1].

Detailed investigation of the critical currents of grain boundaries within a single bridge revealed that there was a significant spread in their properties. These large variations in the grain boundary properties mean that the bridge technique yields an average of the grain boundary properties on a particular

sample. This averaging process complicates the interpretation of the experimental data and makes the production of more uniform grain boundaries highly desirable.

The effect of severely deoxygenating one of the samples was also assessed. After an anneal and subsequent quench the 30° symmetric boundary had its critical temperature reduced from 92 K to 43 K. At optimal doping, the resistance area product was almost temperature independent between 4 K and room temperature, while after the anneal it increased approximately linearly as the sample was cooled from room temperature until approximately 120 K, after which a sharper increase was observed. The high temperature behaviour was remarkably similar to that of the as-grown higher angle grain boundaries. The lower temperature behaviour may be indicative of the opening up of a normal state psuedogap.

**The Conductance Voltage Curves of High Angle $YBa_2Cu_3O_{7-\delta}$ Grain Boundaries**

The conductance–voltage curve obtained from an optimally doped 45° asymmetric [001] tilt boundary in Chapter 6 is, to the author's knowledge, the first time such a non-linear conductance voltage curve has been observed in an optimally doped $YBa_2Cu_3O_{7-\delta}$ grain boundary. Non linear conductance-voltage curves are not usually observed in the lower angle grain boundaries that most groups study because of the more limited voltage range accessible. The 30° symmetric [001] tilt boundary showed a similar conductance–voltage characteristic after an anneal that reduced its critical temperature to 43 K, as did the slightly underdoped 36° symmetric [001] tilt boundary. In all cases the conductance–voltage curves obtained were not quadratic, indicating that a simple spherical Fermi surface tunneling model does not apply.

**Development of a Tunneling/Band Bending Model and comparison of the Conductance–Voltage and Resistance Area Product Temperature Characteristics with this and other models.**

In Chapter 7, a direct tunneling model for grain boundary transport was developed, using a barrier form similar to that predicted by the band bending model. The model was characterised in detail and the effects of varying the extent of the band bending, the barrier height and the misorientation angle were assessed. Reasonable fits to both conductance–voltage and resistance area product–temperature characteristics were obtained by varying the barrier shape and height in a manner consistent with the band bending model. Importantly the correct magnitude of the normal resistance area product is

predicted by this model.

Similar comparisons with the conductance–voltage and resistance area product–temperature characteristics were performed for other models in the literature. The resonant tunneling model was compared with the data and while its functional form is in good agreement with the predictions of the model, the magnitude of the resistance area products measured seems too low to be consistent with a multiple step tunneling process. The experimental data is also shown to be inconsistent with transport through constrictions caused by pinholes in the grain boundary. The direct tunneling, band bending, scenario is therefore the most plausible model.

## 8.2 Suggestions for Further Work

The capacitance work described in Chapter 4 could be significantly improved by eliminating thermal noise transmitted down the wires of the measurement apparatus. A simple solution to this problem would be to add resistors to the current lines at the low temperature end of the cryostat, so that the majority of the resistance of the current biasing circuit is held at the measurement temperature. Further precautions to eliminate noise from the measurement would probably require the construction of a new probe (and possibly new electronics), which may be worthwhile if similar measurements are to be pursued much further. This work highlighted the importance of field and temperature dependent measurements for understanding the substrate contribution to the capacitance. Unfortunately this technique was employed later in the study and only applied to a 30% Calcium doped sample. It might be interesting to investigate the substrate effect on other grain boundaries with different doping levels. Additionally, for lower capacitance samples, it may be possible to correlate such measurements with the results obtained from Fiske resonances. Measurements of grain boundary capacitance as a single sample is progressively underdoped would also be interesting to perform. In particular such measurements may help clarify the issue of the scaling of the critical voltage with the critical current, discussed in section 2.4.5.

A theme that runs throughout this thesis and indeed throughout the literature on grain boundaries is the important issue of grain boundary uniformity. It is highly desirable to repeat the both the capacitance and the normal state measurements on grain boundaries with more uniform properties. In the former case the use of atomically uniform grain boundaries would eliminate any possibility of effects due to grain boundary inhomogeneity. In the latter case the problems associated with the averaging of the properties along the boundary will be avoided. Two techniques offer the possibility of

more uniform grain boundary microstructures. The first is liquid phase epitaxy (LPE) [2]. Meander free grain boundaries have been grown by LPE with a variety of misorientation angles. In addition for 45° symmetric [001] tilt boundaries single facet boundaries are obtainable, making the grain boundary structure uniform on an atomic scale. It may be possible to fabricate single facet boundaries with other misorientation angles by restricting the boundary geometry to produce orientations preferable for facet formation [3, 4]. A second technique for obtaining more homogenous boundaries is the use of vicinal substrate grain boundaries [5, 6]. On such substrates the film grows by step-flow growth and a more homogenous boundary structure is produced [6]. However, more detailed characterisation is desirable to confirm the facet structure produced by this technique.

A large number of possibilities for further work are offered by the work on the normal state properties of grain boundaries. The present data set on [001] tilt boundaries could be significantly expanded, and in addition there is the possibility of investigating other grain boundary configurations (such as [100] tilt and [100] twist type boundaries). A more detailed study on the effect of grain boundary oxygenation is desirable. By taking one sample and annealing it several times to progressively underdope it, a systematic set of curves could be generated. In addition it would be interesting to investigate the effect of underdoping higher angle boundaries. More systematic data on underdoped samples may also help to understand the effect of the pseudogap on the measurements and allow the possibility of studying the pseudogap with grain boundaries to be assessed. The progressive annealing of overdoped $Y_{1-x}Ca_xBa_2Cu_3O_{7-\delta}$ samples should help to assess the effect of changes in the carrier density in the absence of pseudogap effects.

The model developed in Chapter 7 is a reasonable starting point for a more detailed model of high angle boundaries. It has already been developed to include a more detailed band structure by Karl Sandeman [7]. The use of an exact expression for the tunnel current might improve the accuracy of the calculations (but will also increase the calculation time). The model could be adapted to include simple pseudogap effects fairly straightforwardly, by adding an energy dependent gap function in front of each of the 'D factors' in equation 7.24. A detailed band bending tunneling model would need to account for the distortion of the local bandstructure in the region of the boundary, and is well beyond the scope of this work.

# Appendix A

# A Model for Heating in High $T_C$ Thin Film Grain Boundary Junctions

A simple model for predicting the heating of a grain boundary junction is presented. It is assumed that the $YBa_2Cu_3O_{7-\delta}$ track across the grain boundary can be modelled as a one-dimensional system, and that heat loss occurs by flow of heat away from the grain boundary and into the substrate, which is treated as a heat bath at the same temperature as the surroundings. Heat flow from the track directly into the liquid helium can be neglected [8]. The concept of the model is illustrated in Fig. A.1. The system is assumed to be in thermal equilibrium on the time scale of the measurement.

Consider an element of the track at a distance $x$ from the grain boundary. The temperature $T(x)$ is related to the heat current per unit area of the track by the equation:

$$T\left(x+dx\right) = T\left(x\right) - \frac{1}{\kappa} J\left(x\right) dx, \tag{A.1}$$

where $\kappa$ is thermal conductivity of the track. The heat losses to the substrate, at temperature $T_b$, are governed by the equation:

$$J\left(x+dx\right) = J\left(x\right) - \frac{\alpha\left(T-T_b\right)}{h} dx, \tag{A.2}$$

where $\alpha$ is the heat transfer coefficient per unit area of the substrate/film boundary and $h$ is the film thickness.

By eliminating $J(x)$ the following second order differential equation can be derived:

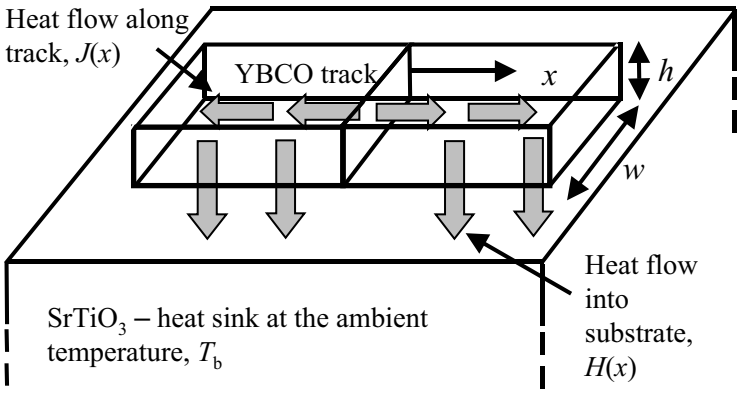


Figure A.1: Illustration of the model used to predict the effect of heating on the grain boundary. Heat flows away from the grain boundary and as it does so, into the substrate. The system is equivalent to a lossy transmission line.

$$\frac{d^2T}{dx^2} = \frac{\alpha}{\kappa h}\left(T - T_b\right). \tag{A.3}$$

If it is assumed that $\kappa$ and $\alpha$ are temperature independent, this equation can be solved with the boundary conditions $T \to T_b$ as $x \to \infty$ and $J(0) = IV/(2hw)$, giving the solution:

$$T = T_b + \sqrt{\frac{1}{\alpha h \kappa}}\frac{IV}{2w}\exp\left(-\sqrt{\frac{\alpha}{\kappa h}}x\right), \tag{A.4}$$

where $I$ is the current flowing through the track, $V$ is the voltage dropped across the junction and $w$ is the width of the track.

However both $\alpha$ and $\kappa$ are strong functions of temperature for $YBa_2Cu_3O_{7-\delta}$ on $SrTiO_3$, so this solution is only applicable if the temperature rises predicted are small compared to $T_b$. $\alpha$ is determined by the acoustic mismatch model at temperatures significantly less than the Debye temperature [9], and is given by $\alpha = T^3/B$. $B$ can be calculated from the properties of the materials on either side of the boundary [9], for $YBa_2Cu_3O_{7-\delta}$ on $SrTiO_3$ $B = 9.6 \times 10^4$ $\mathrm{m^2K^4W^{-1}}$. Between 0 K and 10 K the thermal conductivity of $YBa_2Cu_3O_{7-\delta}$ can be reasonably approximated by the empirical expression $\kappa = \kappa_0 T^2$, where $\kappa_0 \approx 0.17$ $\mathrm{Wm^{-1}K^{-3}}$ [10]. Using these approximations we derive a second differential equation:

$$\frac{d^2T}{dx^2} = \frac{1}{\kappa_0 B h}T\left(T - T_b\right). \tag{A.5}$$

This equation can be solved (with the integrating factor dT/dx), to give:

$$T = \frac{T_b}{2}\left(3\coth^2\left(D + \frac{x}{2}\sqrt{\frac{T_b}{\kappa_0 B h}} - 1\right)\right), \tag{A.6}$$

where the boundary condition $T \to T_b$ as $x \to \infty$ is satisfied and the integration constant $D$ can be eliminated using $J(0) = IV/(2hw)$.

Equation A.4 was used to calculate the temperature rises at 15 K in Table 4.2, whilst A.6 was used to calculate the temperature rises at 4.2 K in the same table and to assess the effect of heating on the $J$–$V$ characteristics presented in Section 6.4 (in this case, because of the higher temperatures involved, the constant $\kappa_0$ in the equation $\kappa = \kappa_0 T^2$, was taken as $\kappa_0 \approx 0.07$ $\mathrm{Wm^{-1}K^{-3}}$, which is more reasonable in the temperature range under consideration [10]). In solving Equation A.6 the constant $D$ was determined by numerical solution of equation resulting from the boundary condition on $J(0)$.

The assumption of thermal equilibrium can be tested by calculating the time it would take to heat up a length of track comparable to the decay length, given the power input $IV$. In this case the time is of order 1 ns, in good agreement with experiment [11]. This is much less than the measurement time (of order 1 s) so thermal equilibrium is a valid assumption.

# Bibliography


[1] H. Hilgenkamp and J. Mannhart, Applied Physics Letters **73**, 265 (1998).

[2] J. G. Wen, T. Takagi, and N. Koshizuka, Superconductor Science and Technology **13**, 820 (2000).

[3] Q. Jin and S.-W. Chan, Journal of Materials Research **17**, 323 (2002).

[4] S.-W. Chan, Q. Jin, J. W. H. Tsai, S. C. Tidrow, and Q. Jiang, IEEE Transactions on Applied Superconductivity **13**, 2829 (2003).

[5] U. Poppe et al., IEEE Transactions on Applied Superconductivity **11**, 3768 (2001).

[6] Y. Y. Divin, U. Poppe, J. L. Jia, P. M. Shadrin, and K. Urban, Physica C **372-376**, 115 (2002).

[7] J. H. T. Ransley et al., cond-mat/0311386, 2003.

[8] W. J. Skockpol, M. R. Beasley, and M. Tinkham, Journal of Applied Physics **45**, 4054 (1974).

[9] J. D. N. Cheeke, H. Ettinger, and B. Hebral, Canadian Journal of Physics **54**, 1749 (1976).

[10] C. Uher, *Physical Properties of High Temperature Superconductors II*, World Scientific, 1992.

[11] M. Nahum, S. Verghesse, P. L. Richards, and K. Char, Applied Physics Letters **59**, 2034 (1991).

# Appendix B

# List of Publications

**J. H. T. Ransley**, P. F. McBrien, G. Burnell, E. J. Tarte, J. E. Evetts, R. R. Schulz, C. W. Schneider, A. Schmehl, B. Goetz, H. Bielefeldt, H. Hilgenkamp and J. Mannhart "Capacitance Measurements on Grain Boundaries in $Y_{1-x}Ca_xBa_2Cu_3O_{7-\delta}$", Proceedings of the International Workshop on Critical Currents, Gttingen, 2001, edited by Christian Jooss (University of Gttingen, Germany, 2001), p. 31-33

E.J. Tarte, P. F. Mcbrien, **J. H. T. Ransley**, R. H. Hadfield, E. I. Inglessi, W. E. Booij, G. Burnell and J. E. Evetts, " "Capacitance as a probe of high angle grain boundary transport in oxide superconductors", IEEE transactions on Applied Superconductivty **11**(1), 418-421 (2001)

**J. H. T. Ransley**, S. H. Mennema, G. Burnell, U. Balasumbramaniam, E. J. Tarte, M. G. Blamire, J. E. Evetts, J. Kye and B. Oh, "Y-Ba-Cu-O Grain Boundary Resistivity above and below the Critical Temperature", IEEE transactions on Applied Superconductivity **13**(2), 2886-2889 (2003)

**J. H. T. Ransley**, S. H. Mennema, K. G. Sandeman, G. Burnell, E. J. Tarte, M. G. Blamire, J. E. Evetts, J. Kye and B. Oh, "Normal State Resistance of Grain Boundaries in $YBa_2Cu_3O_{7-\delta}$", submitted to Applied Physics Letters. Preprint available at cond-mat\031136